

NUMERICAL SIMULATION OF THE MAY 15 AND  
APRIL 26, 1991 TORNADIC THUNDERSTORMS

by

**Lewis Donald Grasso**

Department of Atmospheric Science

Colorado State University

Fort Collins, CO 80523

Research Supported by

**National Science Foundation**

under Grant ATM-9420045

January 25, 1996

Atmospheric Science Paper No. 596

## ABSTRACT

### NUMERICAL SIMULATION OF THE MAY 15 AND APRIL 26, 1991 TORNADIC THUNDERSTORMS

Two tornado simulations were performed for this study. The first was for May 15, 1991. On this day a strong F2/F3 tornado struck Laverne, Oklahoma. The second was for April 26, 1991. A violent F4/F5 moved across north central Oklahoma. Both tornadic storms were triggered by a dry line.

The RAMS mesoscale model was initialized with standard synoptic scale data. The soil moisture was initialized with station precipitation reports. A total of six grids were used in both cases.

The model was able to generate a dry line in both cases. Deep tropospheric convection formed along the dry lines in the third grid. This grid had a horizontal grid spacing of 5.0km. No cumulus parameterization, warm bubbles or any other numerical technique was used to aid the development of convection.

A supercell thunderstorm formed approximately one hour after convection was initiated in both cases. As the storms moved towards the northeast an eastward bulge formed in the dry line. Cyclonic rotation began at the nose of the bulge in the lower boundary layer, beneath the convective storms. While the storms moved away from the dry line the forward flanking precipitation downdrafts expanded. Horizontal vorticity was positively tilted in the southern side of the downdrafts. The resulting vertical vorticity was horizontally converged to feed the intensifying tornadoes. In time the downdrafts wrapped around to the rear flanks of the storms causing vertical vorticity to be produced in a larger area. The tornadoes were mature at this time.



Both tornadoes formed within the boundary layer and moved upward into the parent thunderstorm. At the mature stage, both tornadoes reached the storms' top. The origin of rotation was vertical vorticity generated by positive tilting of horizontal vorticity in the lowest few hundred meters *in the downdrafts*.

The maximum horizontal wind speed for the May case was 60m/s at 50m. The pressure drop in the core was 30mb. The April tornado had a maximum horizontal wind speed of 102m/s at 50m with a pressure drop of 95mb in the core.

Lewis D. Grasso  
Department of Atmospheric Science  
Colorado State University  
Fort Collins, Colorado 80523  
Spring 1996

## ACKNOWLEDGEMENTS

My warmest thanks are extended to the following people: Dr. William Cotton, Dr. Robert Walko, and Dr. John Weaver for their guidance and discussions on the subject of tornadoes. I am grateful to my wife for her love, support, and patience while I worked towards the Ph.D degree.

## TABLE OF CONTENTS

<b>1</b>	<b>Introduction</b>	<b>1</b>
1.1	Purpose of Research . . . . .	1
1.2	Tornadic Supercell Environment . . . . .	2
1.3	Previous Modeling Work . . . . .	5
<b>2</b>	<b>Model Description and Initialization</b>	<b>9</b>
2.1	Model Setup . . . . .	9
2.2	Model Initialization . . . . .	12
<b>3</b>	<b>May 15, 1991 Simulation</b>	<b>17</b>
3.1	Introduction . . . . .	17
3.2	May 15, 1991 Observations . . . . .	17
3.3	Dry Line Evolution . . . . .	22
3.4	Dry Line Dynamics . . . . .	26
3.5	Supercell Evolution . . . . .	38
3.6	Tornado Evolution . . . . .	48
3.7	Tornado Characteristics . . . . .	57
3.8	Summary of May Simulation . . . . .	60
<b>4</b>	<b>April 26, 1991 Simulation</b>	<b>62</b>
4.1	Introduction . . . . .	62
4.2	April 26, 1991 Observations . . . . .	62
4.3	Dry Line Evolution . . . . .	65
4.4	Dry Line Dynamics . . . . .	72
4.5	Supercell Evolution . . . . .	80
4.6	Tornado Evolution . . . . .	86
4.7	Tornado Characteristics . . . . .	96
<b>5</b>	<b>Circulation and Vorticity Analysis</b>	<b>101</b>
5.1	Circulation Analysis . . . . .	101
5.2	Numerical Tests . . . . .	114
5.3	May 15, 1991 Tornado . . . . .	117
5.4	Vorticity Analysis . . . . .	122
5.5	Summary of the May 15, 1991 Tornado Genesis Process . . . . .	129
5.6	April 26, 1991 Tornado . . . . .	130
5.7	Summary of the April 26, 1991 Tornado Genesis Process . . . . .	135

<b>6</b>	<b>Summary and Conclusions</b>	<b>137</b>
6.1	Summary of Both Cases . . . . .	137
6.2	Conclusions . . . . .	139
6.3	Future Research . . . . .	140
<b>7</b>	<b>References</b>	<b>145</b>

## Chapter 1

### INTRODUCTION

#### 1.1 Purpose of Research

Before discussing any scientific concepts concerning the tornado, the author decided to present the reader with two very different views about the most intense geophysical vortex, the tornado. These views have been presented in the introduction of my Masters Thesis, (Grasso, 1992) they are worth repeating here with modification.

Each spring in the central plains of the United States, groups of people get very excited with the appearance of a morning “shotgun” sounding displayed on a workstation. Quickly they click the mouse to see if colder air will advect in aloft, and they jump up and down if they see positive vorticity advection over the region in question. Some people lose composure, as the mouse is clicked to display the jet stream winds to see where the right entrance region or the left exit region is in relation to other features. Although these people have individual names, collectively they are called “tornado chasers” or “tornado groupies”. After they examine all the different fields and it looks like tornadic storms are possible, their hearts start pounding, the blood rushes through their veins, some may even hyper-ventilate, the excitement is overwhelming, quite similar to children on Christmas morning waiting to rush to the tree to open their gifts!

The next thing these people must do is find someone who is willing to sacrifice their car; in case of large hail, core punching, as it’s called. Some people do this for fun! That one lucky person must also be willing to risk getting a speeding ticket, as it is often necessary to exceed legal speed limits to get better video. Oh my God, who has the camcorder? Once this person is found, off they go, racing aimlessly across unfamiliar territory

in the hopes of witnessing one of mother natures' most awesome, beautiful and devastating phenomena...the tornado!

If these people are lucky enough to see a tornado their reaction is all the same, blurred indistinguishable speech. Just listen to any video as testimony. Suddenly they are overwhelmed by shock and their speech slows to a grinding halt as though a divine event has occurred. They all try to say "wow" while their lower jaw falls to the ground. What they are witnessing is incomprehensible.

For the people who are directly effected by the tornado, however, there is nothing exciting about it, in fact, it is more like a living hell. Loved ones killed, dream homes completely destroyed, one's sense of security is lost, and in some cases entire towns are wiped off the face of the earth in a matter of a few short horrifying moments that ironically seems like forever to end. It is for this very reason that tornadoes must be understood...to save lives.

## 1.2 Tornadic Supercell Environment

Major tornado outbreaks are generally associated with synoptic scale baroclinic waves (Newton et al. 1978). Thirty tornadoes associated with a severe weather event is not uncommon. As an extreme case, nearly one hundred and fifty tornadoes formed on April 3-4, 1974.

In the first few kilometers above the ground, a baroclinic wave causes warm moist air to flow northward from the Gulf of Mexico. Above the boundary layer, warmer and drier air flows towards the northeast from the desert southwest. This air mass forms a capping inversion and acts to prevent convection from occurring until the afternoon. The low level winds will display significant veering. Speed shear is characteristic of the middle to upper tropospheric winds (Fawbush and Miller, 1954). Temperature and moisture soundings, in the warm sector of the baroclinic wave, may exhibit large amounts, up to 5000 J/kg, of convective available potential energy (CAPE).

Jet streams, associated with synoptic scale baroclinic waves, have smaller scale wind speed maxima, called jet streaks (Palmen and Newton, 1969, pg 199), embedded in them.

Secondary circulations associated with jet streaks provide favorable locations for severe weather events.

As a air parcel enters the jet streak the pressure gradient, acting to the left of the parcel movement, increases and dominates the coriolis force. Because of the imbalance of the two forces, a secondary circulation forms at the entrance region. As a result of the secondary circulation, the right side of the entrance to the jet streak is a region of upward vertical motion.

Air parcels exiting the jet streak will experience a larger coriolis force compared to the pressure gradient. A secondary circulation forms and causes upward vertical motion on the left side of the exit region. The two regions of upward vertical motion are preferred regions of severe weather events (Uccellini and Johnson,1979).

A long-lived supercell required a balance between the vertical shear and CAPE. Numerical experiments (Weisman and Klemp,1982) have demonstrated that very large values of shear, relative to CAPE, can cause a growing thunderstorm to lean significantly and experience too much entrainment of midlevel air. The entrainment will erode the warm interior of the storm and cause it to dissipate. At the other extreme, large values of CAPE, relative to vertical shear, have produced storms that form rapidly moving gustfronts. The horizontal convergence and vertical lifting, associated with the gustfront, move away from the storm. Without the lifting the parent storm dissipates.

Weisman and Klemp (1982) were able to classify thunderstorm type based on the bulk Richardson number, the ratio of CAPE to the vertical shear. Tornadic supercells fell in the range from 15 to 35. Multicell storms occurred when the bulk Richardson number exceeded 40. The reader is cautioned, however, that a given storm may exhibit characteristics of both (Cotton and Anthes,1989,pg 526).

The location where the middle to upper tropospheric southwesterly jet flows over the low level southerly jet is a region of large vertical shear. The large shear causes the thunderstorms to lean and causing precipitation to fall outside the updraft (Ludlam,1963). Numerical experiments have shown that the strength of the vertical shear is critical for supercell development (Klemp and Wilhelmson,1978a,b; Lilly,1982).

Lilly (1986a,b) suggests that the long life of supercell thunderstorms may be explained by helicity, the inner product of the vorticity and wind vector. The idea is that highly helical flows do not suffer as much turbulent dissipation. Thus less energy flows into the smaller scales. The supercell environment is characterised by large values of helicity and this may explain the longevity of these types of thunderstorms. This explanation, however, is not sufficient. The supercell will dissipate if the gustfront moves away from the storm's base, regardless of how helical the flow is.

In the warm sector of the baroclinic wave the explosive release of convective energy in a strongly sheared environment can be realized by the action of one more necessary ingredient, a lifting mechanism. Lifting can be accomplished by a frontal boundary, terrain, the dry line (Rhea,1966) or an outflow boundary of an existing thunderstorm.

The dry line is of particular interest for this study. In both simulations, thunderstorms formed above a dry line. In the early morning the thickness of the moist layer decreases towards the west due to the increase in elevation of the terrain in the central plains. Daytime heating has been proposed to erode the shallow moist layer by vertical mixing and to give the appearance that the dry line moved rapidly eastward (Schafer,1974).

In the afternoon vertical circulations associated with the dry line increase. As a result, horizontal convergence increases as does the horizontal gradient of moisture. Solenoidal processes, formed by virtual potential temperature gradients across the dry line, may enhance the dry line circulation (Benjamin and Carlson,1986; Sun and Wu,1992; Ziegler et al.,1995). Recently Shaw (1995) demonstrated the importance of surface characteristics on dry line evolution. He was able to show that gradients in soil moisture were necessary for dry line development. Ziegler et al. (1995) demonstrated that the water vapor field, denoting the dry line, experienced a positive frontogenetic forcing in the lower boundary layer. If the vertical motion at the dry line is strong enough and there is sufficient CAPE then thunderstorms can form.

Once thunderstorms develop, they generally move eastward continually ingesting boundary layer air that is rich with convective available energy. These long-lived supercells can spawn violent tornadoes.



An unanswered question is "do tornadoes develop from the midlevels of supercell thunderstorms downward or from the ground upward?". Early observations of tornadic supercell thunderstorms indicate that strong midlevel rotation in the updraft often precedes the formation of tornadoes by thirty minutes (Burgess,1976). The midlevel rotation was observed to lower in the Union City, Oklahoma, tornado (Brown et al.,1978).

The rotation seen by radar is called the tornado vortex signature, TVS. The TVS is a large velocity difference,  $\Delta v$ , between two adjacent gates at the same range (Brown et al.,1978). Many time-height plots of  $\Delta v$  can be seen in Vasiloff (1993). The dynamic pipe effect has been used as a possible explanation for the downward development of tornadoes (Smith and Leslie,1979). The main feature of this theory is that the descending vortex is required to maintain cyclostrophic balance. Since the sides of the vortex are in a balance, air can only enter from below. As air converges beneath the vortex it achieves cyclostrophic balance, thus lowering the vortex. Is the tornado in exact cyclostrophic balance? If so, what prevents the condensate in the visible funnel from being centrifuged away? Photographs show that the condensate in tornadoes have well defined, sharp boundaries.

To keep our study of tornadoes interesting, non-supercell thunderstorms also produce tornadoes without an associated mesocyclone (Brady and Szoke,1989). These types of storms grow in environments with a very deep adiabatic layer (Davies,1993). The thunderstorms grow rapidly on wind shift boundaries. Pre-existing vertical vorticity, in the boundary layer, associated with the wind shift line is amplified to produce a tornado. These thunderstorms have been shown to develop tornadoes upwards from the boundary layer (Wakimoto and Wilson,1989) rather than downwards from the pre-existing mesocyclone.

Obtaining direct measurements of the tornado is not a simple task. Bluestein (1983) attempted to place a 400 pound barrel, equipped with instruments, in the path of a tornado. Try after try, the instruments were rarely put in the direct path of a tornado. For the more violent tornadoes, the instruments would probably be completely destroyed, if they could be found at all.

A safer approach is to use a numerical model. First the model must demonstrate its ability to simulate such an event. It will be shown that the model used for this study does have the capability of simulating a strong and violent tornado.

### 1.3 Previous Modeling Work

The use of three dimensional numerical cloud models to study thunderstorm dynamics made its debut in the 1970's. Since that time many simulations of thunderstorms have been conducted (Wilhelmson, 1974; Schlesinger, 1978; Klemp and Wilhelmson, 1978a,b; Schlesinger, 1980; Klemp et al., 1981; Rotunno and Klemp, 1982; Weisman and Klemp, 1982). The knowledge of thunderstorms was advanced a great deal by these studies.

Even though a tornado was not explicitly resolved, Klemp and Rotunno (1983) and Rotunno and Klemp (1985) were able to deduce a theory for low level rotation, but not ground rotation, from a thunderstorm simulation. Basically they argue that the main vorticity source is generated in a baroclinic zone along the forward-flanking outflow boundary between cool and warm air. This horizontal vorticity is then tilted upward while the parcel ascends. They also conducted a circulation analysis, assuming a non-rotating frictionless frame, to show that buoyancy did increase circulation as a material curve moved toward a vertical vorticity maximum at 250m.

There are few numerical simulations of tornadoes that include the parent thunderstorm. Grasso (1992) and Grasso and Cotton (1995) initialized a three dimensional grid domain horizontally homogeneous with a special sounding taken near the May 20, 1977 Del City, OK tornadic thunderstorm. Convection was initiated by placing a warm bubble in the center of the grid near the ground. With a total of three two-way interactive grids, a weak tornado was simulated along with the parent thunderstorm.

They concluded that massless particles that originated near cloud base on the northeast side of the storm moved westward into the precipitation downdraft. Maintaining a cyclonic trajectory, the particles descended in the downdraft on the west side of the storm. The particles continued to turn cyclonically near the surface and were ingested into the vortex. This implied that vertical vorticity was generated within the forward downdraft

and that the source of air for the tornado was within the boundary layer and not within the mesocyclone.

Using a similar procedure, Wicker and Wilhelmson (1995) with a different model and an idealized sounding, simulated a weak tornado and the parent thunderstorm. This was an important first step as these studies demonstrated a numerical model's ability to simulate a tornado along with the parent thunderstorm. Their results demonstrate that parcels passing through the forward flanking downdraft acquire positive vertical vorticity from tilting of horizontal vorticity. Horizontal convergence then amplifies the vertical vorticity as the parcel ascends to the analysed positive vertical vorticity maximum at 100m.

Recently Davies-Jones and Brooks (1993) examined the origin of a positive vertical vorticity maximum at 100m for a non-tornadic supercell. The horizontal vorticity was divided into two components, one baroclinic and the other barotropic. The pre-storm horizontal vorticity is the barotropic part while the vorticity generated by the storm's buoyancy gradient was termed baroclinic. They conducted a circulation analysis for the positive vertical vorticity maximum. They assumed a non-rotating frictionless frame and showed that buoyancy increased the circulation along a material curve. That is, the storm enhanced the barotropic vorticity baroclinically. The resulting vorticity was postulated to have been tilted in the downdraft. The resulting vertical vorticity was then amplified by horizontal convergence.

Two dimensional axisymmetric models have also been used to study the tornado (Lewellen, 1993). Although these models cannot address tornado genesis they can be used to study characteristics of an intense vortex. A non-dimensional parameter commonly used is the swirl number,  $S = \frac{v_0}{w_0}$ , where  $v_0$  is the tangential wind speed at some fixed radius  $r_0$  and  $w_0$  is the updraft on top of the vortex. Results demonstrated that when the swirl increased the vortex developed a central downdraft. For very large values of swirl, the central downdraft reached the lower boundary and multiple vortices formed (Davies-Jones, 1986 and Ward, 1972).

In free slip simulations, vertical vorticity existed at the lower boundary while the tangential winds achieved cyclostrophic balance. When a no slip lower boundary was used,

cyclostrophic balance was not obtained. Radial inflow was enhanced and the radius of maximum tangential winds decreased (Walko and Gall,1986 and Howells et al.,1988).

The intent of this study is to perform a tornado simulation starting with a realistic variable initial state. Two cases, May 15, 1991 and April 26, 1991, were chosen. In both cases, tornadic thunderstorms formed on a dry line. Three questions were asked. First, could the numerical model being used, trigger deep tropospheric convection without the aid of data assimilation, warm bubbles or cumulus parameterization? Second, would there be enough meteorological information in the initial synoptic scale to allow for tornadic thunderstorms? Third, will the simulated tornadoes form within the boundary layer, then upward into the thunderstorms mesocyclone or downward from the elevated mesocyclone?

## Chapter 2

### MODEL DESCRIPTION AND INITIALIZATION

#### 2.1 Model Setup

The numerical model used for the April 26 and May 15, 1991 tornadic simulations was the moving grids, Version 3a, of the Regional Atmospheric Modeling System (referred to as RAMS) developed at Colorado State University (Pielke et al.,1992). The following features of the model were used:

- Non-hydrostatic and compressible (Tripoli and Cotton,1986a).
- Mahrer-Pielke (Mahrer and Pielke,1977) radiation scheme for both longwave and shortwave radiation with longitudinal variations of short wave irradiance. The frequency of calculated radiation tendencies was 900s.
- A soil model for the first 50 cm below ground using eleven prognostic levels (Tremback and Kessler,1985). The soil type used was sandy clay loam throughout the entire model domain. As the model was advanced, soil moisture at the ground was reduced due to the flux of moisture upward. Any precipitation that fell to the ground increased the soil moisture.
- A vegetation model (Avissar and Pielke,1989). This was run using variable vegetation types (Loveland et al.,1991) on all grids.
- Hybrid timestep scheme. Momentum was advanced using a leapfrog scheme while scalars were advanced using a forward scheme. Both used second order advection.
- Vertical and horizontal turbulence was parameterized using a Smagorinsky deformation based K (Smagorinsky,1963) with stability modifications (Lilly,1962).

- A bulk microphysical scheme that included the following hydrometeor species: cloud, rain, aggregates, grauple, hail, snow, and pristine ice (Walko et al.,1995).
- The prognostic variables were the three components of momentum,  $u$ ,  $v$  and  $w$ , Exner function  $\pi$ , total water  $r_t$  and ice-liquid potential temperature  $\theta_{il}$  (Tripoli and Cotton,1980,1982,1989a,b).
- Terrain-following sigma coordinate system (Tripoli and Cotton,1980).
- Two way interactive moving nested grids (Clark and Farley,1984).
- Arakawa fully staggered C grid (Arakawa and Lamb,1981).
- Exner function tendencies used to update the momentum variables were computed using a time split scheme, similar to Klemp and Wilhelmson (1978a).

Surface fluxes of heat and moisture were computed using a leaf area index, LAI, a multiplication factor in the vegetation model. The LAI is a constant, depending on the vegetation type, that multiplies the fluxes. As a result, unrealistically large surface fluxes have occurred at some grid points, particularly those with large soil moisture values. It was observed that the winds, generally at the lowest model level, became very irregular, looking somewhat noisy at these regions. To correct this situation, the LAI was not permitted to exceed 3.0. This limit on LAI is reasonable because at (realistic) higher values, the lower levels of the canopy will not be exposed to as much sunlight and wind as higher up, and will thus transpire less. Numerically the values of LAI larger than 3.0 would result in producing unrealistically large fluxes.

It is interesting to note that changes in the soil moisture and vegetation types can have a profound influence on simulated convection associated with a dry line (Shaw, 1995).

The two way interactive nested grids are able to move within a parent grid (Walko et al.,1995). This is a valuable feature for the model as this allows one to use smaller nested grids, thus producing smaller computer memory requirements. It is important to understand how a nested grid moves. Consider two grids, the first with a grid spacing of 1000 meters in the x-direction and the second having a 50 km side in the y-direction. Grid

#2 will move east at 5.0 m/s, including the grid for the soil model. Dividing the Grid #1  $\Delta x$  by the Grid #2 speed will give a time that the model must advance before Grid #2 changes its position. For this example, Grid #2 will change its position toward the east every 200s. When the second grid moves, a new region, one Grid #1  $\Delta x$  and 50km in  $y$ , will be added to the east side of Grid #2. This new strip will have the same grid spacing as Grid #2 and all Grid #1 variables will be interpolated into this region, including topography, vegetation type and soil moisture. The western part of Grid #2 having the same dimensions as the new strip, will be removed. The new position of Grid #2 will be one Grid #1  $\Delta x$  to the east of its original location. Any number of nested grids can move simultaneously during a simulation.

When the model is started at time  $T_0$ , a reference state is computed and kept fixed for the entire simulation. This has very interesting consequences when considering vertical tendencies. The buoyancy tendency is computed by comparing the temperature at a grid point at  $T+N\Delta T$ , where  $N \geq 1$ , to the temperature at the same grid point at time  $T_0$ . If the  $T+N\Delta T$  temperature is warmer than the  $T_0$  temperature then the buoyancy will be positive. This means that if the model is started in the morning, the warmer afternoon boundary layer will be positively buoyant. The vertical gradient of Exner function will be negative to keep the boundary layer from rising. That is, the sign of the vertical gradient of Exner function and buoyancy are dependent on the time the model is started. It is not necessarily correct to examine either of these two terms independently or attach much physical significance to them. The buoyancy and vertical gradient of Exner function must be considered acting together in the vertical equation of motion. It should be mentioned that the total condensate mixing ratio is also included in the buoyancy calculation and is a negative acceleration.

In the model the horizontal components of the wind,  $u$  and  $v$ , were computed at  $z_t$  levels and the vertical component,  $w$ , at  $z_m$  levels (Figure 2.1). The first  $z_m$  level is the ground. There are no tendencies of  $w$  at this level, rather  $w$  is diagnosed from  $u$  and  $v$  at the second  $z_t$  level, one half  $\Delta z$  above, and the slope of the sigma surface. The first  $z_t$  level is one half  $\Delta z$  below ground and at this level  $u$  and  $v$  are set equal to those at the

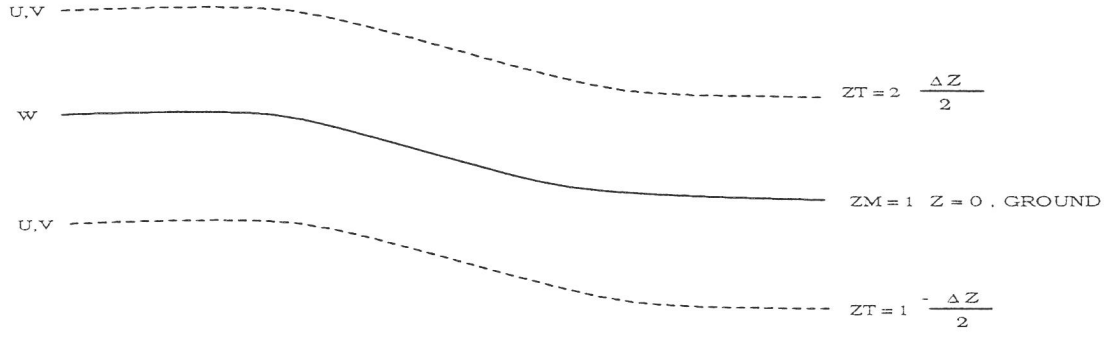


Figure 2.1: An example of a vertical cross section of the RAMS grid showing the first vertical sigma levels. The dashed lines, referred to as  $z_t$  levels, are where  $u$  and  $v$  are defined. The solid line, referred to as a  $z_m$  level, is where  $w$  is defined.

second  $z_t$  level. Since  $u$  and  $v$  are vertically-homogeneous from the first to second  $z_t$  level, the interpolated  $u$  and  $v$  at the ground are not zero and thus the lower boundary is not a no-slip boundary. There is, however, a drag imposed on  $u$  and  $v$  at the second  $z_t$  level. This makes the lower boundary not a true free slip boundary. As a result the lower boundary can be called quasi-no slip.

If the reader wishes to delve deeper into the model design, the following papers may prove useful: Tripoli and Cotton(1981), Cotton et al. (1982;1986), Tremback et al. (1985), Tripoli (1986), Peilke et al. (1992), and Walko et al. (1995).

## 2.2 Model Initialization

The April 26, 1991 Red Rock, Oklahoma tornado simulation was initialized with archived standard synoptic scale data from 1200 UTC April 26, 1991. This included 2.5 degree gridded data on pressure surfaces, soundings, and surface observations. Displayed in Figure 2.2 are the initial water vapor mixing ratio field and the horizontal wind vectors at 49m for grid one.

The soil moisture was initialized using a technique based on the Antecedent Precipitation Index, API, (Wetzel and Chang,1988 and Copeland, 1995). This procedure uses the three months of archived station precipitation reports in the continental United States prior to model start time. Precipitation values were weighted more if the dates of the station



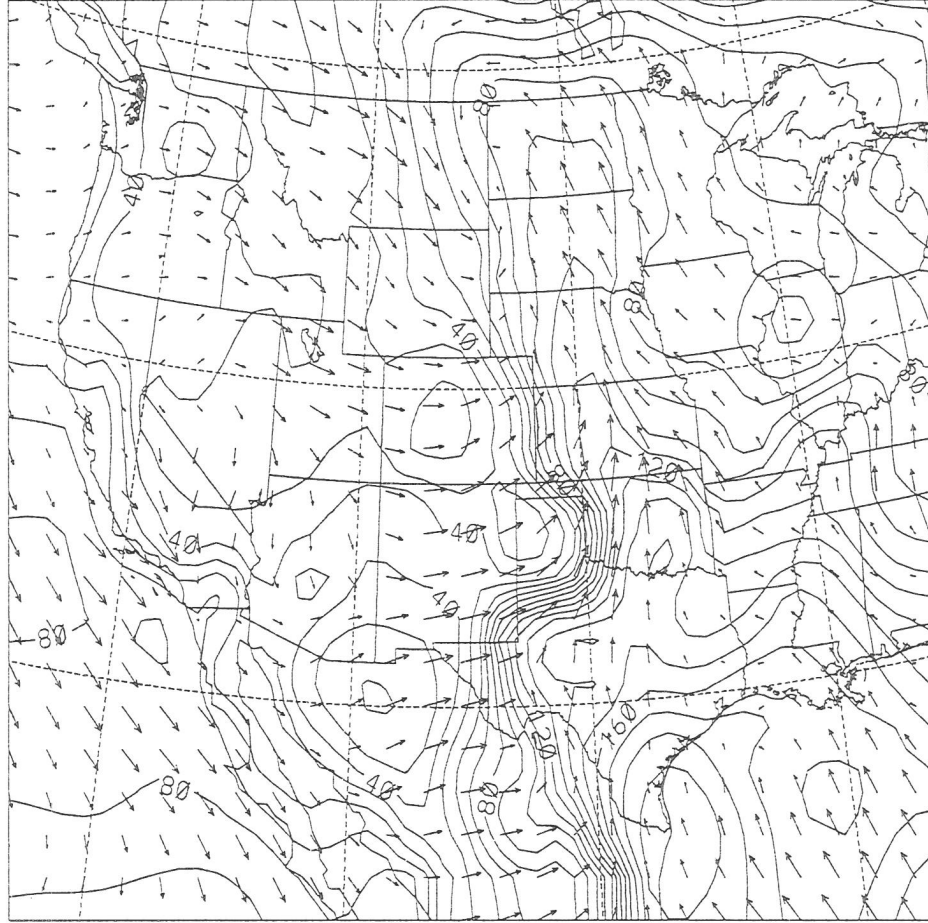


Figure 2.2: Initial fields for April 26, 1991 in Grid #1 at 49m. Solid lines, contoured every 1 g/kg, represent the water vapor mixing ratio. The contours have been multiplied by 10.0. A contour label of 120 represents a value of 12 g/kg. The arrows are horizontal wind vectors. A vector having a length equal to the distance between the tails of any two vectors has a speed of 17 m/s.

reports were closer to model start time. For the April case, the soil moisture values were smoothed and reduced ten percent in value; see Figure 2.3.

The horizontal grid spacing,  $\Delta x = \Delta y$ , used for this study was 75km, 25km, 5km, 1km, 333m, and 111m for grids one through six, respectively. The vertical grid spacing started at 100m and was increased using a stretching ratio of 1.1. The model top was just over 23km.

The lateral and top boundaries were nudged during the simulation using the 1200 UTC April 26, 1991 and the 0000 UTC April 27, 1991 archived synoptic scale data.

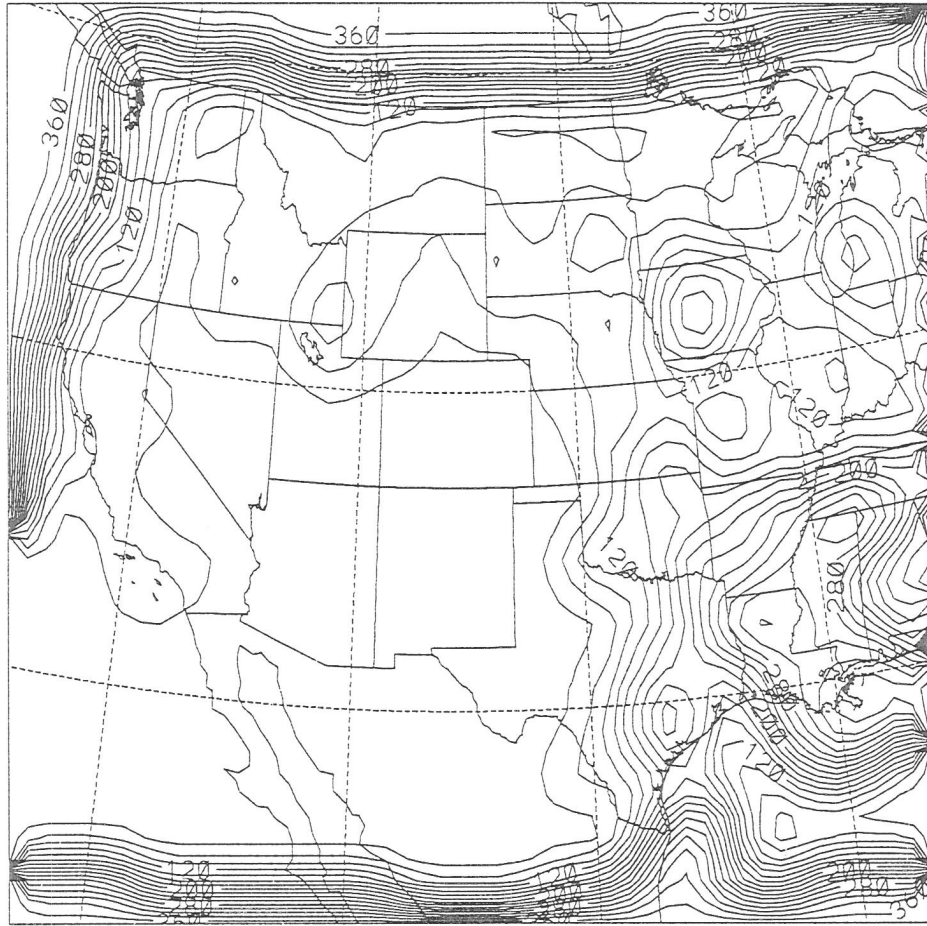


Figure 2.3: Initial soil moisture for April 26, 1991 in Grid #1. The values were smoothed and reduced by ten percent. All soil levels were initialized with the same horizontal profile. A contour labeled 120 represents a value of  $.12 \text{ m}^3 \text{ water} / \text{m}^3 \text{ scl}$  where scl stands for sandy clay loam. This particular soil type saturates at a value of .42 (Tremback and Kessler, 1985).

For the May 15, 1991 Laverne, Oklahoma tornado simulation, the initialization was similar to the April case. The initial winds and water vapor mixing ratio field at 49m is shown in Figure 2.4. Soil moisture was initialized from the API procedure and was not smoothed or reduced in value; the initial field is shown in Figure 2.5. The large gradients in soil moisture near the boundaries for both cases are a result of the grid extending beyond station sites where precipitation is reported. These regions are assumed to have no influence on the simulations, particularly on tornado genesis.

The horizontal grid spacing,  $\Delta x = \Delta y$ , used for this study was 60km, 20km, 5km, 1km, 333m, and 111m for grids one through six, respectively. The vertical grid spacing

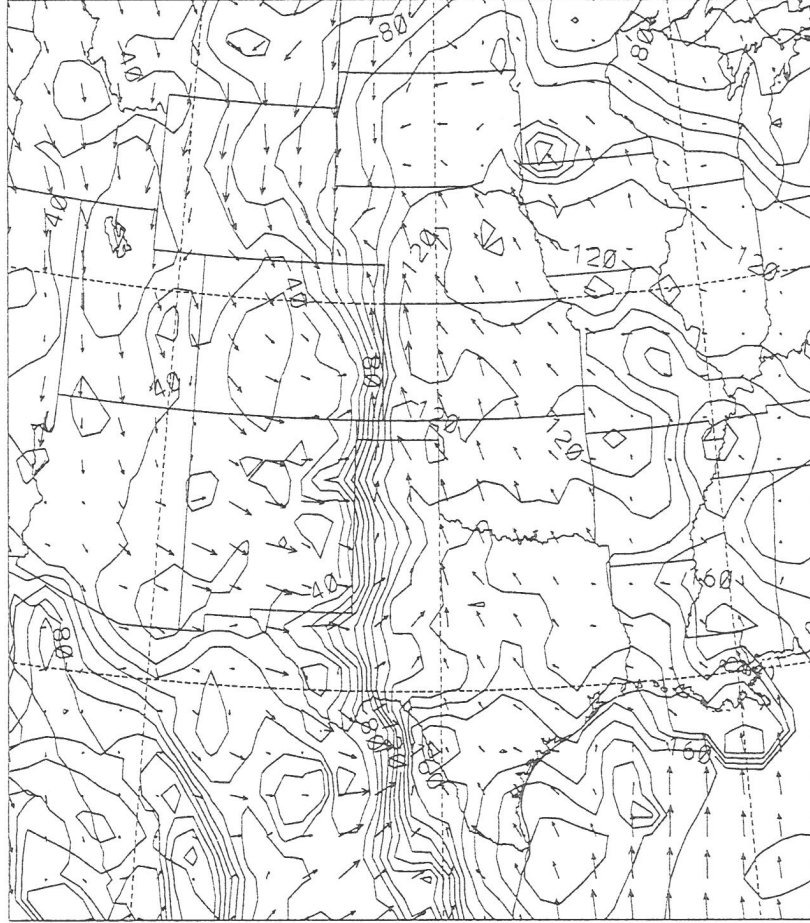


Figure 2.4: The initial fields for May 15, 1991 in Grid #1 at 49m. Solid lines, contoured every 1 g/kg, represent the water vapor mixing ratio. The contours have been multiplied by 10.0. A contour label of 120 represents a value of 12 g/kg. The arrows are horizontal wind vectors. A vector having a length equal to the distance between the tails of any two vectors has a speed of 10 m/s.

started at 100m and was increased using a stretching ratio of 1.075. The model top was just over 19km.

The lateral and top boundaries were nudged during the simulation using the 1200 UTC May 15, 1991 and the 0000 UTC May 16, 1991 archived synoptic scale data. Both simulations used a 30s topography data set in all grids.

It is very important to remember that no data assimilation techniques (other than nudging at the lateral boundaries of the coarse grid), cumulus parameterization, or warm bubbles were used in any grid at any time during the simulations for either case.

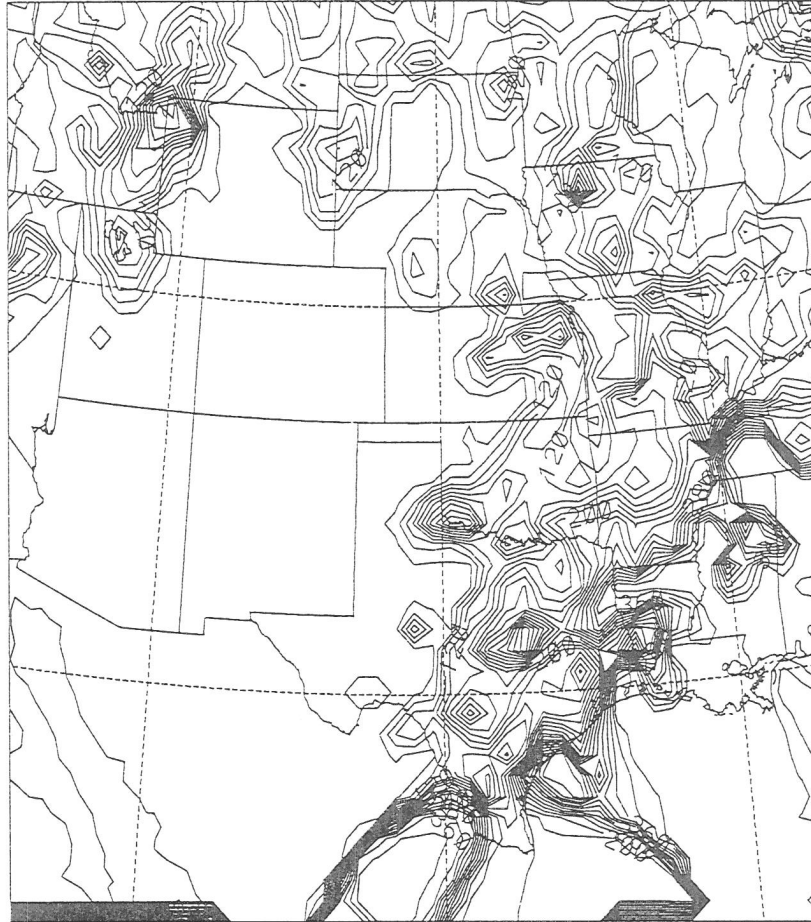


Figure 2.5: Initial soil moisture for May 15, 1991 in Grid #1. The values were not smoothed or reduced. All soil levels were initialized with the same horizontal profile.

## Chapter 3

### MAY 15, 1991 SIMULATION

#### 3.1 Introduction

Results of the May 15, 1991 Laverne, Oklahoma tornado simulation will be presented in this chapter. With a total of six grids, a wide range of meteorological scales were resved. The first grid contained the synoptic scale while grids four and six contained the thunderstorm and tornado scale, respectively. The majority of this chapter will focus on the smaller simulated scales. A discussion on the observed events of this day will be addressed first.

#### 3.2 May 15, 1991 Observations

At 1200 UTC a broad region of low pressure existed from southeast Wyoming and western Nebraska south to western Texas. The center of the low was in northeast Colorado. A moisture gradient extended from the low southward west of the Texas Panhandle. To the east morning temperatures varied from 16 to 20C with dew points also in this range. Dew points in eastern New Mexico were near -10C. Surface winds, in the central plains, were generally from the south or southeast at approximately ten knots (Figure 3.1).

A cut off low at 500 mb was situated just north of the Four Corners region at 1200 UTC. The winds associated with the low were not very strong, maximum winds were 24.0 m/s to the south of the low over the Arizona-New Mexico border. A well-defined diffluent pattern existed to the southeast of the Texas Panhandle and western Oklahoma due to a short wave orientated over eastern Texas southeastward into the Gulf of Mexico (Figure 3.2a). Similar flow features existed at 300 mb. The wind speeds were slightly

stronger at this level; a 30.0 m/s speed maximum existed in eastern New Mexico (Figure 3.2b). As the low moved eastward into Colorado, temperatures warmed between 28 and 31°C over the central and southern plains.

The convective available potential energy, CAPE, was computed by first calculating the lowest 100mb mean temperature and mixing ratio. A hypothetical parcel was lifted dry adiabatically, from the surface, until saturation, then along a moist adiabat. The positive area was summed and is referred to as CAPE. As indicated in Figure 3.2c, values of 1200 J/kg are in west central Texas while values over 800 J/kg are in the panhandle. Note the rapid decrease in values from the central panhandle toward the west. This was due to the reduction of water vapor in the boundary layer.

A sounding and hodograph at 1200 UTC, Figure 3.2 d, was taken at the location where the simulated tornado formed later in the afternoon. The boundary layer could be characterized as stable and there was also a considerable reduction of moisture with height. At this time only 724 J/kg of energy is available to convection. Although the winds veered with height, curvature of the hodograph was lacking in the lower atmosphere. The tropospheric wind speeds were all less than or equal to 35 knots.

This is a good example of how a sounding can be misleading when one is trying to identify regions with the potential for tornadic thunderstorms. Although not a simple task, one must also consider how the meteorological fields evolve with time to change the sounding and hodograph.

This particular dry line was observed as part of the COPS-91 field experiment (Hane et al., 1993). The gradient of moisture, approximately 18°C/100km, moved into the eastern Texas Panhandle by 1800 UTC. East to southeast winds on the moist side of the dry line converged with dry westerly winds to the west. The dry line remained stationary and in the late afternoon two tornado watch boxes existed. One covered an area from much of western Oklahoma and the eastern Texas Panhandle. The other covered the western third of Kansas and a small portion of northeast Colorado.

Thunderstorms did form along the dry line in the late afternoon. A weak short lived tornado was spawned in Shamrock, Texas. A more significant F2-F3 tornado formed

at 0135 UTC near Laverne, Oklahoma in Harper County. The tornado was on the ground

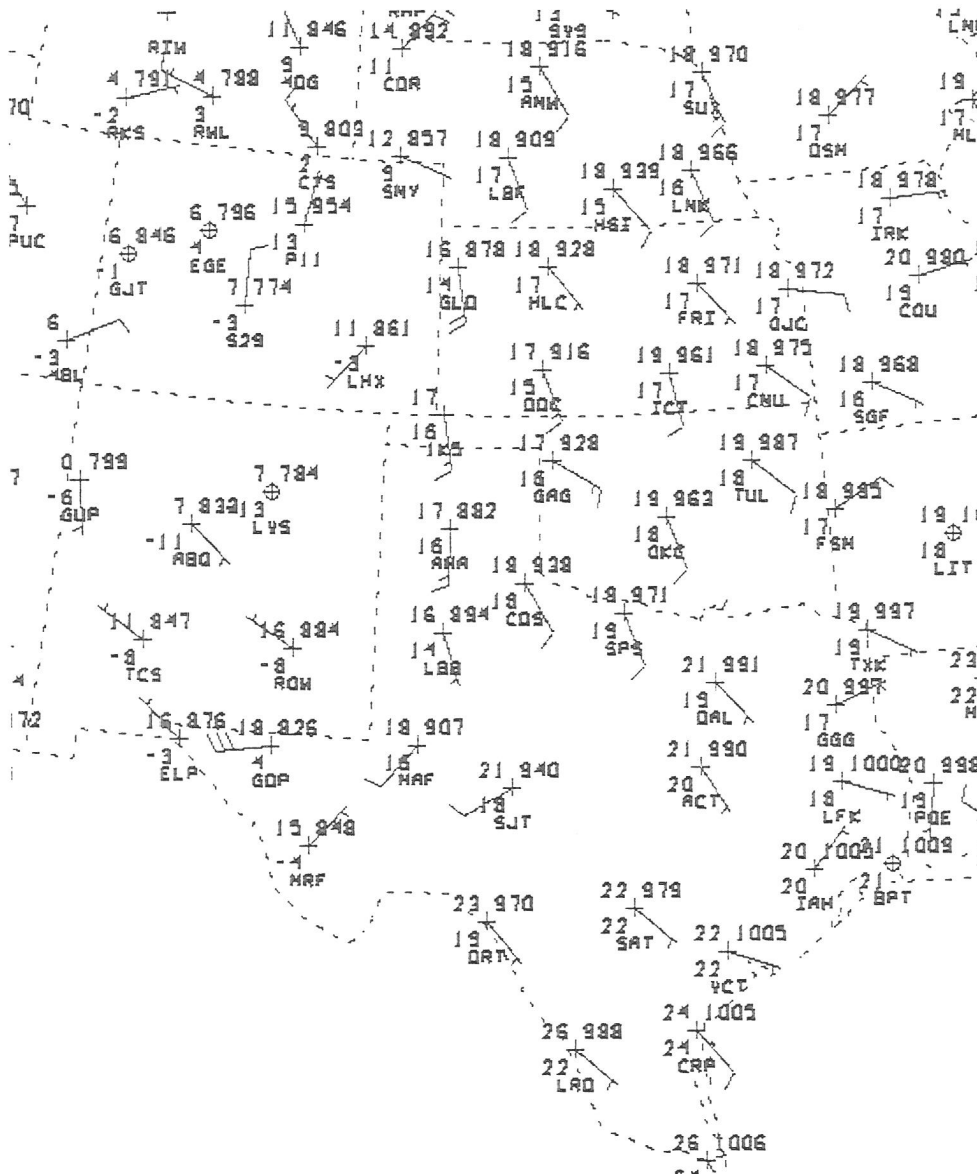


Figure 3.1: 1200 UTC May 15, 1991 surface chart, temperatures and dewpoints are in degrees Celsius. Wind barbs are in knots.

for thirty six minutes and had a path length of just under twelve miles. Hailstones with a diameter of four inches occurred with this storm. The simulation of the Laverne tornado is the focus of this chapter.

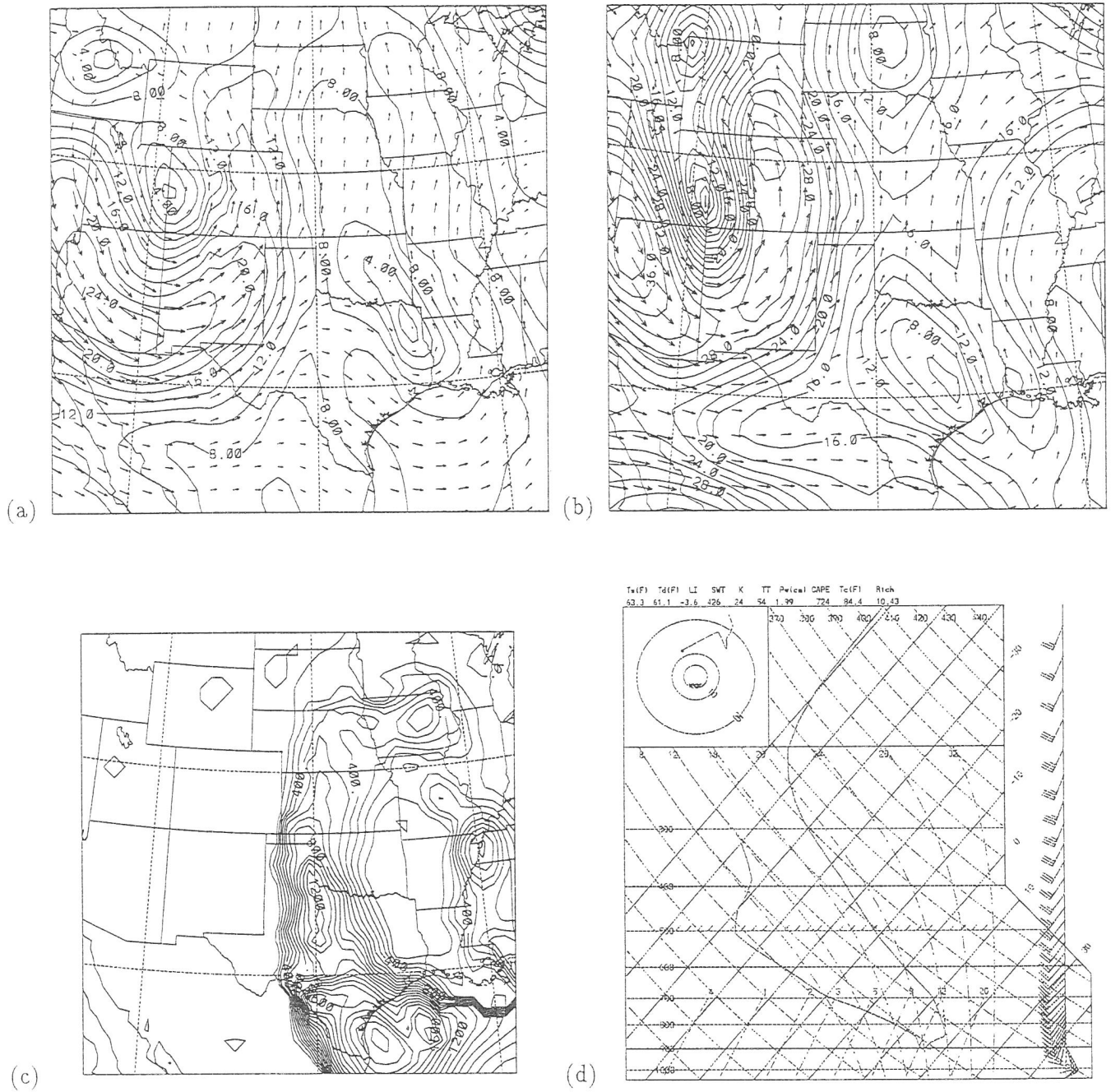


Figure 3.2: (a) and (b) Horizontal wind vectors and speed, contoured every 2.0 m/s, at 500 mb and 300 mb, respectively, (c) Convective available potential energy, contoured every 100 J/kg, and (d) A sounding in the north central Texas panhandle. All figures were at 1200 UTC.



### 3.3 Dry Line Evolution

As the simulation ran forward in time, the moisture gradient was quite weak in the northern Texas panhandle until early afternoon. At 1800 UTC the water vapor mixing ratio in Figure 3.3 shows the weak gradient. The maximum of 18 g/kg in the lower right portion of the Figure was due to large fluxes of moisture from the wet soil below. The soil may have been too wet but its influence on the water vapor field was restricted to near the surface. One can see the gradient was larger in the southern panhandle as southerly winds converged with southeasterly winds south of the wet soil. In the northern regions of the panhandle, although the moisture gradient was weak, moist southeasterly winds were converging with dry southwesterly winds.

Due to the convergence in the boundary layer, water vapor was transported to higher levels. In Figure 3.4 a noticeable maximum in water vapor mixing ratio values of 8 g/kg can be seen near the center and lower left side of the figure. This maximum is embedded in winds that turn cyclonically from the southwest to the north. One would expect to find a maximum of upward vertical motion where the water vapor mixing ratios were large. Upward vertical motion did exist in a 200km region in the bottom half of Figure 3.5. The magnitudes of the upward motion were not particularly large but it was enough to indicate the beginnings of a circulation along the dry line.

One hour later, 1900 UTC, the overall flow at 49m was the persistent moist southeasterly flow converging with dry southwesterly flow in the central panhandle. As a result the water vapor mixing ratio gradient increased in the central and northern panhandle compared to 1800 UTC (Figure 3.6).

At 1515m the flow remained the same as one hour earlier. The water vapor mixing ratio field changed considerably. The environmental winds had advected the moist air northward from where it was transported vertically. As a result, a larger portion of Grid #3 had been moistened (Figure 3.7).

Upward vertical motion at 1515m and 1900 UTC had grown in horizontal extent and was directly over the large gradient in water vapor mixing ratio at 49m. The ascent

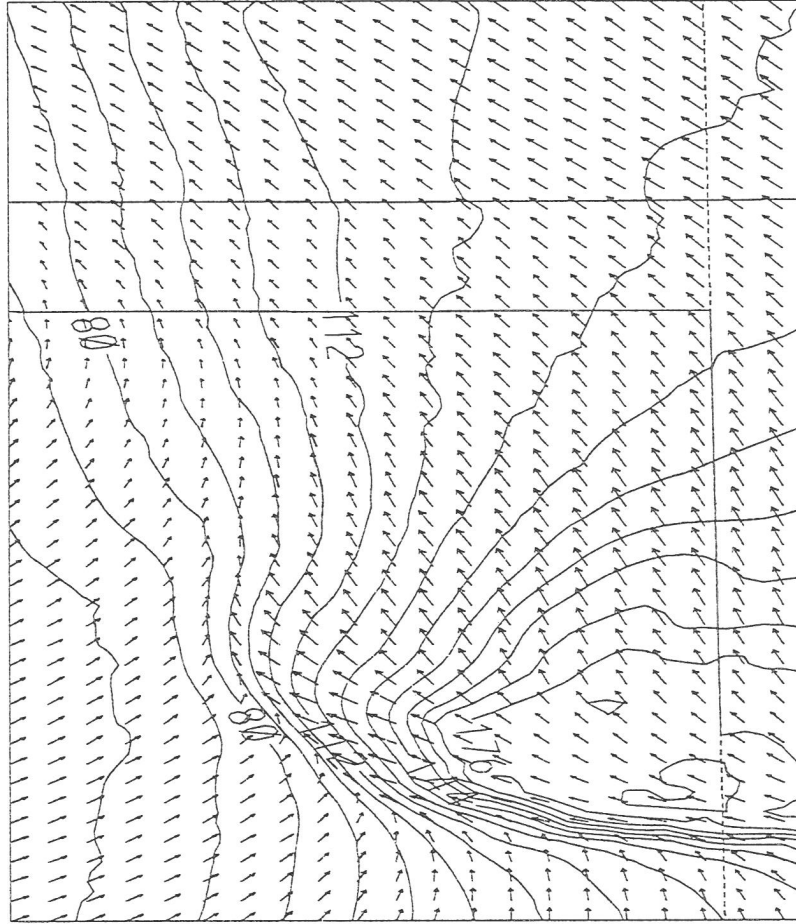


Figure 3.3: Horizontal winds and water vapor mixing ratio values for Grid#3 at 49m and 1800 UTC. From a minimum of 5.6 g/kg, the mixing ratio field is contoured every 0.8 g/kg to a maximum of 18.4 g/kg. A wind vector having a length equal to the distance between two wind vector tails represents a speed of 9.4 m/s.

also increased from 18.0 cm/s one hour earlier to 77 cm/s. This was a clear indication that the vertical circulation along the dry line was strengthening (Figure 3.8).

At 2000 UTC, the large gradient of water vapor mixing ratio in the central Texas panhandle was the main feature at 49m (Figure 3.9). Convergence of the horizontal winds was very strong in the central panhandle compared to 1800 UTC. From a numerical point of view, the large gradient in water vapor covered only a few  $\Delta x$ . One might expect turbulent diffusion to prevent the large gradient from occurring. The fact that diffusion did not remove the large gradient was an indication of just how strong the forcing was associated with the rapid intensification of the dry line.

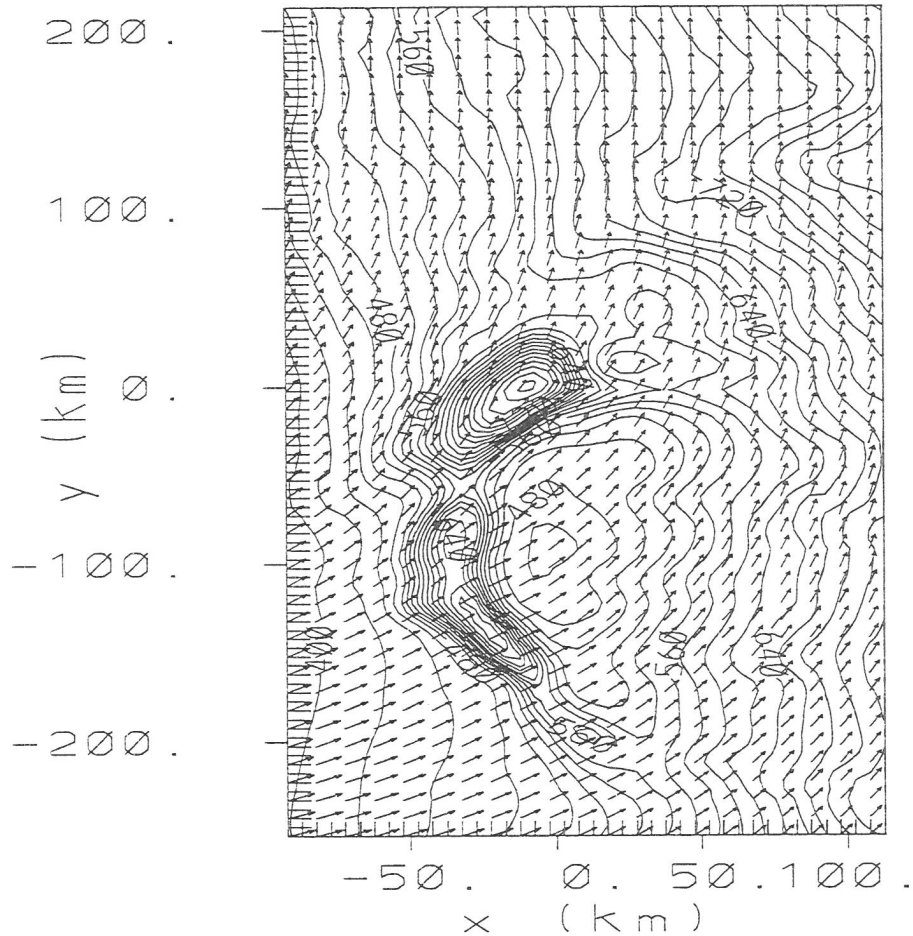


Figure 3.4: Horizontal winds and water vapor mixing ratio values for Grid #3 at 1515m and 1800 UTC. Mixing ratio values range from 3.8 g/kg to a maximum of 8.4 g/kg contoured every 0.2 g/kg. A wind vector having a length equal to the distance between two wind vector tails represents a speed of 11.5 m/s.

The winds have backed in the northern portion of the grid, compared to earlier times, at 1515m. Dry air to the right of the center of the grid is flanked by moist air transported upward by the dry line circulation (Figure 3.10).

A well-defined band of upward vertical motion dominated the interior of Grid #3 at 1515m and 2000 UTC. Upward vertical speeds of 1.0 to 2.8 m/s were common in this 300 km long region (Figure 3.11). It is surprising that cumulus convection was initiated at this time and within this grid having  $\Delta x$  and  $\Delta y$  equal 5.0 km. Numerically, one could argue that it is quite surprising that convection survived in this grid for the next few hours

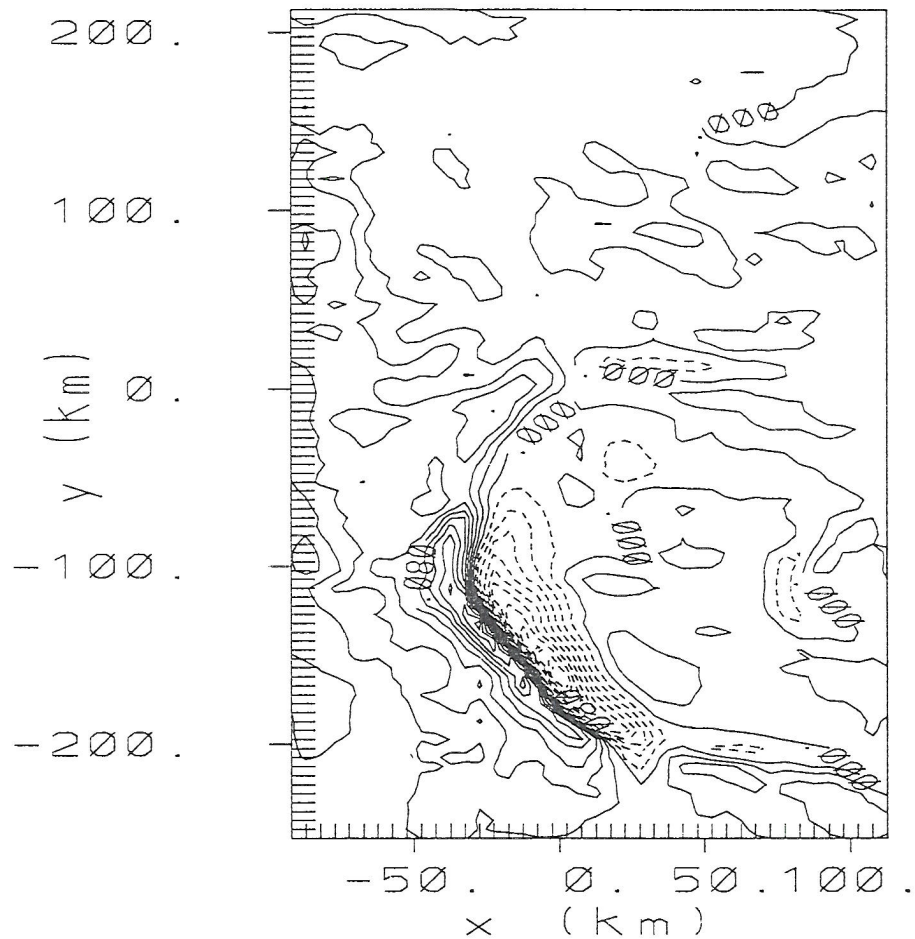


Figure 3.5: Upward vertical motion at 1515m for grid #3 at 1800 UTC. With a contouring of 2.0 cm/s, the minimum and maximum values are -18.0 and 18.0 cm/s respectively.

with no finer nest spawned. This is another indication of the forcing associated with the intensification of the dry line and the conditional instability of the atmosphere.

The next two figures, Figure 3.12 and Figure 3.13, show the well-defined dry line at 2100 UTC at 49m and the vertical motion at 3063m in the Texas panhandle. A line of convection approximately 100 km in length existed at this time along the dry line. One can see individual convective cells with updraft speeds of 10m/s.

Strong convergence can be seen along the dry line just west of the maximum in water vapor mixing ratio at 49m and 2100 UTC. No convection, however, developed in this region. As was mentioned previously, the wet soil was responsible for the maximum in the water vapor near the bottom right in Figure 3.12. As a result of the wet soil, the boundary

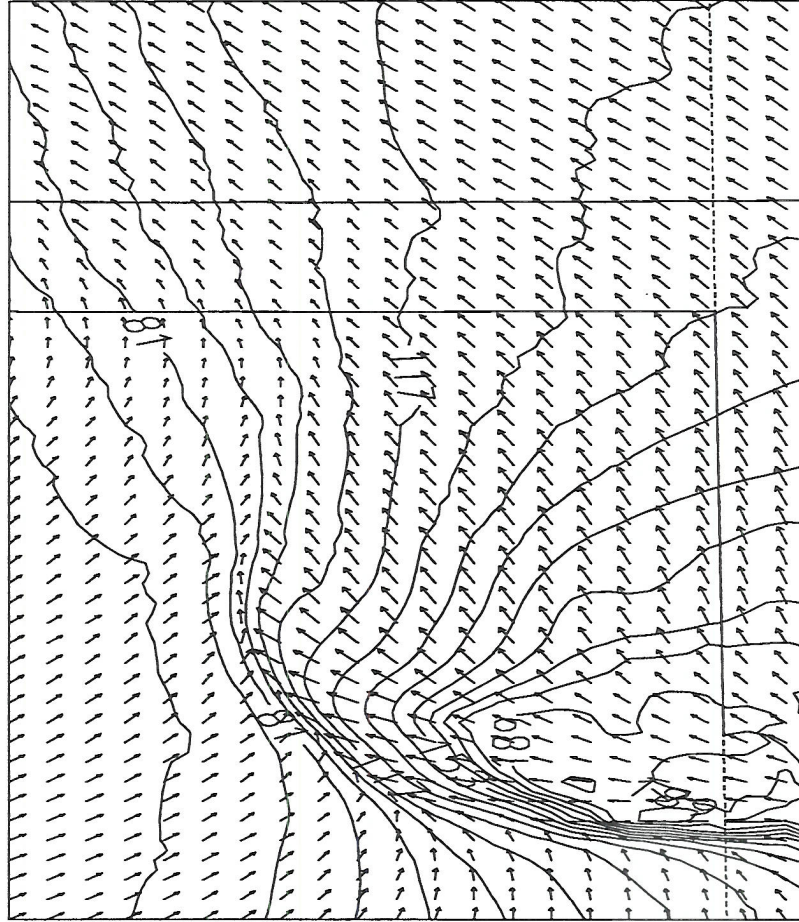


Figure 3.6: Horizontal winds and water vapor mixing ratio values for Grid #3 at 49m and 1900 UTC. From a minimum of 5.4 g/kg, the mixing ratio field is contoured every 0.9 g/kg to a maximum of 19.8 g/kg. A wind vector having a length equal to the distance between two wind vector tails represents a speed of 10.2 m/s.

layer was cooler in this region and prevented convection from occurring. A sensitivity run was done in which the soil moisture was reduced (Shaw, 1995). As a result, the boundary layer was warmer and deep tropospheric convection occurred in this region.

### 3.4 Dry Line Dynamics

It is interesting that the gradient of water vapor did not gradually increase, in time, near the surface. A numerical study of a dry line, by Ziegler et al. 1995, produced this feature as well. In their Figure 4a the moisture gradient remained relatively constant from early morning to early afternoon, after which time the gradient increased rapidly. They



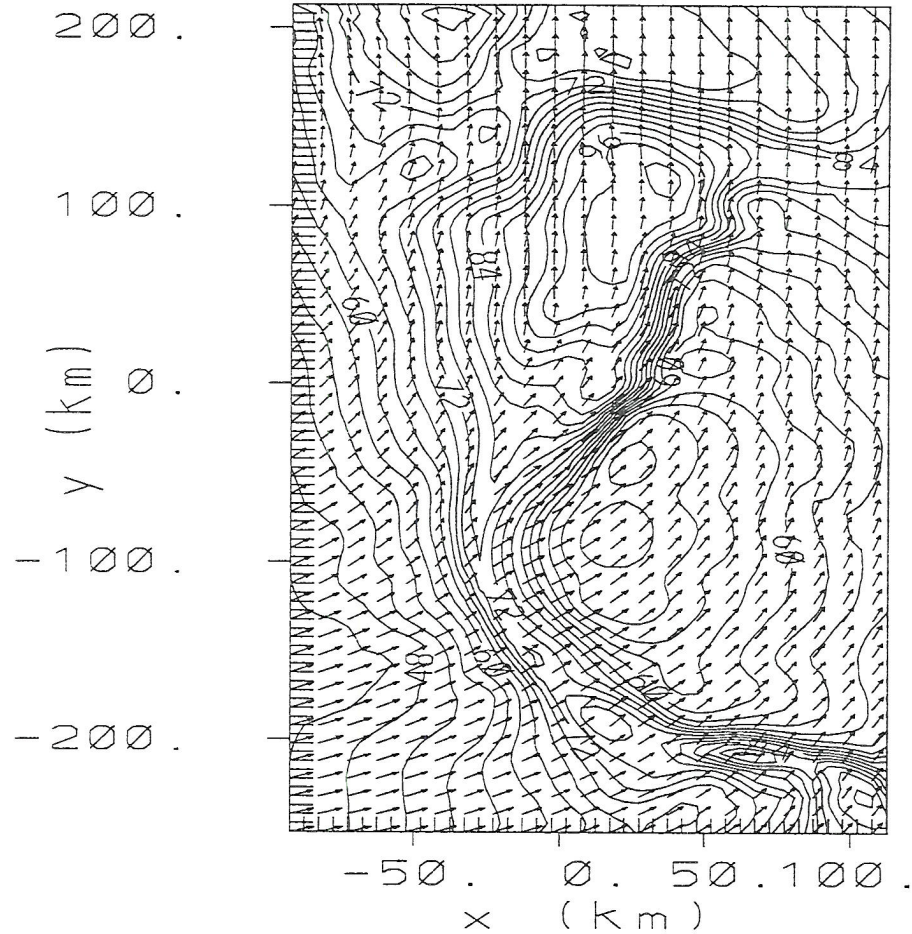


Figure 3.7: Horizontal winds and water vapor mixing ratio values for Grid #3 at 1515m and 1900 UTC. From a minimum of 4.2 g/kg, the mixing ratio field is contoured every 0.3 g/kg to a maximum of 10.2 g/kg. A wind vector having a length equal to the distance between two wind vector tails represents a speed of 12.1 m/s.

investigated the role of a thermally driven solenoid to explain the dry line evolution. In their Figure 7, the solenodal forcing was the dominant term in the Lagrangian frame. They also demonstrated that frontogenesis was occurring along the dryline in the lower boundary layer; see their Figure 8a.

Thermal solenoids and frontogenesis will be examined for the May 15, 1991 dry line in a manner similar to Ziegler et al. 1995. The solenoids will be analysed by examining the baroclinic generation of horizontal vorticity (the eastward gradient of model buoyancy) in the north-south direction. Frontogenesis will be analysed by examining two terms;  $-\frac{\partial u}{\partial x} \frac{\partial q}{\partial x}$ , and  $-\frac{\partial v}{\partial x} \frac{\partial q}{\partial z}$ .

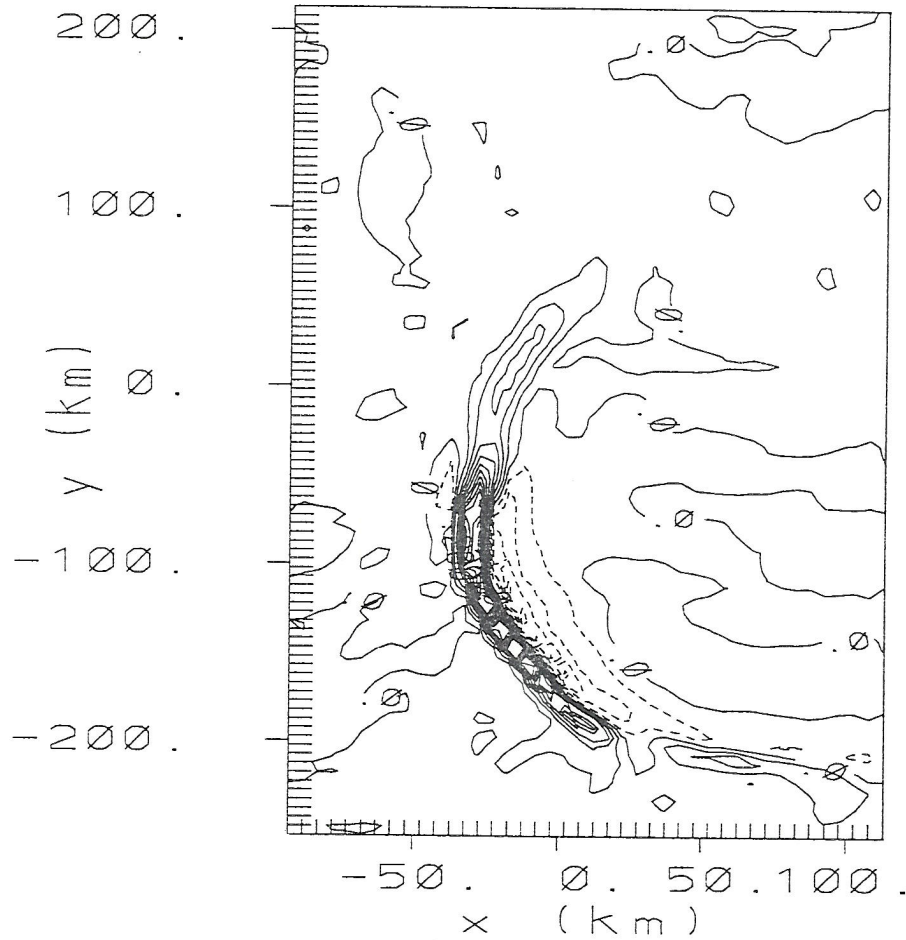


Figure 3.8: Upward vertical motion at 1515m for grid #3 at 1900 UTC. With a contouring of 7.0 cm/s, the minimum and maximum values are -28.0 and 77.0 cm/s respectively.

An east-west vertical cross section of the U component of wind and water vapor mixing ratio at 1200 UTC is displayed in Figure 3.14. The winds are westerly and increase with height while the water vapor mixing ratio decreases with height. From the figure the two frontogenetic terms are nearly zero since there is no vertical motion at this time and because the contours of water vapor are nearly horizontal. Thermal solenoidal forcing is also small, reaching a value of  $-1.0\text{E-}6\text{s}^{-2}$  in the lower right part of Figure 3.15.

A slight change had occurred in the water vapor mixing ratio field at 1400 UTC, Figure 3.16. The 12.0 g/kg contour intersected the ground. The winds remained westerly and increased with height up to 1.0km above which they decreased. Frontogenetic forcing was near zero due to  $\frac{\partial u}{\partial x}$  being approximately zero and since the vertical motion was on

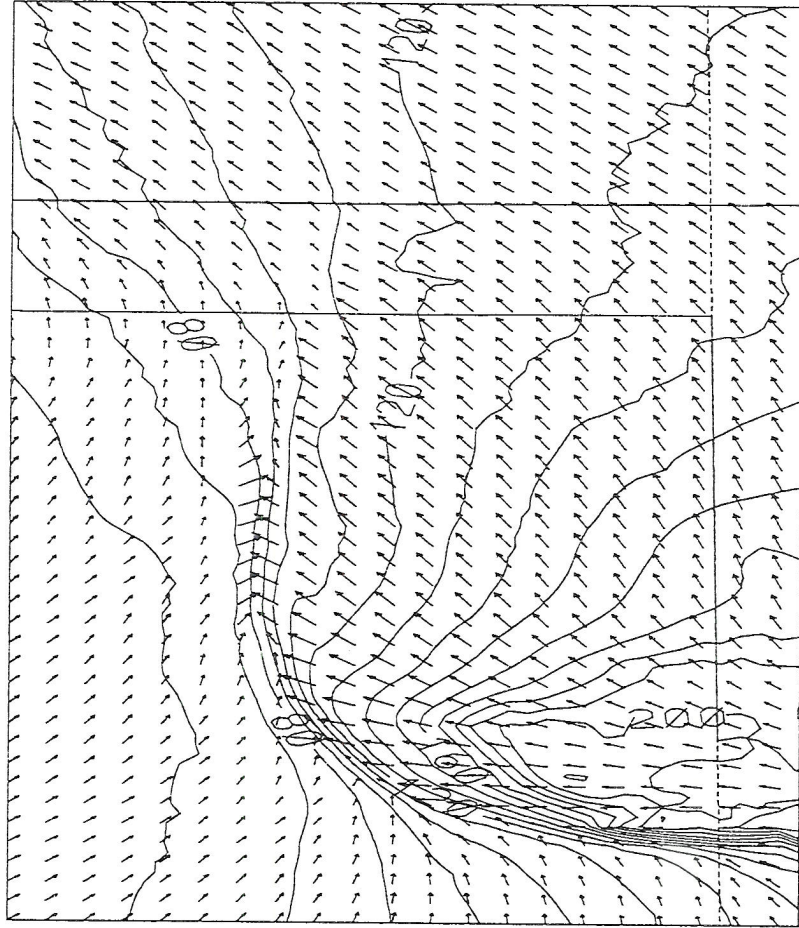


Figure 3.9: Horizontal winds and water vapor mixing ratio values for Grid #3 at 49m and 2000 UTC. From a minimum of 5.0 g/kg, the mixing ratio field is contoured every 1.0 g/kg to a maximum of 21.0 g/kg. A wind vector having a length equal to the distance between two wind vector tails represents a speed of 12.7 m/s.

the order of a few centimeters per second over a 5.0km horizontal distance giving  $\frac{\partial w}{\partial x}$  a magnitude of  $2.0E-6s^{-1}$ . The thermal solenoidal forcing at this time was essentially absent as can be seen in Figure 3.17.

At 1600 UTC horizontal convergence was evident in the lowest kilometer in Figure 3.18. Easterly winds appeared at this time in the lower right portion of the figure. The zero line intersected the ground just to the west  $X=75\text{km}$  and moved upward and to the right to intersect the vertical axis at  $Z=900\text{m}$ . An eastward gradient of water vapor existed, although weak. The two frontogenetic terms are both weak and of the order  $10^{-12}m^{-1}s^{-1}$ . The solenoidal forcing was weak as can be seen in Figure 3.19. Two zero contours bound a



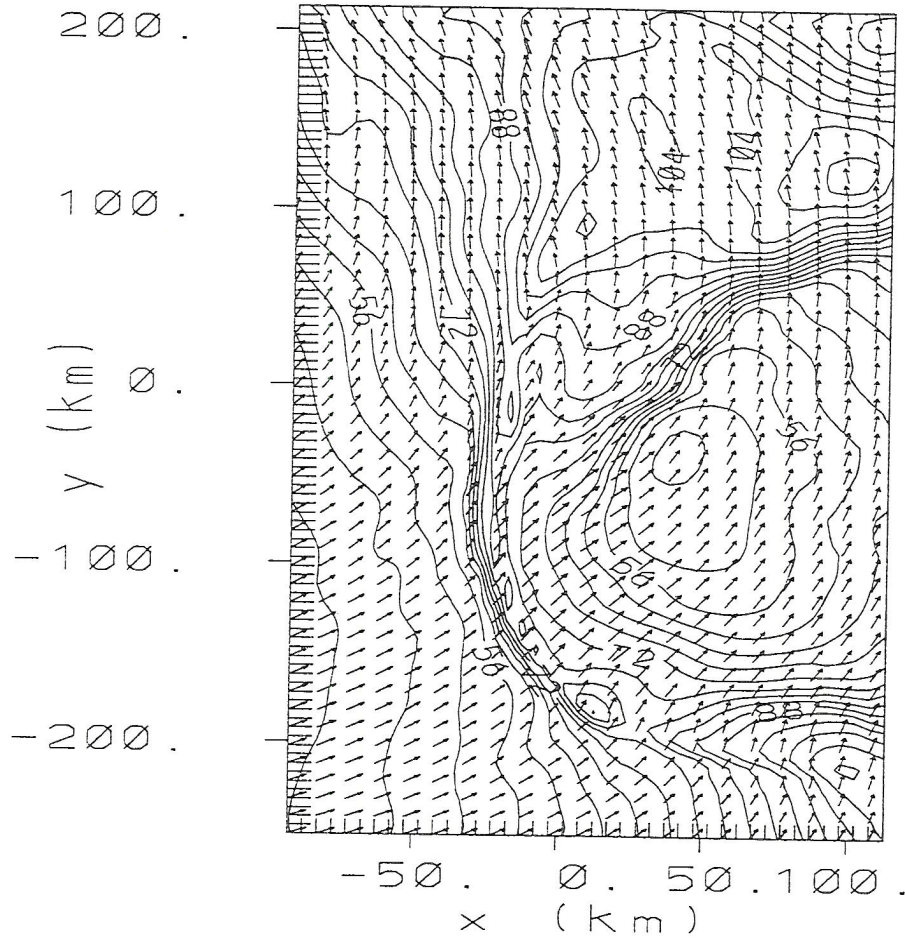


Figure 3.10: Horizontal winds and water vapor mixing ratio values for Grid #3 at 1515m and 2000 UTC. From a minimum of 4.0 g/kg, the mixing ratio field is contoured every 0.4 g/kg to a maximum of 11.2 g/kg. A wind vector having a length equal to the distance between two wind vector tails represents a speed of 13.7 m/s.

region of weak positive forcing (smaller than  $10^{-6}s^{-2}$ ) from the center of the figure upwards and to the left.

The easterly winds have moved westerward from 1600 UTC to 1800 UTC. The zero contour was located at  $X=62\text{km}$  in Figure 3.20. The eastward gradient of water vapor and the eastward convergence of momentum have approximately doubled in the lower boundary layer from 1600 UTC. The vertical gradient in water vapor and the vertical motion in the lower boundary layer were weak at this time. As a result, the frontogenetic forcing was only weakly positive. The solenoidal forcing grew in magnitude as can be seen in Figure 3.21. Values between  $10^{-6}s^{-2}$  and  $2 \times 10^{-6}s^{-2}$  dominated the central portion of the figure below

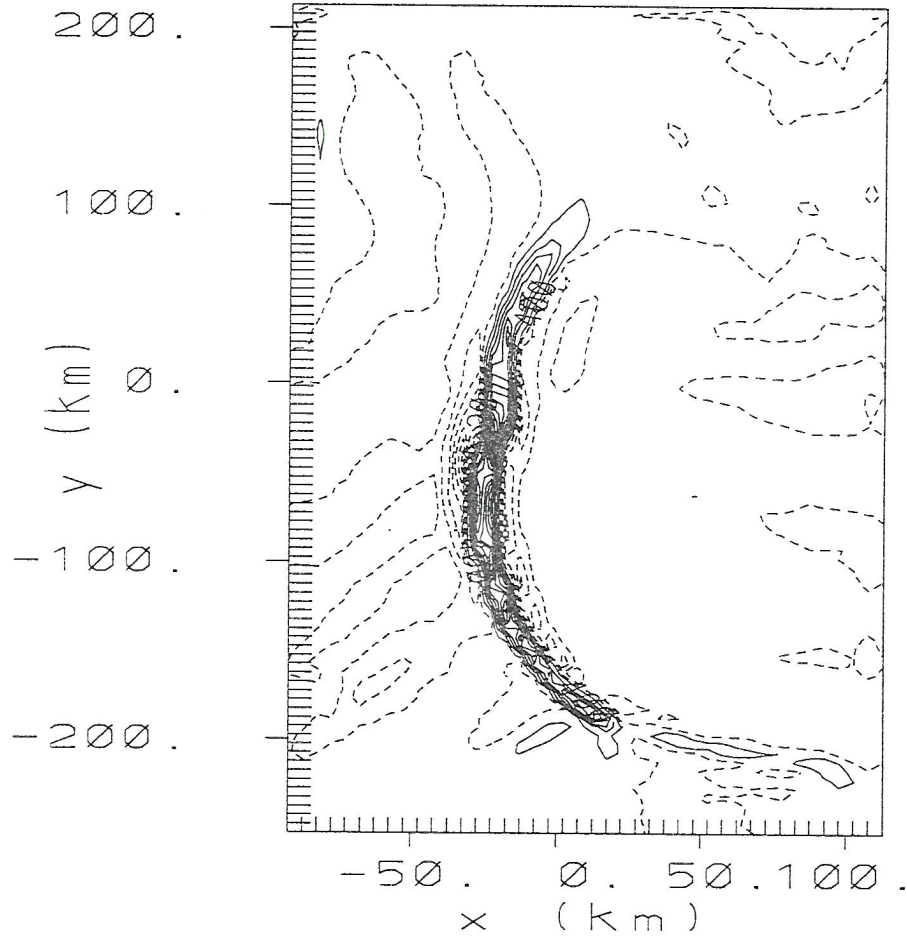


Figure 3.11: Upward vertical motion at 1515m for grid #3 at 2000 UTC. With a contouring of 20.0 cm/s, the minimum and maximum values are -1.2 and 2.8 m/s respectively.

1400m. Negative values having the same magnitude are seen at the left side of the figure below 1400m.

Dramatic changes occurred in the two hour period from 1800 UTC to 2000 UTC as can be seen in Figure 3.22 and Figure 3.23. The frontogenetic forcing was large and positive in the lower boundary layer due to the nearly vertical contours of water vapor combined with the strong convergence and large eastward gradient of water vapor. The negative product of convergence and the eastward gradient of water vapor has a magnitude of  $10^{-9}m^{-1}s^{-1}$ . Well defined positive and negative solenoidal forcing regions existed at 2000 UTC having maximum magnitudes of  $6 \times 10^{-6}s^{-2}$  and  $5 \times 10^{-6}s^{-2}$ , respectively.

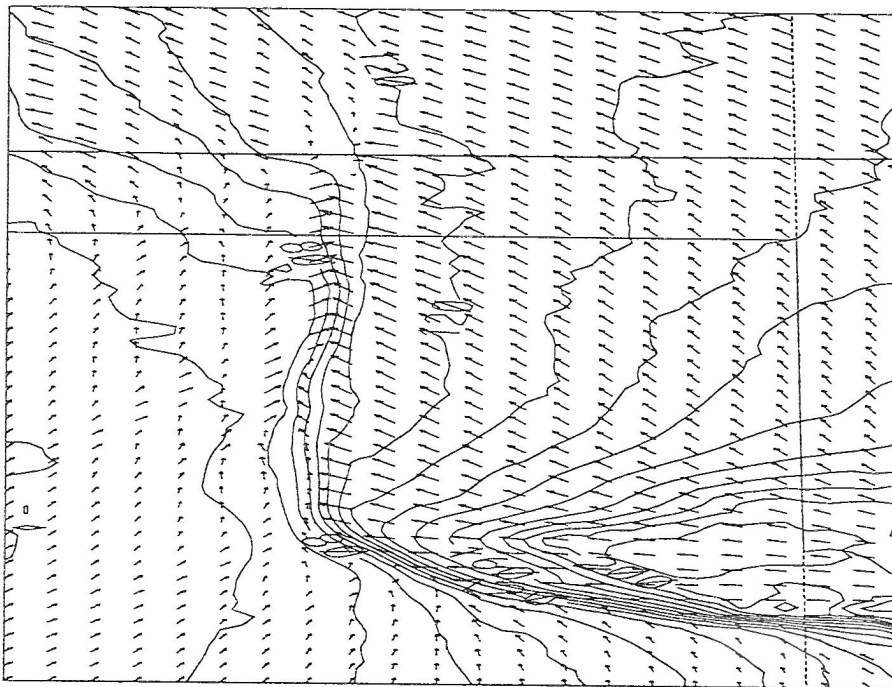


Figure 3.12: Winds and mixing ratio at 49m at 2100 UTC for Grid #3. From a minimum of 4.0 g/kg the mixing ratio field is contoured every 1.0 g/kg to a maximum of 22.0 g/kg.

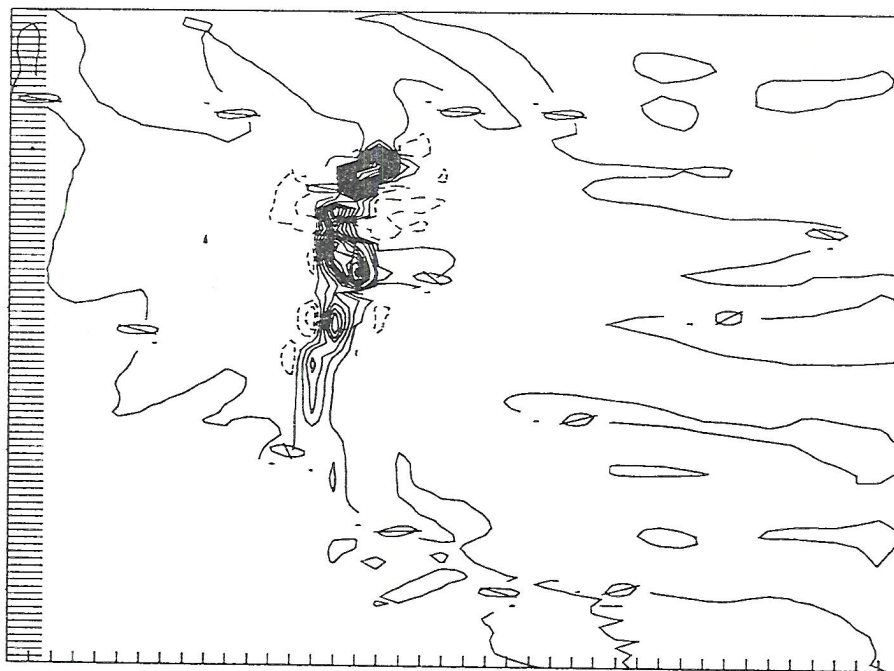
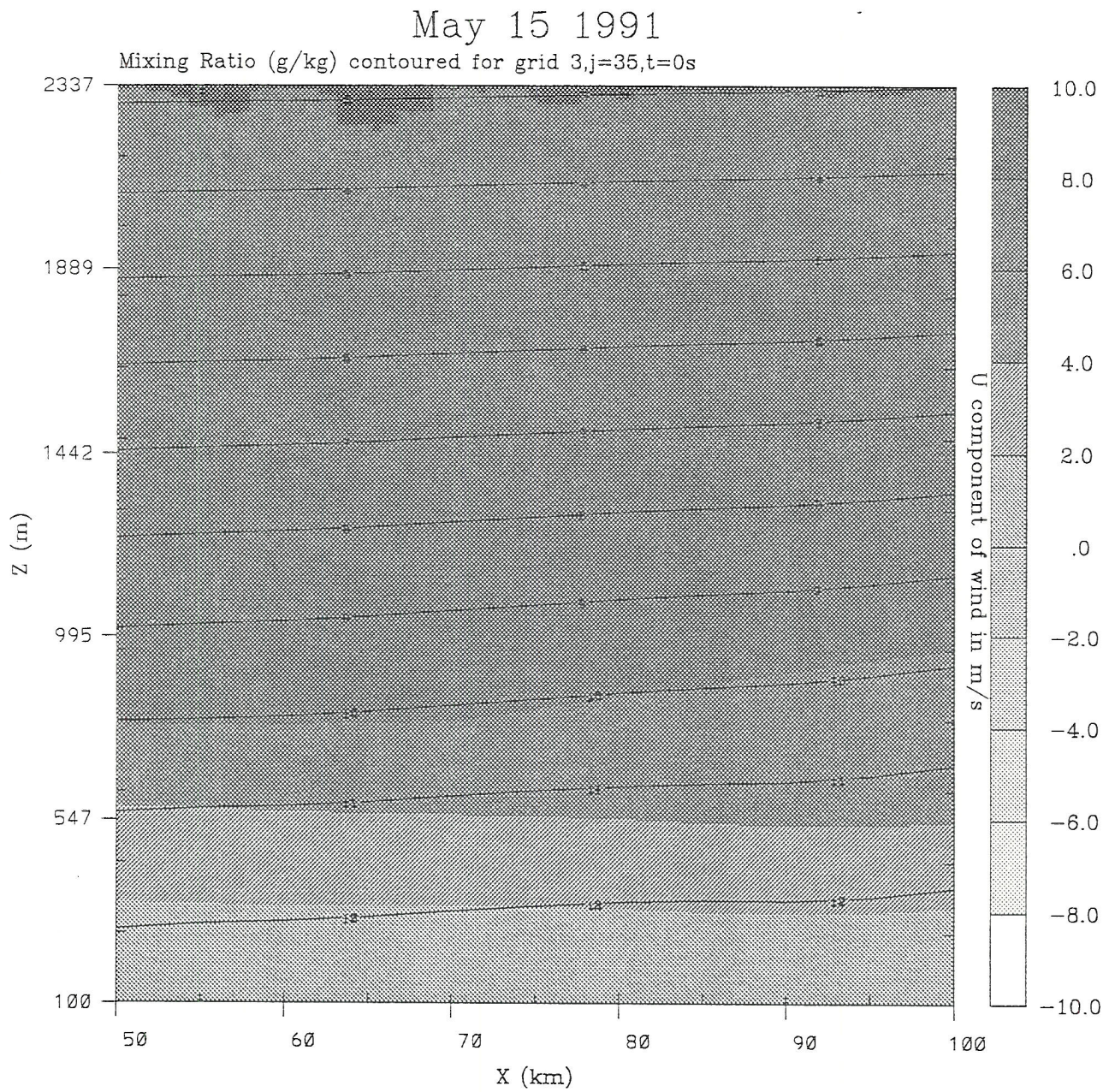


Figure 3.13: Vertical motion at 3063m at 2100 UTC for Grid #3. The contours are 80 cm/s with a minimum and maximum of -1.6 and 10.4 m/s.







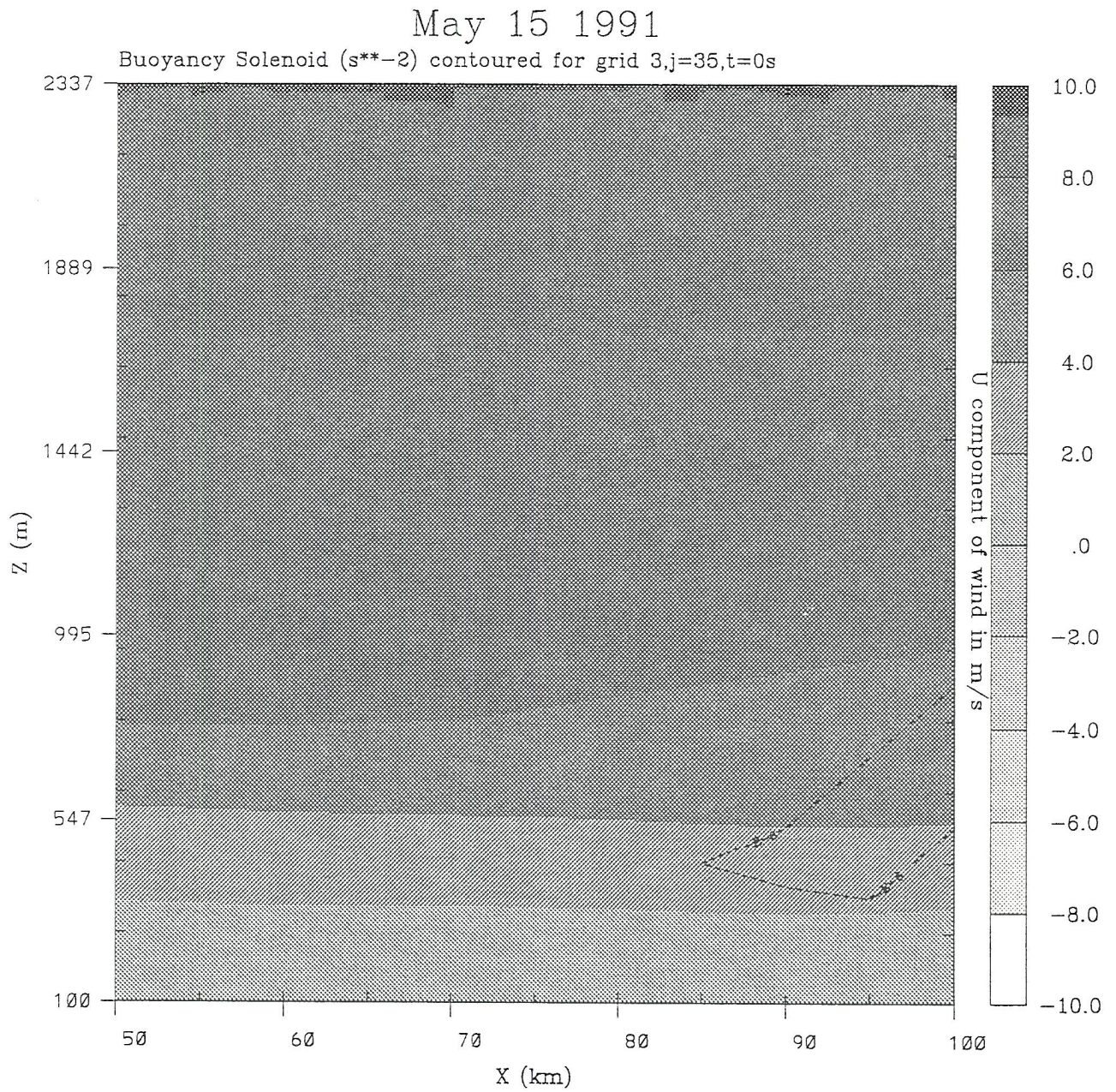
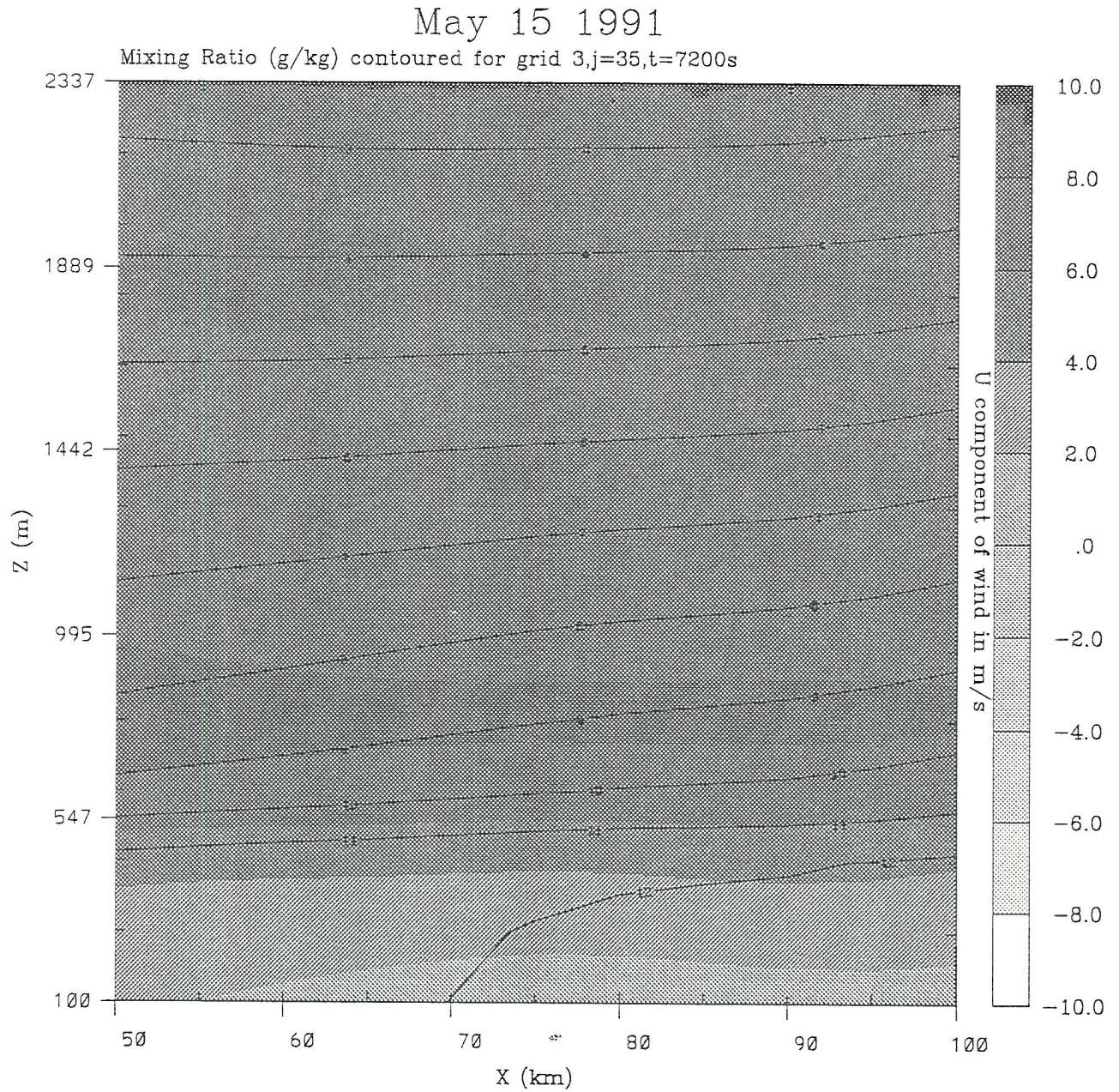


Figure 3.15: Vertical cross section through Grid #3 looking north at 1200 UTC. The cross section was taken 170.0 km north of the southern boundary of the grid. The U component of wind is shaded in 2.0 m/s intervals. The solenoid forcing is contoured every  $10^{-6}s^{-2}$ .







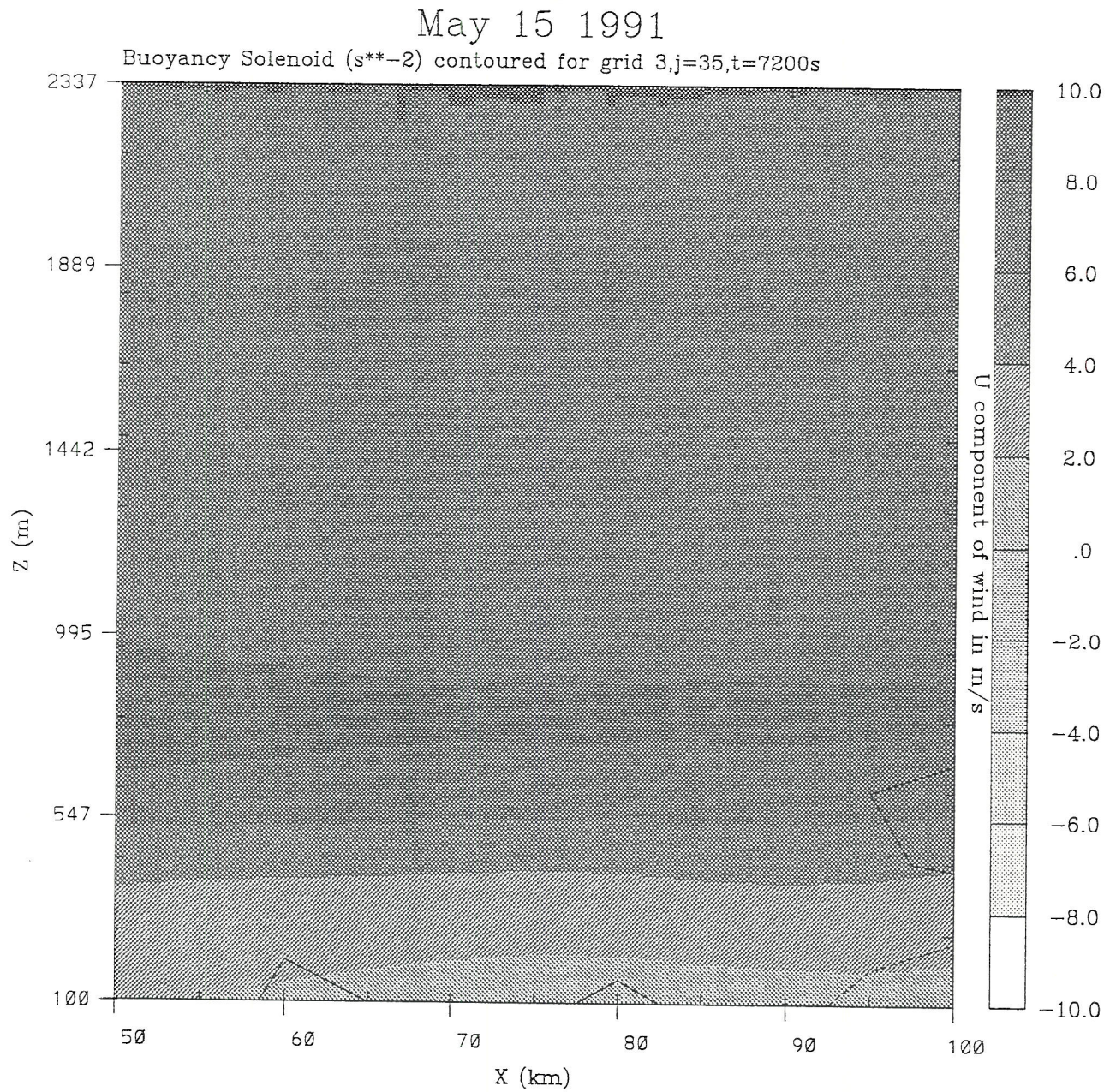


Figure 3.17: Vertical cross section through Grid #3 looking north at 1400 UTC. The cross section was taken 170.0 km north of the southern boundary of the grid. The U component of wind is shaded in 2.0 m/s intervals. The solenoid forcing is contoured every  $10^{-6}s^{-2}$ .



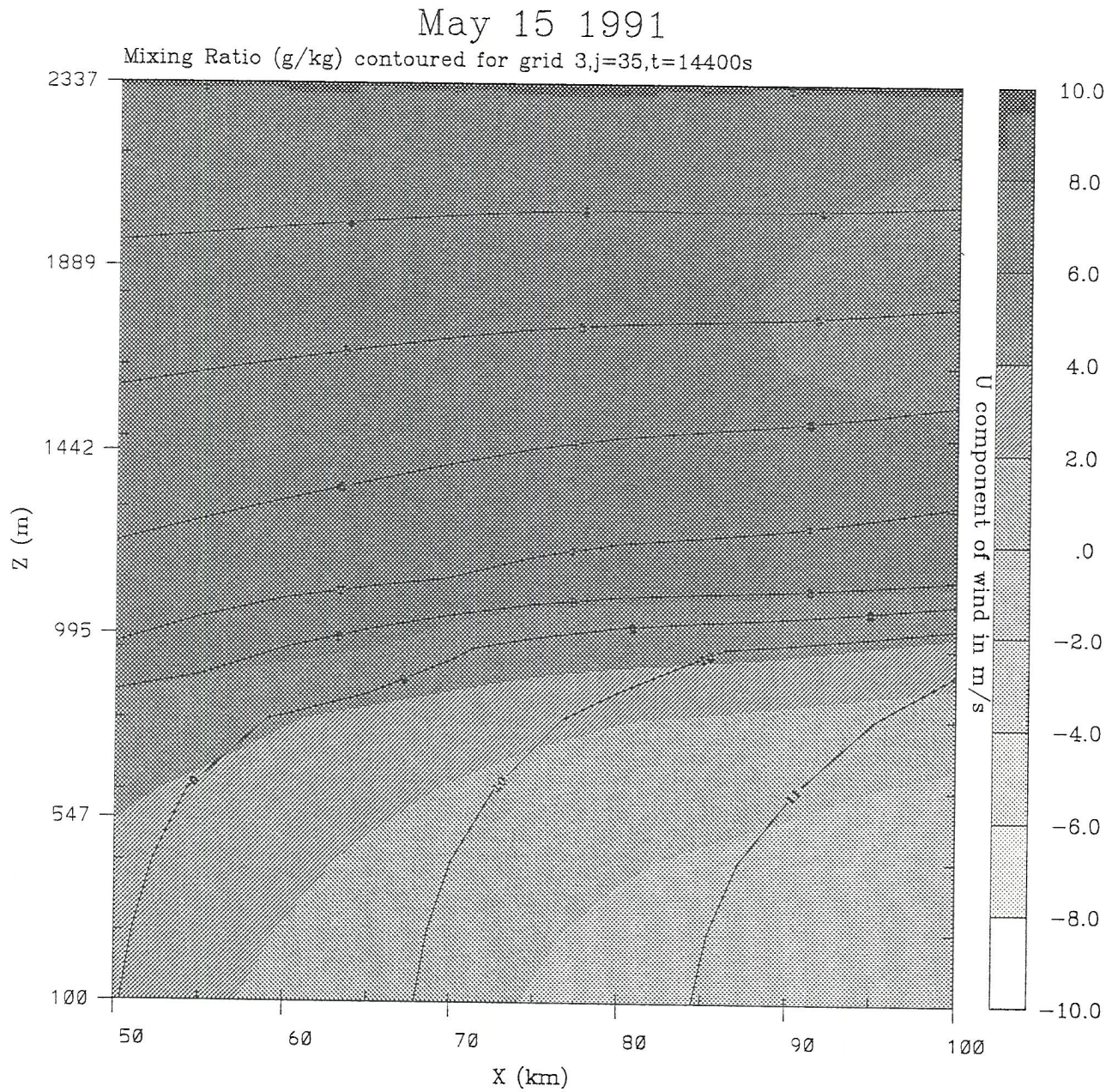


Figure 3.18: Vertical cross section through Grid #3 looking north at 1600 UTC. The cross section was taken 170.0 km north of the southern boundary of the grid. The U component of wind is shaded in 2.0 m/s intervals. The mixing ratio is contoured every 1.0 g/kg.



The solenoids were an indication of gradients in the model buoyancy. Just west of the dry line a region of air was warmer than the moist air to the east. The presence of this warm air appeared to be in response to the surface characteristics, soil type, wetness, and vegetation type. A more complete investigation into the dry line evolution is planned.

Grid #3 was run until 2300 UTC. The convection moved towards the north and developed a well-defined anvil canopy. Plots of the vertically-averaged cloud water for 1900, 2000, 2100, and 2200 UTC were made and looped together. This was used to place Grid #4 at the southern most portion of the convective line that developed.

### 3.5 Supercell Evolution

With a grid spacing of 1.0 km for both horizontal directions, Grid #4 was spawned at 2000 UTC in the central Texas Panhandle. During this simulation this grid was the first to be moved and it moved towards the northeast. With Grid #4 running for thirty minutes, the water vapor mixing ratio gradient increased significantly at 49m (Figure 3.24a). The horizontal winds accelerated into the convergence zone from both sides of the dry line.

It is postulated that the convection directly over the dry line was lowering the pressure at the surface due to the warm interior of the deep updrafts. The lower pressure enhanced the acceleration of boundary-layer air into the dry line convergence zone, consequently increasing the water vapor gradient.

The vertical motion in the middle troposphere is shown in Figure 3.24b at 2030 UTC. A well defined continuous north-south line of updraft was evident. The line was approximately 40 km long. This line persisted for thirty minutes. It was anticipated that thunderstorm splitting would occur during this time interval and that once the splitting process had occurred, the right moving supercell would be located at the southern portion of this line. Intersecting the southern portion of the convective line with the grid was a real possibility and not desirable because that was where the supercell was expected to form. Preventing the southern boundary of Grid #4 from intersecting the line of convection was quite a challenge.



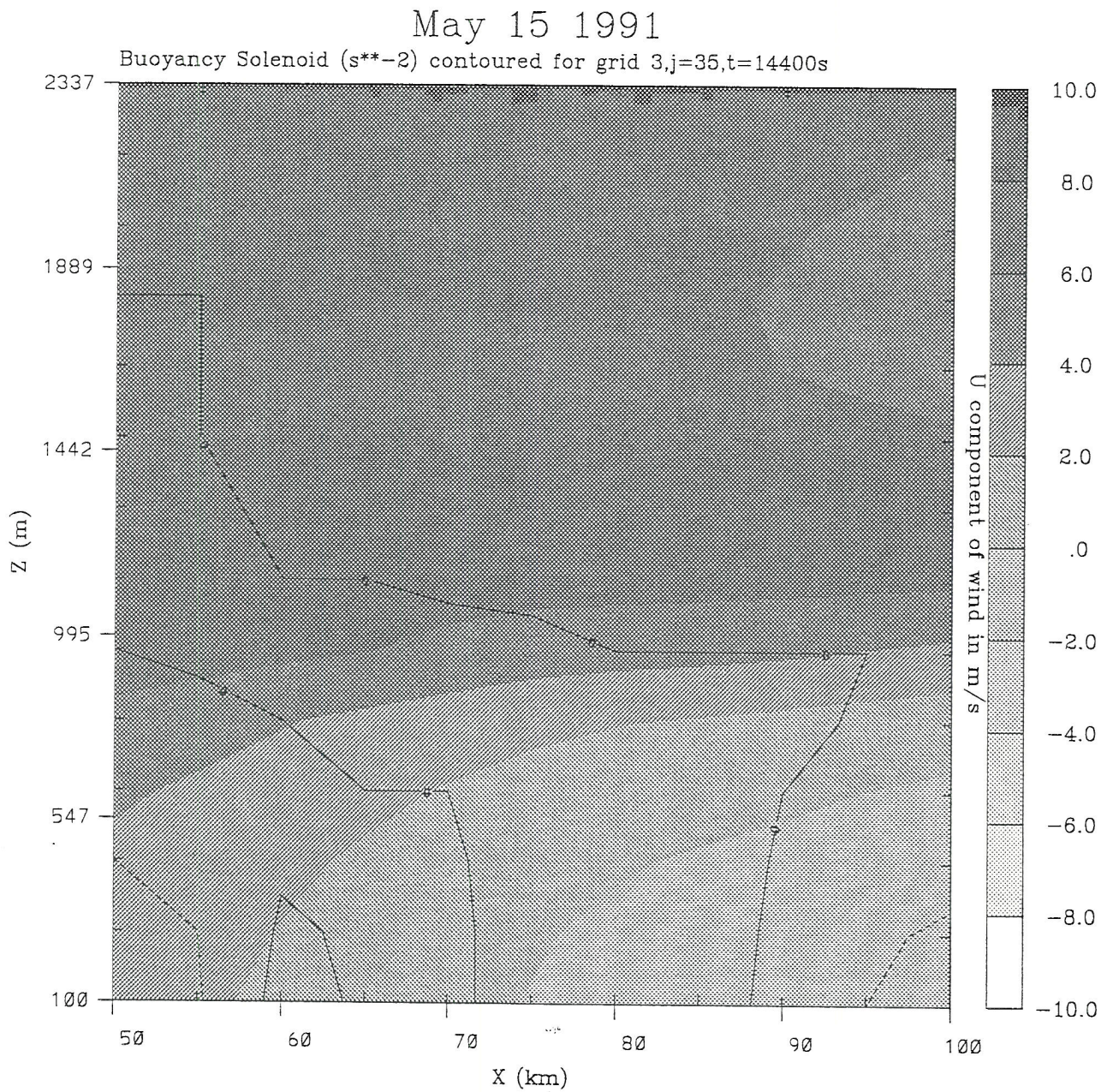


Figure 3.19: Vertical cross section through Grid #3 looking north at 1600 UTC. The cross section was taken 170.0 km north of the southern boundary of the grid. The U component of wind is shaded in 2.0 m/s intervals. The solenoid forcing is contoured every  $10^{-6}s^{-2}$ .



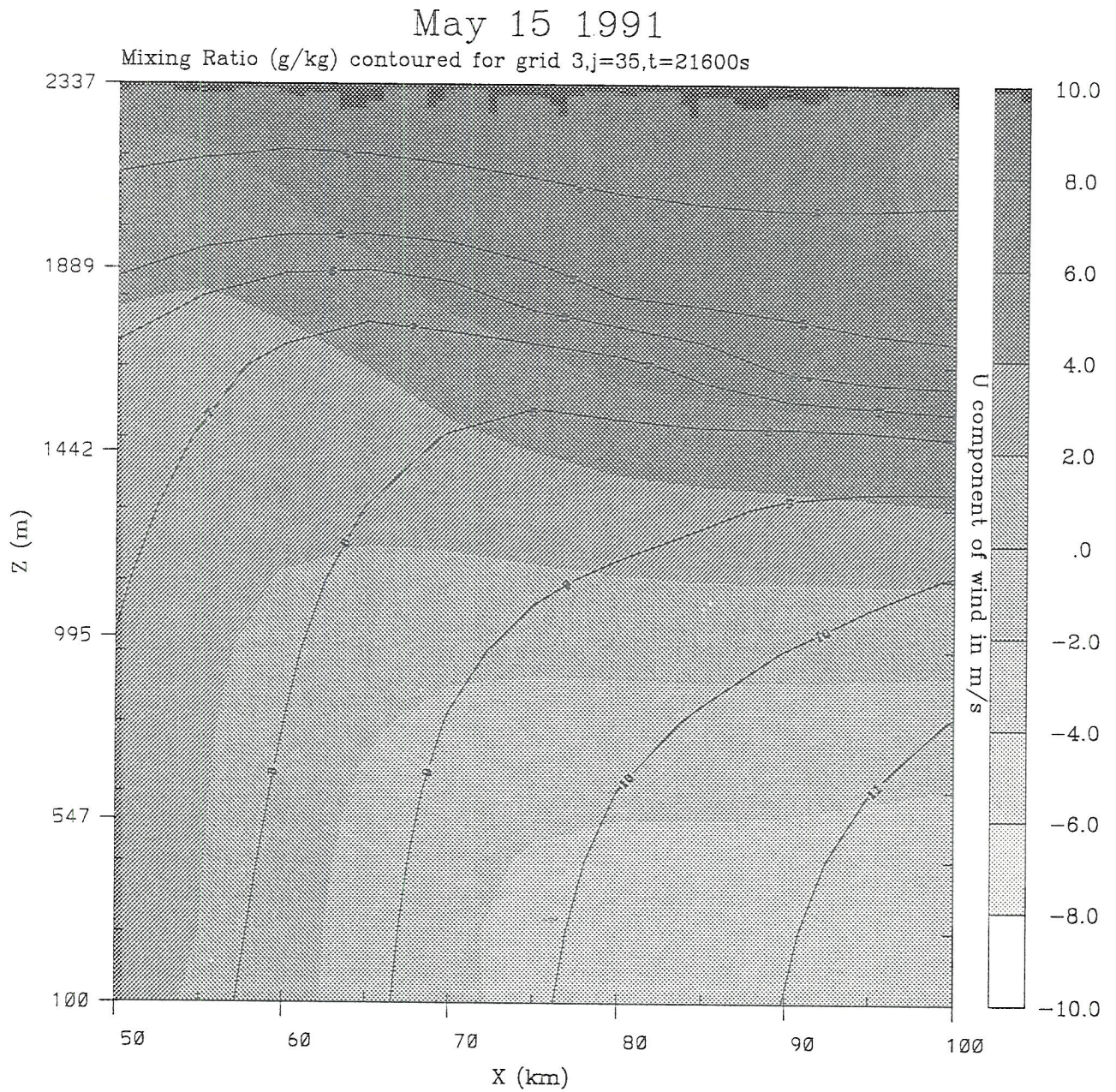


Figure 3.20: Vertical cross section through Grid #3 looking north at 1800 UTC. The cross section was taken 170.0 km north of the southern boundary of the grid. The U component of wind is shaded in 2.0 m/s intervals. The mixing ratio is contoured every 1.0 g/kg.



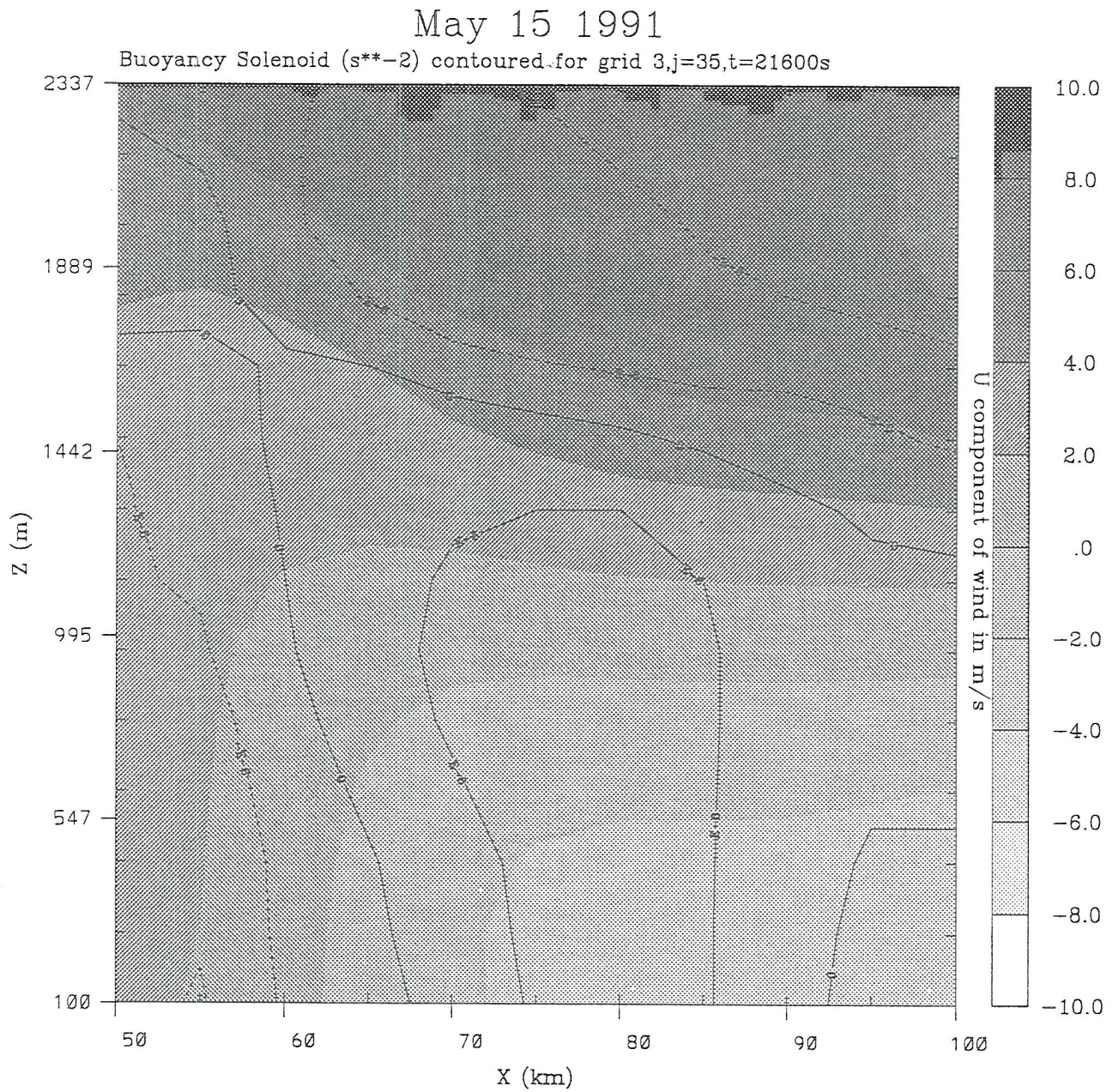


Figure 3.21: Vertical cross section through Grid #3 looking north at 1800 UTC. The cross section was taken 170.0 km north of the southern boundary of the grid. The U component of wind is shaded in 2.0 m/s intervals. The solenoid forcing is contoured every  $10^{-6}s^{-2}$ .



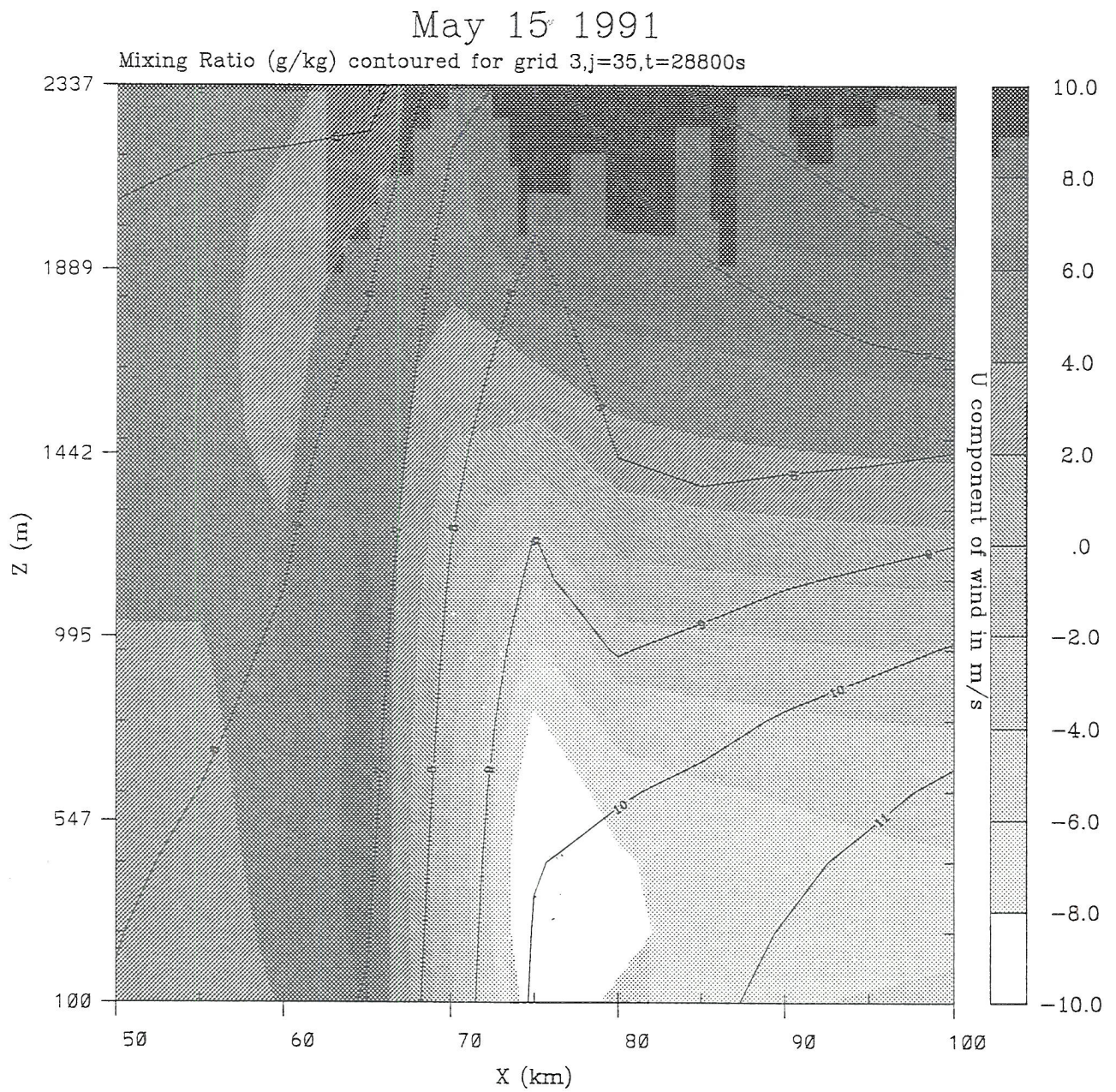


Figure 3.22: Vertical cross section through Grid #3 looking north at 2000 UTC. The cross section was taken 170.0 km north of the southern boundary of the grid. The U component of wind is shaded in 2.0 m/s intervals. The mixing ratio is contoured every 1.0 g/kg.



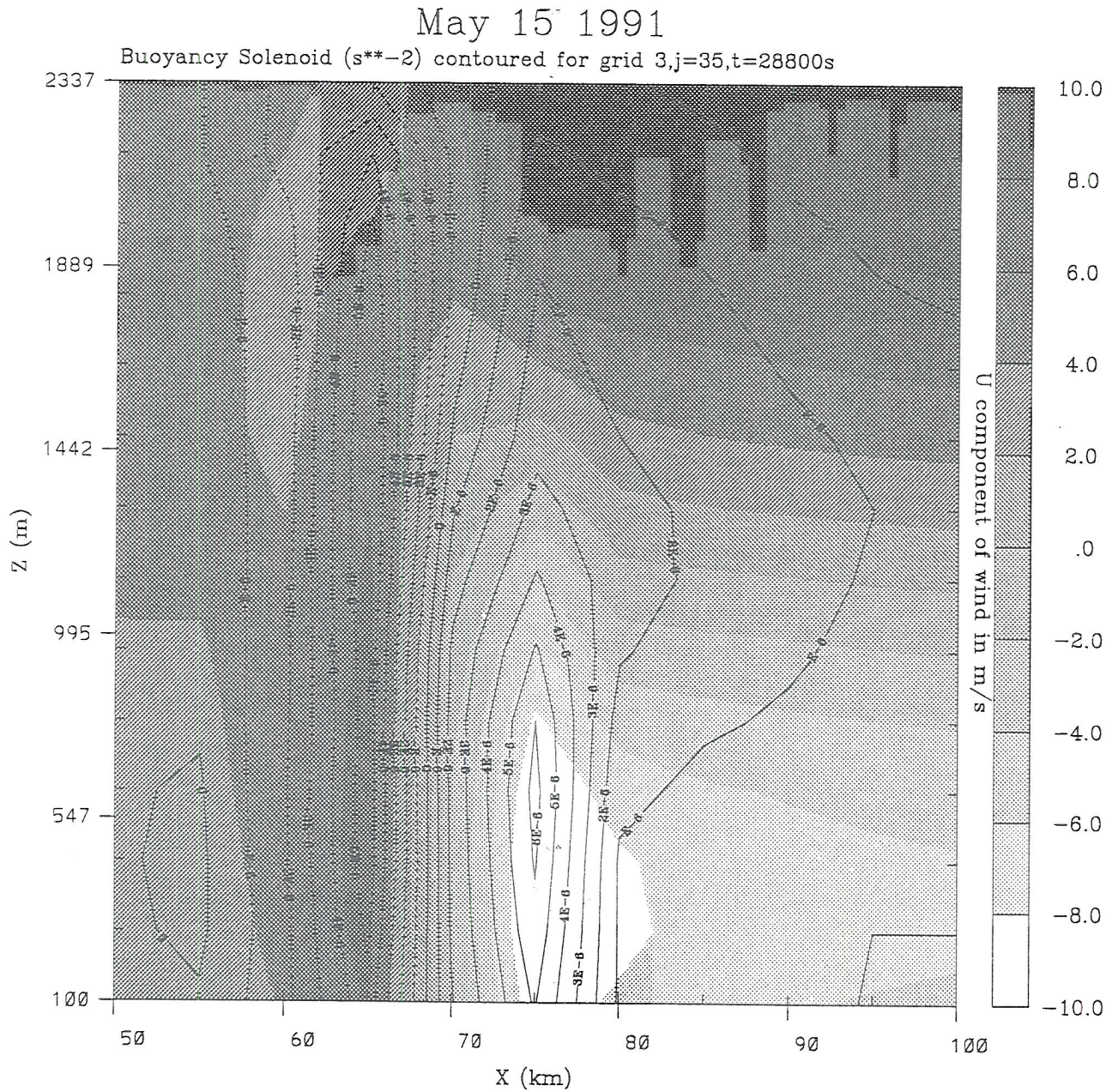


Figure 3.23: Vertical cross section through Grid #3 looking north at 2000 UTC. The cross section was taken 170.0 km north of the southern boundary of the grid. The U component of wind is shaded in 2.0 m/s intervals. The solenoid forcing is contoured every  $10^{-6}s^{-2}$ .



At 2100 UTC a noticeable eastward bulge occurred along the southern portion of the dryline (Figure 3.24c). At this time the right moving supercell was over this part of the dry line, see Figure 3.24d. As the storm moved towards the northeast, the strong boundary layer flow to the west advected the dry line eastward producing the bulge.

Evidence of the splitting process was seen at 2045 UTC. Three distinct updraft maxima were evident although still embedded in a north-south line. The two cells to the north were left movers while the one to the south was a right mover. In Figure 3.24d the well-defined right mover had a maximum updraft speed of 30 m/s. A small left mover, seen near the top left portion of the figure, moved out of Grid #4 quickly.

Simulations of supercells that are formed by releasing a warm bubble in a horizontally homogeneous domain show signs of the splitting process within the first thirty minutes (Klemp and Wilhelmson, 1978b, and Grasso, 1992). For this study a longer time was required. This suggests to the author that the splitting process was dependent to some degree on the size of the physical process forcing convection.

As the storm continued to move toward the northeast, the eastward bulge became more pronounced, Figure 3.25a. Strong horizontal divergence occurred just to the north as the downdraft descended to the ground. A well-defined cyclonic circulation was also present at this time on the northern portion of the dry line bulge in the strong water vapor mixing ratio gradient. Both of these features were not present fifteen minutes earlier, see Figure 3.24c. The rain mixing ratio field is shown in Figure 3.25b and, as would be expected, was located at the same position as the divergent winds.

Fifteen minutes later, significant changes had occurred. Strong horizontal divergence dominated the flow to the north of the dry line bulge, as winds accelerated westward toward the dry line. A large region of cyclonic circulation can be seen just to the left of the center of Figure 3.25c. The rotation moved northeast of the bulge. The beginning of a hook signature was forming at this time and the rain mixing ratio field had expanded; see Figure 3.25d. The ground relative position of Grid #4 at 2115 UTC is the same at 2130 UTC in Figure 3.25.



Figure 3.24: Grid #4; (a) and (c) Winds and mixing ratio at 49m for 2030 UTC, contoured every .3g/kg, and 2100 UTC, contoured every .4g/kg, respectively (b) and (d) Vertical motion, contoured every 2.0m/s, at 5961m for 2030 and 2100 UTC, respectively. The maximum upward vertical motion was 32m/s and 30m/s for (b) and (d), respectively



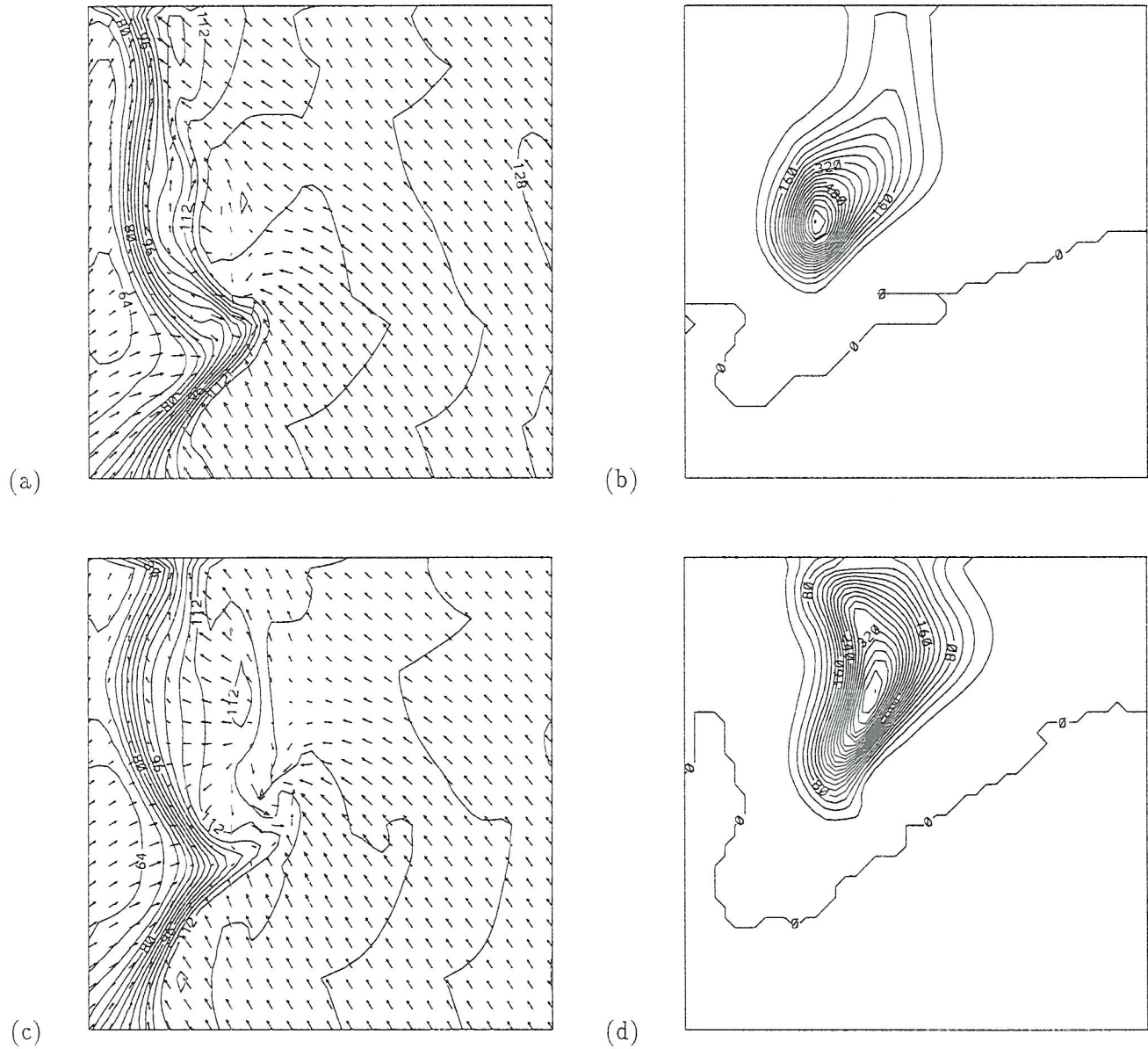
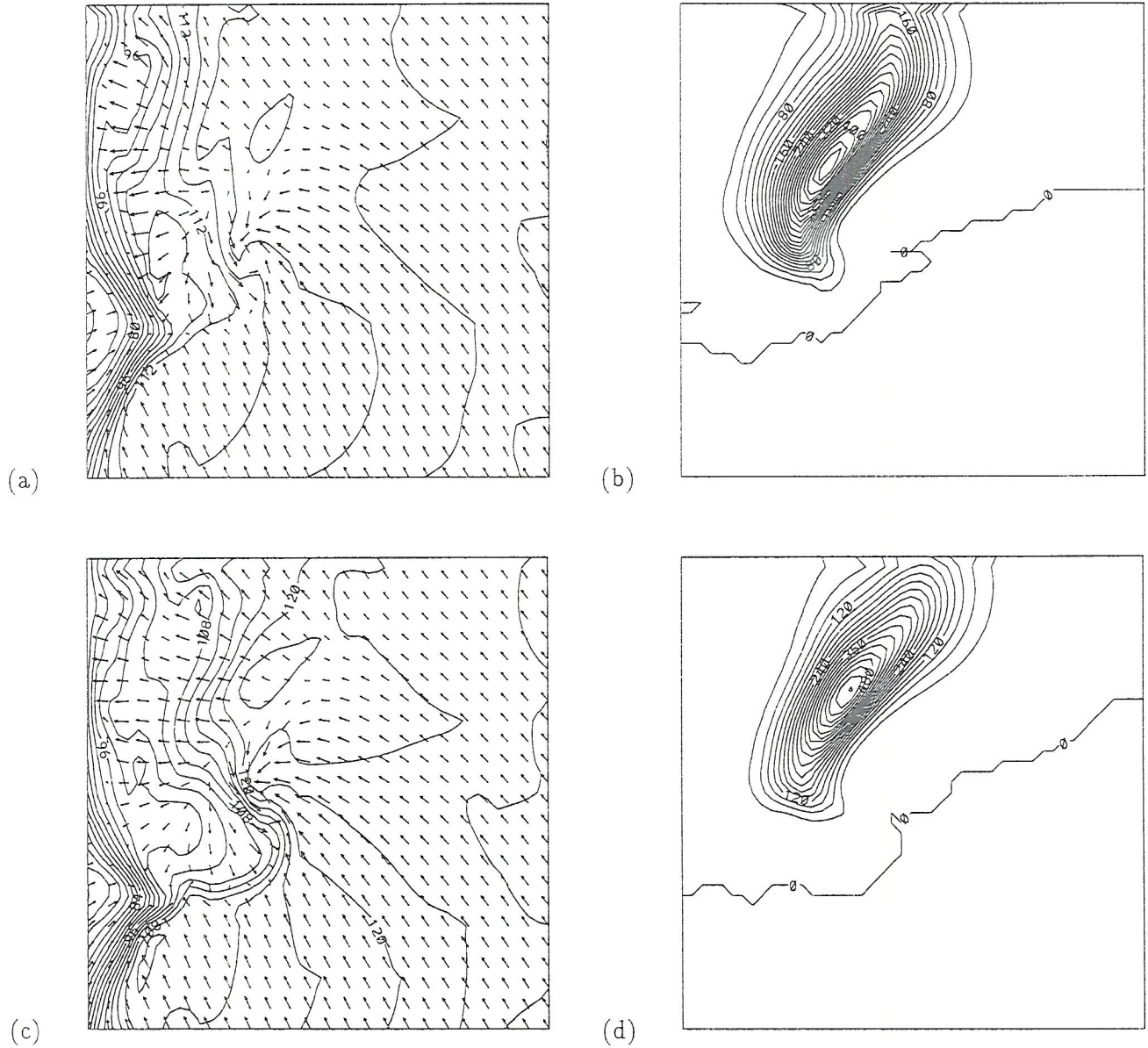


Figure 3.25: Grid #4; (a) and (c) Winds and mixing ratio, contoured every .4g/kg, at 49m for 2115 and 2130 UTC, respectively. (b) and (d) Rain mixing ratio at 49m for 2115 UTC, contoured every .04g/kg to a maximum of .76g/kg, and 2130 UTC, contoured every .02g/kg to a maximum of .42g/kg, respectively.



At 2145 UTC, Grid #4 had moved east and north 5.0 km. The cyclonic circulation was clearly evident to the left of the center of Figure 3.26a, at this time. The center of the downdraft was a few kilometers to the north. Strong horizontal divergence from the downdraft dominated the upper left quadrant of the figure. The westward flow from this region towards the dry line was stronger than fifteen minutes earlier. To the southwest of the circulation center towards the dry line bulge, a strong convergence zone was apparent along the developing pseudo-gustfront. The rain field became more elongated from the southwest to the northeast. The gradient to the southeast of the maximum also elongated in this direction. The hook signature became more pronounced at this time; Figure 3.26b.

Grid #4 moved north 5.0 km from 2145 to 2200 UTC. The storm continued to move away from the dry line during this time. Northwest of the circulation center the flow from the downdraft had a different characteristic. The air accelerated 6.0 km from the downdraft towards the dry line. From there the flow slowed before finally accelerating into the dry line. The pseudo-gust front moved east of the circulation center quite similar to the occlusion process for synoptic scale low pressure systems; see Figure 3.26c. Along the leading edge of the gustfront a significant gradient in water vapor mixing ratio developed. The hook in the rain field (Figure 3.26d) was still present but not as pronounced as it was fifteen minutes earlier.

There appears to have been significant feedback between the dry line and the supercell thunderstorm from 2000 to 2200 UTC. As convection first developed along the dry line, stronger boundary layer convergence increased the horizontal water vapor gradient. As the storm moved it appeared to pull the dry line east producing a bulge. To the north, downdraft air accelerated to the west perhaps advecting the dry line in that direction or preventing any eastward movement.

### 3.6 Tornado Evolution

Grid #5 was spawned at 2100 UTC when the main precipitation downdraft was forming. Six minutes later (Figure 3.27a), the initial stage of vortex at 49m can be seen at the tip of the dry line bulge. To the north a convergence zone formed by outflow from



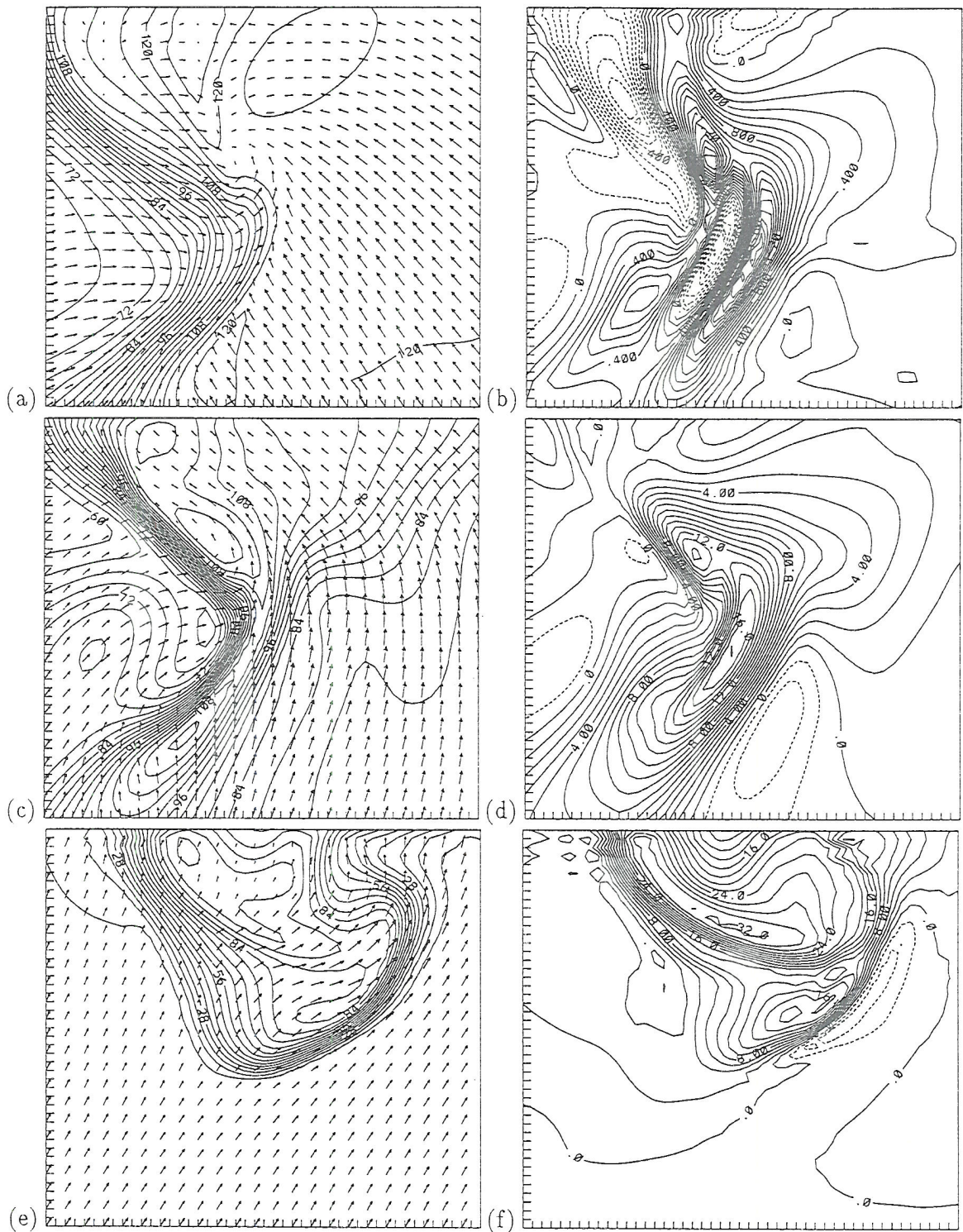


Figure 3.27: Grid #5; (a) (c) and (e) Winds and mixing ratio, contoured every .3g/kg in (a) at 49m, (c) at 1317m, and .7g/kg for (e) at 5962m. Mixing ratio contours labeled 84 represents a value of 8.4 g/kg. Vertical motion (b) at 49m (contoured every .01m/s to a maximum of 2.0m/s), (d) at 1317m (contoured every 1.0m/s to a maximum of 18.0m/s), and (f) at 5962m (contoured every 2.0m/s to a maximum of 32.0m/s), respectively for 2106 UTC.

two downdrafts (Figure 3.27b). Note how the winds were basically from the west to the northwest of the circulation center. Associated with the vortex was an updraft maximum. Two bands of updraft orientated southwest to northeast were south of the vortex. The eastern most band and the updraft in the vortex gave the vertical motion field a comma shape appearance.

At 1317m, little evidence of a vortex was apparent. In the western portion of Figure 3.27c, winds were flowing towards the northeast and parallel to the large gradient in water vapor mixing ratio. On the other side of the water vapor gradient, southeasterly winds existed. The comma-shaped updraft (Figure 3.27d), had two maxima embedded within. One in the head of the comma was 14.0 m/s while the other, to the southeast, was over 15.0 m/s and occupied a larger region. There was also a lack of downdraft within the northern portion of the figure.

Higher up at 5962m, the flow was basically from the southwest with no indication of a tornadic vortex (Figure 3.27e). There was a large and narrow band of updraft exceeding 30.0 m/s. A secondary maximum existed to the south with a speed of 18.0 m/s (Figure 3.27f).

With Grid #5 running for twelve minutes, important changes occurred at 49m. The flow to the northwest of the circulation center was no longer from the west as it was at 2106 UTC. This region was dominated by winds having a significant northerly component. As the storm moved away from the dry line, the vortex was embedded in a water vapor gradient that was distinct from the gradient associated with the dry line a few kilometers to the southwest (Figure 3.28a). The updraft along the convergence zone associated with the outflow from the two downdrafts was further west of the surface vortex than at 2106 UTC. The downdraft to the northeast of the vortex, six minutes earlier, had expanded in area and was positioned north-northwest of the circulation center (Figure 3.28b).

Slightly higher up at 1317m there was now evidence of the vortex. A closed circulation was seen just to the left of the center of Figure 3.28c. A dry slot developed on the east side of the vortex, near the center of the figure, as dry environmental air was ingested into the cyclonic circulation. An updraft maximum associated with the vortex can be seen in the center of Figure 3.28d. Drier environmental air sank along the southern flank of the



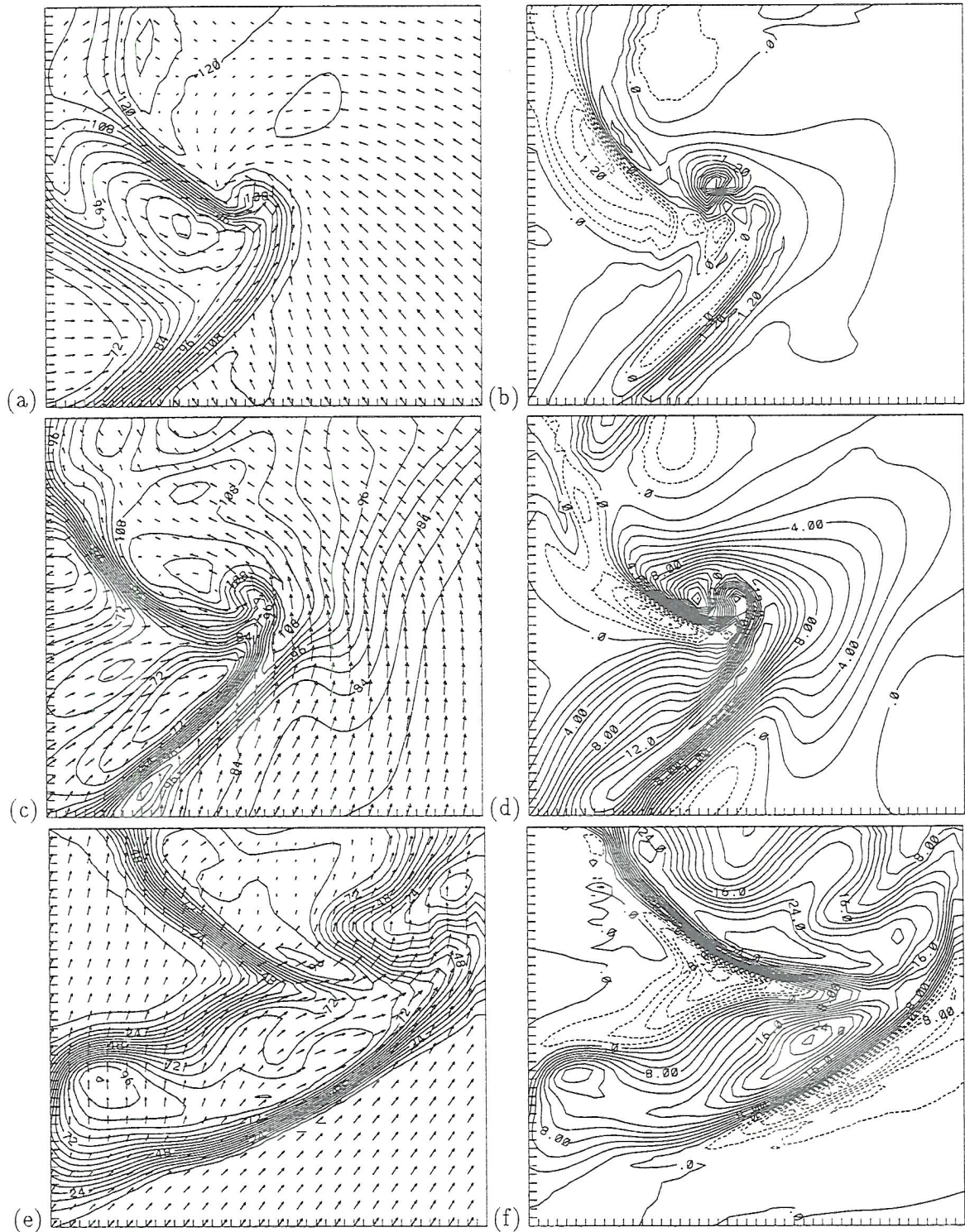


Figure 3.28: Grid #5; (a) (c) and (e) Winds and mixing ratio contoured every .3g/kg for (a) at 49m, (c) at 1317m, and .6g/kg for (e) at 5962m. Vertical motion (b) at 49m (contoured every .3m/s to a maximum of 3.6m/s), (d) at 1317m (contoured every 1.0m/s to a maximum of 18.0m/s), and (f) at 5962m (contoured every 2.0m/s to a maximum of 28.0m/s), respectively for 2112 UTC.

vortex. Note the minimum in updraft speed to the east of the vortex associated with the dry slot. A region of downdraft to the north of the vortex had become evident at this time.

Middle tropospheric mixing ratios were quite different compared to 2106 UTC. A large region of high mixing ratio developed, as seen in the lower half of Figure 3.28e. However, rotation associated with the vortex was absent. A significant change in the vertical motion field (see Figure 3.28f) was the new and strong downdraft in the center of the figure. Maximum downdraft speeds of 12.0 m/s were flanking the updraft gradient that increased from 2106 UTC.

A well defined cyclonic circulation at 49m dominated much of Figure 3.29a at 2118 UTC. The storm had moved far enough to the northeast, at this time, that the water vapor mixing ratio gradient seen in the figure was no longer associated with the dry line. The air just to the northwest of the vortex continued to accelerate towards the south. The downdraft to the north-northwest of the vortex at 2112 UTC now dominated the northwest quadrant of Figure 3.29b. The convergent zone between the two downdrafts and associated upward motion was basically west of the vortex at 2118 UTC.

As shown in Figure 3.29c the vortex at 1317m was well defined and occupied more area compared to six minutes earlier. Dry air continued to be ingested by the circulation maintaining the dry slot to the southeast of the vortex. The updraft curled in a circular arch due to the rotation of the vortex. Note the appearance of a strong central downdraft bounded by the updraft near the center of Figure 3.29d. Downdraft-dominated regions to the north of the vortex and weak vertical motion existed in the dry slot. The updraft maximum in the flanking line was now east of the vortex in response to the strong low level convergence associated with the gust front to the east south east of the vortex; see Figure 3.29a.

Fields at 5962m for 2118 UTC were very different from the last six minutes. A new feature was the highly divergent flow from the mixing ratio maximum just to the left of the center of Figure 3.29e. Perhaps this was a precursor to the vortex. Vertical motion at this level was also quite different than six minutes earlier. Downdraft in the center of Figure 3.28f was bounded by new updraft in Figure 3.29f.



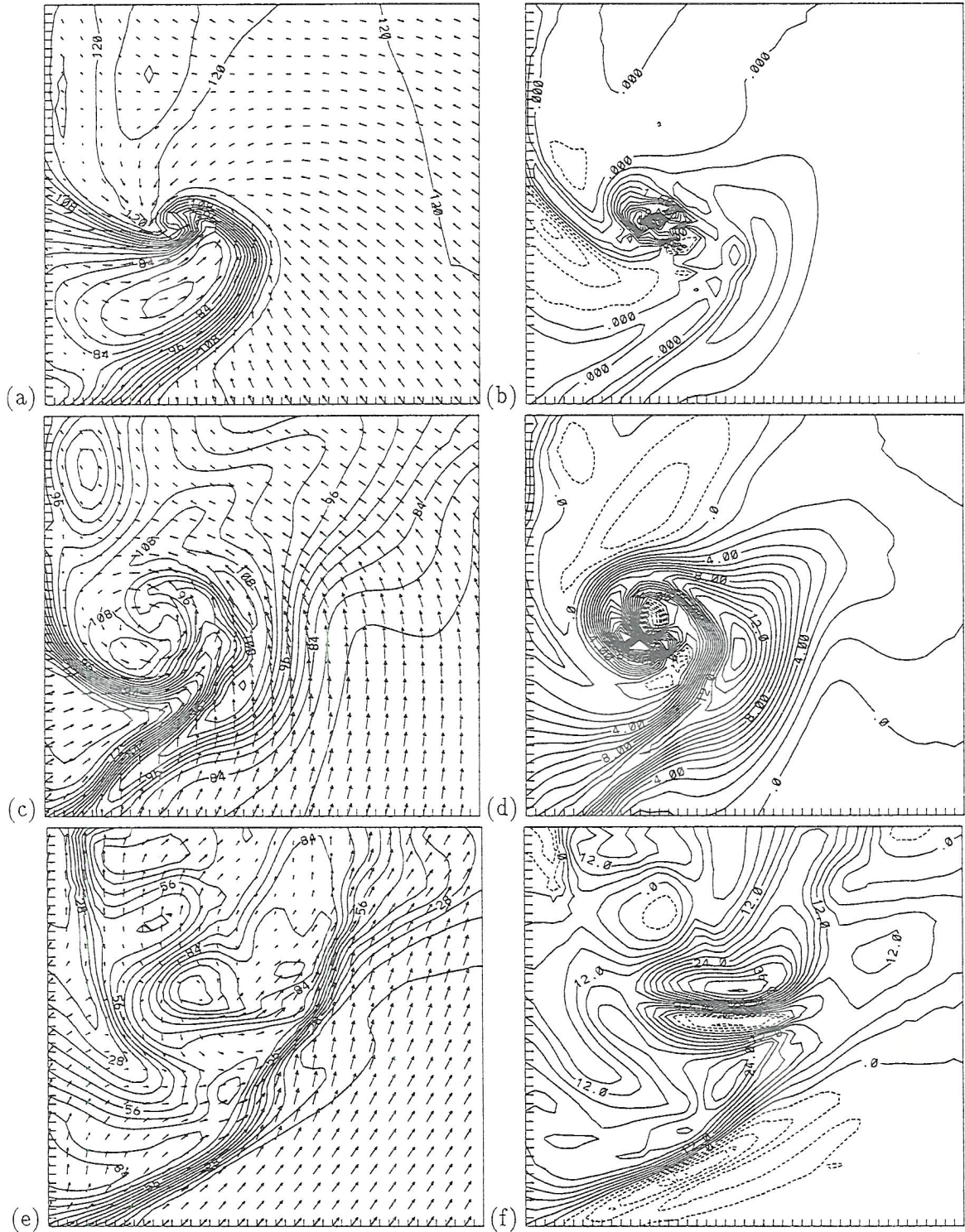


Figure 3.29: Grid #5; (a) (c) and (e) Winds and mixing ratio contoured every  $.3\text{g/kg}$  for (a) at 49m, (c) at 1317m, and  $.7\text{g/kg}$  for (e) at 5962m. Vertical motion (b) at 49m (contoured every  $.4\text{m/s}$  to a maximum of  $4.8\text{m/s}$ ) (d) at 1317m (contoured every  $1.0\text{m/s}$  to a maximum of  $21.0\text{m/s}$ ) (f) at 5962m (contoured every  $3.0\text{m/s}$  to a maximum of  $42.0\text{m/s}$ ), respectively for 2118 UTC.



Six minutes later (2124 UTC) outflow from the downdraft was evident in the top left quadrant in Figure 3.30a. Air was still accelerating to the south from the downdraft just northwest of the mature vortex at 49m. The water vapor mixing ratio minimum south of the vortex at 2118 UTC is called the surface dry slot. The flow field has changed the dry slot into a thin region from the southwest curving cyclonically to the east of the vortex at 2124 UTC. Downdrafts bounded the vortex on all sides but the northeast; see Figure 3.30b. Downdrafts also filled the central part of the cyclonic circulation at 49m.

The horizontal winds and mixing ratio fields at 1317m (Figure 3.30c) had not changed much compared to six minutes earlier. Main features were broad counter clockwise flow around the vortex and the continued evidence of the dry slot along its southern flanks. The downdraft had strengthened considerably and bounded the vortex on all but the northeast side (Figure 3.30d) similar to that at 49m. A maximum downdraft speed of 11.0 m/s was on the southeast side of the vortex. The updraft maximum to the east increased from 16.0 m/s to 18.0 m/s.

Cyclonic circulation associated with the vortex was now evident at 5962m for 2124 UTC near the center of Figure 3.30e and was colocated with the mixing ratio maximum first seen at 2118 UTC in Figure 3.29e. Vertical motion at the same height and time changed quite significantly from 2118 UTC. Ascent within the vortex was in excess of 24.0 m/s.

These past figures have clearly demonstrated that the vortex developed first near the surface then was transported vertically into the storm. A vertical cross section in Grid #5, shown in Figure 3.31, indicates that the vortex was in fact a deep tropospheric entity. This was indicated by the large horizontal gradient and the change in sign in the u-component of the wind from the surface to 10.0 km in the center of the figure. Also shown is the perturbation pressure field. The large horizontal shear and the sign change in u-correspond well with low pressure in the vortex.

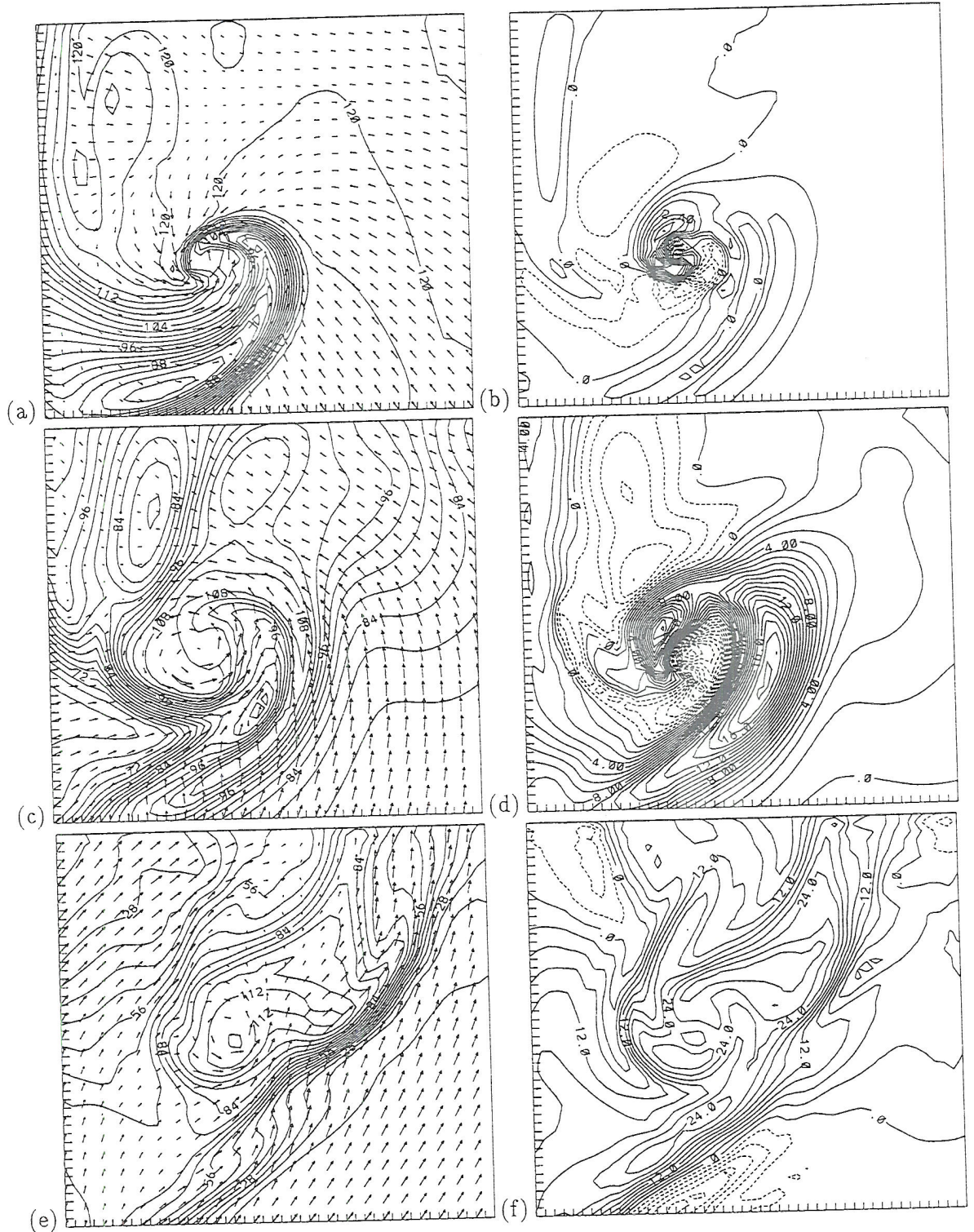


Figure 3.30: Grid #5; (a) (c) and (e) Winds and mixing ratio contoured every .2g/kg for (a) at 49m, .3g/kg for (c) at 1319m, and .7g/kg for (e) at 5962m. Vertical motion (b) at 49m (contoured every .6m/s to a maximum of 5.4m/s), (d) at 1317m (contoured every 1.0m/s to a maximum of 19m/s), and (f) at 5962m (contoured every 3.0m/s to a maximum of 30.0m/s), respectively for 2124 UTC.



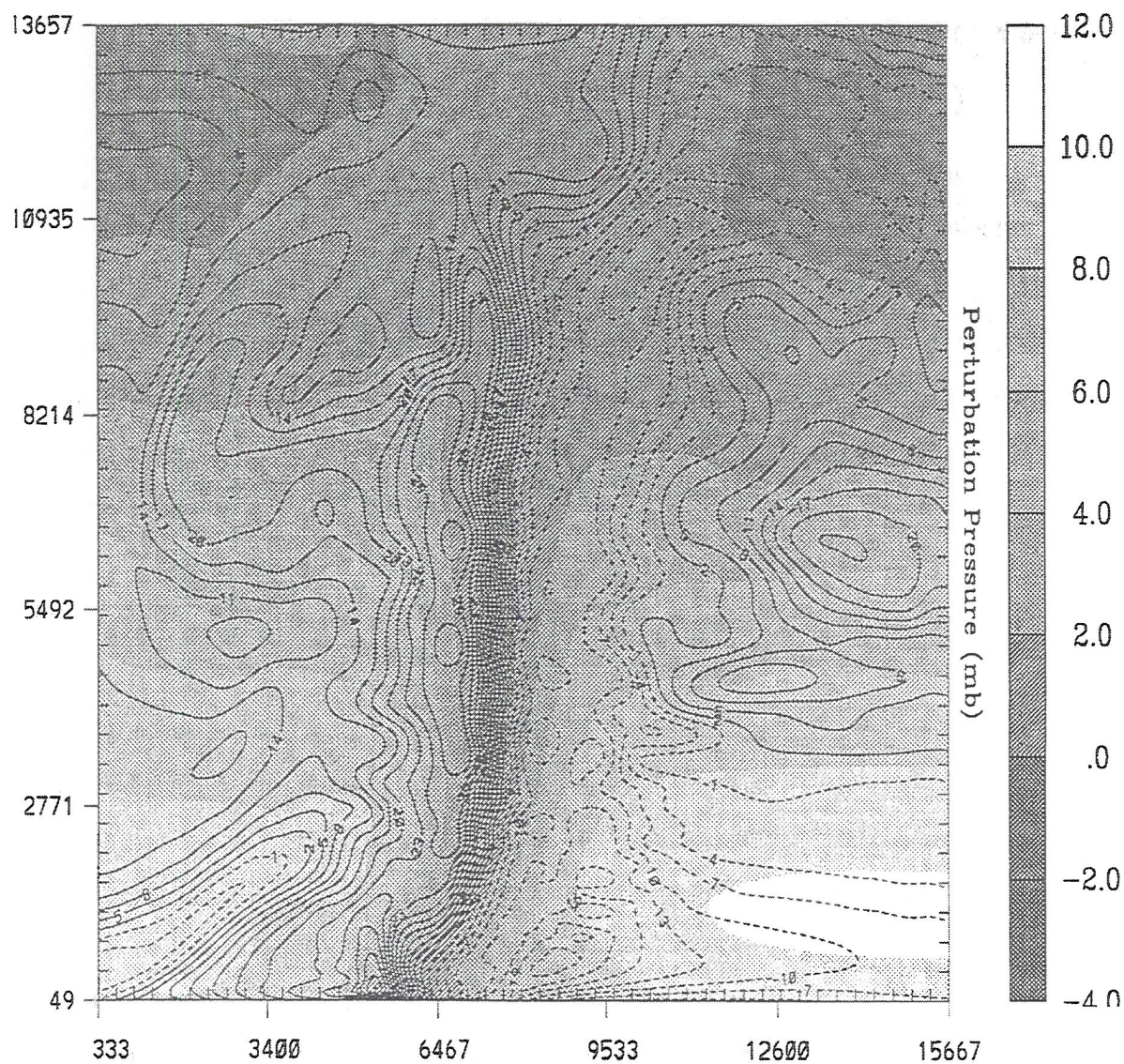


Figure 3.31: Vertical cross section through Grid #5 at 2124 UTC looking west. The u-component of the wind is contoured every 3.0 m/s. Solid/dashed contours are for positive/negative values. Perturbation pressure is shaded with the scale on the right side of the figure. The horizontal and vertical axes are measured in meters.

### 3.7 Tornado Characteristics

The sixth and final nested grid was spawned at 2100 UTC and had a grid spacing of 111.1 m in both horizontal directions over a 6.0 km domain. Characteristics of the mature tornado at 2124 UTC will be discussed in this section.

At 2124 UTC the interior of Grid #6 was dominated by strong cyclonic flow at 49m (Figure 3.32a). High values of horizontal convergence were evident along the large gradients of mixing ratio. The wind speeds shown in Figure 3.32b display some interesting features. There were two secondary speed maxima regions orientated in clockwise bands from the tornado center. One within the top half of the figure and the other in the bottom half. Since the tornado was moving northeast, one would expect to find the largest tangential wind speed on its southeast side. A maximum speed of 60.0 m/s existed in that location placing the tornado in the strong F2 category.

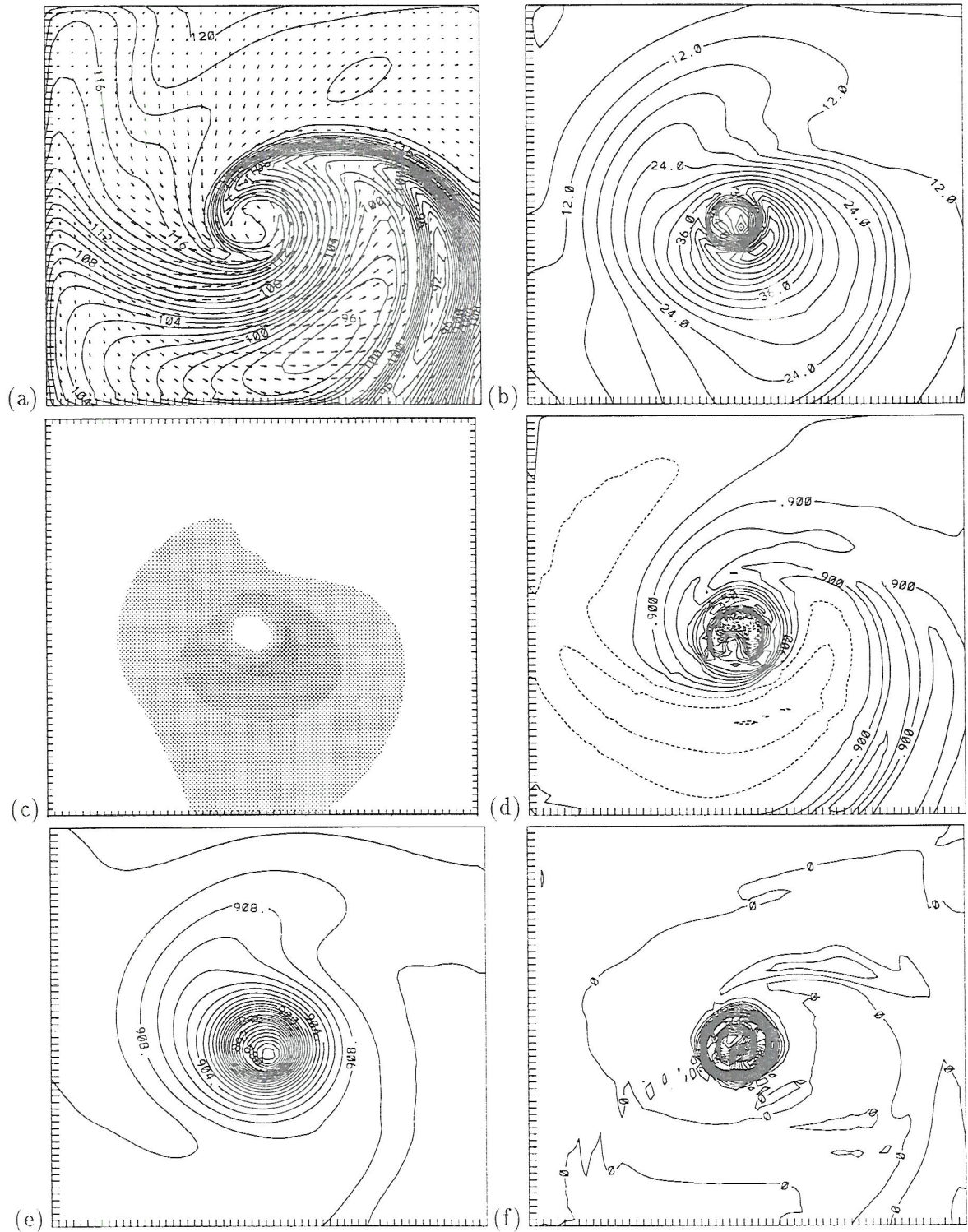
A shade plot of the F scale can be seen in Figure 3.32c. Each gray shade represents a distinct F scale starting from F0. The darkest, crescent shaped, gray shading denotes the region of F2 strength winds on the southeast side of the tornado. It is interesting to see just how much area was occupied by F0 strength winds.

Vertical motion at 49m exhibited a circular ring of updraft bounding a central downdraft. The upward vertical motion also existed along cyclonically orientated, spiraling bands that fed into the tornado from the east. A large downdraft bounded the tornado on all but the northeast side (Figure 3.32d).

Pressures in the center of the tornado were 27.0 mb lower, at 49m, than the environment (Figure 3.32e). Two low pressure regions existed in the same locations as the two secondary wind maxima, seen in Figure 3.32b. The maximum horizontal wind speed occurred on the southeast side of the vortex where the horizontal pressure gradient was the largest.

Values of vertical vorticity of  $0.27 \text{ s}^{-1}$  existed at this time at 49m (Figure 3.32f). The values of vertical vorticity did not increase all the way into the center. The vorticity





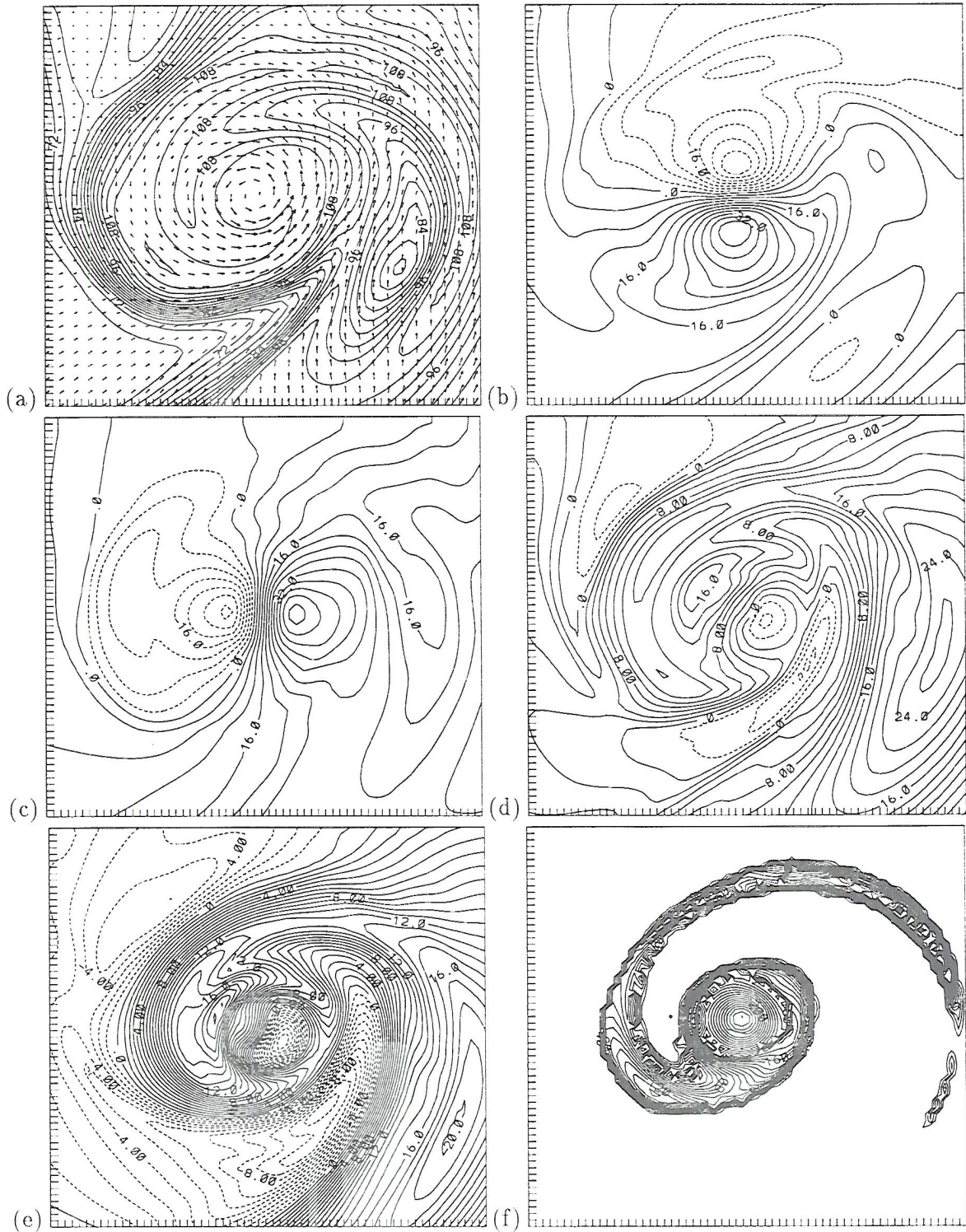


Figure 3.33: Grid #6; (a) Winds and mixing ratio, contoured every  $.3\text{g/kg}$  (b) u-component of wind, contoured every  $4.0\text{m/s}$  (c) v-component of wind, contoured every  $4.0\text{m/s}$  (d) Vertical motion, contoured every  $2.0\text{m/s}$  to a maximum of  $26.0\text{m/s}$  (e) Vertical motion at  $1317\text{m}$ , contoured every  $1.0\text{m/s}$  to a maximum of  $20.0\text{m/s}$ . All plots are at 2124 UTC.



field formed an annulus ring with low values in the center. The author wonders if a seventh nested grid was spawned, would suction vortices form on this vorticity annulus?

The horizontal winds at 2206m revealed a large cyclonic vortex in the center of Figure 3.33a. The u and v-components are shown in Figure 3.33 b and c, respectively. The diameter of maximum winds was just over 1.0 km. A secondary wind maximum existed to the north arching counter clockwise to the west of the vortex.

Upward vertical motion within the vortex was found on the northwest side arching around it like the letter C with a -4.0 m/s downdraft within its concave region. Although the downdraft was almost bounded by updraft at this height (Figure 3.33d) it was not in the center of the cyclonic circulation seen in Figure 3.33a. At a height of 1317m the downdraft, -11.0 m/s, was stronger (Figure 3.33e) and completely bounded by updraft making this a two-celled tornado. The clear slot downdraft, along the right flank of the vortex, is also evident in this figure.

A dramatic spiral in the cloud field is seen in Figure 3.33f. Although the temperatures were cooler in the core of the tornado, a condensation funnel did not form below the thunderstorm to the ground. Perhaps the grid spacing in Grid #6 was too coarse for this feature.

As the simulation was advanced past 2124 UTC, the tornado began to weaken. Since the focus of this study was the genesis of the tornado, the simulation was terminated.

### 3.8 Summary of May Simulation

A diffuse horizontal moisture gradient existed in the Texas Panhandle from 1200 UTC to 1800 UTC. After 1800 UTC the horizontal moisture gradient increased rapidly due to the horizontal convergence of boundary layer air. The increased convergence was a result of two strong thermal solenoids that existed in the first few kilometers above the ground.

Convection was initiated at 2000 UTC. A north-south line of updraft, approximately 45.0 km long, formed rapidly. At 2030 UTC an eastward bulge in the dry line began to form beneath the southern portion of the updraft field. The convective line evolved into three distinct updrafts at 2045 UTC. The bulge in the dry line continued to grow. An isolated

supercell thunderstorm existed at 2100 UTC. The dry line bulge was situated underneath the storm.

Vertical vorticity associated with the dry line bulge was amplified by horizontal convergence beneath the storms' updraft. The infant stage of a cyclonically rotating vortex, in the boundary layer, was evident at 2106 UTC. By 2112 UTC the rotation had been transported vertically into the lower levels of the parent storm.

From 2112 to 2124 UTC positive tilting of horizontal vorticity generated vertical vorticity in both the rear flank and the precipitation downdrafts. The vertical vorticity was generated in the lowest few hundred meters in the downdrafts. From the new source, horizontal convergence of the vertical vorticity intensified the vortex in the boundary layer.

The boundary layer vortex was drawn up into the thunderstorm and by 2124 UTC the tornado extended from the ground to a height of 10.0 km. The maximum horizontal wind, at the lowest model level, was 60.0 m/s on the southeast side of the tornado.

After 2124 UTC the thunderstorm rotation caused the precipitation downdraft to wrap cyclonically around the tornado on all sides but the northeast. The tornado began to weaken and the simulation was terminated.



## Chapter 4

### APRIL 26, 1991 SIMULATION

#### 4.1 Introduction

The second case is the April 26, 1991 Red Rock, Oklahoma tornadic storm. This day received national attention as a photojournalist near Andover, Kansas captured on video, a tornado moving towards them. Four people took shelter under an overpass as the tornado moved past them. Andover was hit hard by an F5 tornado on this day.

This chapter will have the same format as the last so the reader may compare the two tornadic storms. Most of the chapter will be devoted to the smaller scales. The chapter will begin with a discussion of the observed events of April 26, 1991.

#### 4.2 April 26, 1991 Observations

A large region of low pressure from western North Dakota south into the Texas Panhandle existed at 1200 UTC on April 26, 1991. A warm front bounded Kansas along the northern and eastern borders. To the west was a moisture gradient from western Kansas south into the Texas Panhandle. Dew points increased from  $-5^{\circ}\text{C}$  in western Texas, Oklahoma, and New Mexico to  $18^{\circ}\text{C}$  in central Kansas and Oklahoma. Morning temperatures were between  $17^{\circ}\text{C}$  and  $20^{\circ}\text{C}$  in response to southerly winds from the Gulf of Mexico north into central Kansas (Figure 4.1).

A strong, negatively tilted, baroclinic wave at 500 mb existed from Idaho southeast into New Mexico (Figure 4.2a). Wind speeds of  $36\text{ms}^{-1}$  to  $40\text{ms}^{-1}$  was entering the base of the trough over Arizona and New Mexico at 1200 UTC. A well-defined diffluent wind pattern existed over Kansas and Oklahoma. At 300 mb (Figure 4.2b) a strong wind maxima

of 56m/s existed over eastern Nevada. Winds speeds at the base of the trough were 40m/s to 46m/s over Arizona and New Mexico. As the low moved eastward, temperatures warmed into the middle to upper seventies.

Values of CAPE as large as 2100 J/kg existed over central Oklahoma as a result of the warm moist flow from the Gulf of Mexico (Figure 4.2c). The sharp western boundary of CAPE values was due to the significant reduction of water vapor towards the west.

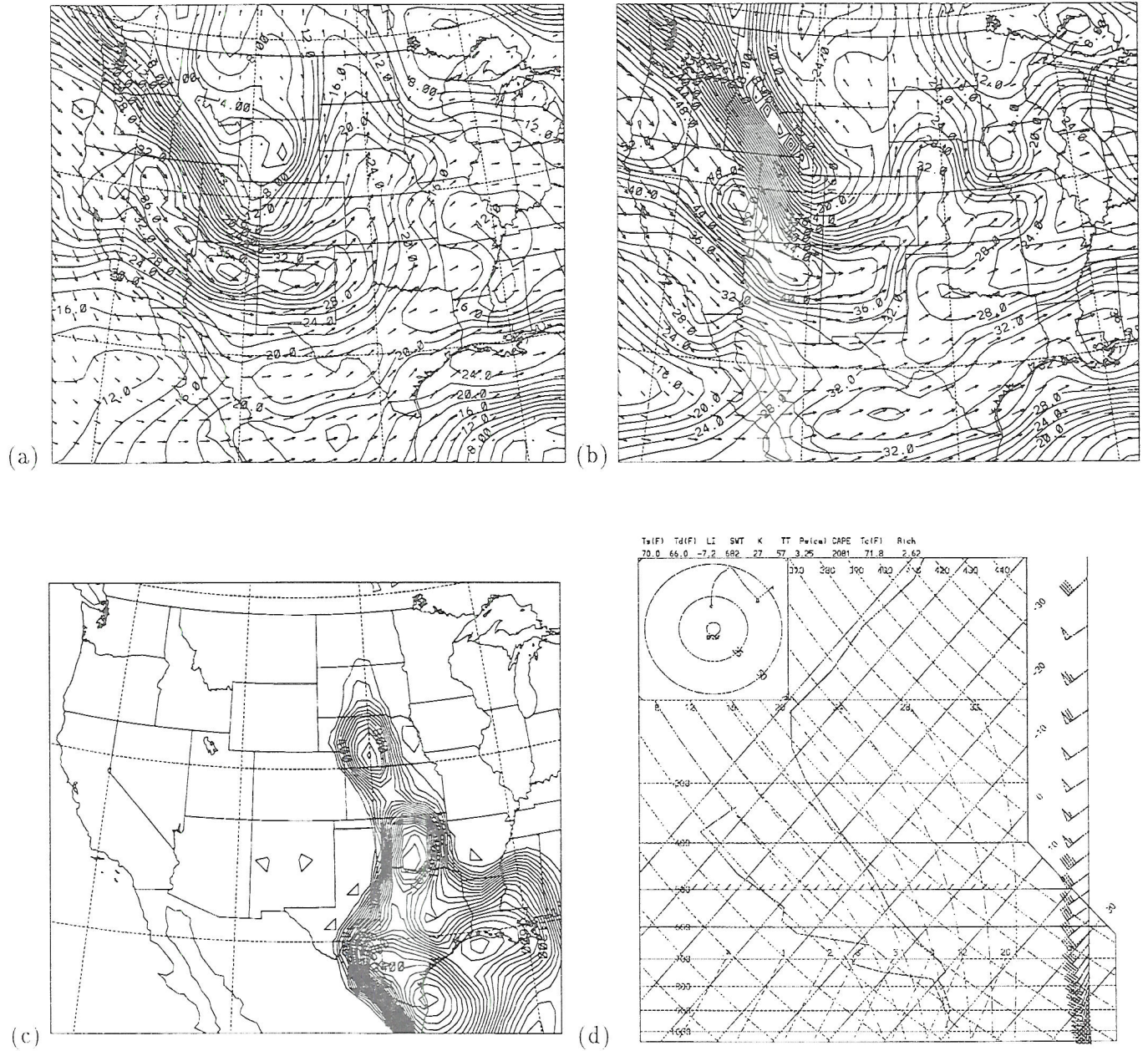


Figure 4.2: (a) and (b) Horizontal wind vectors and speed, contoured every 2.0 m/s to a maximum of 40 m/s at 500 mb and 56 m/s at 300 mb, (c) Convective available potential energy, contoured every 100 J/kg to a maximum of 2800 J/kg, and (d) A sounding at 1200 UTC in north central Oklahoma.



A thermodynamic sounding from north central Oklahoma at 1200 UTC is shown in Figure 4.2d. This sounding was extracted from the model and was in the same location as the tornado that developed later in the simulation. A deep moist layer existed in the lower 200 mb capped by a stable layer around 750mb. Significant clockwise turning in the hodograph can be seen in the top left portion of the figure. There are three noticeable differences between this sounding and the one displayed in Figure 3.2d. First, the CAPE values were almost triple. Secondly, the low level moist layer was deeper. Lastly the hodograph curved clockwise throughout the troposphere.

When the dry line moved into western Oklahoma and Kansas, thunderstorms formed along it in the afternoon. By late afternoon most of central and eastern Kansas and central Oklahoma were under a tornado watch. Most of the fifty five tornadoes that formed from Iowa south into Texas were in Kansas and Oklahoma. Most notable was the Andover, Kansas F5 tornado. This tornado touched down at 2305 UTC and was on the ground for 65 minutes. The path length was approximately 45 miles. Twenty miles to the southeast was a family of three strong to violent tornadoes. The path length of each tornado was between 15-20 miles.

At 2309 UTC a tornado touched down in central Garfield county in north central Oklahoma. The tornado intensified as it moved east and crossed interstate 35 in Noble county. With a total path length of 66 miles the tornado dissipated in northeast Osage county at 0055 UTC. Bluestein (1993), measured winds of 120 to 125 m/s in the Red Rock tornado, placing it along the boundary of an F4 to F5 category. This tornado is the focus of the April 26, 1991 simulation.

### 4.3 Dry Line Evolution

Similar to the May 15, 1991 simulation, the moisture gradient associated with the dryline did not increase until afternoon and it did so rapidly. Figure 4.3 shows the winds and mixing ratio at 49m for 1900 UTC in Grid #3. This grid was located over north central Oklahoma and south central Kansas; the border can be seen in the middle of the figure. The large values of water vapor mixing ratio along the border were due to water vapor fluxing



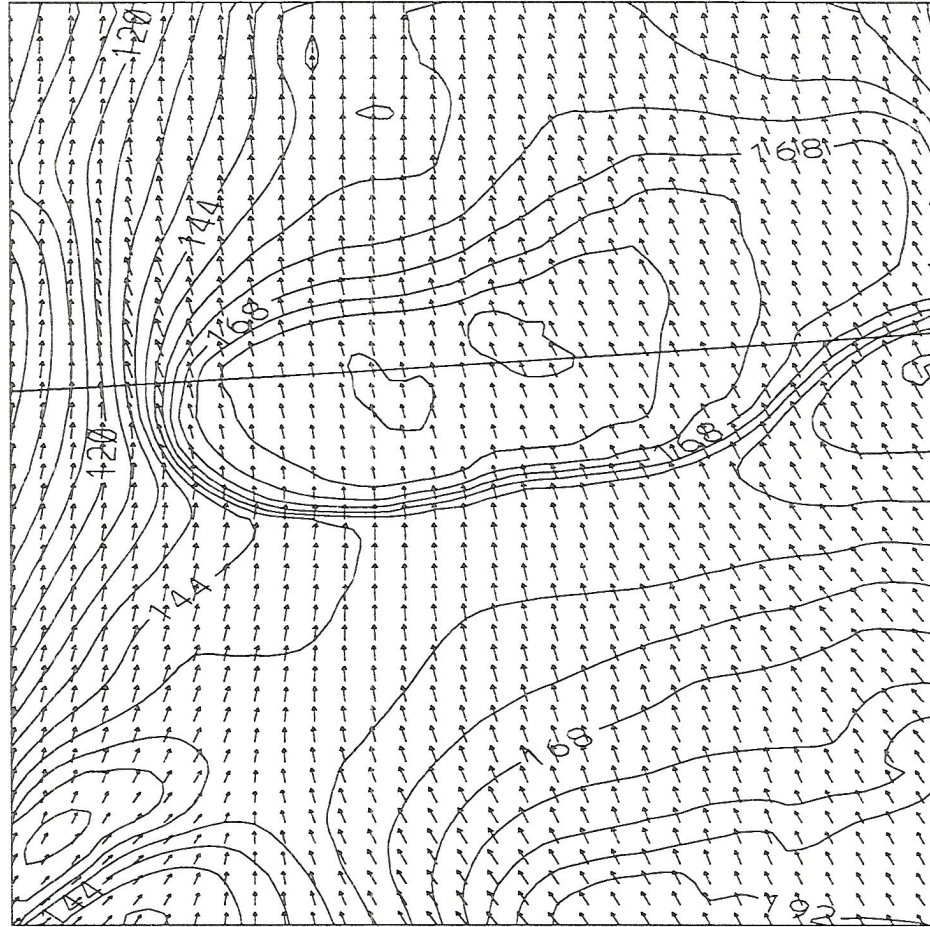


Figure 4.3: Horizontal winds and water vapor mixing ratio values for Grid#3 at 49m and 1900 UTC. From a minimum of 9.0 g/kg, the mixing ratio field is contoured every 0.6 g/kg to a maximum of 19.2 g/kg. A wind vector having a length equal to the distance between two wind vector tails represents a speed of 13.8 m/s.

up from the wet soil below. A convergence zone can be seen in the lower left quadrant of the figure. Notice the weak gradient in water vapor located in the same region.

Water vapor was transported vertically due to convergence near the surface. A ridge in the water vapor mixing ratio field can be seen near the lower left portion of Figure 4.4 at 1992m. A larger region of high water vapor mixing ratio values existed over most of the region on the right side of the figure but was not associated with the convection that occurred later. The winds at this level were strong and from the southwest.

At 1900 UTC there were two main features associated with the vertical motion field at 1992m. A band of upward vertical motion existed along the top left portion of Figure 4.5

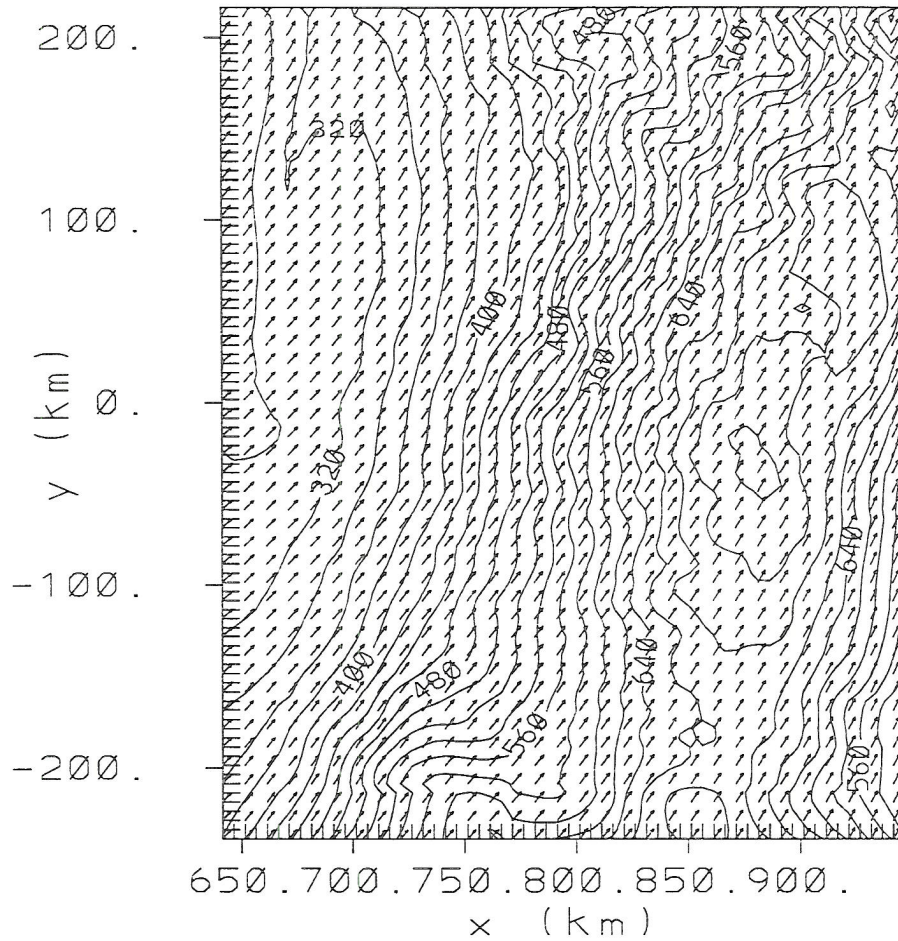


Figure 4.4: Horizontal winds and water vapor mixing ratio values for Grid #3 at 1992m and 1900 UTC. Mixing ratio values range from 2.8 g/kg to a maximum of 7.4 g/kg contoured every 0.2 g/kg. A wind vector having a length equal to the distance between two wind vector tails represents a speed of 25.7 m/s.

orientated in the north-south direction. This was in response to the convergence in the same region near the surface in Figure 4.3. Further nesting was done in that region, however, no convection developed since the air was flowing from the cool region associated with the wet soil. It would be interesting to reduce the soil moisture and do a simulation to see if convection would occur.

The second feature was the local maximum of vertical motion in the lower left portion of the figure. This was associated with the horizontal convergence near the surface and the ridge in the water vapor field. The circulation associated with the dry line was developing rapidly.



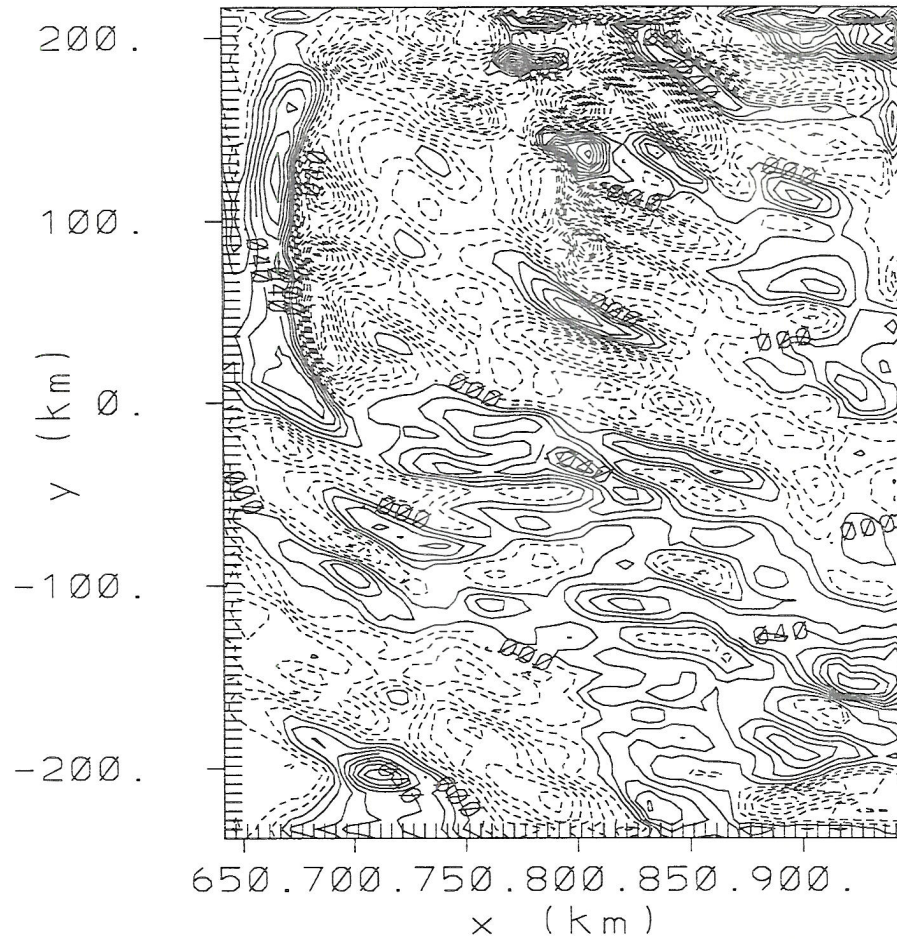


Figure 4.5: Upward vertical motion at 1992m for grid #3 at 1900 UTC. With a contouring of 1.0 cm/s, the minimum and maximum are -11.0 and 11.0 cm/s respectively.

A well-defined convergence zone was apparent near the surface at 2000 UTC in the lower left quadrant of Figure 4.6. This was more pronounced than one hour earlier. Again note the lack of a large moisture gradient within this zone. One can see the beginnings of a moisture gradient becoming more organized near the center of the southern border of the grid, as compared to one hour earlier. A second convergence zone was evident in the upper left portion of the figure.

An increase of water vapor mixing ratio at 1992m due to the enhanced horizontal convergence at lower levels, was clearly evident in the lower left portion of Figure 4.7. Horizontal convergence at lower levels also transported moist air to this height in the upper



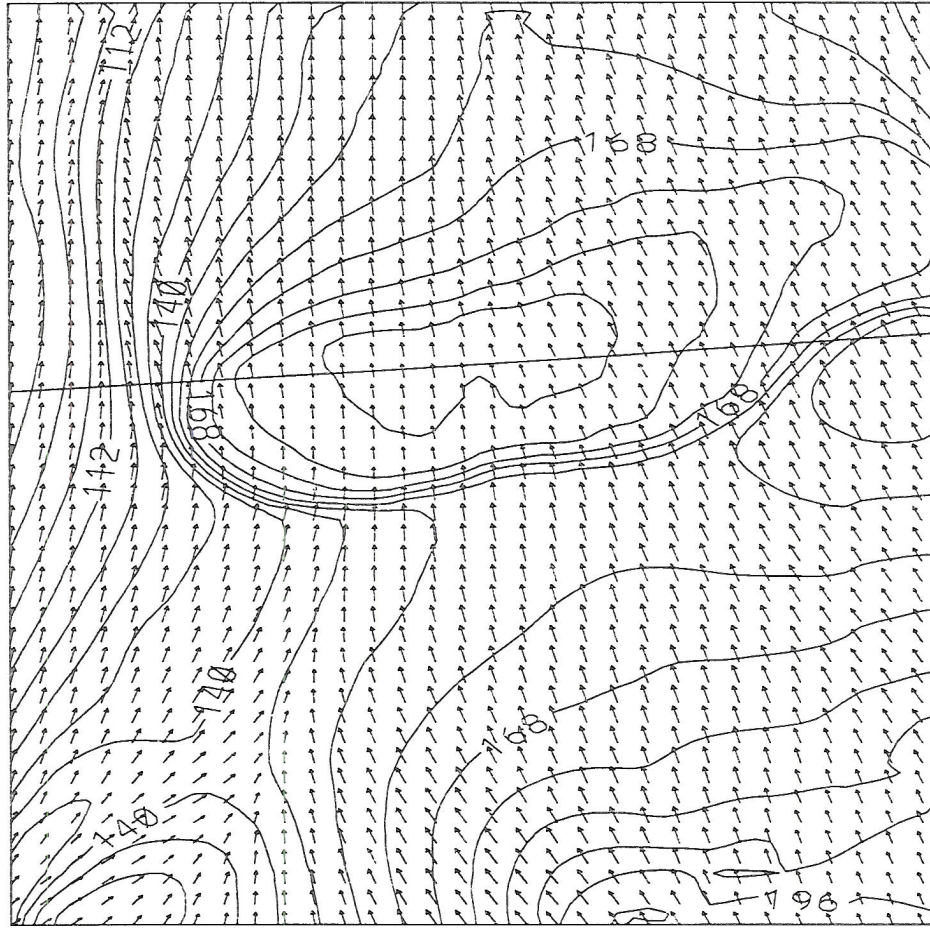


Figure 4.6: Horizontal winds and water vapor mixing ratio values for Grid #3 at 49m and 2000 UTC. From a minimum of 8.4 g/kg, the mixing ratio field is contoured every 0.7 g/kg to a maximum of 20.3 g/kg. A wind vector having a length equal to the distance between two wind vector tails represents a speed of 13.9 m/s.

left region of the figure. The overall flow was still from the southwest with an increase of water vapor from west to east.

The upward vertical motion associated with the two lower level convergence zones, increased from 7.0 cm/s to 26.0 cm/s in the upper left portion of Figure 4.8 and from 8.0 cm/s to 12 cm/s in the lower left region. Note also that the upward vertical motion in the lower left section was orientated more north-south than it was at 1900 UTC. The trends for both regions of upward motion indicate the genesis of deep boundary layer circulations.

At 2100 UTC significant changes had occurred. A horizontal convergence zone existed over a larger region than it had at 2000 UTC. A large eastward gradient of water

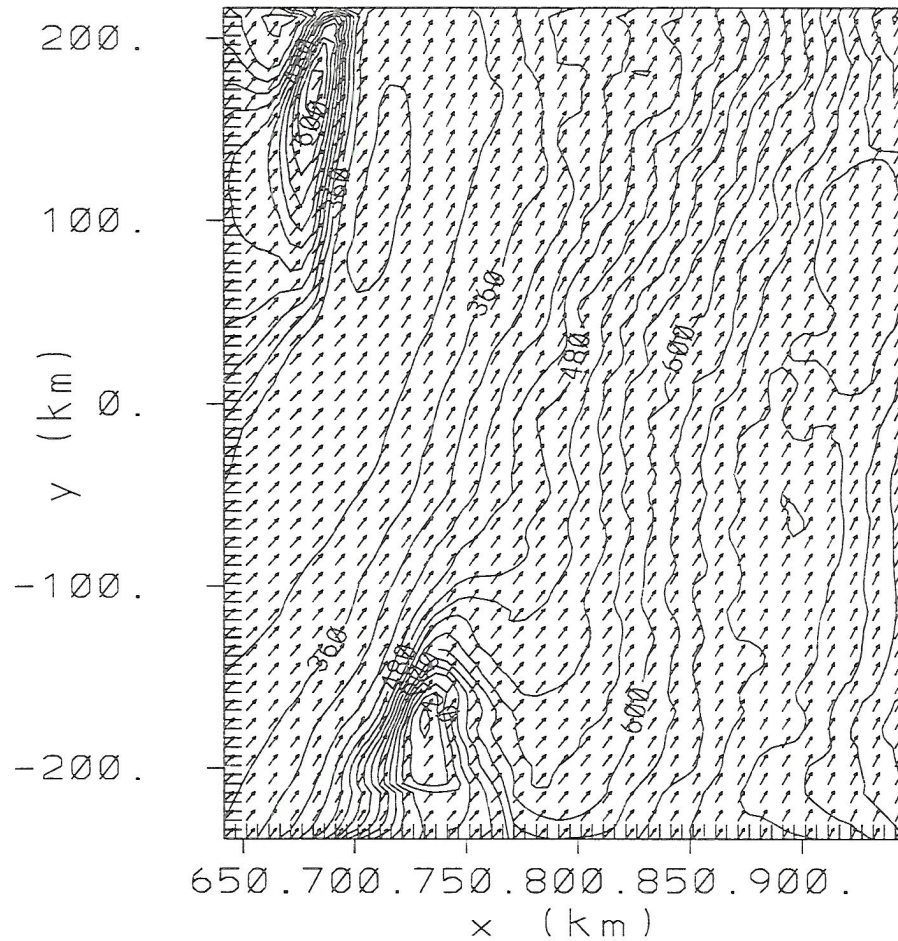


Figure 4.7: Horizontal winds and water vapor mixing ratio values for Grid #3 at 1992m and 2000 UTC. From a minimum of 2.7 g/kg, the mixing ratio field is contoured every 0.3 g/kg to a maximum of 8.1 g/kg. A wind vector having a length equal to the distance between two wind vector tails represents a speed of 25.0 m/s.

vapor was present for the first time along the convergence zone in the lower left section of Figure 4.9. The horizontal convergence zone in the upper right portion was still present but no increase in the water vapor gradient had occurred.

A clear indication of a strong boundary layer vertical circulation was the large values of water vapor mixing ratio in the lower left quadrant of Figure 4.10. The maximum in this region exceeded the previous maximum from one hour earlier by 3.0 g/kg. The local maximum of water vapor in the top left was not as pronounced as it was earlier. This was due to the winds advecting the moisture out of the grid.

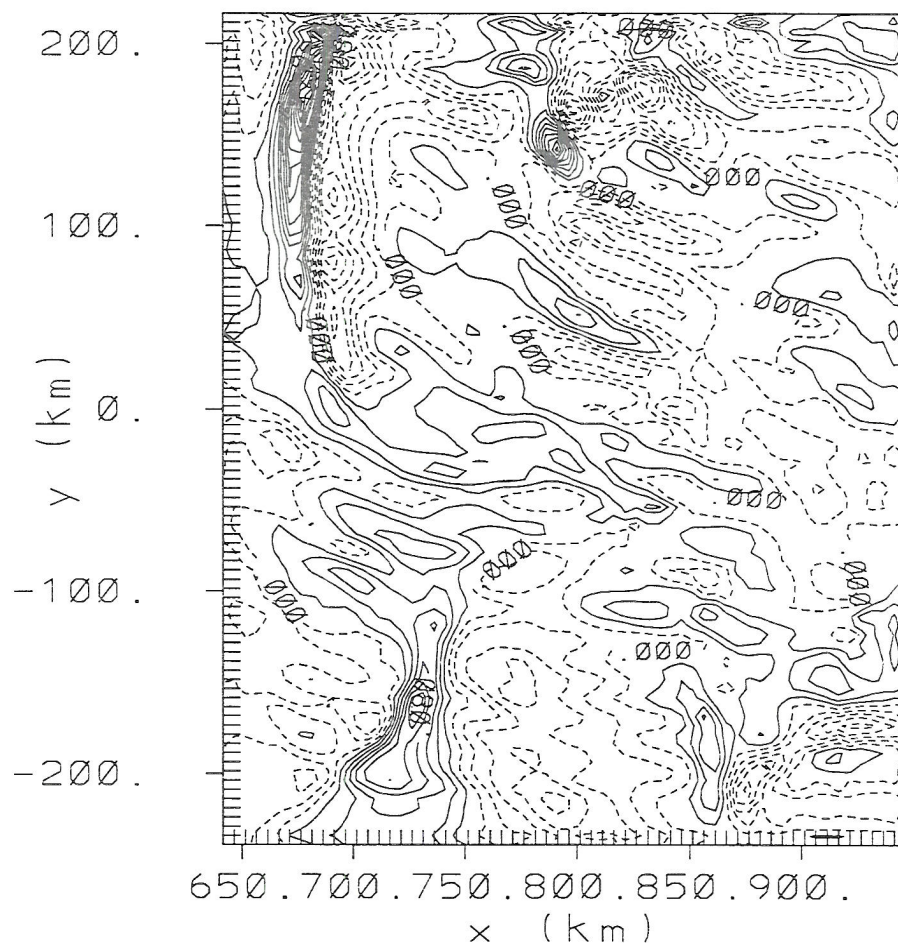


Figure 4.8: Upward vertical motion at 1992m for grid #3 at 2000 UTC. With a contouring of 2.0 cm/s, the minimum and maximum are -14.0 and 26.0 cm/s respectively.

Upward vertical motions had increased considerably at this time. Peak upward motions of 70.0 cm/s existed in the lower left region while 1.3 m/s speeds were attained in the upper left portion of Figure 4.11.

At 2200 UTC the horizontal convergence zone at 49m had extended further to the north (Figure 4.12). A large gradient in water vapor, marking the dry line, resulted from the convergence. The vertical motion along the dry line was very strong and the largest value at this time was 6.5 m/s at 1992m: see Figure 4.13.

The third grid was run until 2300 UTC. Deep tropospheric convection developed and, while moving northeast, produced large anvil canopies. The vertically-averaged cloud-water field was animated in time to determine that convection started at 2100 UTC along



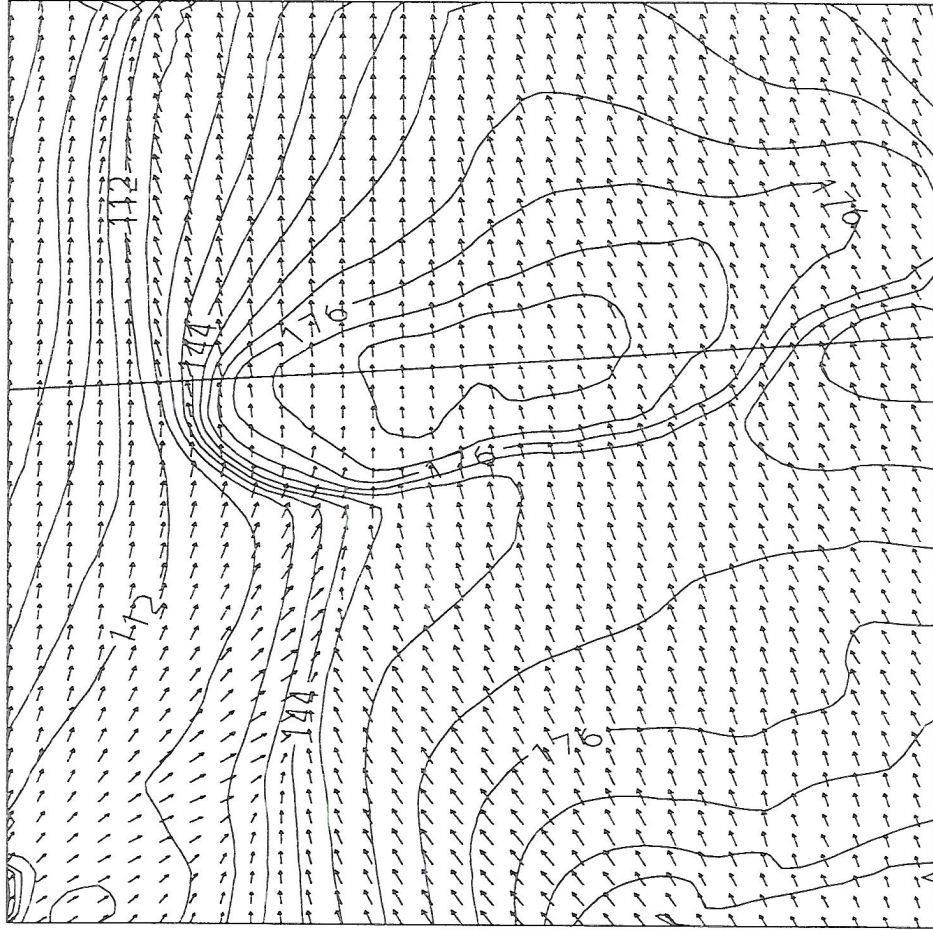


Figure 4.9: Horizontal winds and water vapor mixing ratio values for Grid #3 at 49m and 2100 UTC. From a minimum of 7.2 g/kg, the mixing ratio field is contoured every 0.8 g/kg to a maximum of 20.8 g/kg. A wind vector having a length equal to the distance between two wind vector tails represents a speed of 14.2 m/s.

the rapidly forming dry line in north-central Oklahoma. The fourth nested grid was spawned at that time.

From 1900 UTC to 2100 UTC notice the horizontal winds at 49m had backed in time from southerly to the southeasterly direction. This may have a significant impact on the dynamics of supercell thunderstorms and tornado by changing the shape of the hodograph and horizontal vorticity vectors in the first kilometer. The storm-relative helicity may also change to larger and more favorable values. This process also occurred in the May storm (compare Figure 3.9 to Figure 3.3). The winds had backed from 1800 to 2000 UTC along and

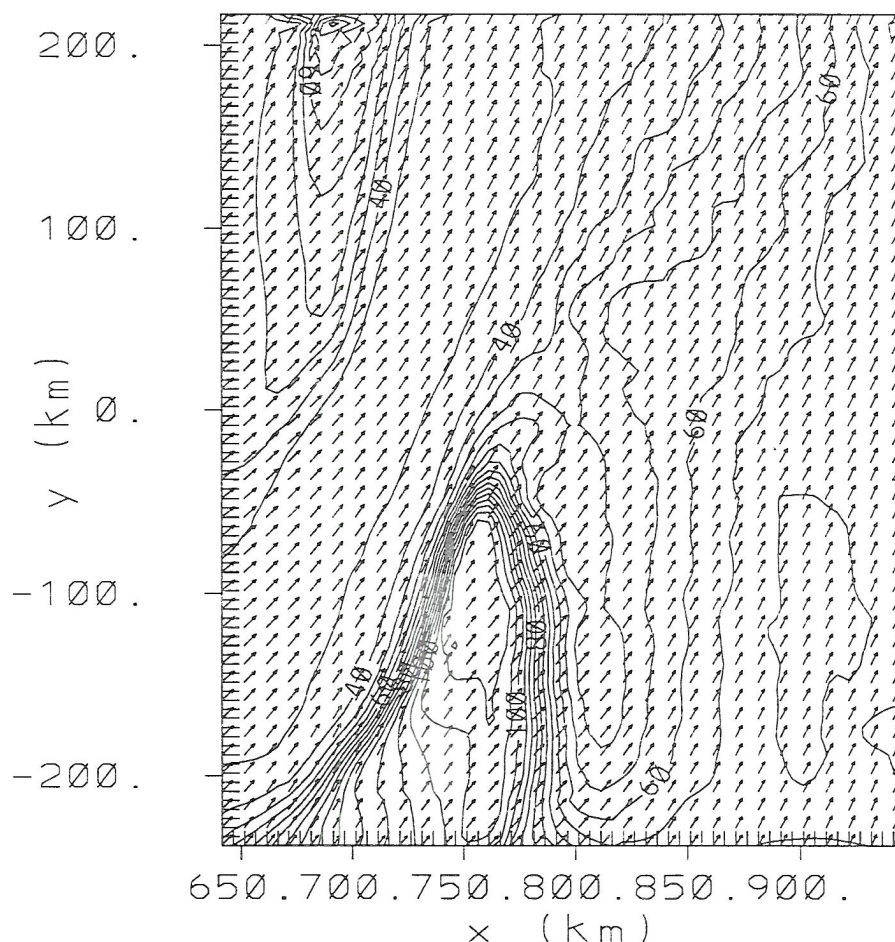


Figure 4.10: Horizontal winds and water vapor mixing ratio values for Grid #3 at 1992m and 2100 UTC. From a minimum of 3.0 g/kg, the mixing ratio field is contoured every 0.5 g/kg to a maximum of 11.0 g/kg. A wind vector having a length equal to the distance between two wind vector tails represents a speed of 24.8 m/s.

ahead of the dryline. This is one way that the 1200 UTC hodograph, shown in Figure 3.2d, can be altered to a clockwise curved profile favorable for long-lived supercell thunderstorms.

#### 4.4 Dry Line Dynamics

The next sequence of figures display a vertical cross section in Grid #3 where the dry line will form. In the morning from 1200 UTC to 1600 UTC (Figure 4.14 through Figure 4.16) the lowest kilometer was moistened by easterly winds (the lowest two shadings in the figures represent easterly winds). The depth of easterlies increased and the vertical gradient in water vapor mixing ratio increased just above 1.0 km. The frontogenetic forcing

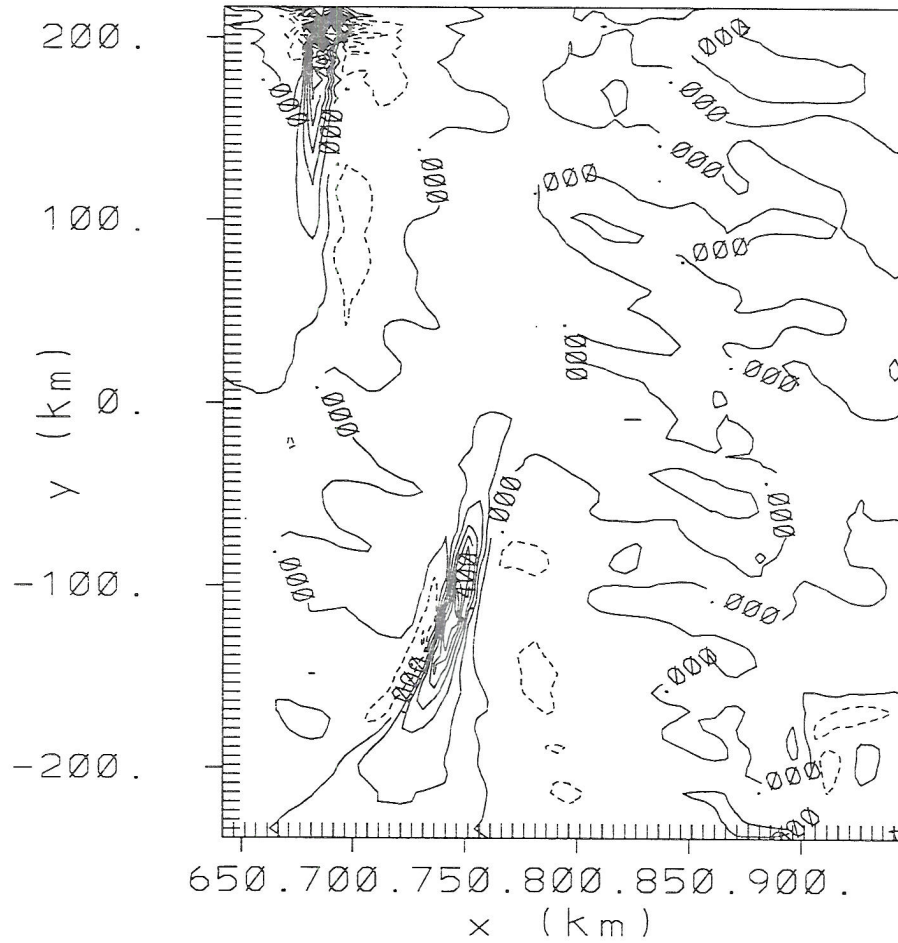


Figure 4.11: Upward vertical motion at 1992m for grid #3 at 2100 UTC. With a contouring of 10.0 cm/s, the minimum and maximum are -0.7 and 1.3 m/s respectively.

terms are very weak in this time interval since  $\frac{\partial u}{\partial x}$ ,  $\frac{\partial q}{\partial x}$ , and  $\frac{\partial w}{\partial x}$  are all small, particularly in the lowest kilometer. The solenoidal forcing was smaller than  $10^{-6}s^{-2}$  from 1200 UTC to 2000 UTC and will not be shown.

In Figure 4.17 the lowest three shadings represent easterly winds. Weak horizontal convergence was evident at this time in the lowest 1.0 km. Due to the small horizontal gradient in water vapor and vertical motion, frontogenetic forcing remained small. Noticable changes had occurred at 2000 UTC (Figure 4.18). An increase in  $\frac{\partial u}{\partial x}$  (the zero contour for the u-component of the wind runs horizontally at 1323m from right to left then curves vertically at the left side of the figure at  $x=78\text{km}$ ) combined with the turning of the water



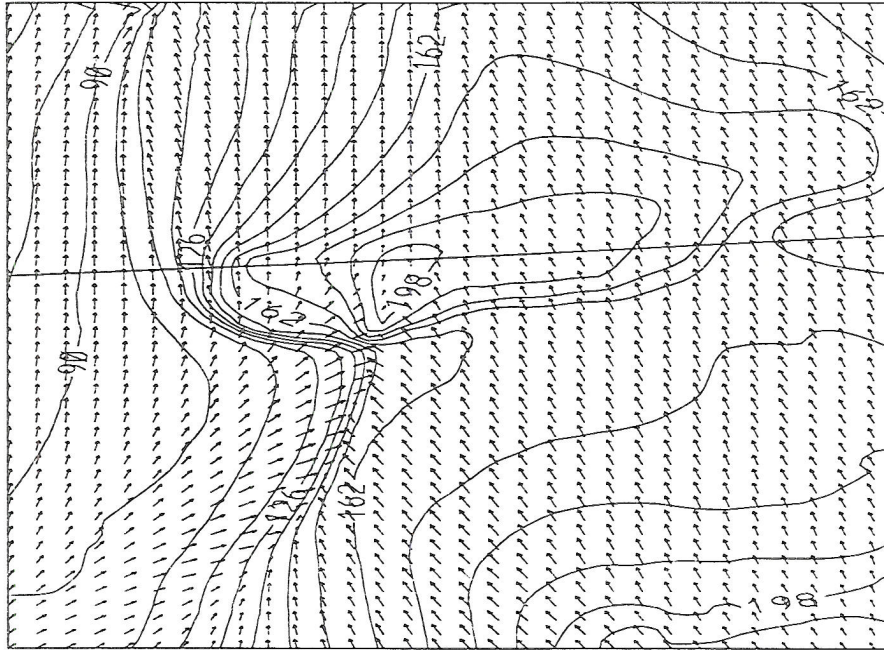


Figure 4.12: Horizontal winds and water vapor mixing ratio values for Grid #3 at 49m and 2200 UTC. From a minimum of 6.3 g/kg, the mixing ratio field is contoured every 0.9 g/kg to a maximum of 20.7 g/kg. A wind vector having a length equal to the distance between two wind vector tails represents a speed of 14.8 m/s.

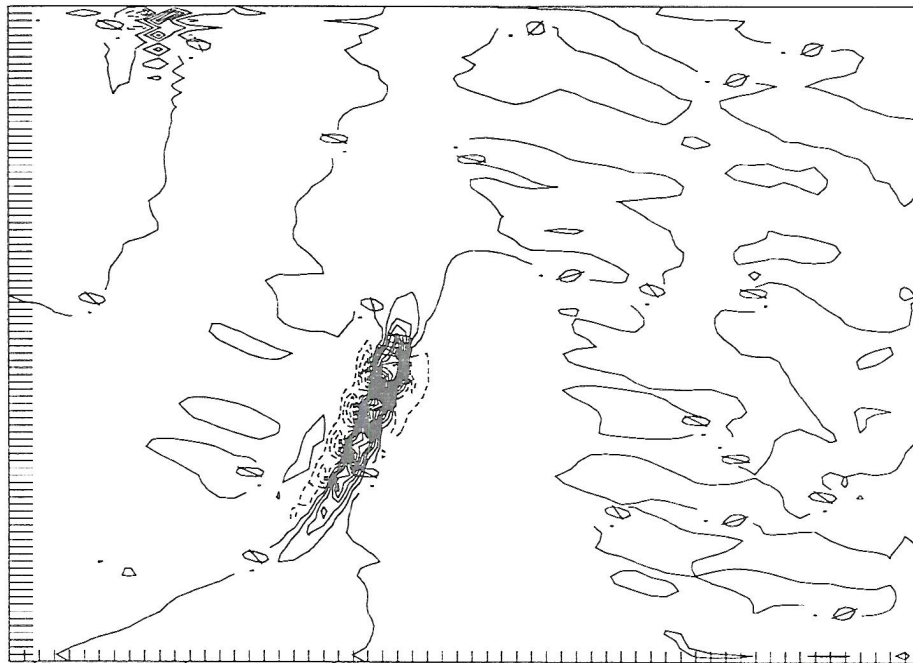


Figure 4.13: Upward vertical motion at 1992m for grid #3 at 2200 UTC. With a contouring of 50.0 cm/s, the minimum and maximum are -2.5 and 6.5 m/s respectively.



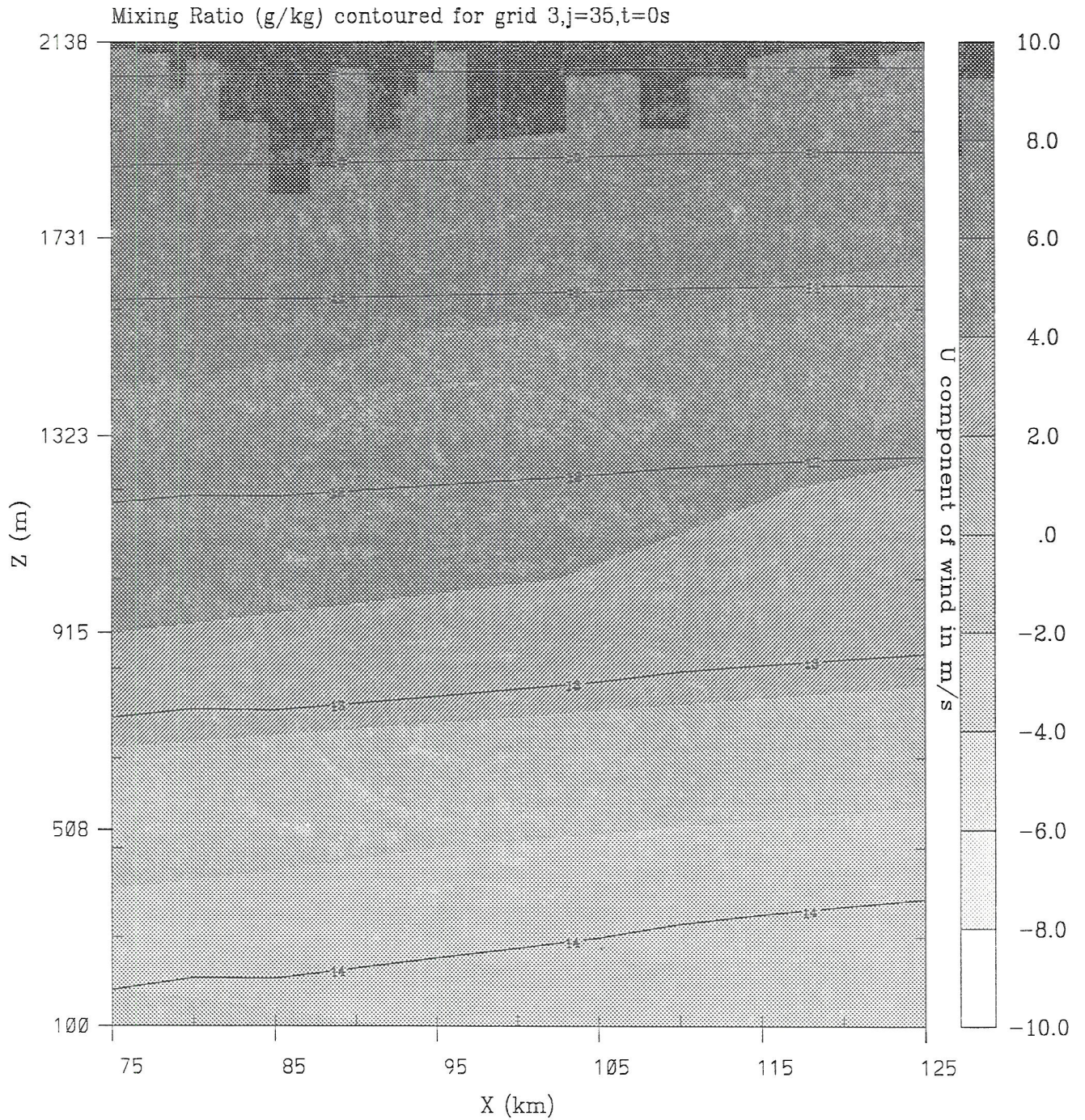


Figure 4.14: East-west vertical cross section of water vapor mixing ratio at 1200 UTC in Grid #3, 110.0 km north of its southern border. This field is contoured every 1.0 g/kg. The u-component of the wind is shaded in increments of 2.0 m/s.



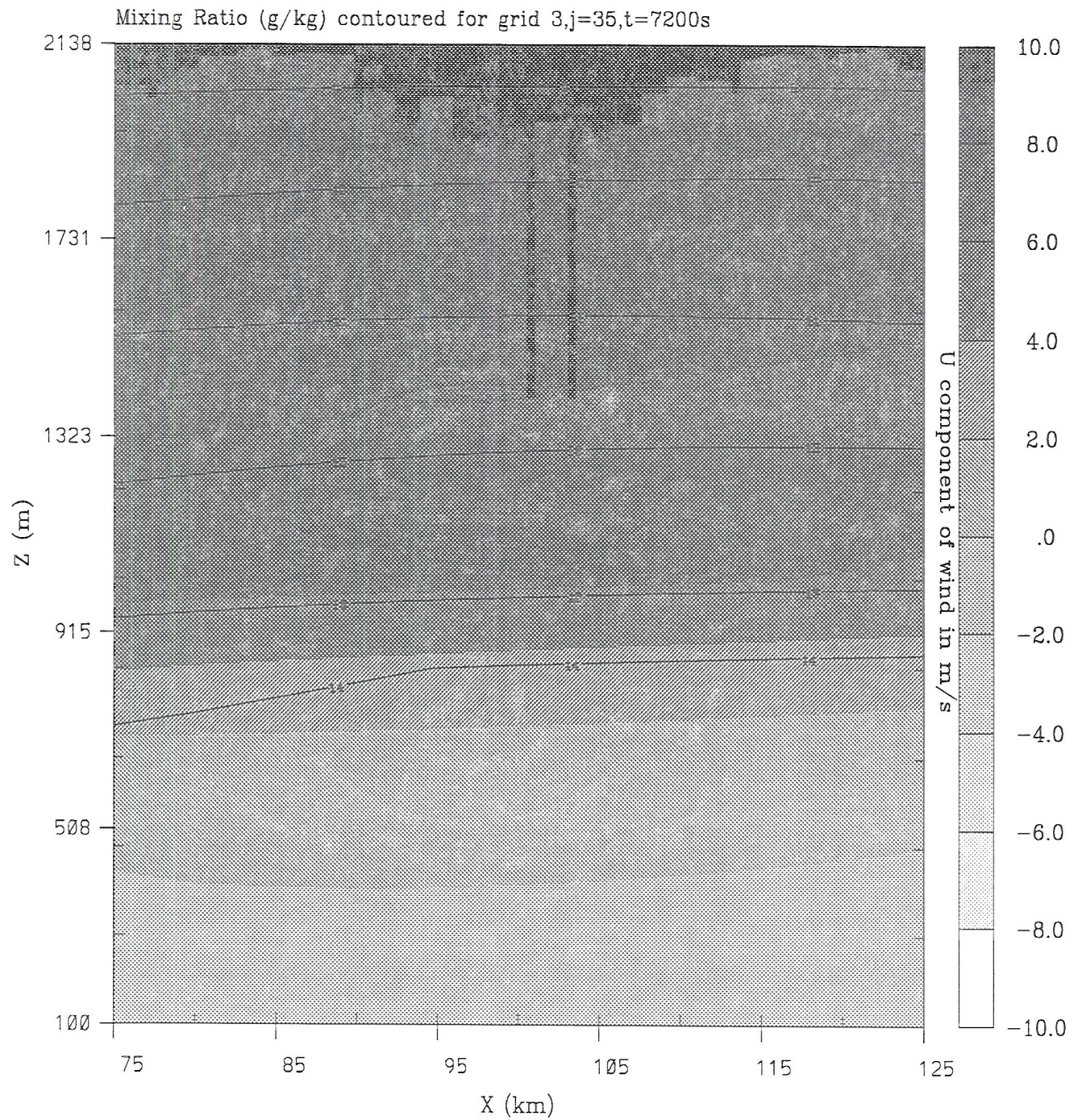


Figure 4.15: East-west vertical cross section of water vapor mixing ratio at 1400 UTC in Grid #3, 110.0 km north of its southern border. This field is contoured every 1.0 g/kg. The u-component of the wind is shaded in increments of 2.0 m/s.



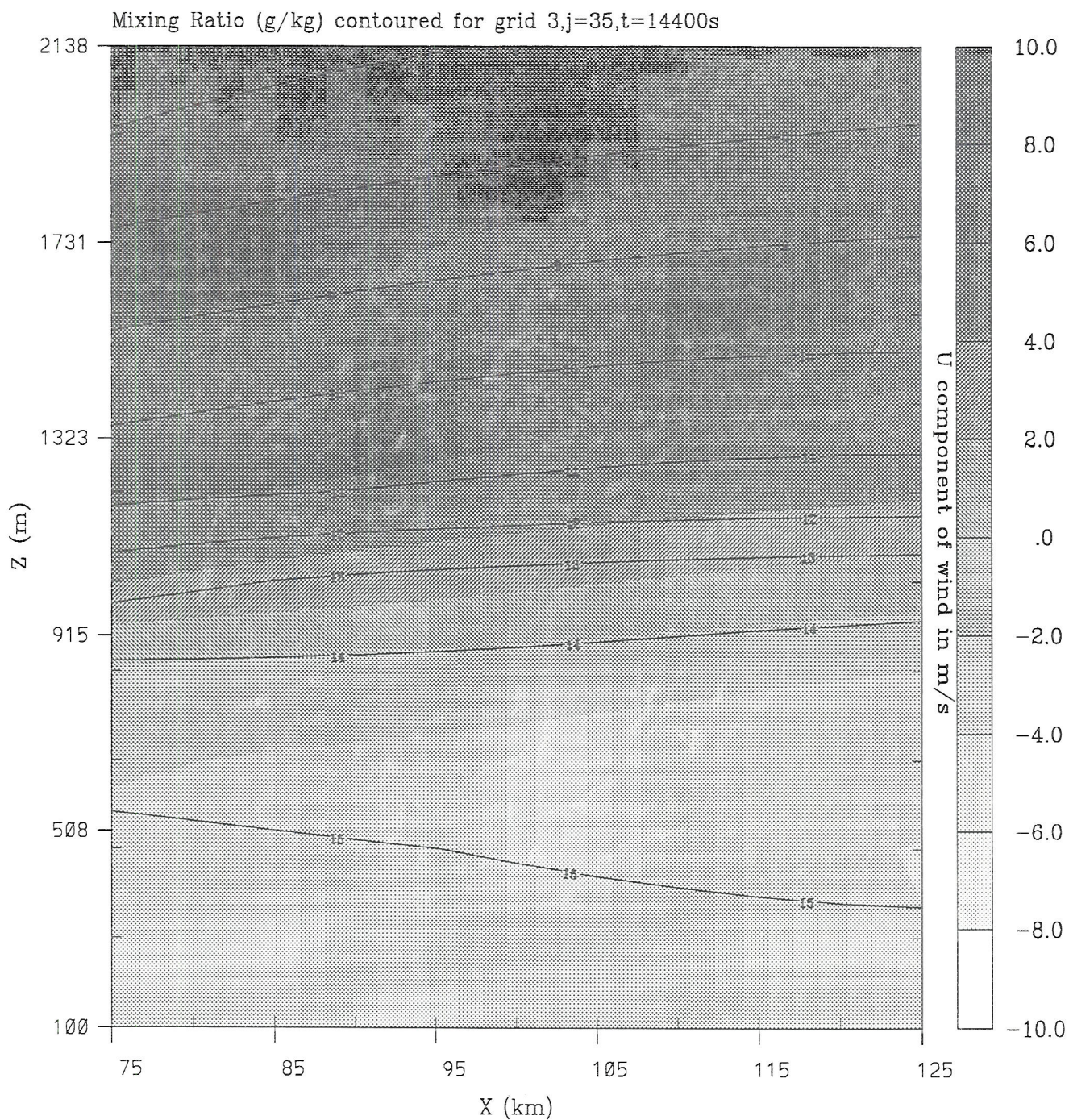


Figure 4.16: East-west vertical cross section of water vapor mixing ratio at 1600 UTC in Grid #3, 110.0 km north of its southern border. This field is contoured every 1.0 g/kg. The u-component of the wind is shaded in increments of 2.0 m/s.



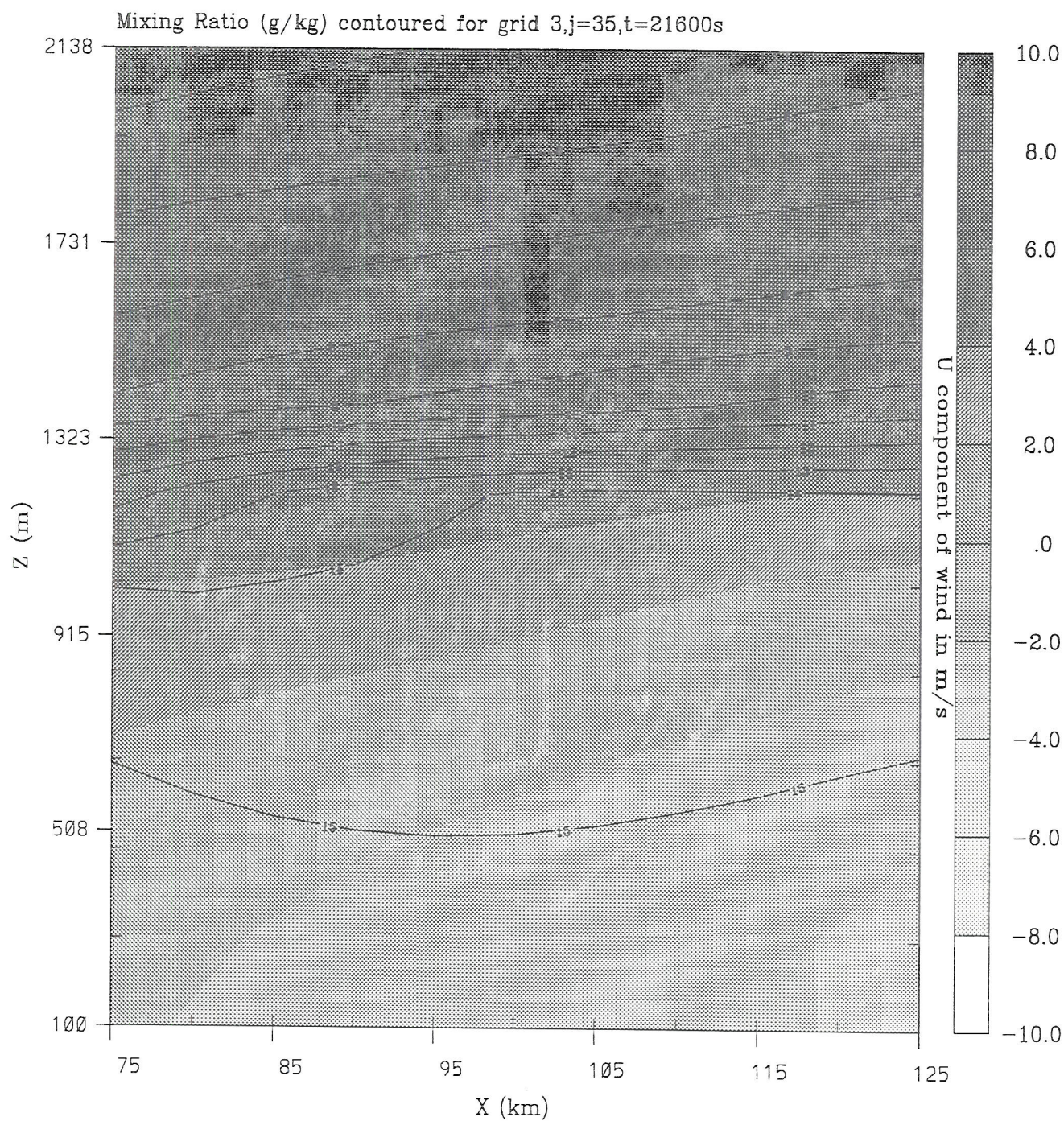


Figure 4.17: East-west vertical cross section of water vapor mixing ratio at 1800 UTC in Grid #3, 110.0 km north of its southern border. This field is contoured every 1.0 g/kg. The u-component of the wind is shaded in increments of 2.0 m/s.



vapor contours at  $x=85\text{km}$  resulted in small positive frontogenetic forcing of the water vapor field in the first kilometer.

At 2100 UTC a strong convergence zone existed centered on  $x=104\text{km}$  in the lowest kilometer of Figure 4.19. The horizontal gradient in water vapor had increased and resulted in the frontogenetic forcing to grow by one order of magnitude from 2000 UTC to  $10^{-10}\text{m}^{-1}\text{s}^{-1}$ . Clearly displayed in the figure is the horizontal convergence of dry westerly winds with moist easterly winds in the lowest 1.0km (the four shadings on the lower right side of the Figure represent easterly winds). The solenoidal forcing grew rapidly from one hour earlier. A large region of positive solenoidal forcing can be seen in Figure 4.20. A maximum value of  $6 \times 10^{-6}\text{s}^{-2}$  is at the center of the figure.

The analysis of this dry line is similar to the May case in that the frontogenetic forcing of water vapor precedes the solenoidal forcing. The magnitudes of the frontogenetic and solenoidal forcing are similar and agree well with Ziegler et al. (1995).

#### 4.5 Supercell Evolution

As was mentioned previously, Grid #4 was spawned at 2100 UTC and was the first nested grid to move. The horizontal grid spacing was 1.0 km in both directions. Thirty minutes later, at 49m, a distinct horizontally convergent wind field existed along with a large eastward gradient of water vapor (Figure 4.21a). Note the axis of convergence was on the moist side of the water vapor gradient, particularly within the top portion of the figure. For the May case the axis of convergence was along the moisture gradient (Figure 3.24a). Note also the horizontal gradient of moisture for the May case was much larger.

It is interesting to speculate why there is a difference between the two cases and what impact this may have had on the evolution of the dry line and the associated convection. The analysis of the dry line suggests it possible that the moisture gradient used to locate the dry line is a consequence of, rather than the cause of, processes leading to convection.

The vertical motion at 5414m (Figure 4.21b) exhibited a large region of updraft in the southern portion of the figure. Continuing towards the north there was a mixture of updraft and downdraft with a stronger updraft center near the top of the figure. Note how



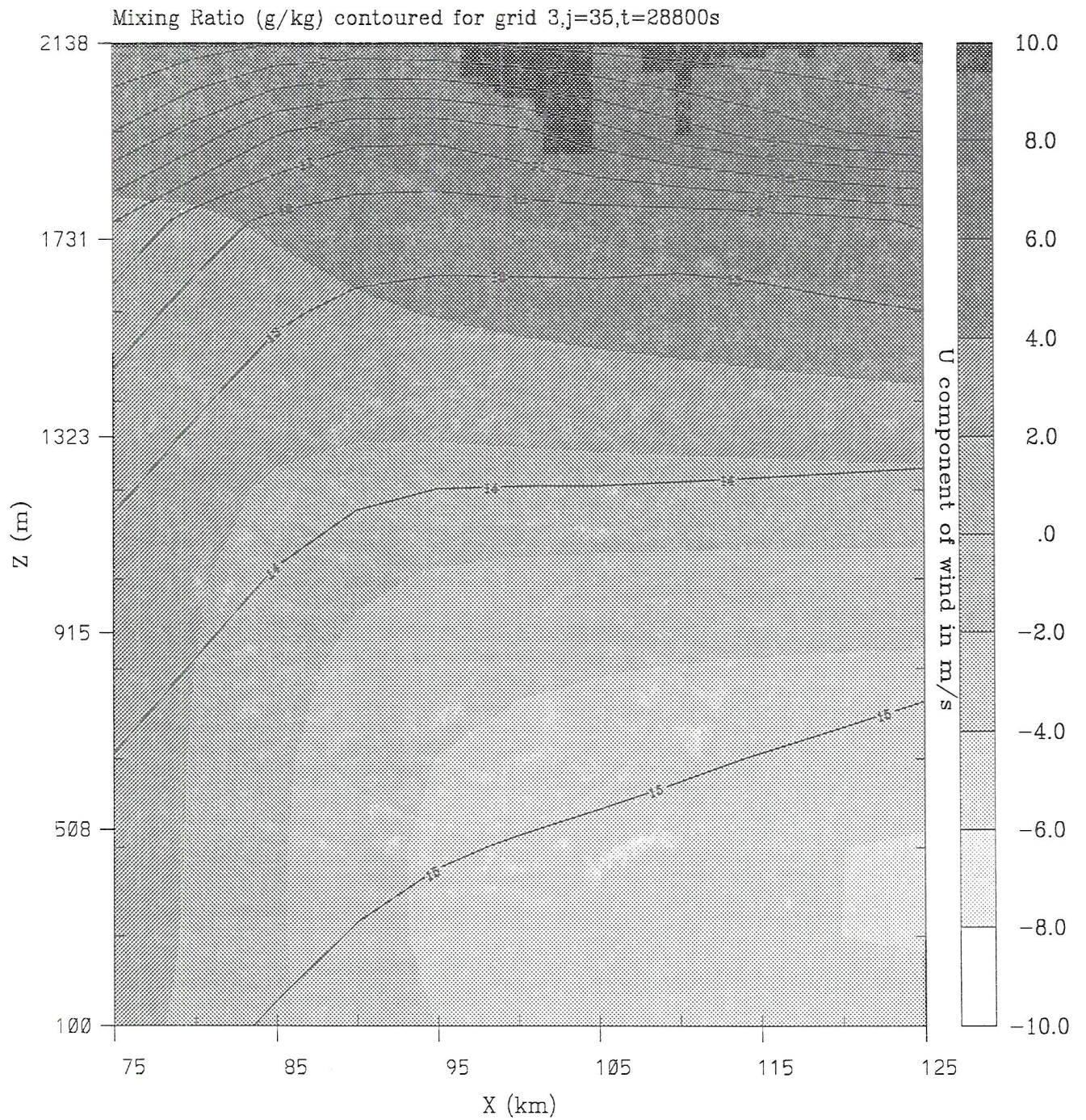


Figure 4.18: East-west vertical cross section of water vapor mixing ratio at 2000 UTC in Grid #3, 110.0 km north of its southern border. This field is contoured every 1.0 g/kg. The u-component of the wind is shaded in increments of 2.0 m/s.



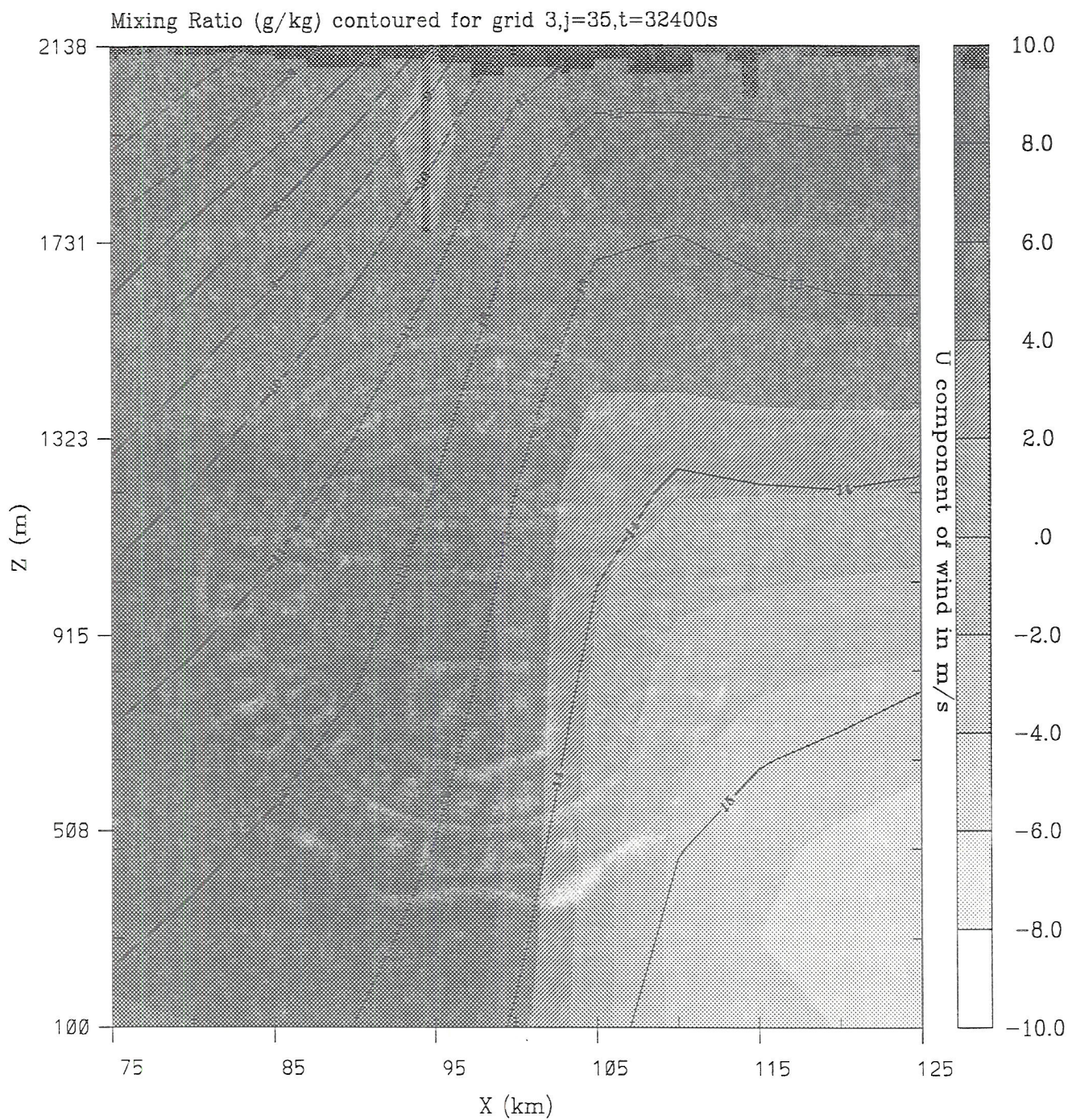


Figure 4.19: East-west vertical cross section of water vapor mixing ratio at 2100 UTC in Grid #3, 110.0 km north of its southern border. This field is contoured every 1.0 g/kg. The u-component of the wind is shaded in increments of 2.0 m/s.



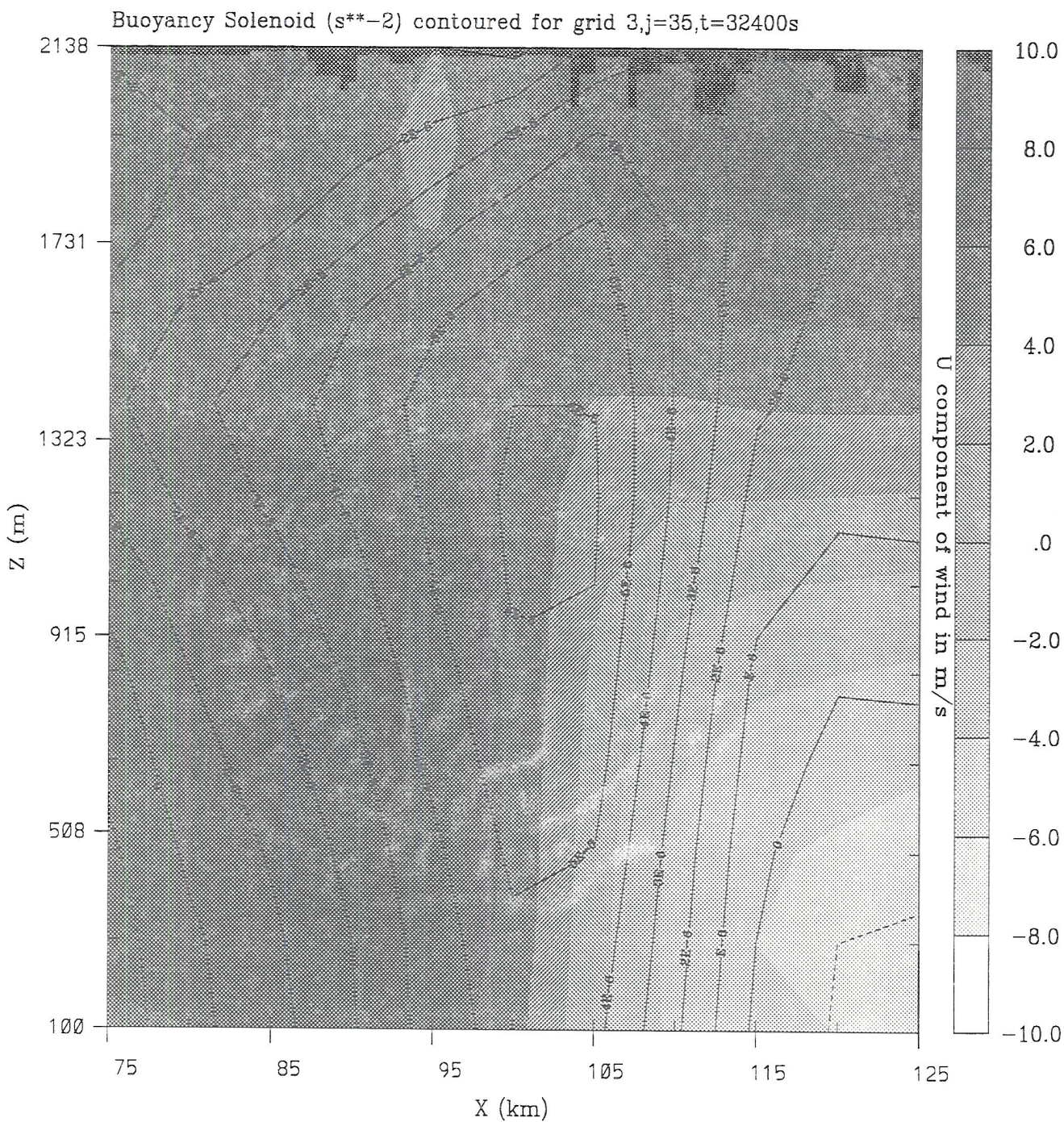


Figure 4.20: East-west vertical cross section of the solenoid forcing at 2100 UTC in Grid #3, 110.0 km north of its southern border. This field is contoured every  $10^{-6} s^{-2}$ . The u-component of the wind is shaded in increments of 2.0 m/s.



the updrafts were further east of the moisture gradient moving from the bottom portion of the figure towards the top.

Thirty minutes later, Grid #4 had moved 20.0 km to the east. As in the May case, a bulge in the dry line developed (see Figure 4.21c) with cyclonic circulation just to its north. The vertical motion at 5414m shows a large region of upward motion with peak values of 45.0 m/s near the center of Figure 4.21d with an east-west band of updraft to the southwest.

The evolution of the convective line into cyclonic and anticyclonic storms was complicated. The line appeared to spawn one large cyclonic storm having an updraft diameter approximately 16km in length. This splitting process did not evolve as it does in a simulation of convection, triggered by a warm bubble and initialized horizontally-homogeneous. This may indicate that the splitting process was somewhat dependent on the size and shape of the convective forcing.

The next sequence of figures shows the evolution of the winds, water vapor mixing ratio, and rain mixing ratio at 49m in fifteen minute intervals. With the fourth grid running for thirty minutes, convection developed and produced rain at the surface (Figure 4.22a) associated with the updraft cell in the lower portion of Figure 4.21b.

At 2145 UTC, Grid #4 had moved 10.0 km to the east. A bulge in the dry line was evident. The winds near the southern portion of the bulge had backed compared to fifteen minutes earlier, (Figure 4.22c). A larger region of rain had developed, as seen in Figure 4.22d, but no hook appendage was evident.

At 2200 UTC, Grid #4 had moved 10.0 km in both the north and east directions. The dry line bulge was very noticeable having cyclonic circulation on its leading edge. To the north of the bulge on the moist side, winds flowing towards the dry line diverged into two distinct branches. One moved to the northwest and the other, associated with the cyclonic circulation, moved south; see Figure 4.23a. The rain mixing ratio field had expanded more and the southern flanks were co-located with the easterly winds that diverged near the dry line. In particular, the southwest corner of the rain field was located in the region where the easterly winds turned to northeasterly winds along the northern flanks of the circulation

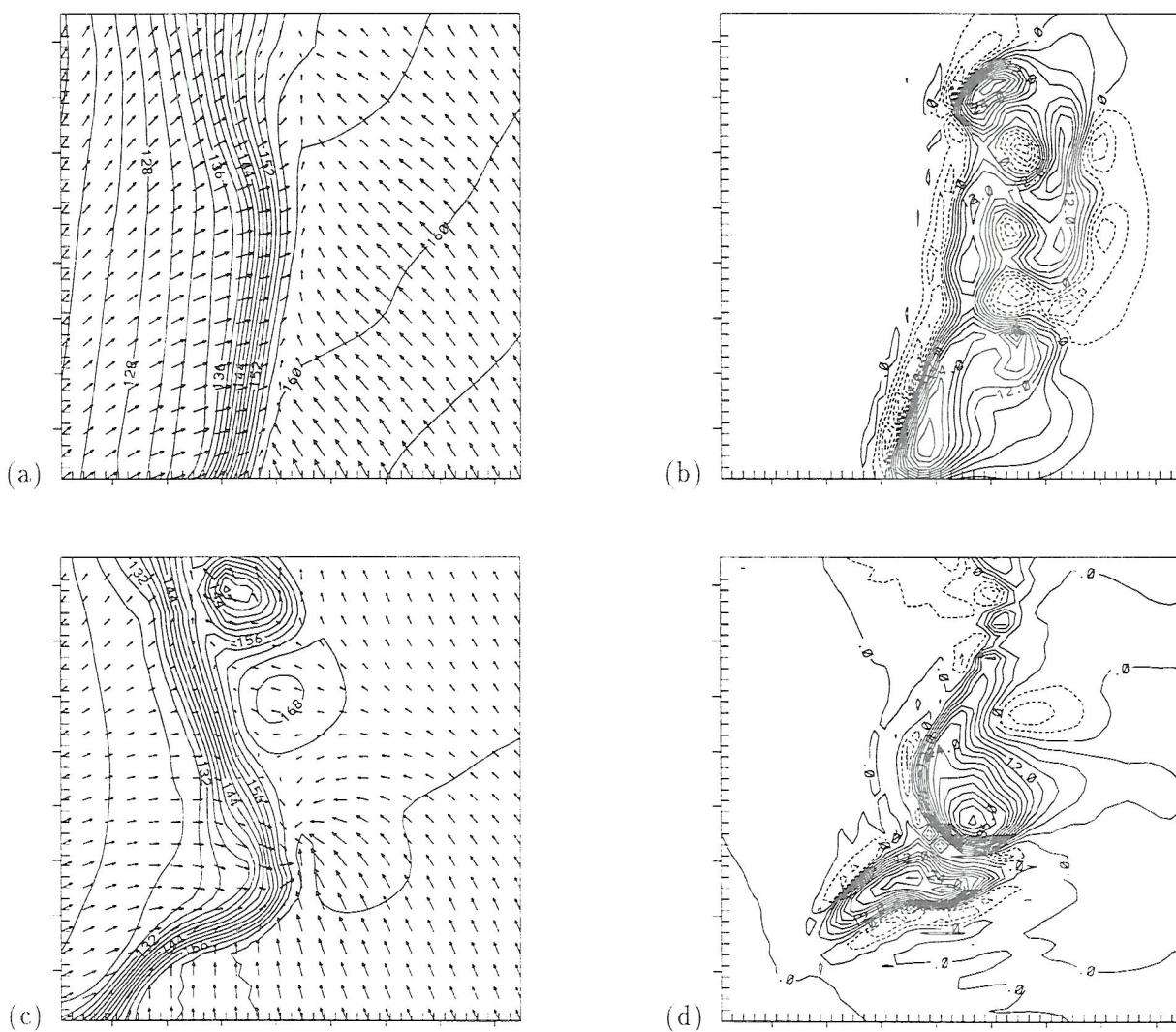


Figure 4.21: Grid #3: (a) and (c) Winds and mixing ratio at 49m, contoured every .2g/kg in (a) at 2130 UTC and .3g/kg in (b) at 2200 UTC. (b) and (d) Vertical motion at 5414m, contoured every 3.0m/s to a maximum of 33.0m/s in (b) at 2130 and 45.0m/s in (d) at 2200 UTC.



center. As one can see in Figure 4.23b, a hook echo had not formed. These two figures just discussed display near surface features that seem to be at the same point in the evolutionary sequence of the storm becoming tornadic as those in Figures 3.25a and b for the May case.

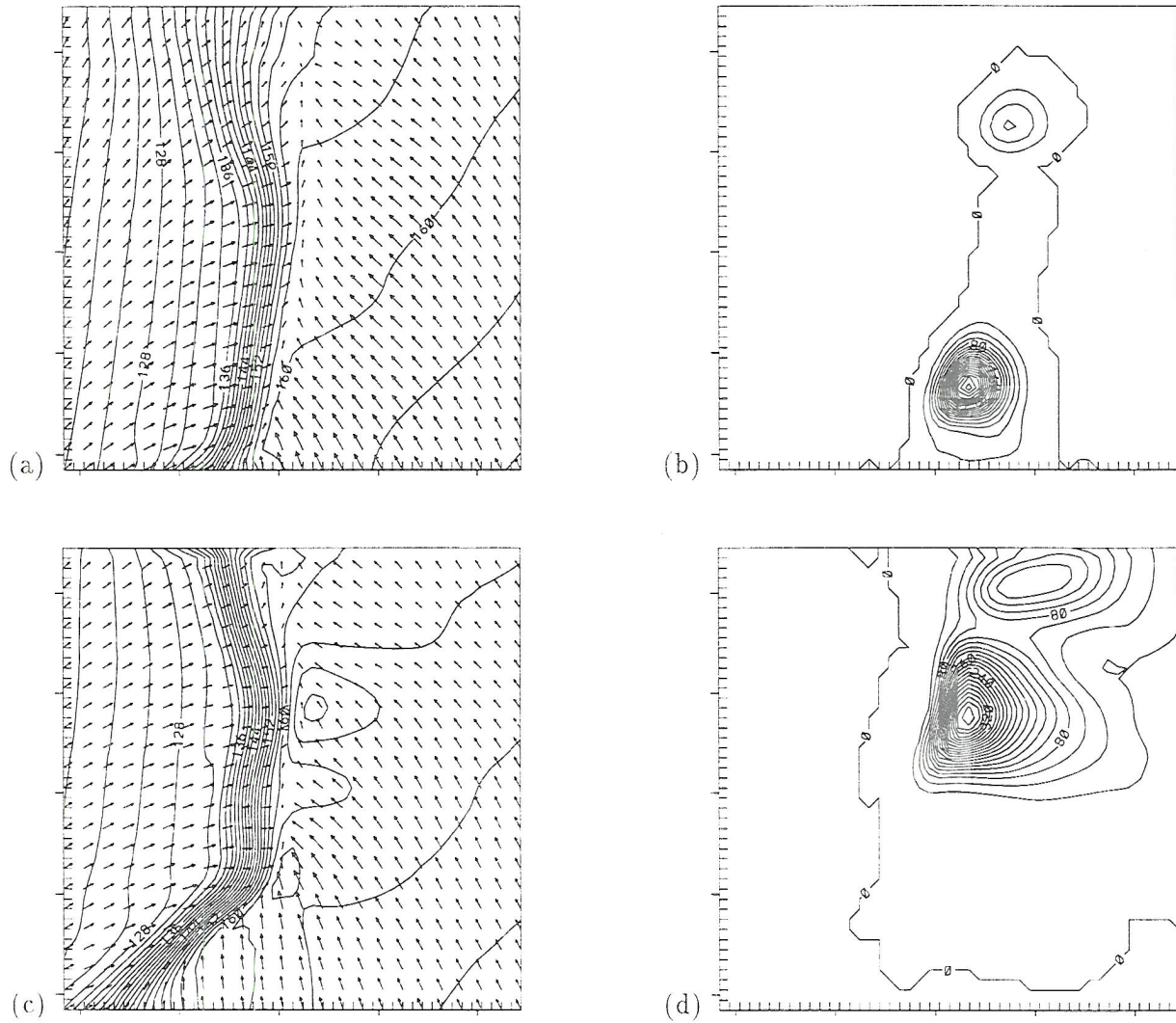
Significant changes occurred fifteen minutes later at 2215 UTC. The grid had moved another 10.0 km north and east. The cyclonic circulation center had moved away from the dry line. To the north of the surface vortex, the winds were divergent with air accelerating towards the moisture gradient. A dry slot extended from the vortex southwest to the dry line and was co-located with the gust front (Figure 4.23c). A well defined hook in the rain water mixing ratio can be seen in Figure 4.23d. A large horizontal gradient in the rain field existed to the southeast of the maximum and was in the same region where the easterly winds had abruptly turned and became north and northeasterly. This occurred to the north of the cyclonic circulation center.

One can compare these two figures with Figures 3.25c and d. In comparing, notice in the April case, that the rain field had developed a much more pronounced hook signature during the last fifteen minutes. The maximum was also aligned from the southwest to the northeast where as in the May case it was along a line orientated more towards the north-northeast.

As in the May case, the dry line developed an eastward bulge where the convective storm was located. This further suggests a strong interaction between the dry line and convection.

#### 4.6 Tornado Evolution

At 2145 UTC the fifth grid was spawned prior to any organized surface rotation. Ten minutes later the beginnings of rotation at 49m can be seen just to the left of the center of Figure 4.24a. To the north and west of the surface vortex the winds were westerly, quite similar to those in Figure 3.27a. As required by mass continuity, a maximum in upward vertical motion existed (Figure 4.24b) where the winds converged, as seen in Figure 4.24a. This maximum was located within a broad region of upward motion resembling the shape of a comma. A second band of upward motion can be seen extending from the head of the





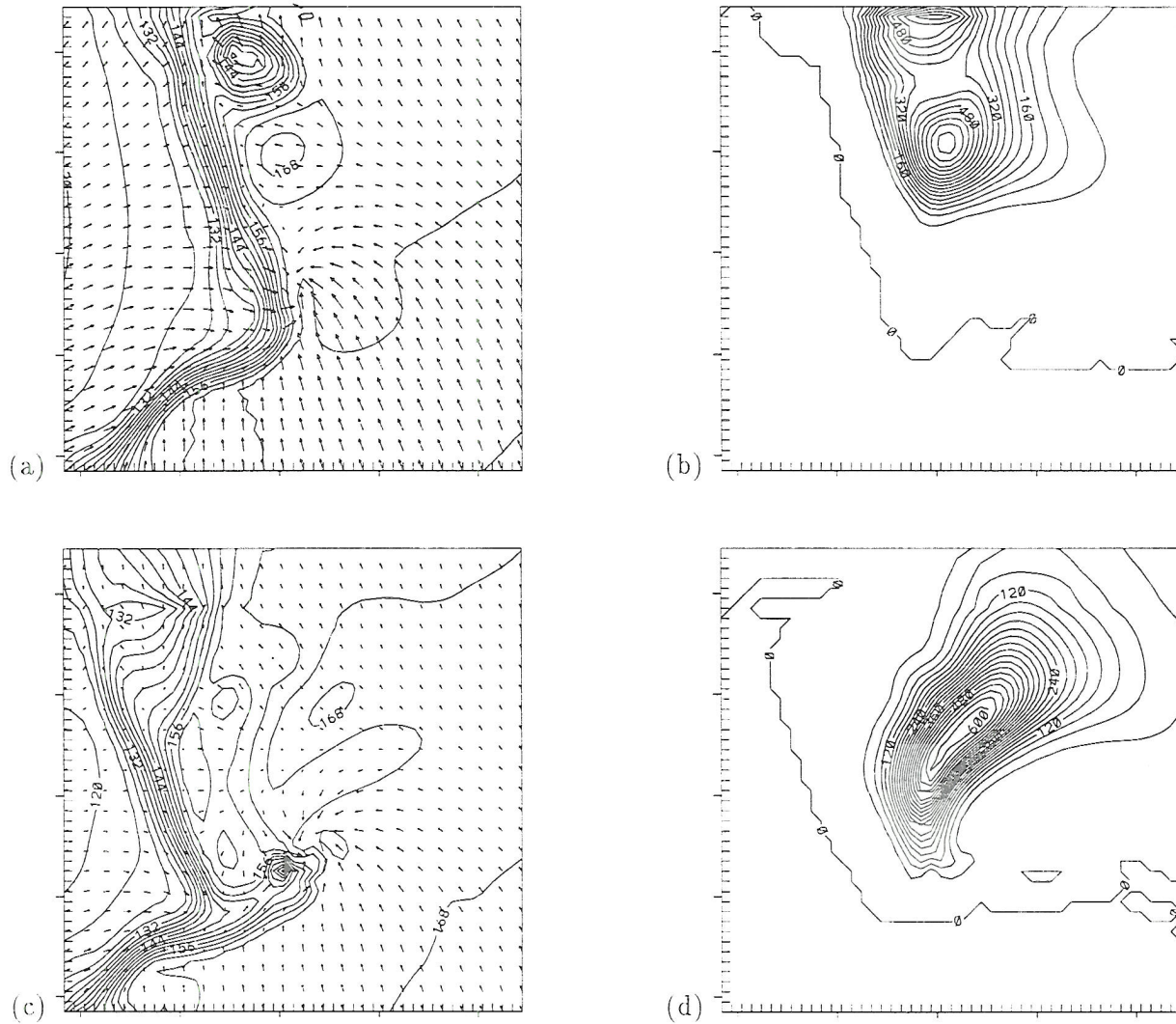


Figure 4.23: Grid #4; (a) and (b) Winds, mixing ratio (contoured every  $.3\text{g/kg}$ ), and rain water (contoured every  $4 \times 10^{-2}\text{g/kg}$  to a maximum of  $.64\text{ g/kg}$ ) at 49m for 2200 UTC, respectively (c) and (d) Winds, mixing ratio (contoured every  $.3\text{g/kg}$ ), and rain water (contoured every  $3 \times 10^{-2}\text{g/kg}$  to a maximum of  $.6\text{g/kg}$ ) at 49m for 2215 UTC, respectively.

comma towards the southwest. There were two regions of downdraft at this time and height located in the top left and just below the center of the Figure. Overall the surface features presented are qualitatively similar to those in Figures 3.27a and b.

The winds at 2291m displayed a large region of cyclonically curved flow. The very sharp curved flow existed to the left of the center of Figure 4.24c in the same location as the water vapor mixing ratio maximum. Just to the west there was a large gradient in the water vapor field. Note how circular the contours of upward vertical motion were in the vicinity of the 38.0 m/s maximum in Figure 4.24d. This portion of the updraft was also located in the same region as the sharp curved flow and the water vapor maximum, an indication of a rotating updraft and that the updraft was transporting moist air upward from below. The large gradient in water vapor was located between the rotating updraft and the downdraft to the west. The existence of the water vapor gradient suggests that little mixing of dry air into the updraft core had occurred.

The flow at 5414m was basically from the southwest. The large moisture gradient in the center of and in the top left of Figure 4.24e bounded the maximum of this field. The flow had weak curvature just to the east of the maximum. A strong updraft of approximately 56.0m/s dominates the center of Figure 4.24f. The large gradient of updraft and moisture at this elevation suggests little mixing had occurred between the environment and the updraft core. To the south of the updraft core was a downdraft with a speed of 12.0 m/s.

Five minutes later, at 49m, the eastward bulge in the dry line was more prominent as seen in Figure 4.25a. At the tip of the bulge, dry air was moving north, and just to the west, moist air was flowing south in response to the close circulation in this region. The rotation was more organized compared to five minutes earlier in Figure 4.24a. It is important to keep in mind that the developing vortex was linked to the dry line at this time. The upward vertical motion maintained its comma shape, with the maximum at the head of the comma. Two downdrafts can be seen, one in a southwest to northeast band from the bottom left to the center of Figure 4.25b, and a second in the top left part of the Figure.



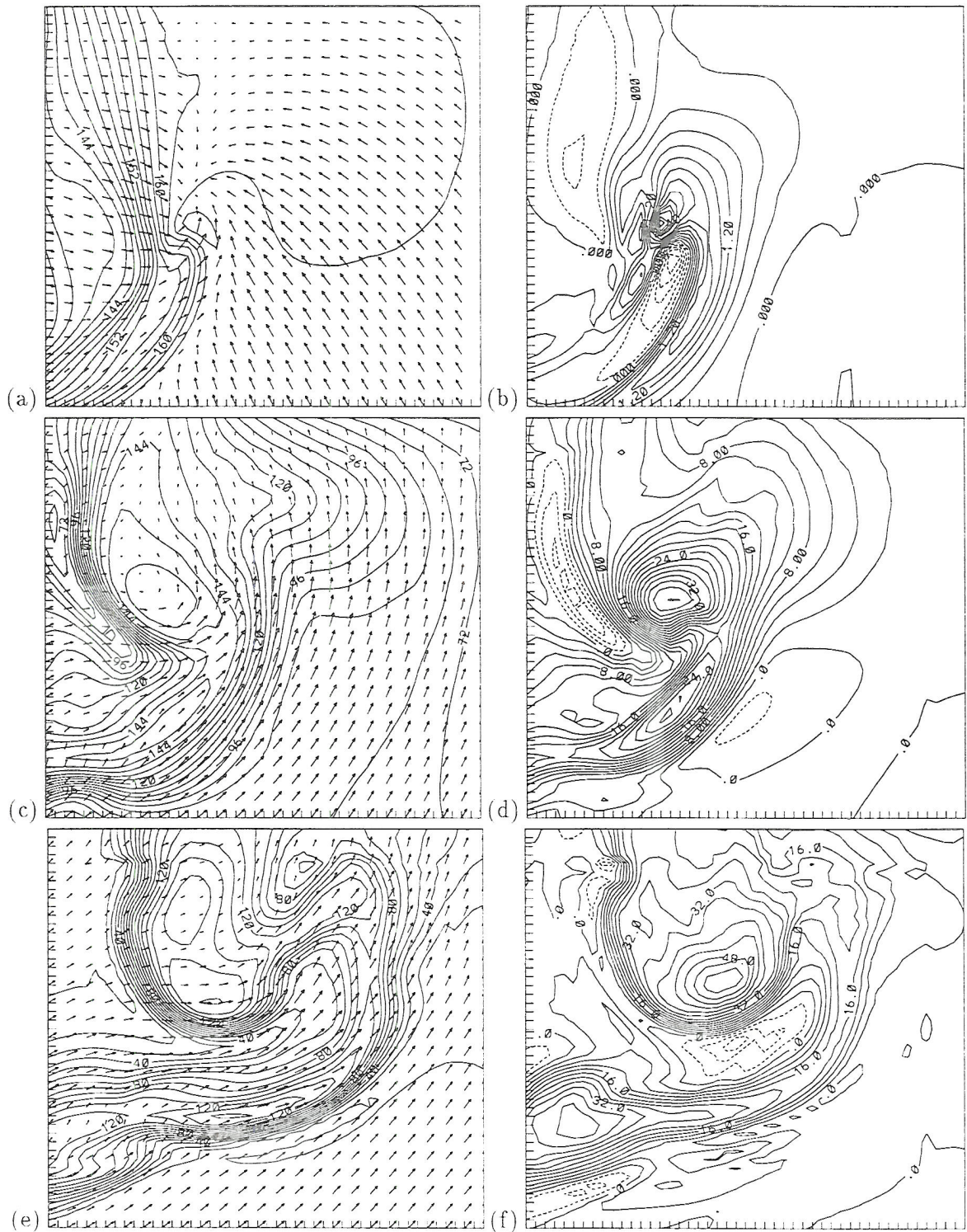


Figure 4.24: Grid #5 at 2155 UTC; (a), (c), and (e) Horizontal wind vectors and total water mixing ratio (a) at 49m (contoured every .2g/kg), (c) at 2291m (contoured every .6g/kg), and (e) at 5414m (contoured every 1.0g/kg). A contour labeled 120 represents a mixing ratio of 12.0 g/kg. (b), (d), and (f) Vertical motion (b) at 49m (contoured every .3m/s to a maximum of 3.9m/s), (d) at 2291m (contoured every 2.0m/s to a maximum of 38.0m/s), and (f) at 5414m (contoured every 4.0m/s to a maximum of 56.0m/s).

At 2291m, a closed cyclonic circulation was evident to the left of the center of Figure 4.25c. The wind speeds were strongest on the southeast side. Even though the winds were very weak on the northwest flank they were strong enough to make the closed circulation visible in the ground relative frame. The updraft contours had changed their shape from circular to that of a horseshoe in Figure 4.25d. A maximum updraft of 42.0 m/s was colocated with the circulation center in the wind field. A pronounced updraft minimum of 15.0 m/s was located just to the east and in the region of strong southerly winds associated with the vortex. A downdraft continued to flank the updraft to the west.

The winds and moisture mixing ratio at 2200 UTC and 5414m are shown in Figure 4.25e. The cyclonic curvature in the winds had increased in the region of the mixing ratio maximum compared with those at 2155 UTC. The wind speeds also increased in the same region. The updraft increased considerably to 70.0 m/s as seen in the center of Figure 4.25f. The region with large curvature of the winds was to the west of the updraft core. Of particular interest was the indentation in the updraft contours just to the southwest of the core, which is most noticeable for the 30.0 m/s updraft contour. One can see that the updraft expanded in area from the previous five minutes and the core appears to have detached from the updraft gradient to its west.

Five minutes later at 2205 UTC, the vortex at 49m was moving away from the dry line. Regions to the north and northwest of the vortex were dominated by air on the moist side of the dry line. The cyclonic circulation center was located at the tip of the moisture gradient bulge in Figure 4.26a. A dry slot to the southwest of the vortex was composed of westerly winds and contributed to the cyclonic circulation that is characteristic of most of the domain of Grid #5. The updraft still had the comma shape appearance with the maximum upward motion at its head (see Figure 4.26b). To the north and northwest of the vortex were downdraft regions.

At 2291m the closed circulation was more apparent than five minutes earlier. This circulation is located to the left of the center of Figure 4.26c. The strongest winds continued to be on the southeast side of the vortex. To the northeast of the circulation center the flow had backed compared to earlier times. An updraft maximum of 42.0 m/s existed just



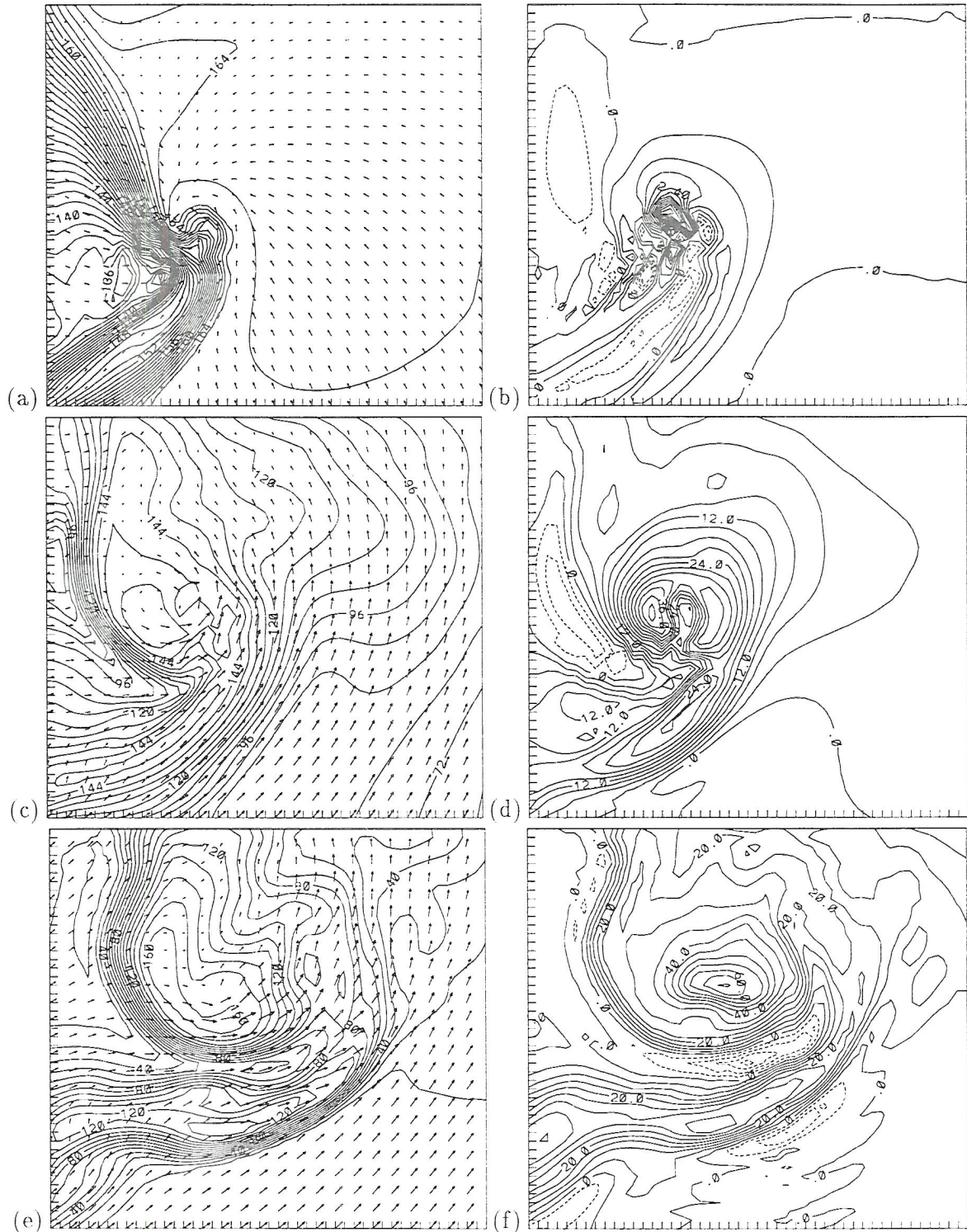
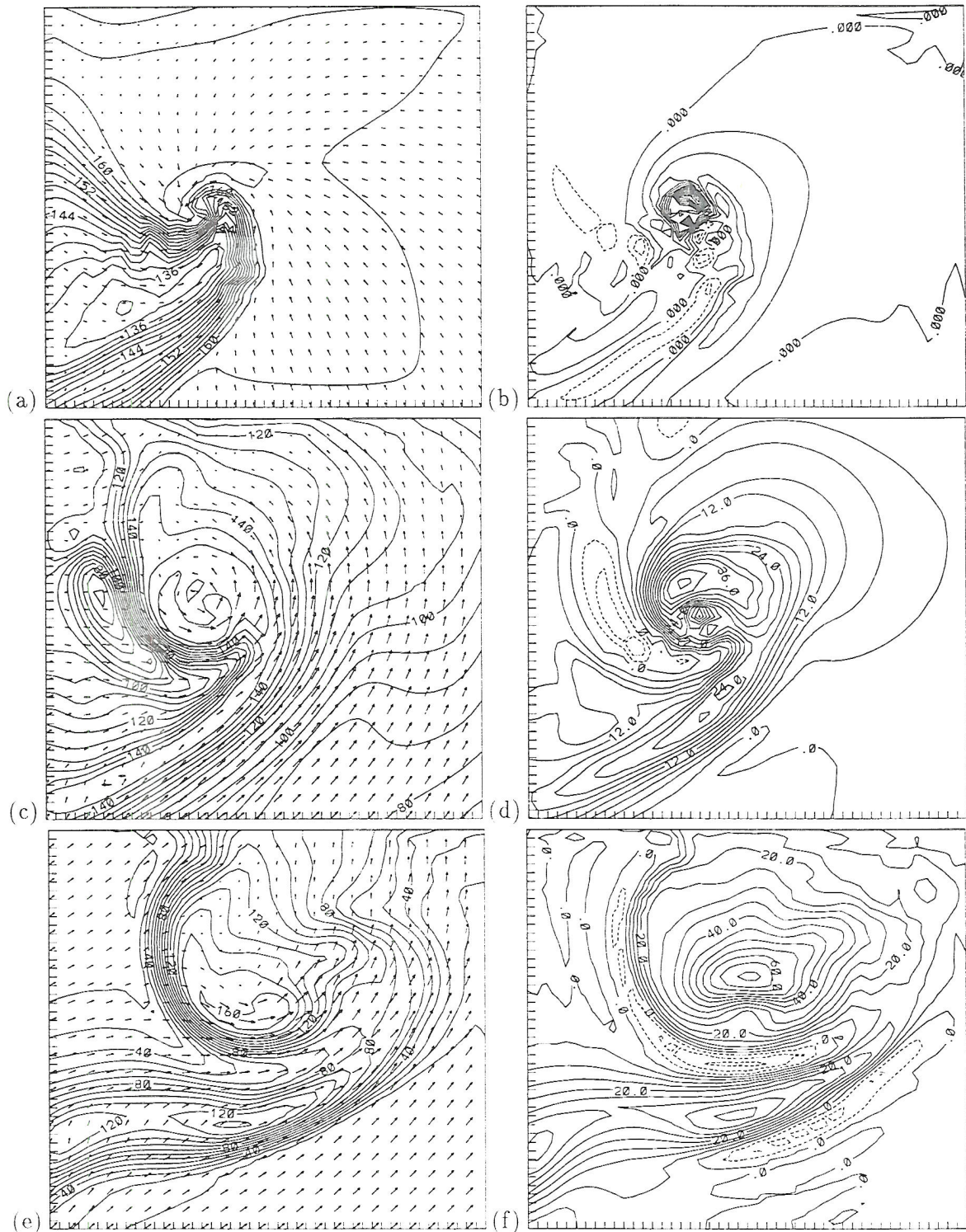


Figure 4.25: Grid #5 at 2200 UTC; (a), (c), and (e) Horizontal wind vectors and total water mixing ratio (a) at 49m (contoured every .1g/kg), (c) at 2291m (contoured every .6g/kg), and (e) at 5414m (contoured every 1.0g/kg). A contour labeled 120 represents a mixing ratio of 12.0 g/kg. (b), (d), and (f) Vertical motion (b) at 49m (contoured every .6m/s to a maximum of 8.4m/s), (d) at 2291m (contoured every 3.0m/s to a maximum of 42.0m/s), and (f) at 5414m (contoured every 5.0m/s to a maximum of 70.0m/s).





to the north of the circulation center as seen in Figure 4.26d. Just to the south of the maximum was a local minimum of 6.0 m/s. The downdraft on the west side of the storm was wrapping further around the southern flanks of the vortex. A second downdraft was becoming evident, near the top portion of the figure. Comparing with Figure 4.25d we see that the updraft speeds weakened in time between the two downdrafts.

The streamlines at 5414m exhibited longer cyclonically curved arcs in the region of the maximum water mixing ratio in Figure 4.26e. When compared to earlier times, winds along these streamlines were strongest on the southeast side. To the northwest of this region, just to the west of the mixing ratio contour labeled 120, the wind speed had weakened although they had not produced a closed circulation. The storm maintained the 70.0 m/s updraft maximum as seen in Figure 4.26f. More pronounced was the indentation of the updraft contours to the south of the maximum. This local minimum had vertical continuity and can be seen in Figure 4.26d. It is proposed that the downward directed perturbation pressure gradient force was larger in this region, in response to the organized circulation in the subcloud layer. This reduced the net upward acceleration on parcels as they moved through this region.

Ten minutes later, at 2215 UTC, the vortex had moved east of the dry line and was no longer coupled to it. The winds were divergent to the northwest of the circulation center at 49m (see Figure 4.27a). Along the left flanks of the vortex, air was moving in a southerly direction from the divergent zone. By looking at Figure 4.27b, one can see that this region was dominated by downdraft. As the vortex moved away from the dry line, Figure 4.26a and Figure 4.27a illustrate that the vortex existed in the interface between northerly downdraft air from the storm and southeasterly environmental air.

The closed circulation at 2291m was more organized and had a stronger northeasterly flow on the northwest side of the vortex than it did ten minutes earlier. The downdraft was stronger and continued to wrap around the southern portion of the updraft maximum of 42.0 m/s as seen in Figure 4.27d. The local updraft minimum of 3.0 m/s was located just to the southeast of the maximum.

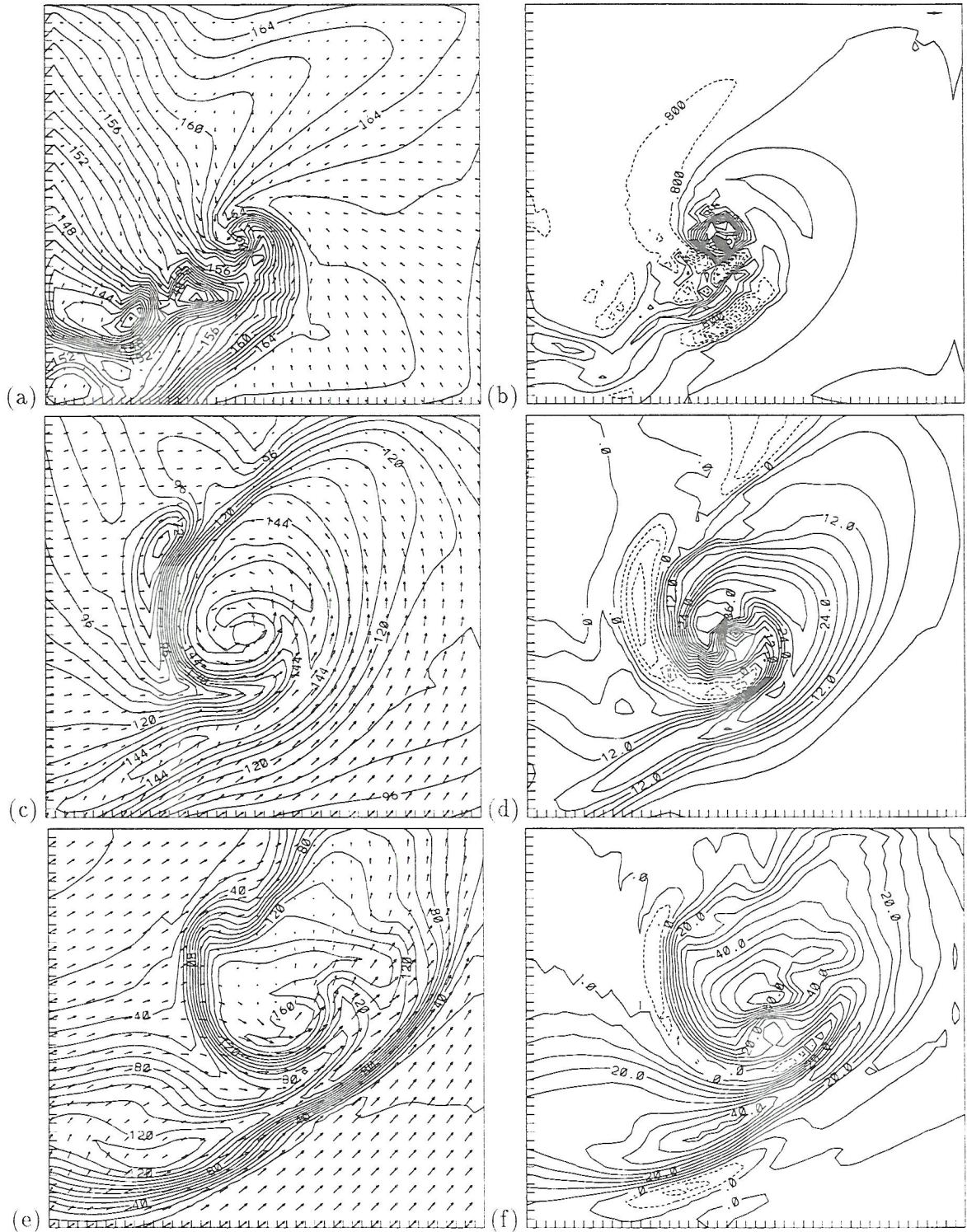


Figure 4.27: Grid #5 at 2215 UTC; (a), (c), and (e) Horizontal wind vectors and total water mixing ratio (a) at 49m (contoured every .1g/kg), (c) at 2291m (contoured every .6g/kg), and (e) at 5414m (contoured every 1.0g/kg). A contour labeled 120 represents a mixing ratio of 12.0 g/kg. (b), (d), and (f) Vertical motion (b) at 49m (contoured every .8m/s to a maximum of 8.8m/s), (d) at 2291m (contoured every 3.0m/s to a maximum of 42.0m/s), and (f) at 5414m (contoured every 5.0m/s to a maximum of 65.0m/s).



At 5414m the winds formed a closed circulation, although it is not obvious. Weak northeasterly and northerly flow existed just to the south of the mixing ratio contour labeled 120 and into the maximum mixing ratio region in Figure 4.27e. An updraft maximum of 65.0 m/s and the local minimum just to the south can be seen in Figure 4.27f. Note the local minimum in the updraft field had moved closer to the maximum when compared to earlier times.

These past figures have demonstrated that the vortex developed at lower levels and was transported vertically by the intense updraft into the mesocyclone. Since the vortex leans to the northeast, a vertical cross section similar to Figure 3.31 could not be produced for this case.

#### 4.7 Tornado Characteristics

The final grid was spawned at 2200 UTC, had a grid spacing of 111.0m, and was 6.0 km in length in both horizontal directions. Selected fields of the mature stage of the tornado will be presented in this section.

Winds and total water mixing ratio at 49m and 2208 UTC are seen in Figure 4.28a. The tornado is clearly illustrated in the center of the figure. Flow from the west and northwest of the vortex accelerated rapidly from the downdraft toward the vortex. Keep in mind that the mixing ratio labels have been multiplied by 10. For example, a contour labeled 160 represents a total water mixing ratio of 16.0 g/kg.

The wind speeds corresponding to Figure 4.28a are shown in Figure 4.28b. Two bands of local wind maxima that arched cyclonically inward existed to the northwest and southeast of the tornado. Strongest winds were on the southeast side with a maximum of 100.0 m/s. With a closed contour of 65.0 m/s, bounding the tornado, a  $\Delta v$  of 165.0 m/s existed across the vortex.

A shade plot of the Fujita F scale is seen in Figure 4.28c. The lightest gray shade represents winds having F0 strength. Along the south side of the tornado winds achieved a strength of F4 placing this vortex in the violent category.

Vertical motion at 49m assumed the shape of an annulus of upward motion, with a maximum of 18.0 m/s on the northwest side, surrounding a central downdraft of -6.0 m/s (see Figure 4.28d). A much larger region of downdraft, occupying much of the western portion of the figure, flanked the tornado on the left side. Note the tornado was in the boundary between environmental southerly flow, to the east, and downdraft northerly flow, to the west.

The central pressure of the tornado at 49m was 95.0 mb lower than its' environment, as seen in Figure 4.28e. One difference between this Figure and Figure 3.32e was the apparent lack of low pressure regions to the north and south of the vortex where the wind speeds were locally strong. This is a consequence of the 5.0 mb contouring interval in this figure as opposed to only 1.0 mb in Figure 3.32e.

As in the Laverne tornado the vertical vorticity was concentrated along an annulus ring at 49m bounding the central downdraft (see Figure 4.28f). The contours in the center denote a region of a local minimum in the vertical vorticity field. The maximum vertical vorticity was  $0.57s^{-1}$ . In both cases the ring of vertical vorticity formed as a result of the horizontally divergent downdraft in the tornado core and the horizontal convergence of air, outside the vortex. Perhaps a seventh nest in this region would resolve the breakdown of the vorticity annulus ring into suction vortices.

At 2291m the vortex dominated a large portion of Grid #6 (see Figure 4.29a). The strongest winds were on the southeast side while much weaker winds existed on the northwest flank. A large region of low values of water vapor mixing ratio bounded the vortex, along a curved band, to the west, south, and southeast.

The u and v-components of the wind are displayed in Figure 4.29b and Figure 4.29c, respectively. At this height the average change in speed across the vortex was 116.0 m/s and the diameter of maximum winds was 1.5 km.

A small, but significant downdraft of 8.0 m/s was bounded by a horseshoe shaped updraft maximum of 60.0 m/s, at 2291m (this can be seen in Figure 4.29d). The entire updraft field had the shape of a comma with the largest upward motion at its head. A large curved downdraft was in the same location as the minimum in water vapor mixing ratio in



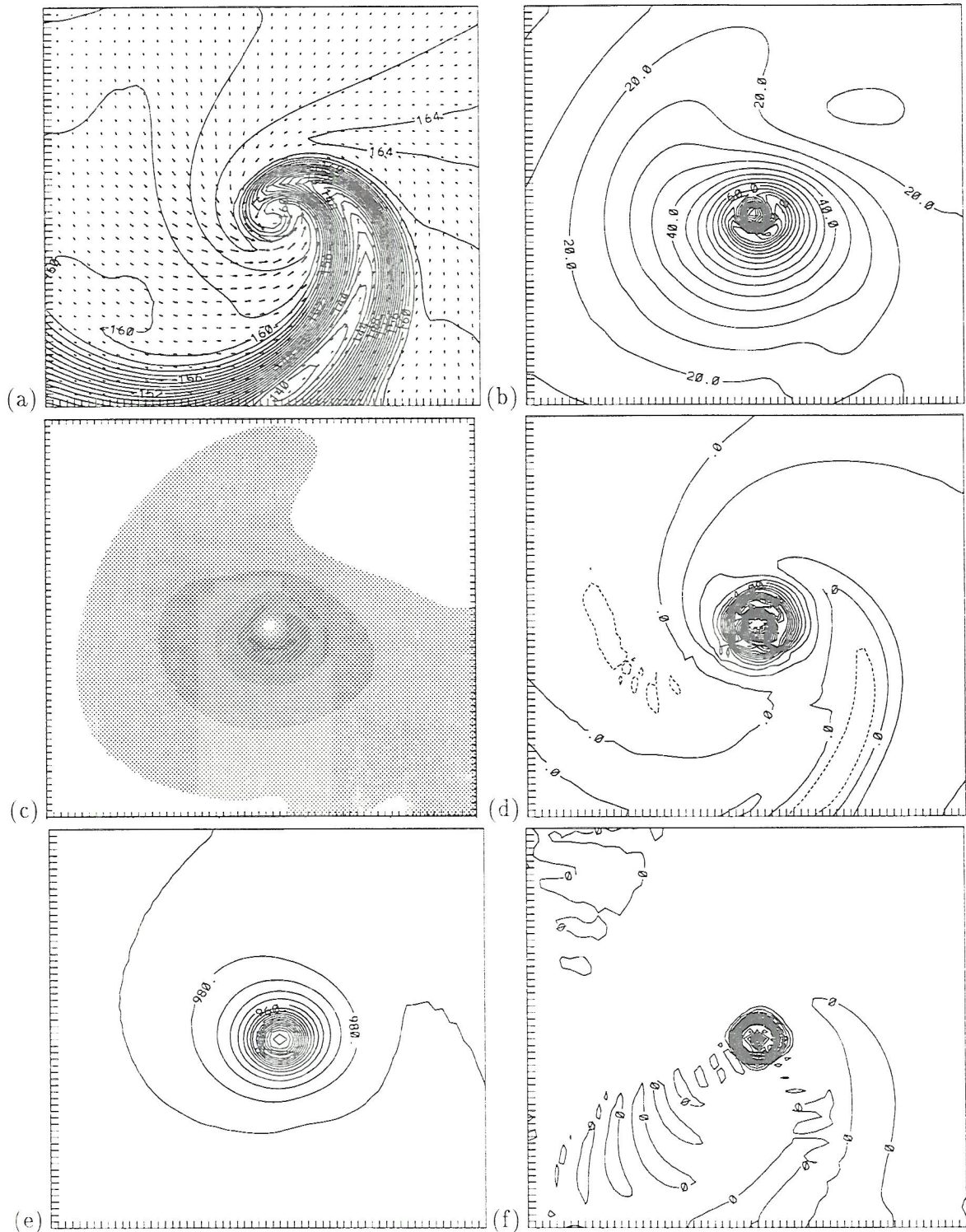


Figure 4.28: Grid #6 at 2208 UTC and 49m; (a) Horizontal wind vectors and total water mixing ratio (contoured every .1g/kg) (b) Wind speed contoured every 5.0m/s to a maximum of 100.0m/s (c) F scale, darkest shading represents a strength of F4 (d) Vertical motion contoured every 1.0m/s to a maximum of 18.0m/s (e) Pressure field contoured every 5.0mb to a minimum of 890mb, the core was 95.0 mb lower than at the grid boundary (f) Vertical vorticity contoured every  $3 \times 10^{-2} s^{-1}$  to a maximum of  $0.57 s^{-1}$ .

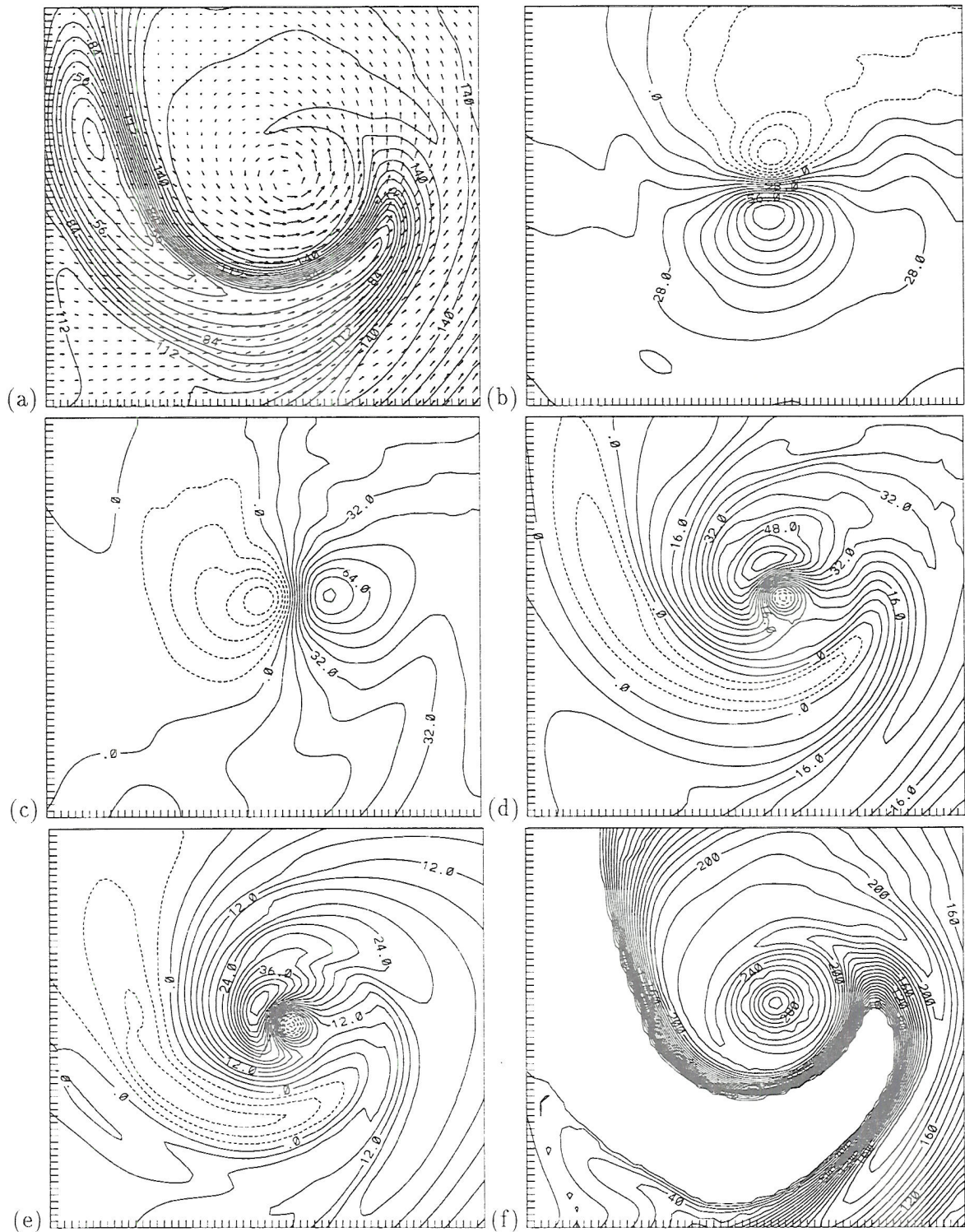


Figure 4.29: Grid #6 at 2208 UTC; (a) Horizontal winds and total water mixing ratio (contoured every  $.7\text{g/kg}$ ) at 2291m (b) u-component of the wind, contoured every  $7\text{m/s}$  at 2291m (c) v-component of the wind contoured every  $8\text{m/s}$  at 2291m (d) Vertical motion (contoured every  $4.0\text{m/s}$  to a maximum of  $60.0\text{m/s}$ ) at 2291m (e) Vertical motion (contoured every  $3.0\text{m/s}$  to a maximum of  $48.0\text{m/s}$ ) at 1248m. This shows vertical continuity of the small downdraft (f) Cloud water (contoured every  $.1\text{g/kg}$  to a maximum of  $3.1\text{g/kg}$ ) at 2291m showing dry slot.



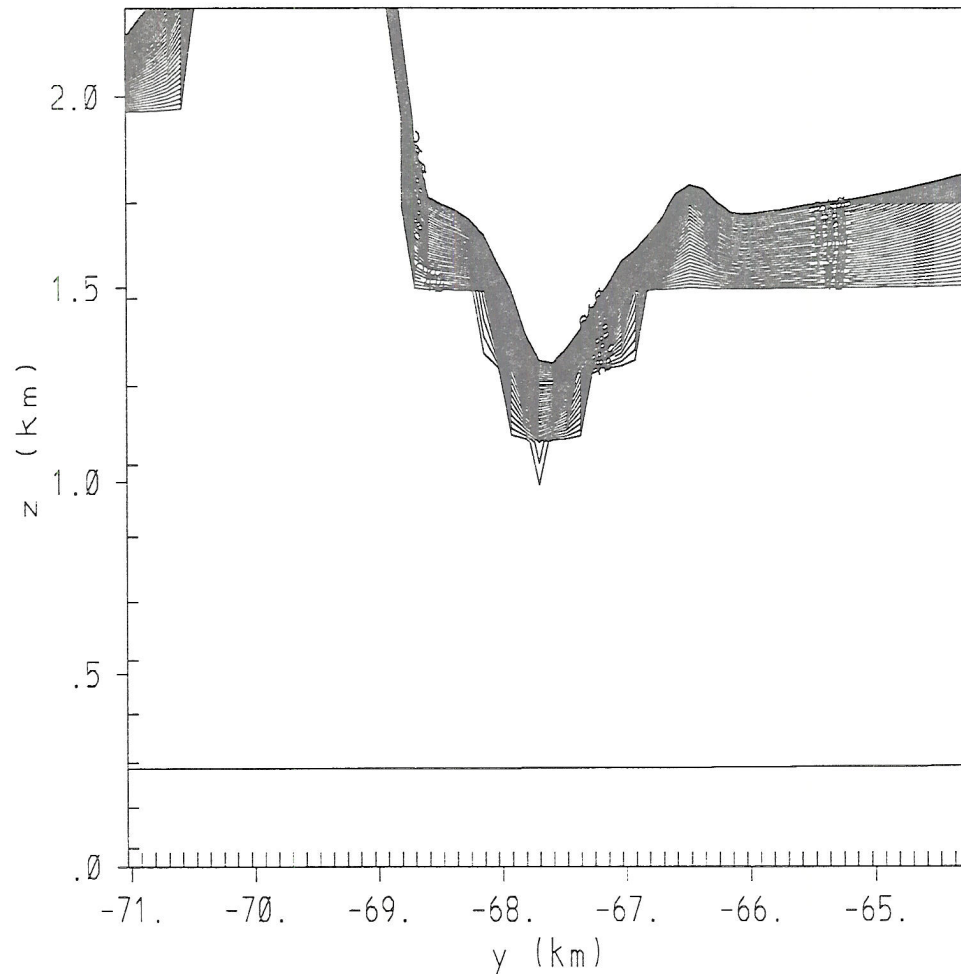


Figure 4.30: Looking west at a north south vertical cross section in Grid #6 of cloud water mixing ratio at 2208 UTC. The distinct lowering was condensate in the tornado. Due to the rapid increase of cloud water, above the funnel, and the small contour interval of .01 g/kg, no contours were plotted in the top right portion of the figure.

Figure 4.29a. This downdraft transported drier air from above the boundary layer, to the surface, and is called the rear flank downdraft. The same field is presented at 1248m in Figure 4.29e to demonstrate the vertical continuity of the small downdraft on the southeast side of the updraft maximum. At this height the downdraft had a speed of -12.0 m/s.

A well-defined clear slot associated with the rear flank downdraft can be seen in the cloud field at 2291m in Figure 4.29f. This particular tornado simulation did produce a condensation funnel well below cloud base but not to the surface (see Figure 4.30). The line at the bottom of the figure represents the ground level.

## Chapter 5

### CIRCULATION AND VORTICITY ANALYSIS

#### 5.1 Circulation Analysis

Concepts of circulation, used as a global descriptor for the tornado, are described in section 1 of this chapter. The first material curve will lie in the horizontal plane and remain near the ground while the second will lie in the vertical plane.

Consider a non-intersecting closed curve in the atmosphere. At any point on the curve two unique vectors exist; a velocity vector and a tangent vector. Circulation is computed by integrating the inner product of these two vectors around the curve,

$$C = \oint \vec{v} \bullet d\vec{r}. \quad (5.1)$$

Since we are interested in the value of circulation around the material curve, the Lagrangian derivative is applied to Eq. 5.1 followed by Stokes Theorem yielding,

$$\frac{DC}{Dt} = \oint \frac{D\vec{v}}{Dt} \bullet d\vec{r} = \iint \vec{\nabla} \times \frac{D\vec{v}}{Dt} \bullet \vec{n} \, ds. \quad (5.2)$$

The double integral is taken on the open, two sided surface bounded by the material curve.

A unit normal to the surface is denoted by  $\vec{n}$ . Taking the acceleration vector,

$$\frac{D\vec{v}}{Dt} = -\theta_{0v} \vec{\nabla} \pi + \left( \frac{\theta'_v}{\theta_{0v}} - r_w \right) g \hat{k} - 2\vec{\Omega} \times \vec{v} + \vec{D}, \quad (5.3)$$

from RAMS and applying the curl operator yields,

$$\vec{\nabla} \times \frac{D\vec{v}}{Dt} = -\vec{\nabla} \theta_{0v} \times \vec{\nabla} \pi + \vec{\nabla} \times (B \hat{k}) + \vec{\nabla} \times (\vec{v} \times 2\vec{\Omega}) + \vec{\nabla} \times \vec{D}, \quad (5.4)$$

where

$$B = \left( \frac{\theta'_v}{\theta_{0v}} - r_w \right) g. \quad (5.5)$$



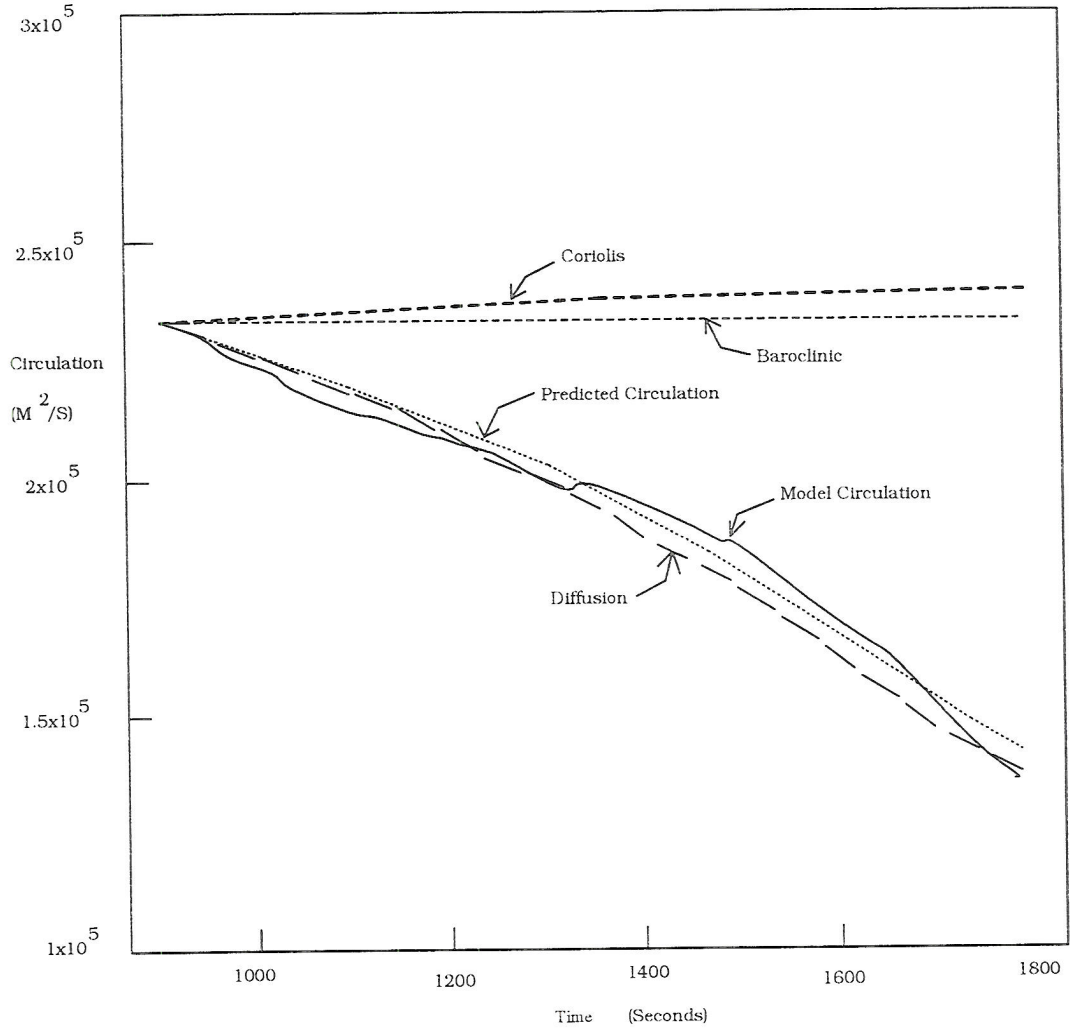


Figure 5.1: Lagrangian circulation tendencies and diagnosed circulation along a material curve that remains horizontal near the surface and converges to a vortex from 900s to 1800s.

In Eq. 5.3 the variables are the reference state virtual potential temperature  $\theta_{0v}$ , perturbation Exner function  $\pi$ , perturbation virtual potential temperature  $\theta'_v$ , total water  $r_w$ , and the diffusion vector  $\vec{D}$ . The variable  $B$  in Eq. 5.5 represents the buoyant acceleration. The last three terms on the right side of Eq. 5.4 are shown in expanded form in Eq. 5.7, Eq. 5.6, and Eq. 5.8,

$$\vec{\nabla} \times \vec{D} = \left( \frac{\partial D_k}{\partial y} - \frac{\partial D_j}{\partial z} \right) \hat{i} + \left( \frac{\partial D_i}{\partial z} - \frac{\partial D_k}{\partial x} \right) \hat{j} + \left( \frac{\partial D_j}{\partial x} - \frac{\partial D_i}{\partial y} \right) \hat{k}. \quad (5.6)$$

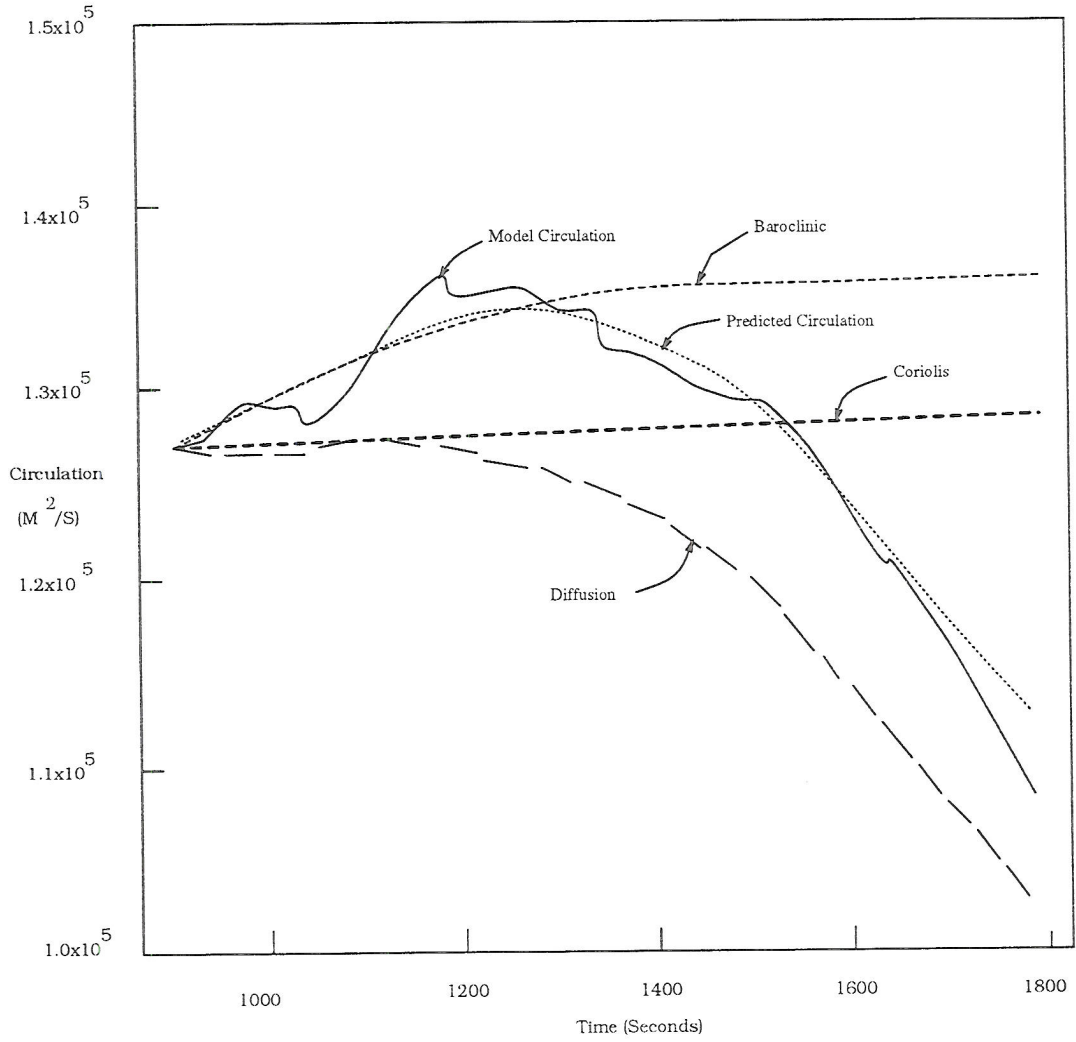


Figure 5.2: Lagrangian circulation tendencies and diagnosed circulation along a material curve that begins in the vertical plane and moves into a horizontal plane at 2206m from 900s to 1800s.

$$\vec{\nabla} \times B \hat{k} = -\frac{\partial B}{\partial x} \hat{j} + \frac{\partial B}{\partial y} \hat{i}. \quad (5.7)$$

$$\vec{\nabla} \times (\vec{v} \times 2\vec{\Omega}) = (2\vec{\Omega} \bullet \vec{\nabla})\vec{v} - 2\vec{\Omega}(\vec{\nabla} \bullet \vec{v}) - (\vec{v} \bullet \vec{\nabla})2\vec{\Omega}. \quad (5.8)$$



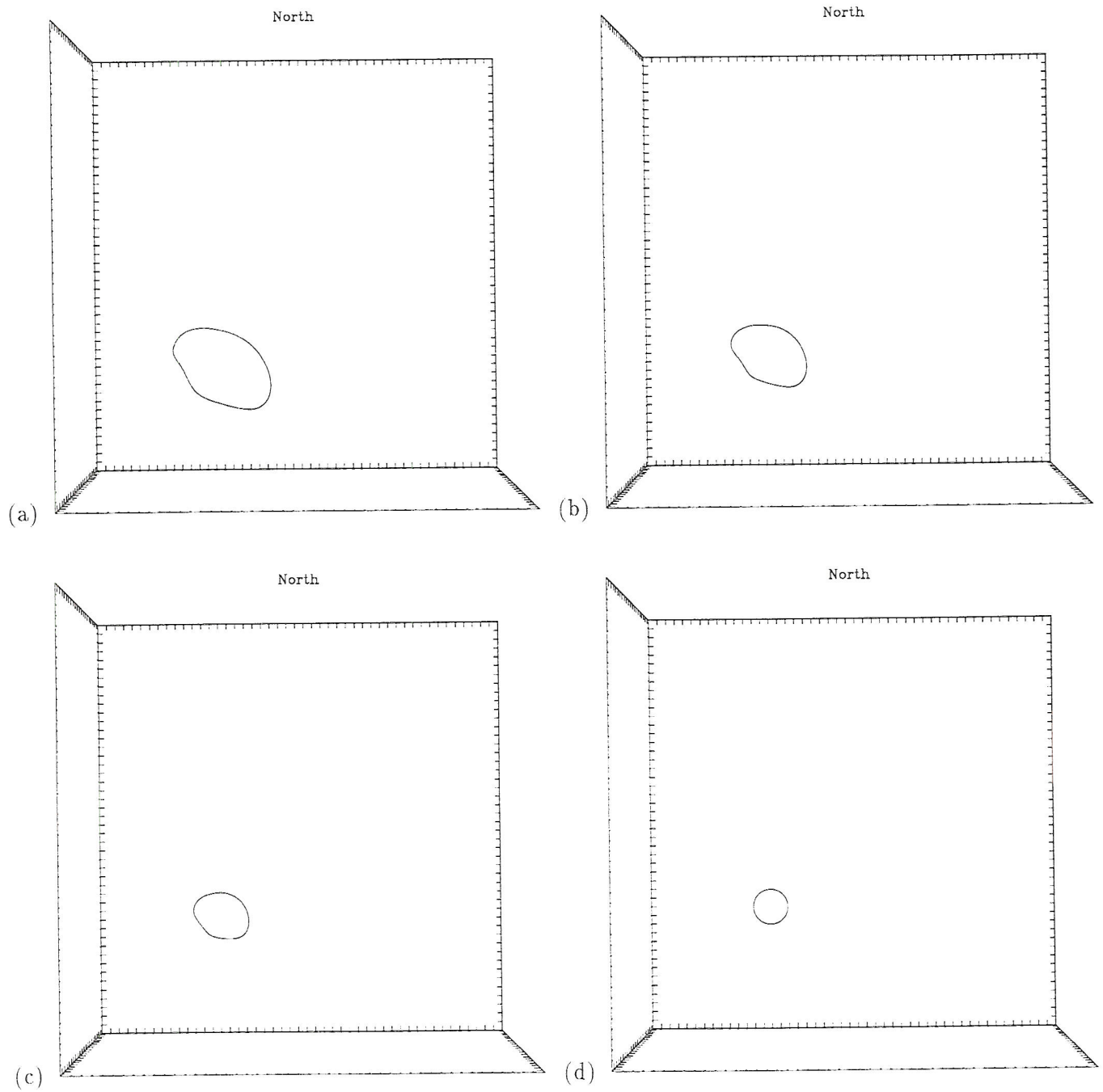


Figure 5.3: Material curve, viewed from above, in Grid #4 at 32409s, 32544s, 32652s, and 32760s.

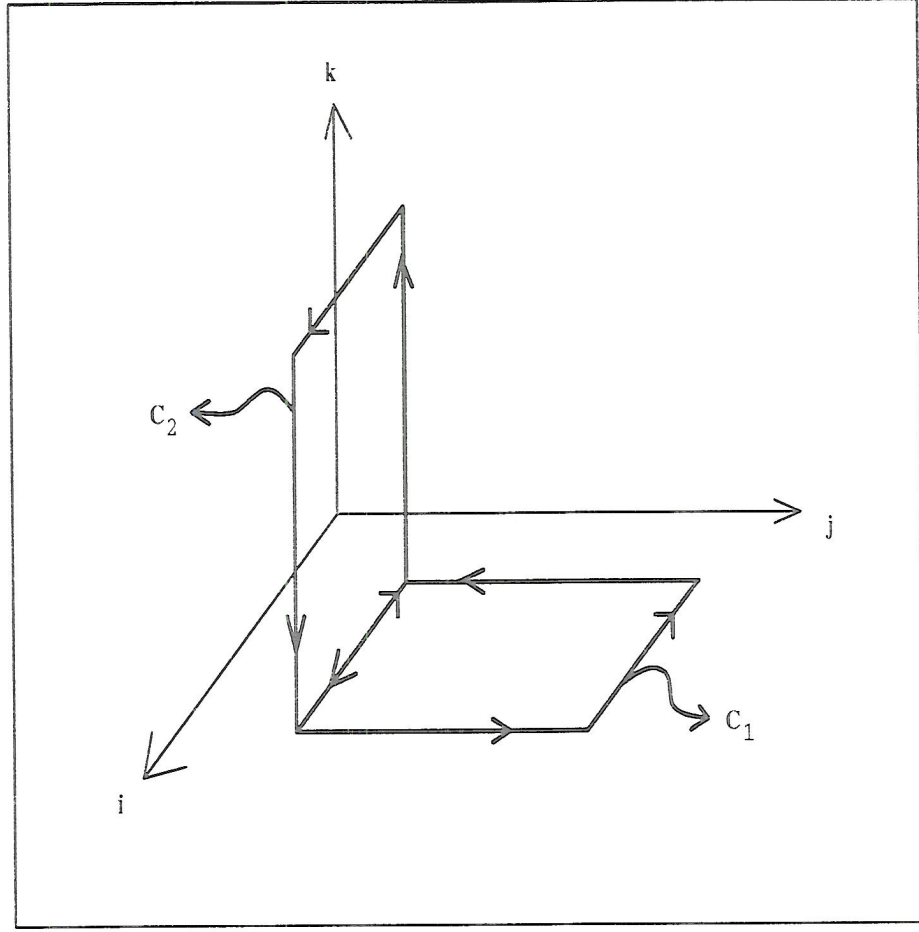


Figure 5.4: Hypothetical material curve

The expanded form of Eq. 5.4 is substituted into Eq. 5.2 to yield,

$$\begin{aligned}
 \frac{DC}{Dt} = & - \iint \vec{\nabla} \theta_{0v} \times \vec{\nabla} \pi \cdot \vec{n} \, ds + \iint \left( -\frac{\partial B}{\partial x} \hat{j} + \frac{\partial B}{\partial y} \hat{i} \right) \cdot \vec{n} \, ds \\
 & + \iint \left( \left( \frac{\partial D_k}{\partial y} - \frac{\partial D_j}{\partial z} \right) \hat{i} + \left( \frac{\partial D_i}{\partial z} - \frac{\partial D_k}{\partial x} \right) \hat{j} + \left( \frac{\partial D_j}{\partial x} - \frac{\partial D_i}{\partial y} \right) \hat{k} \right) \cdot \vec{n} \, ds \\
 & + \iint \left( (2\vec{\Omega} \cdot \vec{\nabla}) \vec{v} - 2\vec{\Omega}(\vec{\nabla} \cdot \vec{v}) - (\vec{v} \cdot \vec{\nabla}) 2\vec{\Omega} \right) \cdot \vec{n} \, ds. \quad (5.9)
 \end{aligned}$$

This equation will be applied to the two material curves shown in Figure 5.4. Curve  $C_1$  lies in the  $\hat{i}$  and  $\hat{j}$  plane and is near the ground. The second curve,  $C_2$ , is in the  $\hat{i}$  and  $\hat{k}$  plane. Note the two curves share a common segment. The arrows on the curves denote the direction of integration for computations of circulation.

For  $C_1$ , the outward normal is vertically upward, so  $\vec{n} = \hat{k}$ . This is substituted into Eq. 5.9. It will be assumed that there are no horizontal gradients in topography. The



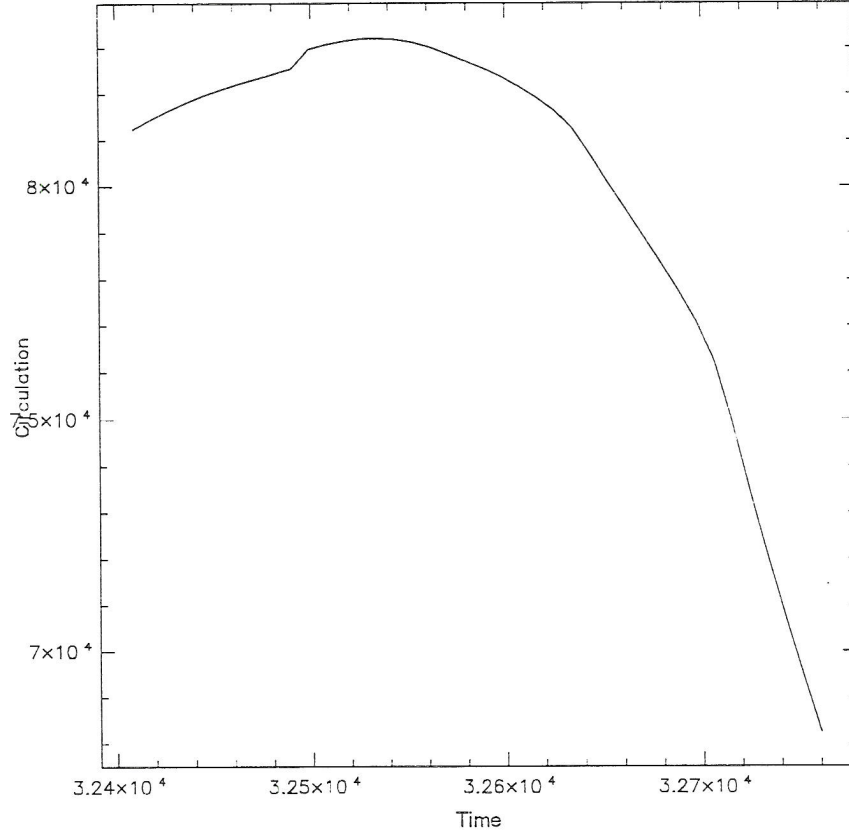


Figure 5.5: Circulation, in  $m^2/s$ , along the material curve in Grid #4 from 32409s to 32760s.

gradient in  $\theta_{0v}$  will then be in the vertical. As a result the first term on the right side of Eq. 5.9 is zero. The second term also vanishes due to the orthogonality of the unit vectors.

The rest of the equation simplifies to

$$\frac{DC_1}{Dt} = \iint \left( \frac{\partial D_j}{\partial x} - \frac{\partial D_i}{\partial y} \right) dx dy + \iint \left( f \frac{\partial w}{\partial z} - f \vec{\nabla} \bullet \vec{v} - \vec{v} \bullet \vec{\nabla} f \right) dx dy. \quad (5.10)$$

Further simplification can be made by assuming that the advection of planetary vorticity has negligible influence on the circulation of a horizontal material curve, converging towards a tornado. The remaining two terms in the second integral on the right side of Eq. 5.10 are combined. The result is

$$\frac{DC_1}{Dt} = \iint \left( \frac{\partial D_j}{\partial x} - \frac{\partial D_i}{\partial y} \right) dx dy + \iint -f \left( \frac{\partial u}{\partial x} + \frac{\partial v}{\partial y} \right) dx dy. \quad (5.11)$$

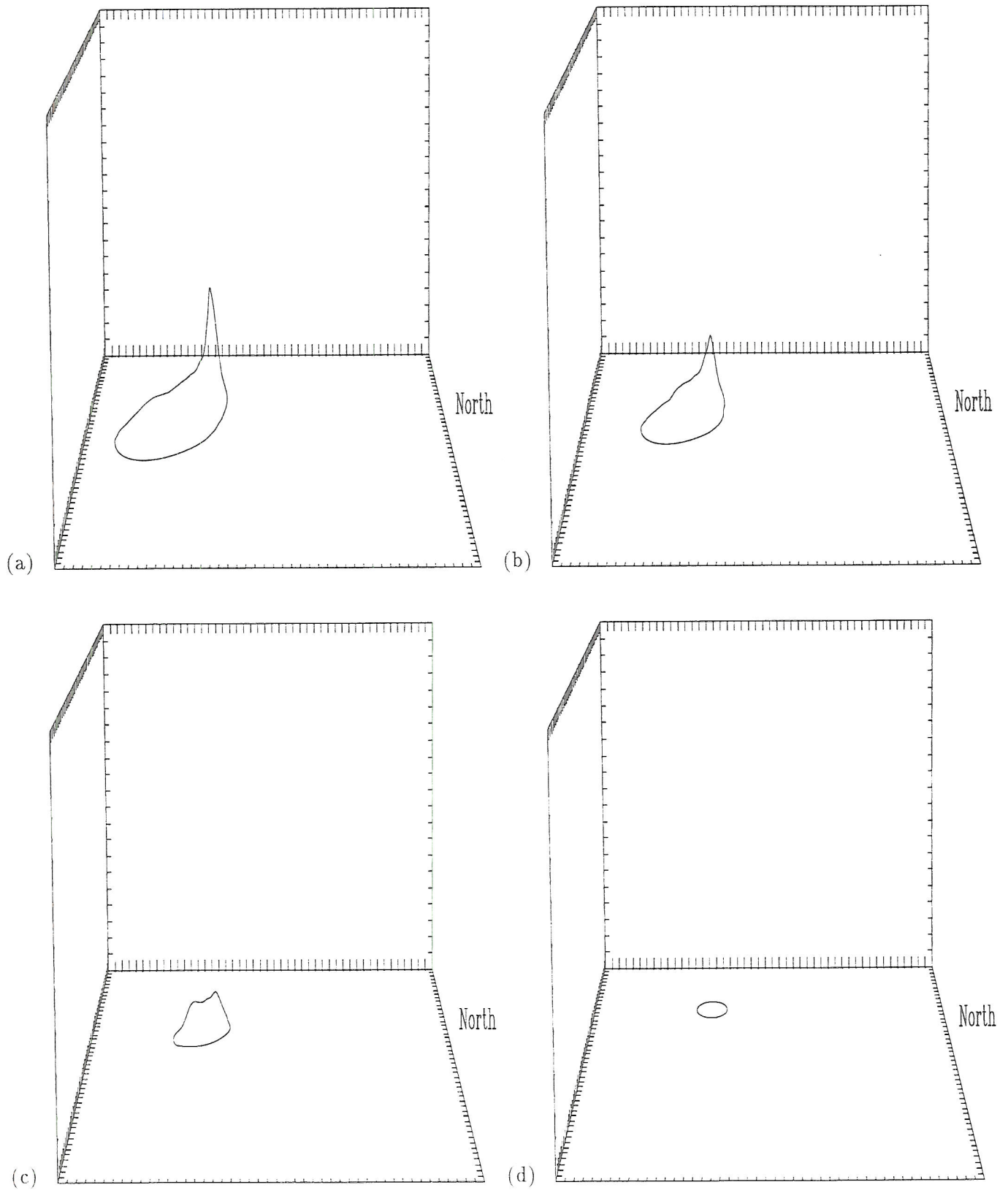


Figure 5.6: Material curve, viewed from East, in Grid #4 at 32409s, 32688s, 32904s, and 33120s. The vertical axis represents a distance of 1.0 km.

This is the Lagrangian tendency for the horizontal material curve  $C_1$ . The first term on the right hand side of Eq. 5.11 is the frictional torque applied to the curve by the ground. This frictional torque acts to slow down the rotation of the air around the material curve and thus acts to reduce the magnitude of the circulation. The second term represents the convergence of planetary vorticity. If the material curve converges, this term will be positive.

Let us consider the evolution of  $C_1$ , in the  $\hat{i}$  and  $\hat{j}$  plane near the ground, for all times  $t \in (t_1, t_2)$ . At time  $t_1$ , the curve bounds a very large area, perhaps many tornado diameters in size, and no tornado exists. At time  $t_2$  the material curve will bound a small area slightly larger than an existing cyclonic tornado. As the curve begins to shrink the convergence of planetary vorticity and frictional torque may be of the same magnitude. The resulting circulation values will remain somewhat constant. As the curve continues to converge the wind speeds will increase. The frictional torque will become more negative and dominate the  $C_1$  tendency. The values of circulation, although somewhat constant to begin with, will decrease significantly in time as the curve shrinks to the tornado.

A straight forward calculation demonstrates that the convergence of planetary vorticity cannot account for tornado development. It would take 27 hours for horizontal convergence, having a value of  $-1 \times 10^{-2} s^{-1}$ , to produce vertical vorticity equal to  $.1 s^{-1}$ . This assumes a coriolis parameter of  $1 \times 10^{-4} s^{-1}$  and no initial vertical vorticity. One can, for all practical purposes, neglect the second integral on the right side of Eq. 5.11. For completeness, it would take 2.7 hours to produce a final vertical vorticity of  $1 \times 10^{-2} s^{-1}$  under the same conditions as above. This value of vertical vorticity is comparable to that found in mesocyclones. Mesocyclones form in 1 hour to 1.5 hours. It seems, therefore, that the coriolis effect has little impact on a severe tornadic supercell thunderstorm.

Since the ground acts to reduce wind speeds, the frictional torque by the ground cannot increase the magnitude of circulation on a material curve converging to a tornado. If the magnitude of circulation does increase significantly, then the curve  $C_1$  did not remain horizontal during the time interval  $(t_1, t_2)$ .



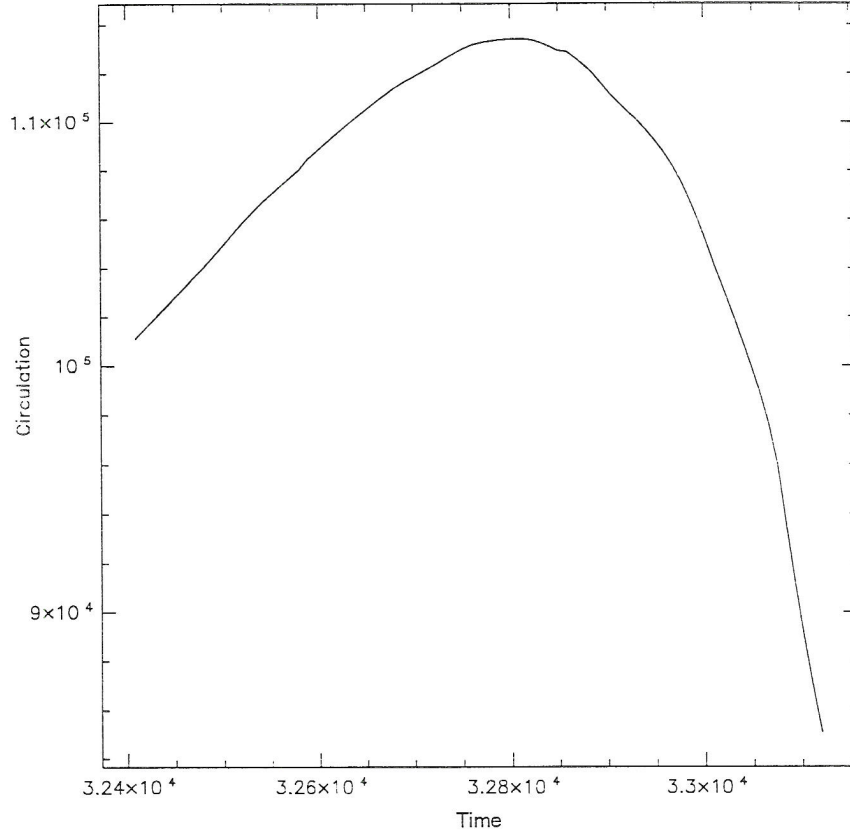


Figure 5.7: Circulation, in  $m^2/s$ , along the material curve in Grid #4 from 32409s to 33120s.

For the curve  $C_2$ , the outward normal is directed to the north, so  $\vec{n} = \hat{j}$ . Substituting this into Eq. 5.9 results in

$$\begin{aligned} \frac{DC_2}{Dt} = & \iint -\frac{\partial\theta_{0v}}{\partial z} \frac{\partial\pi}{\partial x} dx dz + \iint -\frac{\partial B}{\partial x} dx dz + \iint \left( \frac{\partial D_i}{\partial z} - \frac{\partial D_k}{\partial x} \right) dx dz \\ & + \iint f \frac{\partial v}{\partial z} dx dz. \end{aligned} \quad (5.12)$$

Again, the coriolis term will be neglected. The first term on the right hand side of Eq. 5.12 contains information about the vertical gradient of the reference state virtual potential temperature. Since this reference state is arbitrary, one can choose it to be adiabatic in the boundary layer. For this analysis it is assumed the material curve  $C_2$  exists

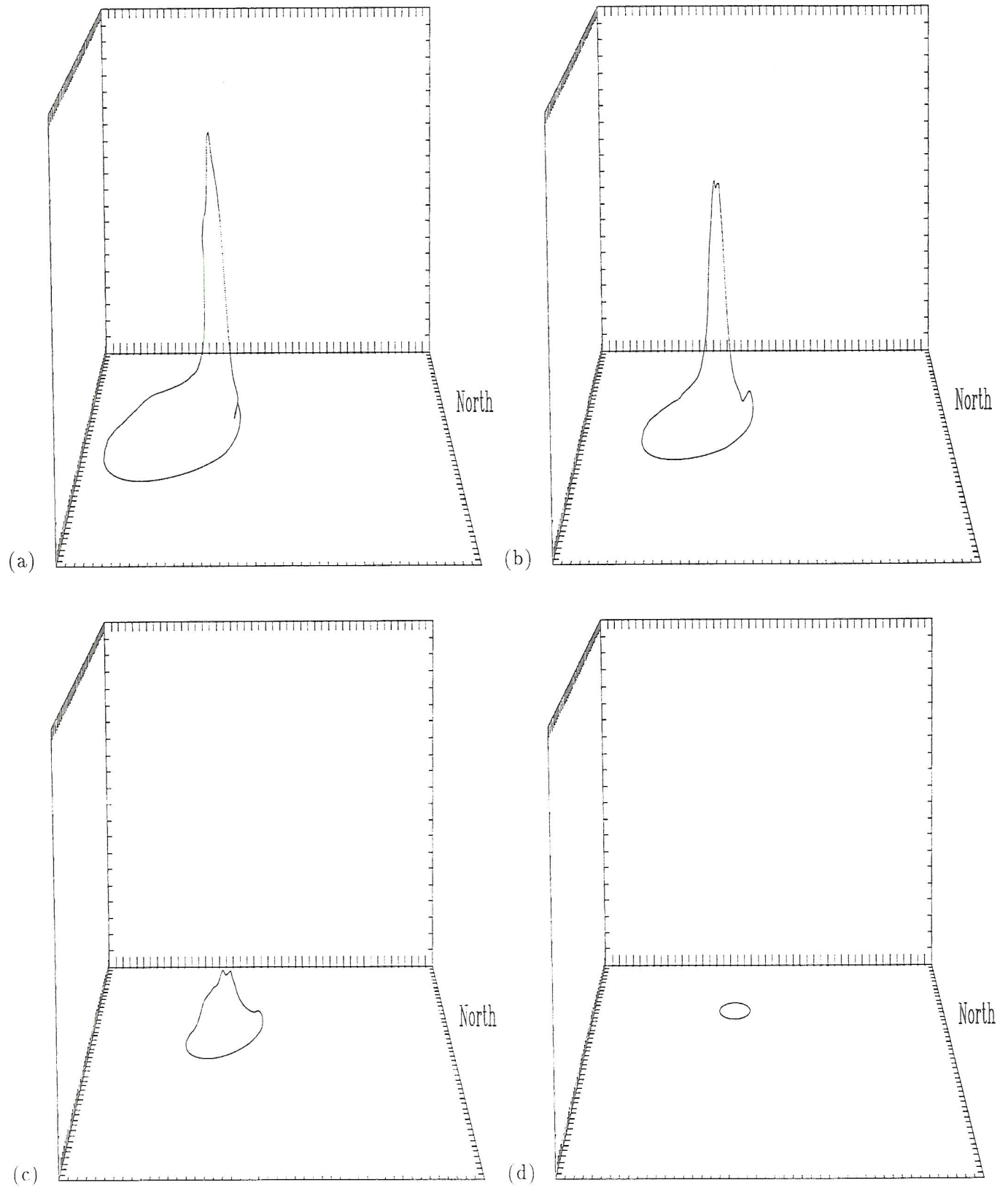


Figure 5.8: Material curve, viewed from the East, in Grid #4 at 32409s 32832s. 33156s, and 33480s. The vertical axis represents a distance of 1.0 km.

only in the boundary layer. As a result Eq. 5.12 simplifies to

$$\frac{DC_2}{Dt} = \iint \left( \frac{\partial D_i}{\partial z} - \frac{\partial D_k}{\partial x} \right) dx dz + \iint -\frac{\partial B}{\partial x} dx dz. \quad (5.13)$$

The first term represents frictional torque acting on the material curve and this can be positive. Suppose the winds are towards the east, and of the same speed initially, on both horizontal segments of  $C_2$ . The ground will act to reduce the wind speed on the segment near the ground and thus increase the circulation.

The second integral is the buoyancy term; the magnitude of which can be very large. In a frictionless, non-rotating frame, this is the only way to change circulation. As a consequence, the material curve must have had a vertical segment at some time during its' evolution if changes in circulation have occurred.

Combining both material curves,  $C_1 + C_2 = C_3$ , the circulation equation will be the sum of Eq. 5.11 and Eq. 5.13. A cancellation of circulation tendencies will occur along the common segment due to the opposing direction of integration. This means that surface friction along this common segment will make no contribution to circulation on  $C_3$ . Therefore, buoyancy will be the only tendency to increase the positive circulation on  $C_3$ .

Based on the above theoretical development, the following is a possible senario for the evolution of circulation on a material curve. Initially orientated somewhat like  $C_3$ , the curve will eventually shrink and bound a cyclonically rotating tornado. At time  $t_0$  the vertical segments of the material curve are in downdraft air on the left and/or rear flanks of the thunderstorm. The vertical legs extend from the ground to 1.0 km. Dimensions of the side of the horizontal part of the curve will be many tornado diameters in length. It will be assumed that at this time the initial value of circulation is too small to account for a tornado.

As time advances, the vertical part of the curve will descend while the horizontal part converges. Buoyancy forces that are along the vertical legs may be positive, large, and dominate the negative circulation tendency due to surface friction on the horizontal part of the curve. The net circulation tendency will be positive, causing the values of circulation to increase in time. This process can continue until some time,  $t_1$ . At this time the vertical



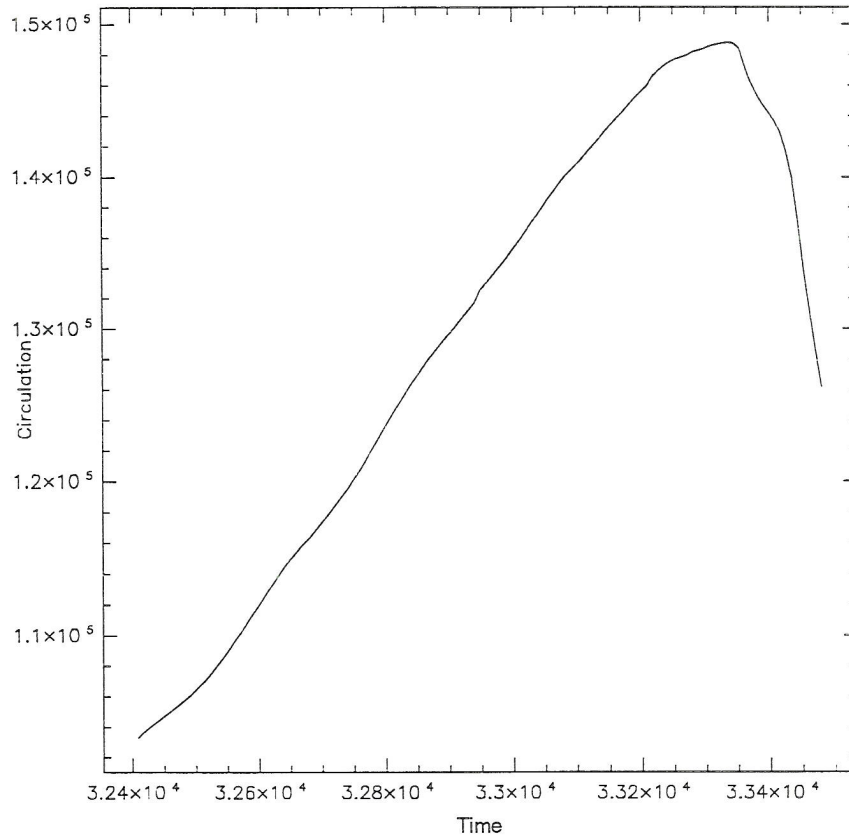


Figure 5.9: Circulation, in  $m^2/s$ , along the material curve in Grid #4 from 32409s to 33480s.

part of the curve has descended enough and the wind speeds have increased enough on the horizontal part so that now, the negative frictional torque dominates the circulation tendency. In the interval of time from  $t_1$  to the final state where the curve just bounds the tornado, values of circulation decrease. However, the final decrease in circulation did not remove all increases that were due to the buoyancy tendency.

It is possible that the increase of circulation, as the material curve descends in the downdraft, can be completely removed by the surface frictional torque. This reduction occurs when the material curve becomes horizontal and converges towards the tornado. If the final value of circulation is too small, a tornado will not form. If, therefore, the initial or environmental circulation is low, then there is more of a demand on the thunderstorm to

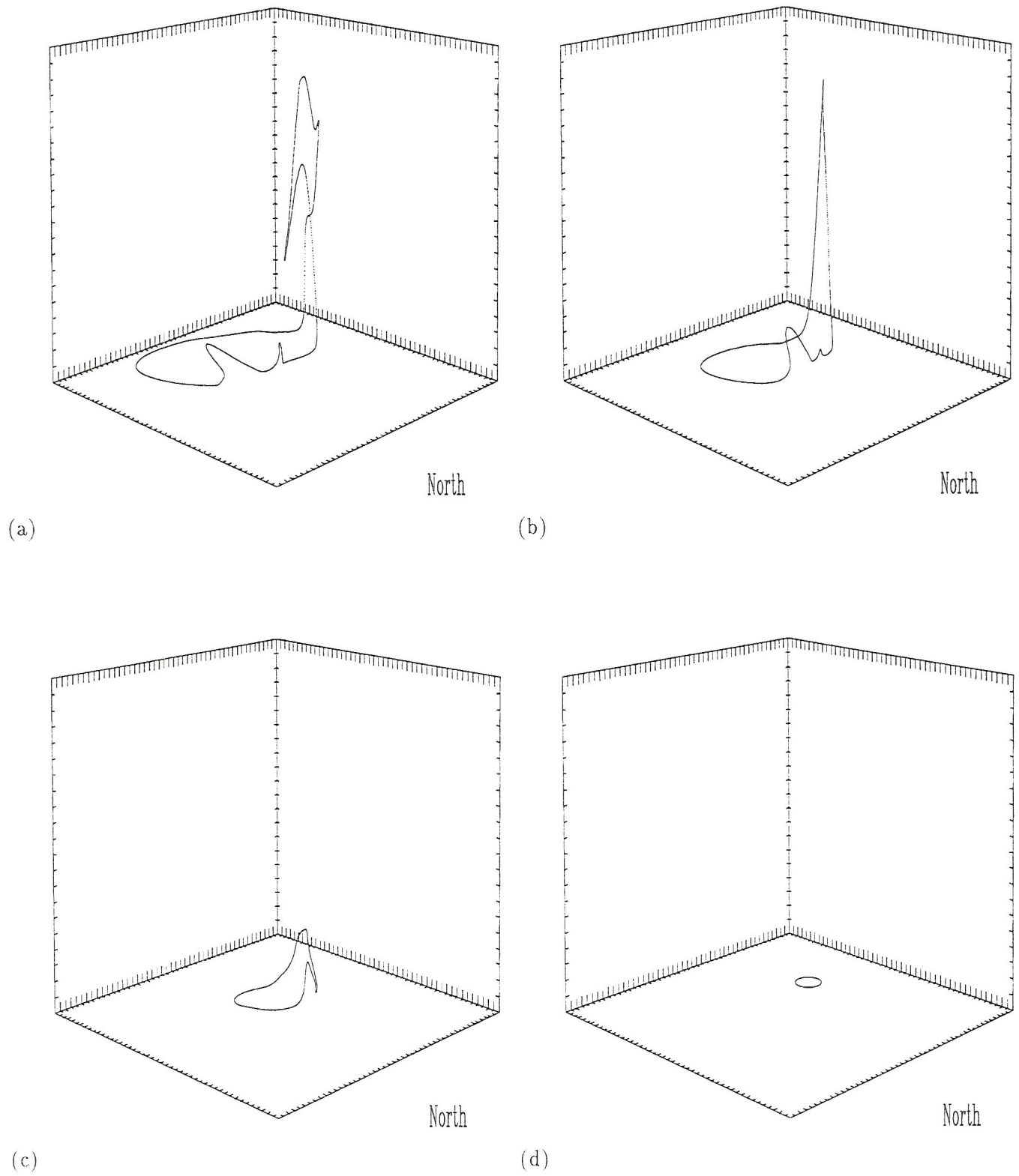


Figure 5.10: Material curve, viewed from the Northeast, in Grid #4 at 32409s 33030s, 33435s, and 33831s. The vertical axis represents a distance of 1.0 km.

produce a favorable buoyancy field. This will increase the circulation significantly, allowing a cyclonic tornado to form. There is less demand on a thunderstorm to produce a favorable buoyancy field if the initial circulation is large, for a tornado to form.

## 5.2 Numerical Tests

To test the above ideas, RAMS was configured with one grid 47.0 km in each horizontal direction and 15.0 km in the vertical. This grid had a horizontal grid spacing of 1.0 km. Vertical grid spacing at the lowest model level was 100.0m and was stretched with a ratio of 1.075. A sounding taken near the May 20, 1977 Del City, OK tornadic thunderstorm was used to initialize the temperature and moisture horizontally homogeneous in the model domain. In the top half of the model domain the winds were set equal to  $U=-5.0\text{m/s}$  while in the bottom half they were set to  $U=5.0\text{m/s}$ . The right half of the domain had winds set to  $V=5.0\text{m/s}$  while the left half of the model domain the winds were set to  $V=-5.0\text{m/s}$ . This produced a weak cyclonic vortex in the model domain. A warm bubble was initially released. As the warm bubble rose, low level air converged horizontally towards the center of the domain causing a vortex to form with tangential winds of 30.0 m/s.

At 1800s into the model run, a material curve having the shape of a circle and composed of 4000 particles was placed around the vortex at the lowest model level. The particles were moved back in time by linearly interpolating between model wind data stored every fifteen seconds and tri-linearly interpolating in space. The material curve was moved back to its position at 900s. As the curve moved back, the circulation and all circulation tendencies were computed and stored.

A plot of the circulation along the material curve and the complete prognostic tendencies are shown in Figure 5.1. The coriolis term increased slightly due to convergence of planetary vorticity; this is the second term on the right hand side of Eq 5.11. Baroclinicity remained flat since the material curve was essentially horizontal from 900s to 1800s. The diffusion tendency was negative over the entire interval. The prognosed circulation was obtained by adding up all tendencies. One can see how well the prognosed and diagnosed



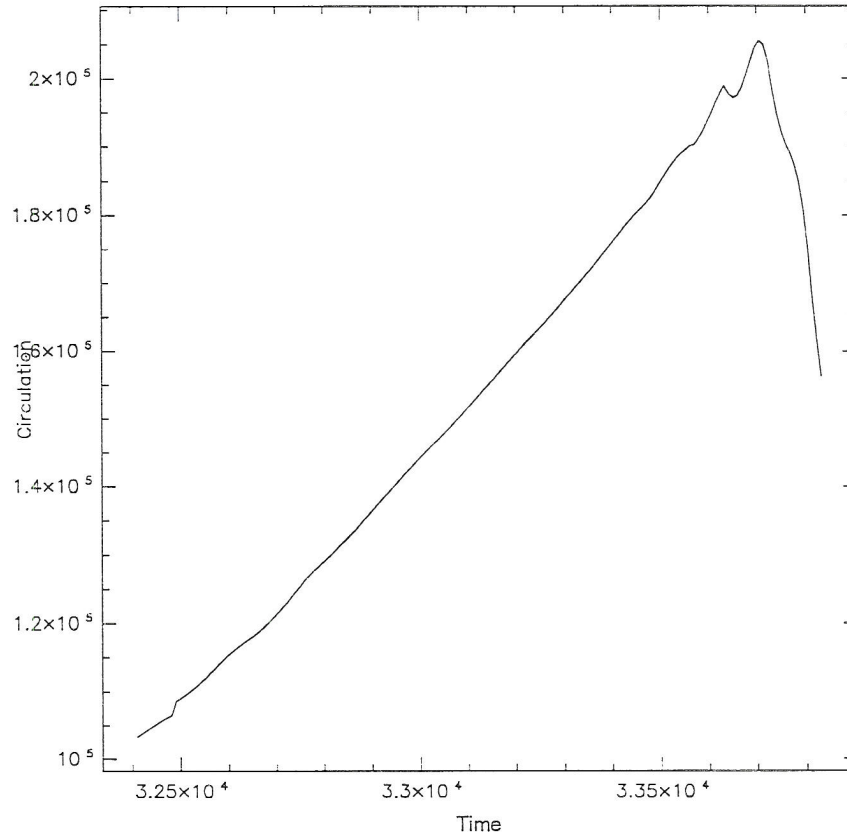


Figure 5.11: Circulation, in  $m^2/s$ , along the material curve in Grid #4 from 32409s to 33831s.

circulation match. The first term on the right hand side of Eq 5.11 dominated the evolution of circulation.

A second test was done with the same model set up except the winds were initialized from the Del City, OK sounding of May 20, 1977. A warm bubble was initially released. As the model was advanced a rotating updraft formed. Early in the storms' life, two vertical vorticity maxima of opposite signs existed in the updraft gradient. The positive/negative vorticity maximum was south/north of the updraft maximum at 2206m and 1800s.

At 1800s a horizontally circular material curve composed of 4000 particles was introduced and bounded the positive vertical vorticity maximum at 2206m. The particles were moved back in time to 900s. Model data were saved every 15.0 seconds and were used

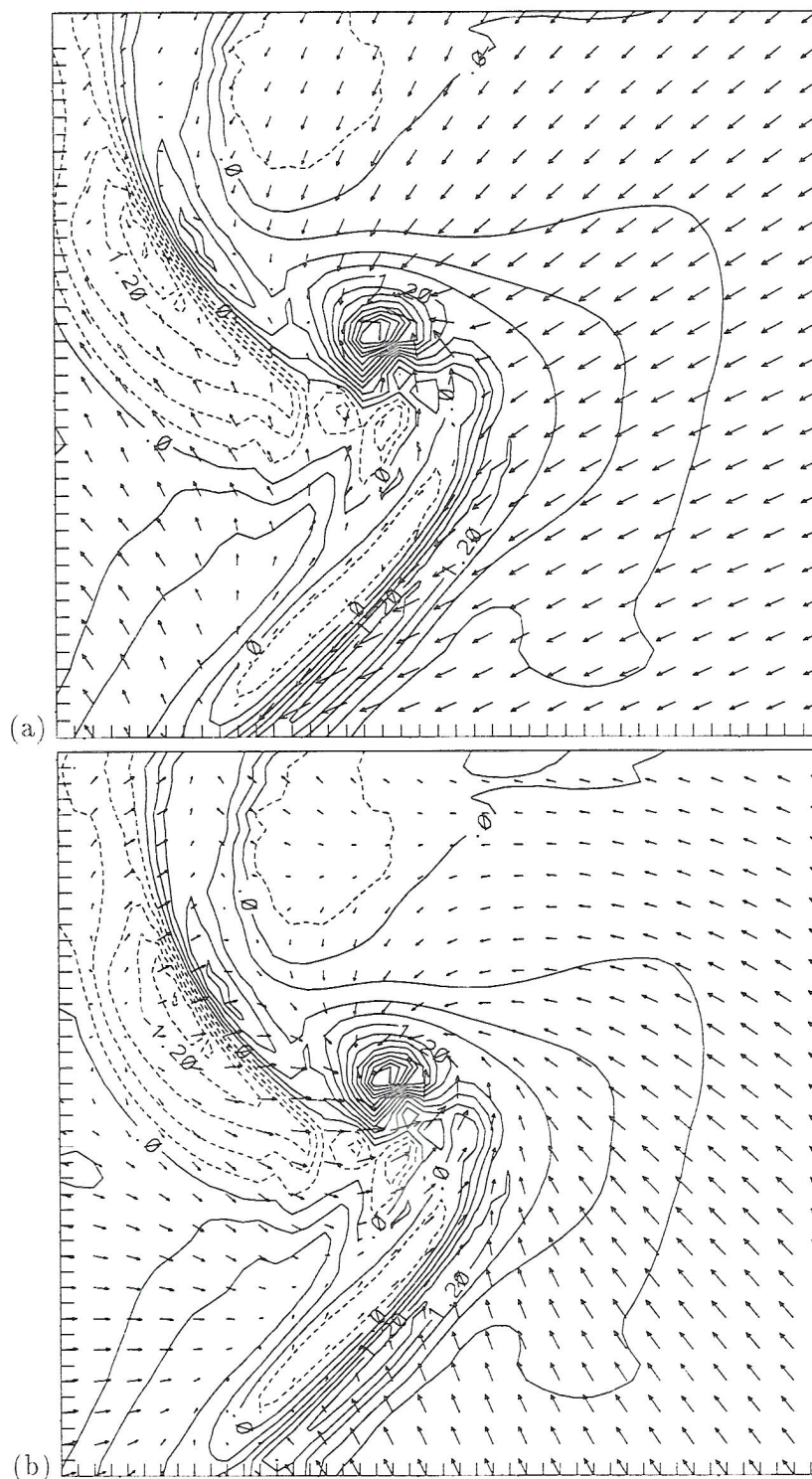


Figure 5.12: Grid #5:(a)Horizontal vorticity vectors (a vector having a length equal to the distance between the tails of two vectors in the x direction has a magnitude of  $6.8 \times 10^{-2} s^{-1}$ ) for the 50m to 150m layer and the vertical motion field (contoured every .3m/s to a maximum of 3.6m/s) at 2112 UTC (b) Horizontal, ground relative, winds at 49m (a vector having a length equal to the distance between the tails of two vectors in the x direction has a magnitude of 29.0m/s) and vertical motion at 2112 UTC. The view is from above with north/east towards the top/right of the page, respectively.

for linear interpolation in time and tri-linear interpolation in space. At 900s the material curve was basically in a vertical plane south of the updraft. From 900s to 1800s the material curve, for the most part, preserved its' circular shape and swung from the vertical plane to the horizontal plane. This movement of the material curve demonstrated quite clearly the tilting of boundary layer horizontal vorticity into the vertical by the updraft.

The results of the circulation analysis are shown in Figure 5.10. The baroclinic tendency acted to increase the circulation when the material curve lived in the vertical plane while diffusion and coriolis remained flat. As the curve moved into the horizontal plane, diffusion dominated all other tendencies while the baroclinic and coriolis terms remained flat. While the curve was orientated in the vertical, the prognostic circulation increased from 900s to 1200s due to baroclinic tendencies. From 1200s to 1800s the curve moved into a horizontal plane where diffusion rapidly reduced the circulation. Again a similarity can be seen when comparing the diagnosed and prognosed circulation in the figure.

The tests described above agree with the theory introduced in the beginning of the chapter. It seems the shape of the material curve as it moved and the diagnosed circulation are enough to infer which tendency terms were responsible for any changes in circulation.

### 5.3 May 15, 1991 Tornado

Due to the small size and movement of Grids #5 and #6, the circulation analysis was done in Grid #4 from 2100 UTC to 2124 UTC. Model data were stored every 9.0 seconds and required about 1.0 Gigabytes of disk space. At 2124 UTC a horizontal material curve composed of 4000 particles bounded the positive vertical vorticity maximum at 49.0m. The curve was the shape of a circle and had a radius of 2.0km. The particles were moved back in time to 2100 UTC as circulation tendencies were computed and stored. The results of the analysis were surprising. The prognosed circulation did not agree with the diagnosed circulation.

This apparent paradox was studied for months to determine why the prognosed and diagnosed circulation did not match. The following test was done at a specific grid point where the V component of wind was calculated. At that grid point, X, the model value of



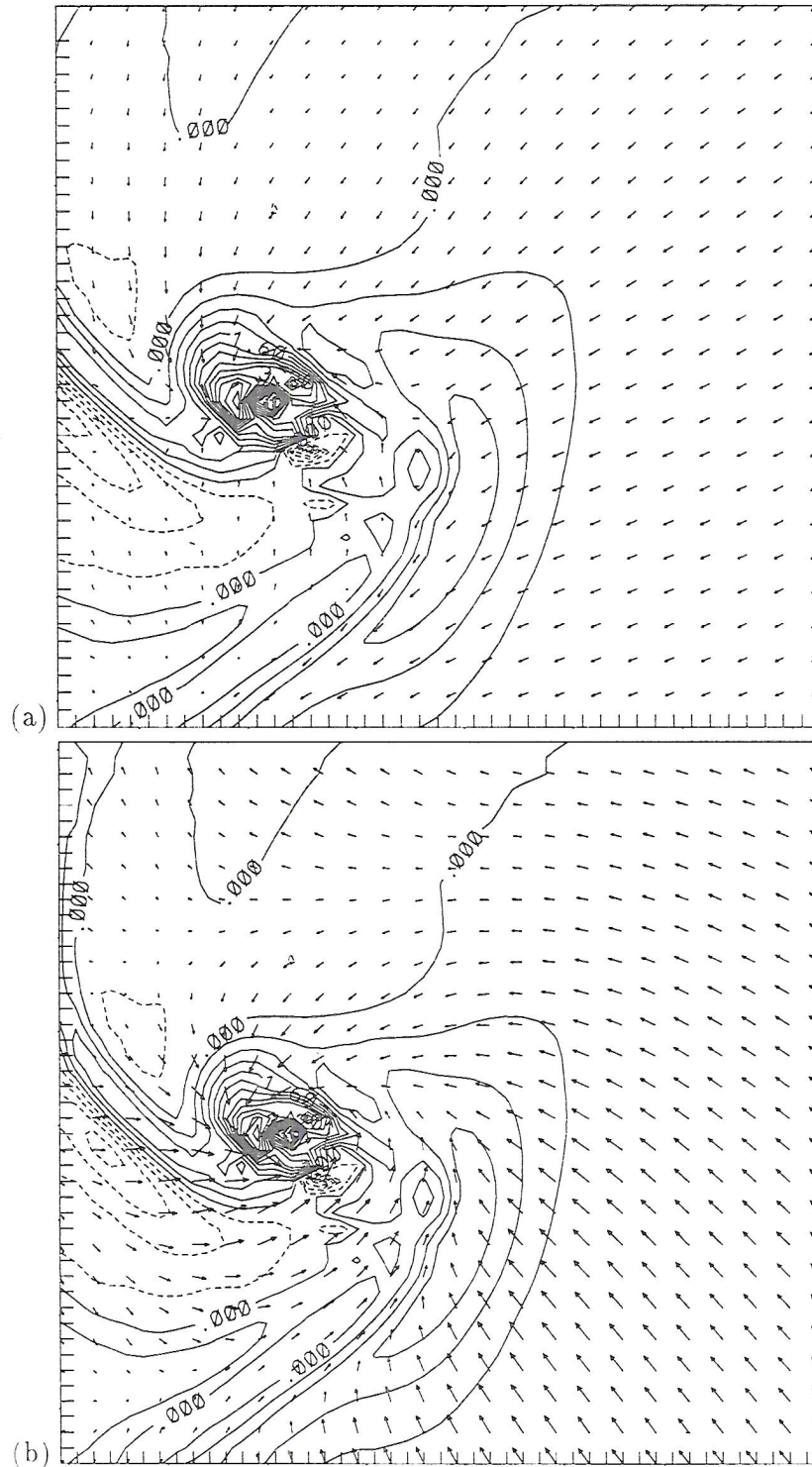


Figure 5.13: Grid #5;(a)Horizontal vorticity vectors (a vector having a length equal to the distance between the tails of two vectors in the x direction has a magnitude of  $1.5 \times 10^{-1} s^{-1}$ ) for the 50m to 150m layer and the vertical motion field (contoured every .4m/s to a maximum of 4.8m/s) at 2118 UTC (b) Horizontal, ground relative, winds at 49m (a vector having a length equal to the distance between the tails of two vectors in the x direction has a magnitude of 29.0m/s) and vertical motion at 2118 UTC. The view is from above with north/east towards the top/right of the page, respectively.

$V(X,t)$  and  $V(X,t + \delta t)$  was used to compute  $\frac{\partial V}{\partial t}$  valid at grid point  $X$  and time  $t$ . The model also provided the value of advection of  $V$  at the grid point  $X$  and time  $t$ . The sum of these two terms is  $\frac{DV}{DT}(X,t)$ . This value was the same as the sum of the model  $\pi$  gradient, coriolis and diffusion terms. A small error occurred due to the Asselin filter being applied to  $V$ .

The Lagrangian derivative of  $V$  was computed from a particle released at grid point  $X$  at time  $t$ . The particle was advanced one time step. At this new position the model winds were interpolated to the particle. The value of  $V(X+\delta X,t+\delta t)$  and  $V(X,t)$  was used to compute  $\frac{DV}{Dt}$  directly.

The Lagrangian derivative of  $V$  was computed two different ways and they were expected to have similar values. The two values were not only of different magnitudes but also different signs! This implies that the prognosed and diagnosed  $V$  will be different and hence the prognosed and diagnosed circulation will not agree.

Further testing indicated when a convective storm was fixed relative to the model grid points the diagnosed and prognosed circulation curves agreed well. When the convective storm moved relative to the model grid points the diagnosed and prognosed circulation curves did not agree well. These results suggest that advection of model variables may have errors that are large enough to corrupt the relationship between Eulerian and Lagrangian frames.

Let us consider the Eulerian grid and the concept of grid volume averaging. The prognostic wind components;  $u,v$ , and  $w$  are grid volume averaged quantities. That is, everywhere in a grid volume centered about a  $u$ -point, for example, has the same value of  $u$ . To extract the Lagrangian frame, the value of  $u$  of a particle, in a grid volume centered about a  $u$ -point, will not necessarily be the same as the value at the  $u$ -point itself. This is due to the tri-linear interpolation scheme used to determine the value of  $u$  for the particle. That is, the value of  $u$  for the particle is not consistent with grid volume averaging in the Eulerian frame and may be another cause for the lack of agreement between the diagnosed and prognosed circulation.

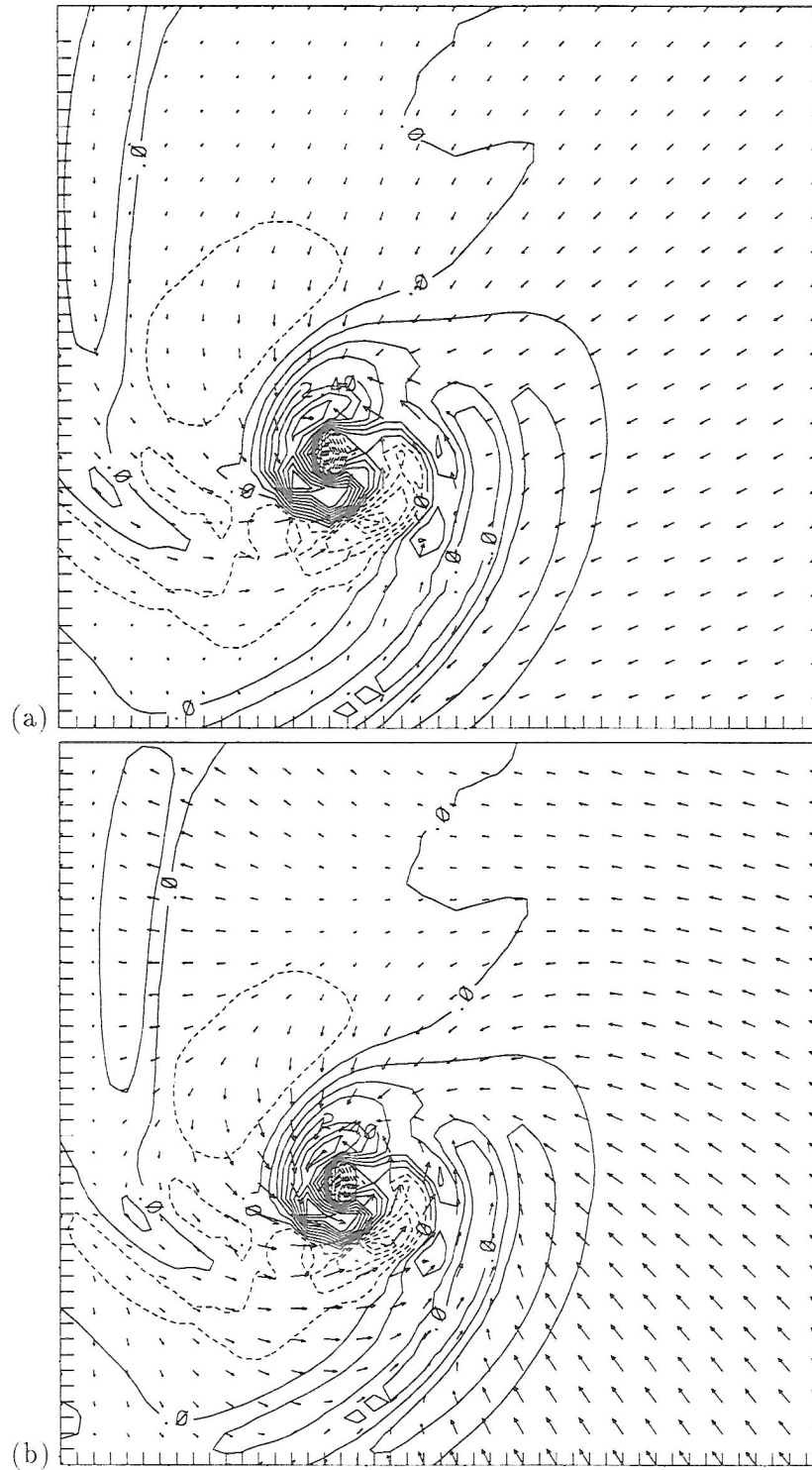


Figure 5.14: Grid #5;(a)Horizontal vorticity vectors (a vector having a length equal to the distance between the tails of two vectors in the x direction has a magnitude of  $1.6 \times 10^{-1} \text{ s}^{-1}$ ) for the 50m to 150m layer and the vertical motion field (contoured every .6m/s to a maximum of 5.4m/s) at 2124 UTC (b) Horizontal, ground relative, winds at 49m (a vector having a length equal to the distance between the tails of two vectors in the x direction has a magnitude of 29.0m/s) and vertical motion at 2124 UTC. The view is from above with north/east towards the top/right of the page, respectively.



Based on the theory introduced in the beginning of the chapter and the numerical tests that followed, the analysis will depend on the shape of the material curve and the diagnosed circulation profile.

The first material curve analysis was conducted from 2100 UTC to 2106 UTC. In this time interval the material curve maintained a horizontal orientation as it converged to the vertical vorticity maximum at 49m. Figure 5.3 presents a view from above the material curve. Circulation increased slightly from 32400s to 32500s due to convergence of planetary vorticity. From 32500s to 32760s the frictional drag decreased the circulation significantly.

A second material curve was spawned at 2100 UTC and followed to 2112 UTC. At 2100 UTC (Figure 5.6a) part of the curve was horizontal and part vertical. Downdraft air moved the vertical segment from 2100 UTC to 2104 UTC. In Figure 5.6b one can see a small segment of the curve remaining in the vertical. Based on the theory, the increase in circulation was a result of baroclinicity; see Figure 5.7. Later the curve assumed a more horizontal orientation (Figure 5.6c and d) and baroclinic effects became negligible. Diffusion removed all increases that were due to baroclinic effects as the curve converged to the positive vertical vorticity maximum at 49m from 32800s to 33120s, see Figure 5.7.

Significant changes occurred in the time period from 2100 UTC to 2118 UTC. For this analysis, the material curve extended well into the boundary layer at 2100 UTC, see Figure 5.8a. Seven minutes later, parts of the curve remained in the vertical, as seen in Figure 5.8b. During this time interval the circulation had increased significantly. The combination of increased circulation and the material curve extending into the vertical, implied that baroclinic effects were primarily responsible for the increase in circulation. This process continued until 33200s after which time the material curve assumed a horizontal orientation. Diffusion decreased the circulation from 33200s to 33480s. Diffusion did not remove all increases that were due to baroclinicity.

The final material curve analysis was from 2100 UTC to 2124 UTC. In Figure 5.10a part of the curve extended upward to just under 1.0 km then bent back down towards the southeast. Near the surface there were two significant bends in the curve, one vertically orientated and a larger one in the horizontal plane. Approximately fifteen minutes later

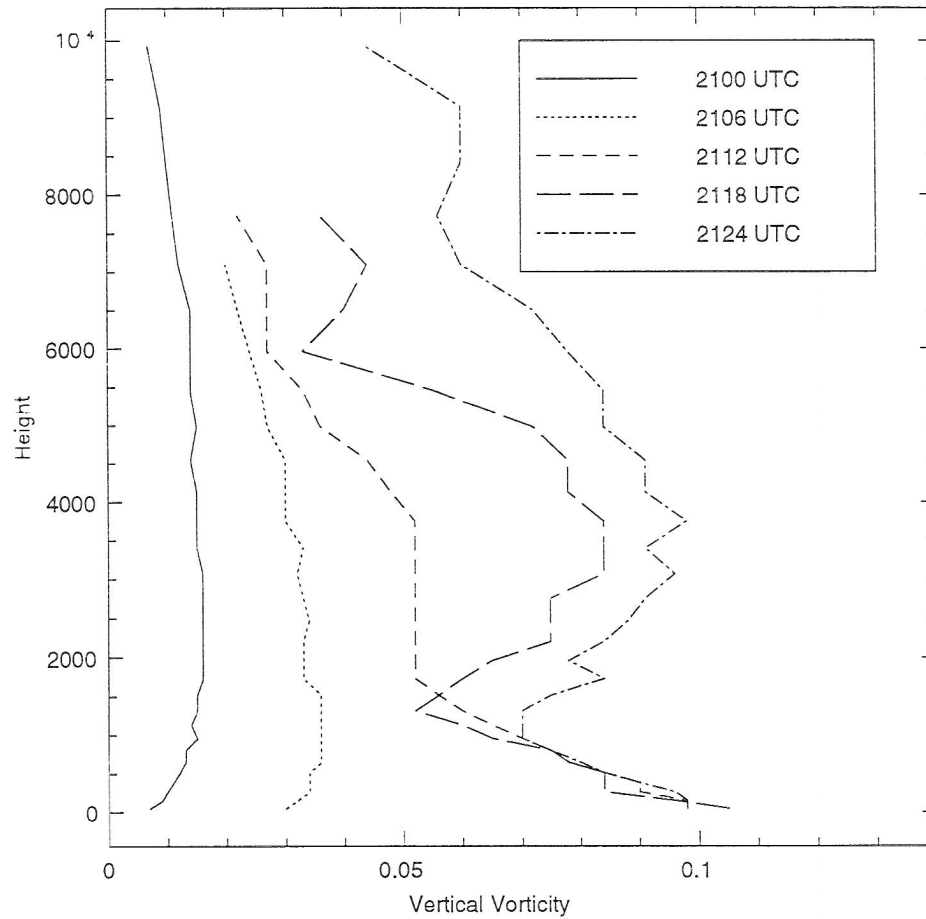


Figure 5.15: Vertical profile of the vertical vorticity maximum in Grid #5 for various times. The height is in meters and vorticity is  $s^{-1}$ .

(Figure 5.10c) the main vertical portion of the curve descended in the downdraft. The large bend in the curve in Figure 5.10a pointing south near the surface, folded upward into the vertical. During this time the circulation doubled and was consistent with baroclinic forces along the curve. From 33435s to 33831s the curve became basically horizontal and this allowed frictional stresses to remove around 40% of the net gain during the period from 32409s to 33700s.

#### 5.4 Vorticity Analysis

Material curve analysis from 2100 UTC to 2112 UTC indicated that thunderstorm downdrafts did not have a significant influence on the circulation and hence the vertical

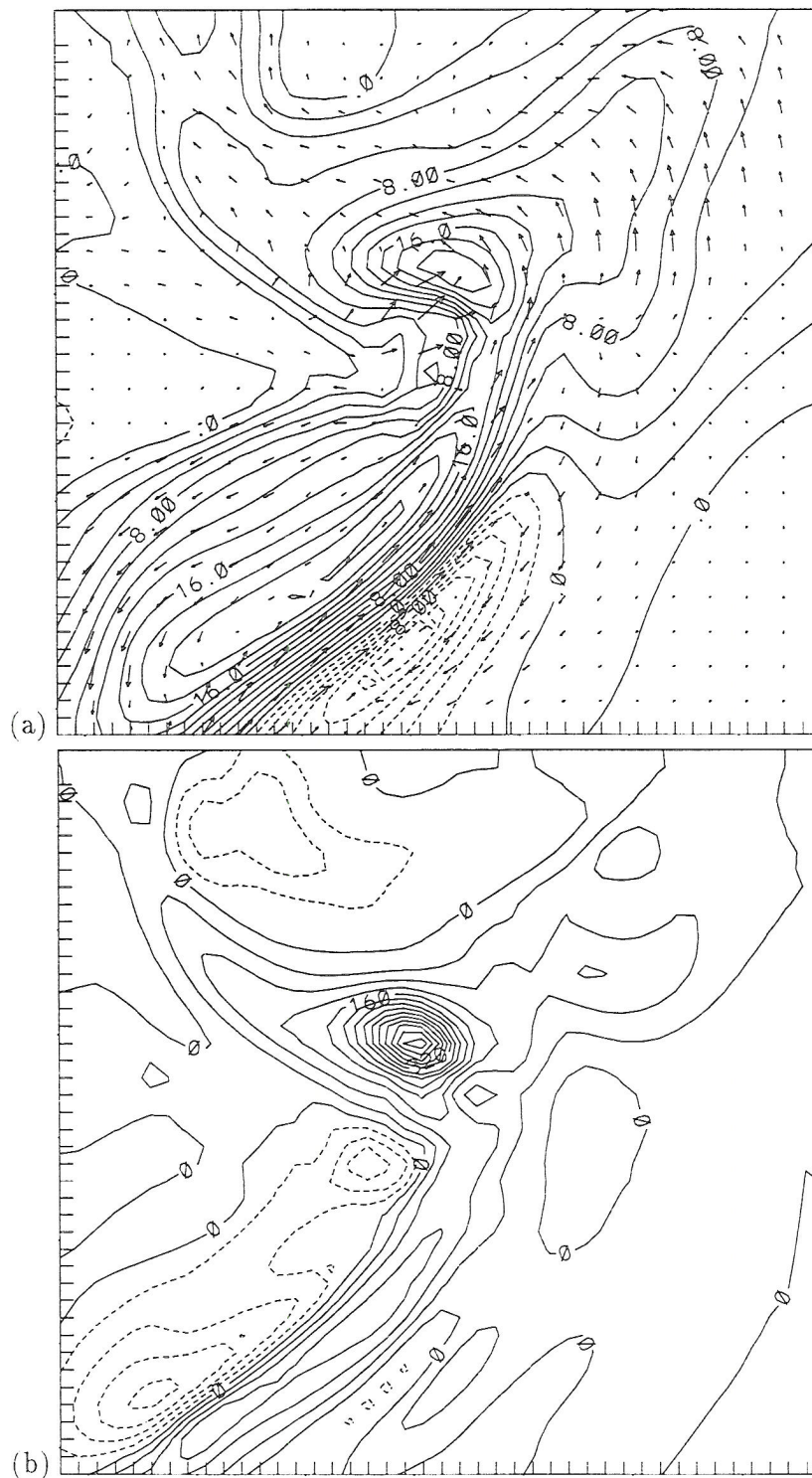


Figure 5.16: Grid #5; (a) Horizontal vorticity vectors (a vector having a length equal to the distance between the tails of two vectors in the x direction has a magnitude of  $3.3 \times 10^{-2} \text{ s}^{-1}$ ) and the vertical motion field at 2757m (contoured every 2.0m/s to a maximum of 22.0m/s) (b) Vertical vorticity corresponding to (a), contoured every  $4 \times 10^{-3} \text{ s}^{-1}$  to a maximum of  $5.2 \times 10^{-2} \text{ s}^{-1}$  at 2112 UTC.



vorticity. The analysis demonstrated that material curves in that time interval essentially converged while maintaining a horizontal orientation near the surface, towards the vortex.

Horizontal vorticity vectors displayed in this section are valid for the layer from 50m to 150m; the first model layer above ground bounded by the horizontal winds. The horizontal vorticity vectors for the layer from 150m to 264m were very similar to the first layer and will not be displayed. As a result the ideas discussed in this section are valid for the 50m to 264m layer.

In this section the vorticity field from 2112 UTC to 2124 UTC will be examined. In Figure 5.12a, the horizontal vorticity vectors in the layer from 50m to 150m are displayed with the vertical motion. Vectors were plotted every 666.6m. Magnitudes of the vectors on the east side of the Figure were approximately  $6.8 \times 10^{-2} s^{-1}$ . Vertical motion was contoured every 30.0 cm/s. The updraft maximum had a speed of 3.6 m/s.

To the east of the updraft maximum the vorticity vectors were being tilted upward. As they ascended into the parent thunderstorm they generated positive vertical vorticity that fed the thunderstorm rotation. Of particular importance were the vectors that pointed south in the downdraft to the northwest of the updraft maximum. The vectors to the south of the strongest downdraft were being tilted as they descended the downdraft to generate positive vertical vorticity. A second region with positive tilting in the downdraft was directly to the south of the updraft maximum. There, the vorticity vectors were pointing north from the strongest downdraft to the updraft.

These two regions of positive tilting in the downdraft did not make any contribution to the positive vertical vorticity associated with the vortex at this time. The region to the northwest was too far away while the one to the south was just forming.

The horizontal wind vectors plot, with vertical motion for the same time and height, is shown in Figure 5.12b. Note the strong divergent flow to the north associated with the downdraft. By comparing this figure with the last one, the reader can see that the vorticity vectors were nearly streamwise to the north and northwest of the updraft maximum while just to the south they were crosswise in the downdraft.

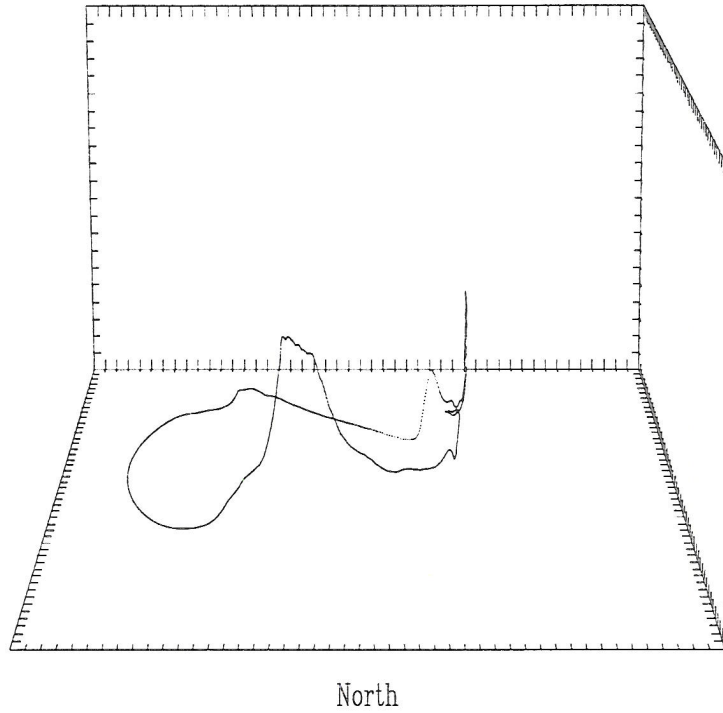


Figure 5.17: Material curve for the April 26, 1991 simulation, in Grid #4 at 36135s. The vertical axis extends from the ground up to 1.0 km. The horizontal dimensions are 47.0 km.

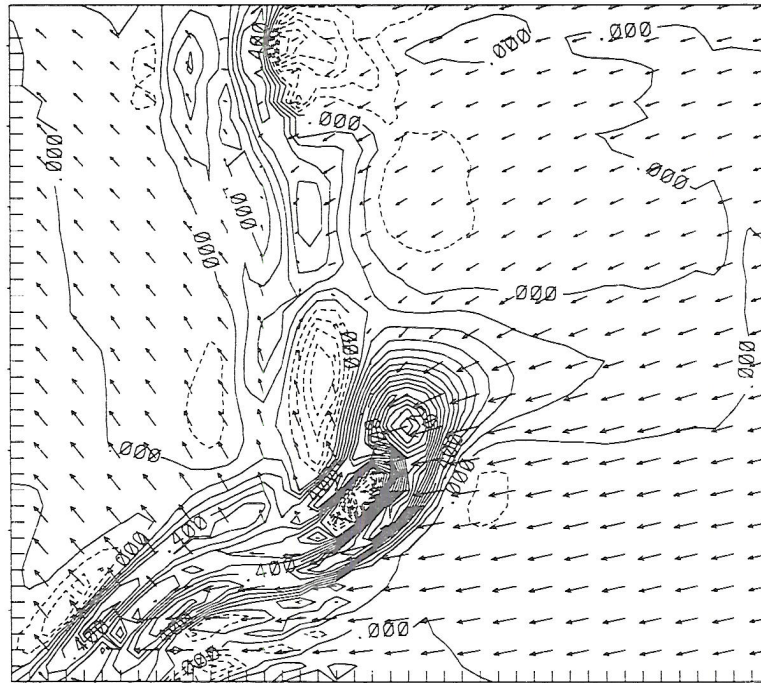


Figure 5.18: Grid #4; Horizontal vorticity vectors (a vector having a length equal to the distance between the tails of two vectors in the x direction has a magnitude of  $3.9 \times 10^{-2} s^{-1}$ ) for the 50.0m to 154.0m layer, and the vertical motion field (contoured every .1m/s to a maximum of 1.7m/s) at 36000s.

Six minutes later, the horizontal vorticity field had changed significantly. The downdraft to the north was wrapping around the west side of the 4.8 m/s updraft maximum. As a result, positive tilting was occurring in the downdraft. A stronger downdraft existed to the south. As before, the horizontal vorticity vectors were pointing north. From 2112 UTC to 2118 UTC this downdraft became more organized and was providing a larger region for positive tilting of horizontal vorticity.

The horizontal wind field at 2118 UTC and 49m is displayed in Figure 5.13b. Noticeable divergent flow existed in the forward downdraft as well as in the rear downdraft. As before, the horizontal vorticity had a large streamwise component to the north and northwest of the updraft maximum while having a large crosswise component to the south.

At 2124 UTC the downdraft surrounded the updraft maximum to the north, west, and south. In Figure 5.14a the horizontal vorticity vectors point from downdraft to updraft on all these flanks. The downdraft positively tilted the horizontal vorticity as air descended within this large area.

At this time the horizontal wind field (Figure 5.14b) had two main regions of significant divergence. One was associated with the forward downdraft, to the north, and the second was associated with the rear downdraft, located to the southwest of the updraft maximum. The horizontal vorticity vectors had a large streamwise component on all sides of the storm occupied by downdraft, even to the south.

As shown in Figure 5.14b, the environmental winds to the east at 49m were from the southeast. The forward flank downdraft produced northerly winds while the rear flank downdraft produced winds with westerly momentum. The two downdrafts produced momentum at 49m that resulted in a large cyclonically rotating wind field. The updraft was able to horizontally converge the rotation allowing the vortex to form.

The vertical profile of vertical vorticity associated with the tornado in Grid #5 is displayed in Figure 5.15. At 2100 UTC Grid #5 was spawned and this curve shows Grid #4 interpolated to the finer grid. Six minutes later, 2106 UTC, the vertical vorticity had increased at all levels as the finer grid was able to resolve stronger convergence. For these two times the vorticity increased with height.



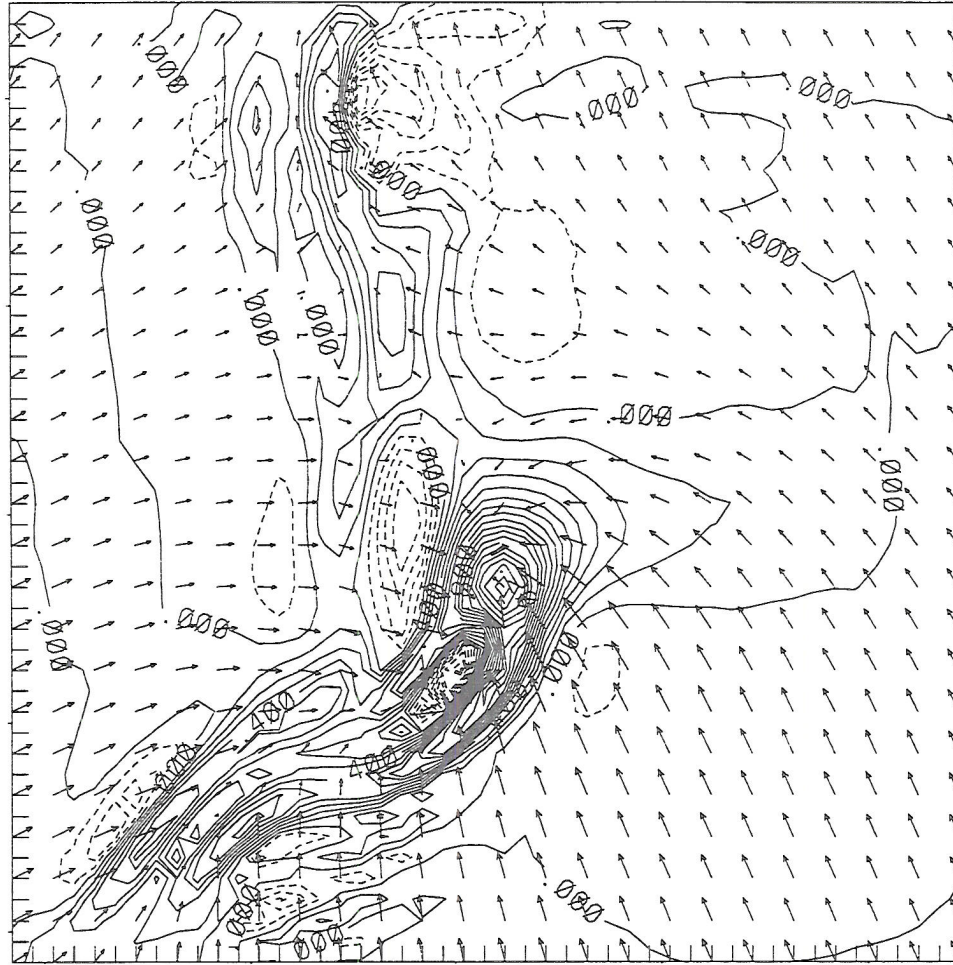


Figure 5.19: Grid #4; Horizontal, ground relative, wind vectors (a vector having a length equal to the distance between the tails of two vectors in the x direction has a magnitude of 28.0m/s) and the vertical motion, both at 50m and 36000s.

Significant changes occurred in the next six minutes. The vorticity had its largest value at the lowest model level. Recall the material curve analysis from 2100 UTC to 2112 UTC, where the curve basically remained horizontal while converging towards the vorticity maximum. Vertical advection transported the vorticity-rich boundary layer air into the storm. Thunderstorm downdrafts did not aid in producing the vorticity maximum seen near the surface.

From 2118 UTC to 2124 UTC, thunderstorm downdrafts were primarily responsible for producing and maintaining the vorticity maximum near the surface. A second maximum was also evident located just below 4.0km. Is this a common feature? Further analysis was done at 2112 UTC to see why this maximum occurred.

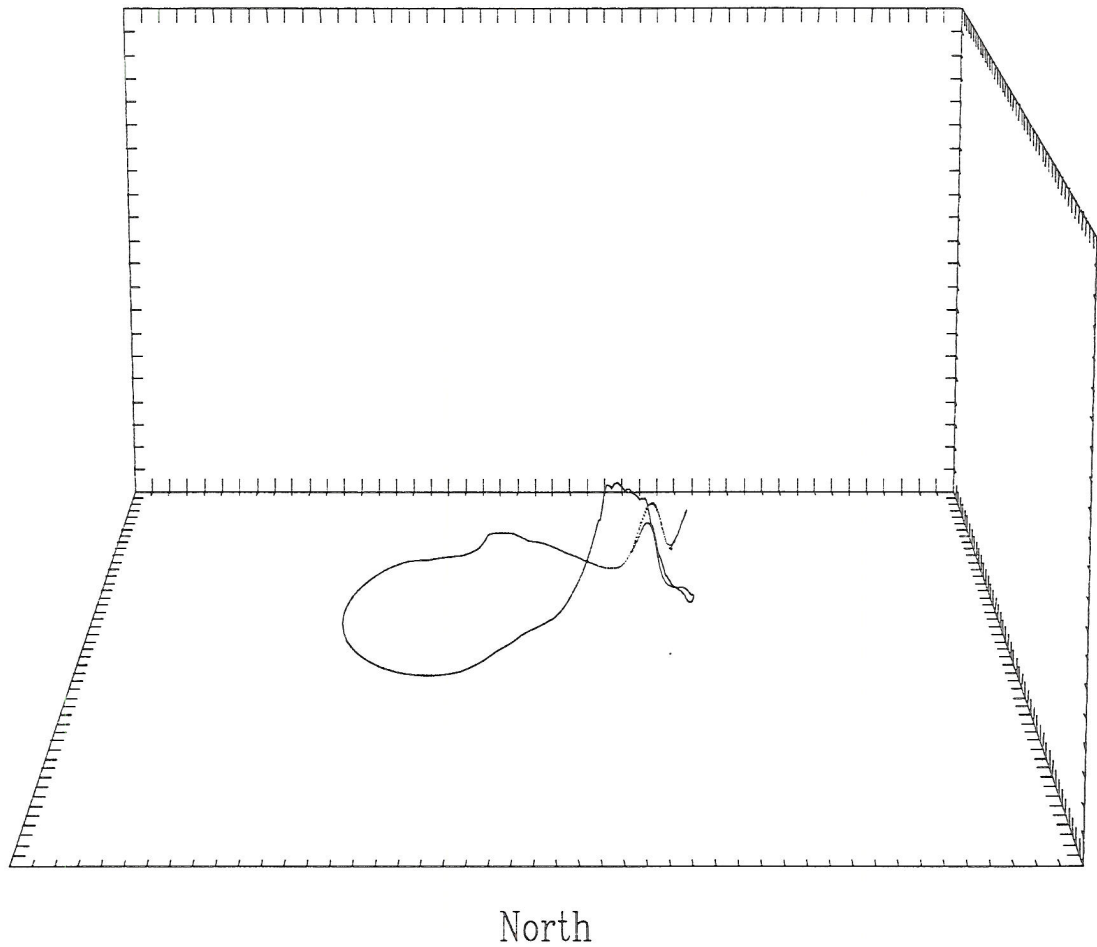


Figure 5.20: Material curve for the April 26, 1991 simulation, in Grid #4 at 36450s. The vertical axis extends from the ground up to 1.0 km. The horizontal dimensions are 47.0 km.

The horizontal vorticity vectors with vertical motion are seen in Figure 5.16a. The vectors were basically parallel to the updraft gradient to the southwest of the updraft maximum, near the center of the figure. This orientation allowed for strong and efficient tilting of horizontal vorticity. The tilting occurred in the layer from below 2.0 km to 4.0 km. The vertical vorticity maximum occurred in the tilting region (ie. the updraft gradient) as is seen in Figure 5.16b. It is proposed that this process, along with convergence, amplified the vertical vorticity in the 2.0 km layer.

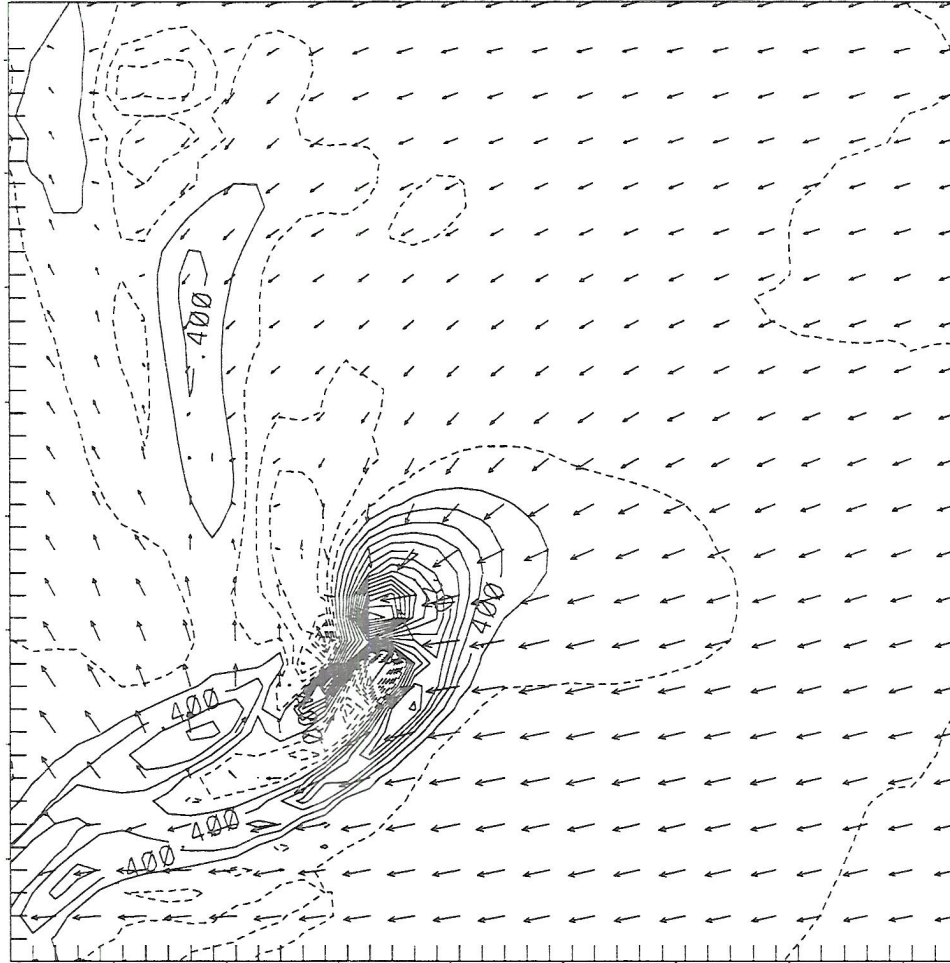


Figure 5.21: Grid #4; Horizontal vorticity vectors (a vector having a length equal to the distance between the tails of two vectors in the x direction has a magnitude of  $4.4 \times 10^{-2} s^{-1}$ ) for the 50.0m to 154.0m layer, and the vertical motion field (contoured every .2m/s to a maximum of 3.2m/s) at 36450s.

### 5.5 Summary of the May 15, 1991 Tornado Genesis Process

The development of the vortex was a two step process. First the thunderstorm caused horizontal convergence of the boundary layer air beneath the updraft. Vertical vorticity associated with the dry line bulge was amplified during the process even though the circulation decreased. As a result winds near the surface began to rotate and the pressure lowered.

It is proposed that the low pressure near the surface contributed to the development of the rear flank downdraft. The rotating thunderstorm began to wrap precipitation from its



north side to the northwest side. The circulation increased due to baroclinic processes while the material curve descended the downdraft. Horizontal vorticity (with an approximate magnitude of  $3 \times 10^{-2} s^{-1}$  to  $4 \times 10^{-2} s^{-1}$  in the first two model layers in Grid #5 at 2124 UTC) was tilted in the lowest few hundred meters above the ground and a few kilometers away from the vortex. As a result vertical vorticity was produced in the downdraft as the air continued to sink towards the surface.

In the second step the vertical vorticity produced by the downdrafts converged horizontally (maximum convergence was  $5.6 \times 10^{-2} s^{-1}$  in Grid #5 at 2124 UTC at 50m) into the vortex causing it to intensify. Frictional stresses decreased the circulation as the material curve shrunk to the vortex. The rotation in the lower part of the storm continued to wrap the precipitation and the downdraft around the rear flanks of the storm, producing a hook echo in the process. The area occupied by downdraft increased thus producing a larger region of vertical vorticity that converged into the vortex. In time the precipitation was completely wrapped around the back side of the storm and merged with the rear flank downdraft. At this time the horizontal vorticity was tilted into the vertical in a large region that surrounded the mature vortex from the north, west and south.

It was found that the tilting in the downdraft occurred in the lowest 250 meters. This is an important point. If tilting in the downdraft occurred only at higher levels, positive vertical vorticity would be produced well above the ground. Horizontal convergence of the vertical vorticity would produce a vortex above the ground, not at the ground.

As the vortex became organized in the boundary layer, the updraft advected it upward. The result was a mature vortex that occupied a 10.0 km vertical column within the thunderstorm.

## 5.6 April 26, 1991 Tornado

The analysis for this case was done for the time interval from 36000s to 36900s or from 2200 UTC to 2215 UTC. A material curve composed of 4000 particles was placed around the cyclonic circulation center at 50m. The curve was the shape of a circle and had a radius of 2.0 km. Model winds were saved every 9.0 seconds for the fifteen minute period.

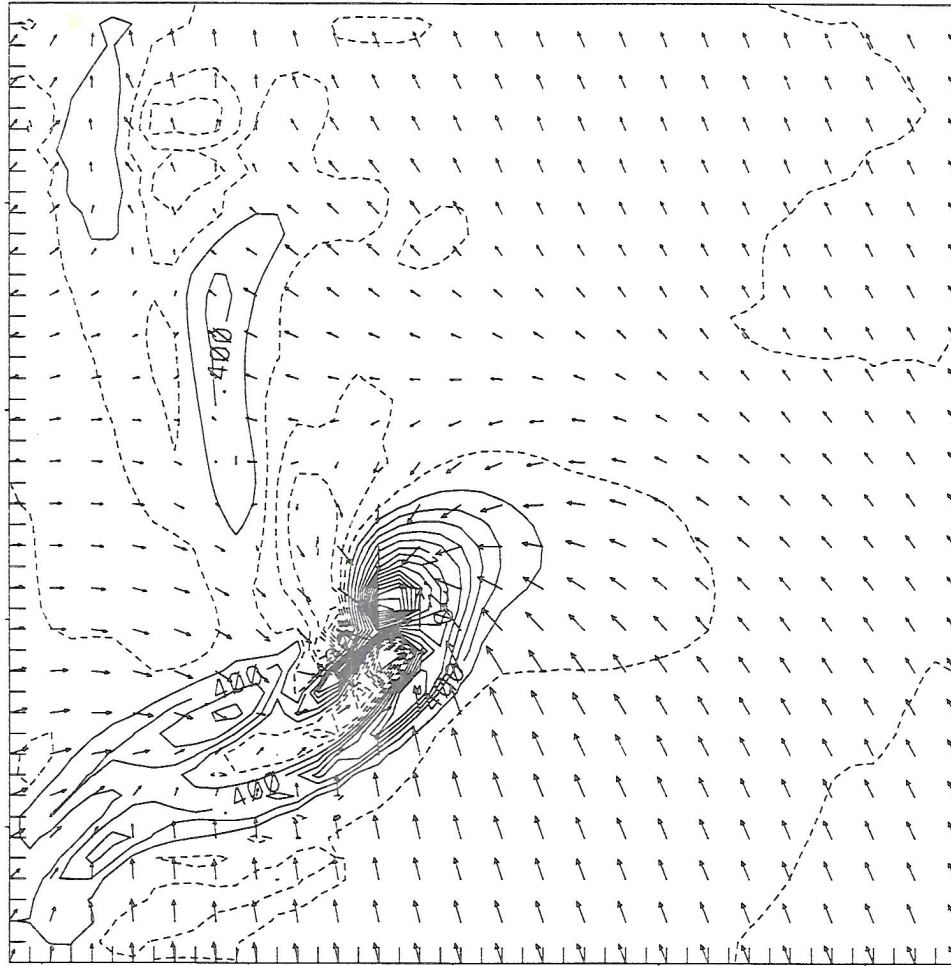


Figure 5.22: Grid #4; Horizontal, ground relative, wind vectors (a vector having a length equal to the distance between the tails of two vectors in the x direction has a magnitude of 33.0m/s) and the vertical motion, both at 50m and 36450s.

Particles were moved back with a time step of 9.0s. Due to the rapid movement of Grid #4, the eastern most section of the curve intersected the grid boundary. Because of this, the analysis could only be done for just under fifteen minutes.

The position of the material curve at 36135s is shown in Figure 5.17. The view is from the north looking to the south. The vertical axis extended from the ground to 1.0 km. As can be seen in the Figure, a significant portion of the curve was in the vertical plane on the north side. The highest particle on the curve was at 503.0m. The circulation at this time was  $2.8 \times 10^5 m^2/s$ .

The horizontal vorticity vectors at 36000s are shown in Figure 5.18. These vectors are for the 50.0m to 154.0m layer. Because Grid #4 moved west at 36115s and intersected

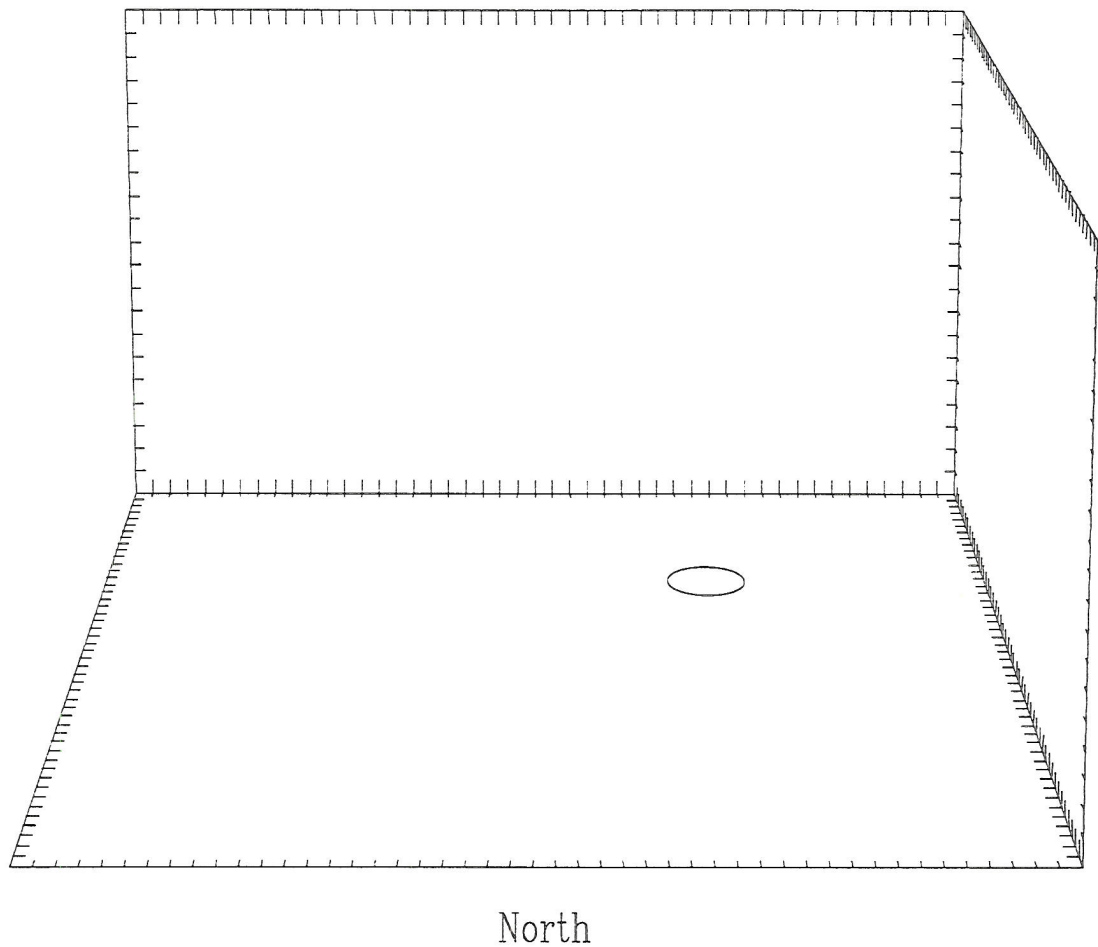


Figure 5.23: Material curve for the April 26, 1991 simulation, in Grid #4 at 36900s. The vertical axis extends from the ground up to 1.0 km. The horizontal dimensions are 47.0 km.

the eastern section of the circuit, the material curve was unable to move any further back in time. This is why the time difference between the two Figures is 135s. The horizontal vorticity vectors in the region from  $x=782.0\text{km}$  to  $x=790.0\text{km}$  along the line  $y=-62.0\text{km}$  had a significant positive projection through the vertical plane bounded by the curve and the ground.

The tilting of horizontal vorticity occurred in the forward flanking precipitation downdraft. The horizontal wind vectors (Figure 5.19) were clearly divergent in the region. The rain water field can be seen in Figure 4.23b.

Seven minutes later the material curve had contracted horizontally (Figure 5.20). The vertical portion rotated cyclonically and descended. The highest particle was at 343m.



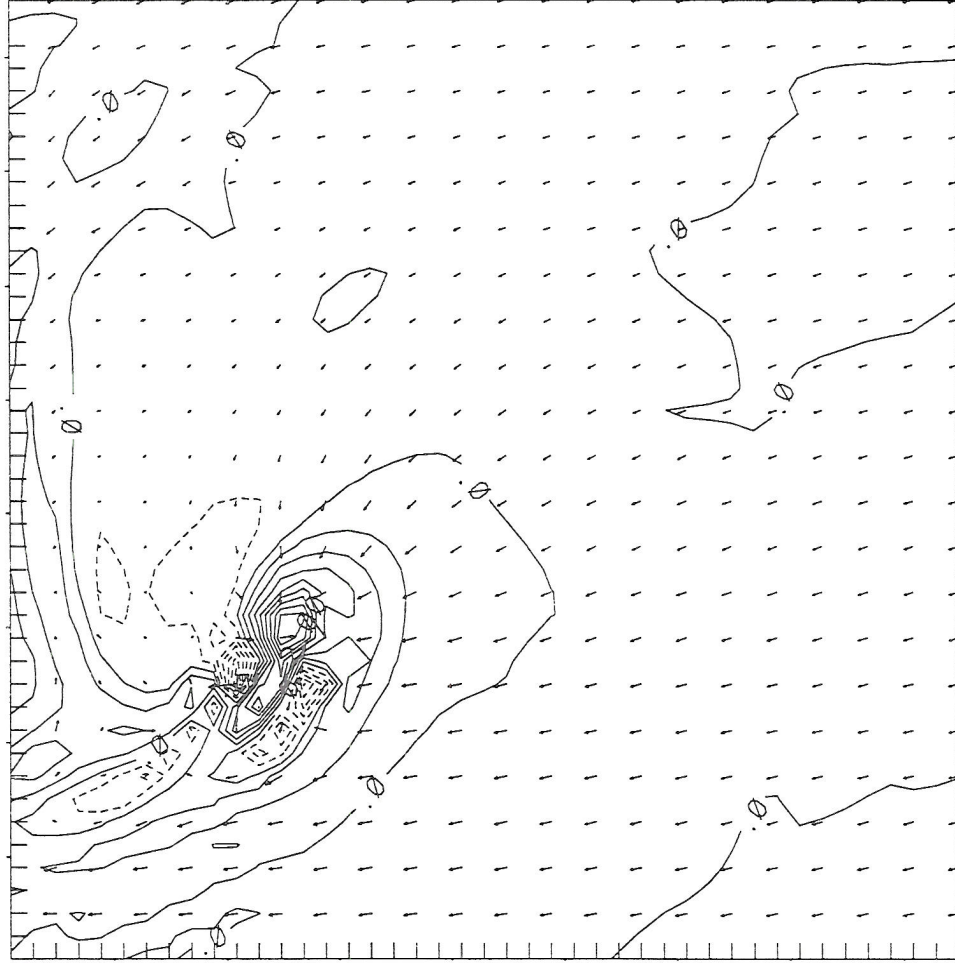


Figure 5.24: Grid #4; Horizontal vorticity vectors (a vector having a length equal to the distance between the tails of two vectors in the x direction has a magnitude of  $9.5 \times 10^{-2} \text{ s}^{-1}$ ) for the 50.0m to 154.0m layer, and the vertical motion field (contoured every .5m/s to a maximum of 4.5m/s) at 36900s.

The circulation reached a maximum value of  $3.5 \times 10^5 \text{ m}^2/\text{s}$  at 36550s. The orientation of the curve and the increase in circulation implied that the growth of circulation was due to baroclinic processes.

The material curve was vertically inclined along the northwest side. In Figure 5.21 one can see that the horizontal vorticity vectors, located to the northwest of the updraft maximum and in the downdraft, maintained the significant positive projection through the vertical surface.

To the north and northwest, horizontal wind vectors can be seen pointing from the downdraft towards the updraft (Figure 5.22). The downdraft was wrapping cyclonically

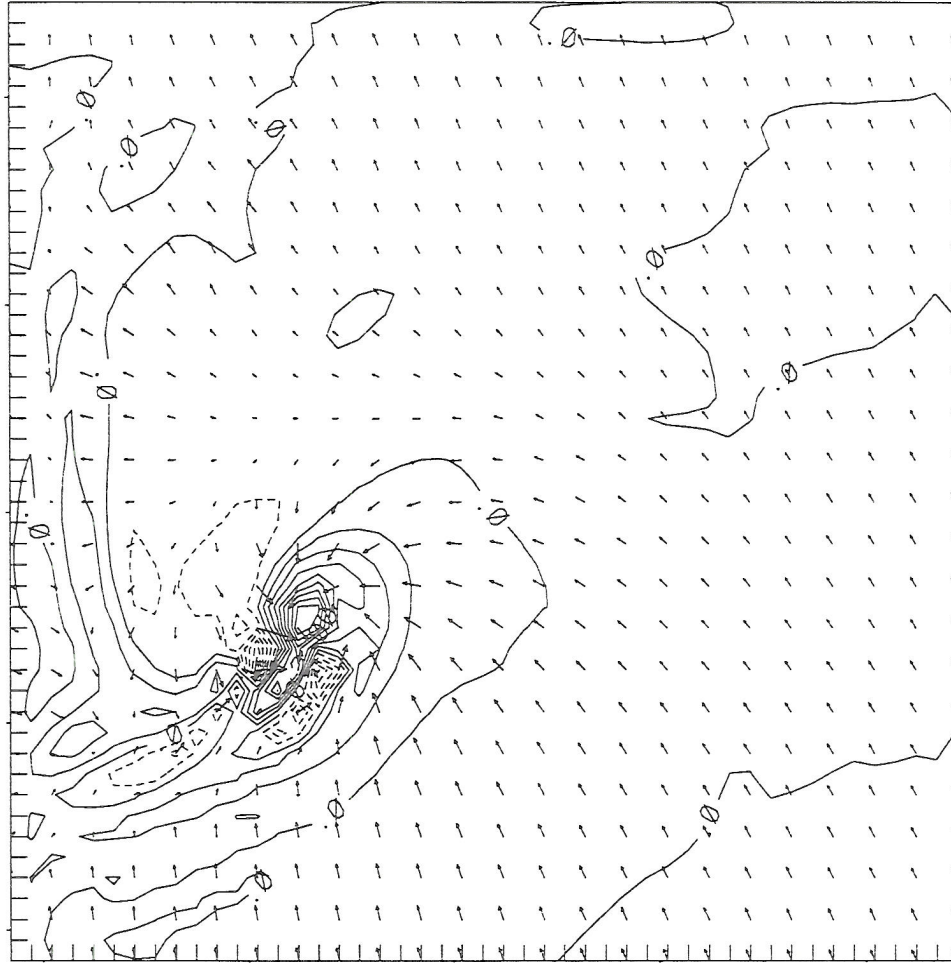


Figure 5.25: Grid #4; Horizontal, ground relative, wind vectors (a vector having a length equal to the distance between the tails of two vectors in the x direction has a magnitude of 52.0m/s) and the vertical motion, both at 50m and 36900s.

around the back side of the storm, due to the precipitation getting caught in the storms' rotation, causing the hook echo.

At 36900s, 2215 UTC, the material curve (Figure 5.23) bounded the rotation at 50m with a circulation value of  $3.0 \times 10^5 \text{ m}^2/\text{s}$ . The decrease from the maximum was due to surface stresses acting on the curve.

The horizontal vorticity vectors were pointing from the downdraft towards the updraft. This happened to the west and northwest of the updraft maximum, as can be seen in Figure 5.24. The divergent downdraft was very prominent in the horizontal wind field (Figure 5.25), and it covered a large region north of the updraft. The rain water field can be seen in Figure 4.23d.

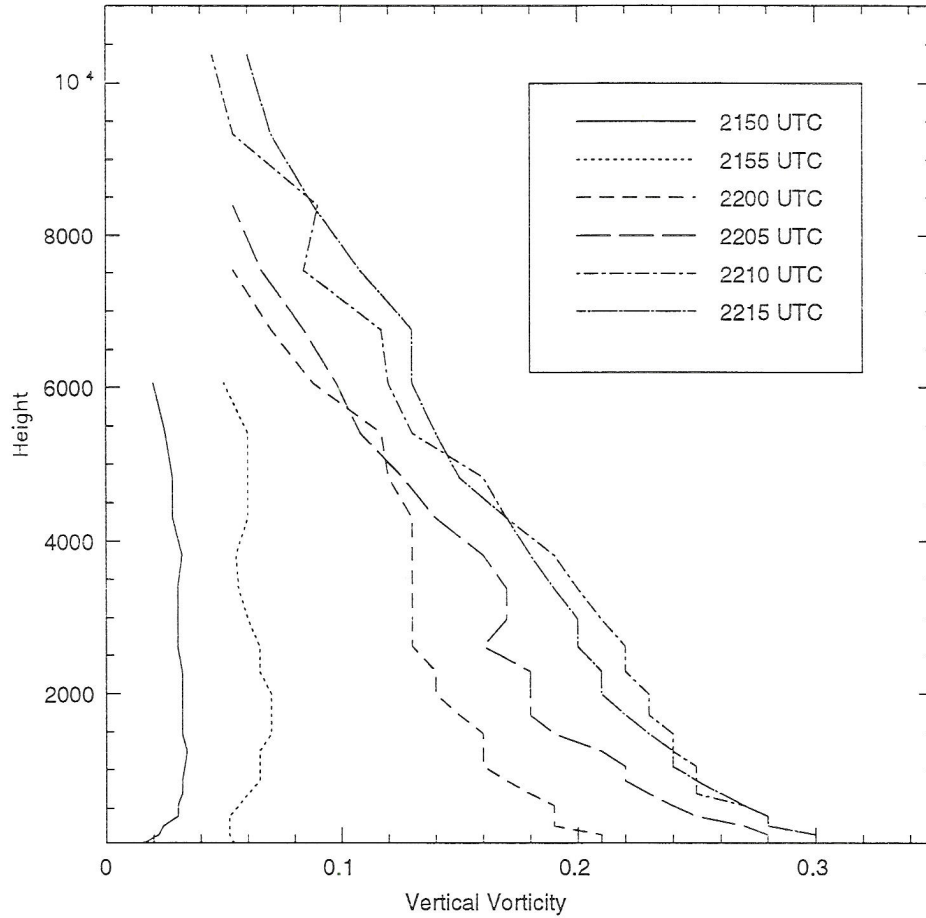


Figure 5.26: Vertical profile of the vertical vorticity maximum in Grid #5 for various times. The height is in meters and vorticity is  $s^{-1}$ .

The evolution of vertical vorticity with height was similar to the May 15, 1991 case. From 2150 UTC to 2155 UTC vertical vorticity increased in the lower levels (Figure 5.26). Five minutes later, low level vorticity increased due to positive tilting of horizontal vorticity in the downdraft. This was followed by strong horizontal convergence. The resulting cyclonic circulation was vertically transported by the updraft. This process continued to 2215 UTC at which time the analysis ended. The only difference between the April case compared to the May case was the absence of a second maximum in vertical vorticity.



### 5.7 Summary of the April 26, 1991 Tornado Genesis Process

The supercell thunderstorm exhibited significant changes from 2200 UTC to 2215 UTC, as seen in Figure 4.23. The large hook echo formed rapidly and the 50.0m horizontal wind speeds in the cyclonic circulation increased from just under 30m/s to just over 50m/s.

Similar to the May 15, 1991 simulation, vertical vorticity associated with the dry line bulge was horizontally converged by the strong storm. The beginnings of rotation at 50m were evident at 2200 UTC (Figure 4.23a).

Intensification of the vortex occurred when the forward precipitation downdraft wrapped around to the rear flanks of the storm. Was horizontal vorticity in the first few hundred meters being positively tilted in the downdraft similar to the May simulation?

Results from the material curve analysis indicate that the horizontal vorticity (with an approximate magnitude of  $5 \times 10^{-2} \text{ s}^{-1}$  to  $6 \times 10^{-2} \text{ s}^{-1}$  in the first two model layers in Grid #5 at 2215 UTC) was positively tilted in the forward downdraft in the lowest few hundred meters. This produced positive vertical vorticity that was intensified by the strong convergence (maximum convergence was  $8.8 \times 10^{-2} \text{ s}^{-1}$  in Grid #5 at 2215 UTC at 50m) in the horizontal plane. As the downdraft wrapped around the back side of the storm the vortex intensified. This was a result of horizontal vorticity being tilted in a larger region.

All of the tilting was in the forward downdraft. The rear flank downdraft was absent in the horizontal winds at 50.0m at 2215 UTC. The material curve analysis demonstrated the lack of rear flank downdraft air being ingested into the surface vortex. Recall, for the May case, the rear flank downdraft was ingested into the tornado.

A thirty minute circulation analysis could not be done due to the rapid speed of Grid #4. As a result, the author can only speculate on the evolution of circulation on the material curve from 2145 UTC to 2200 UTC. The average rate of change of circulation for the simulated April tornado was approximately  $7 \times 10^4 \text{ m}^2 / 400 \text{ s}$  (this value is just under twice that for the simulated May tornado). If this value remain fixed from 2145 UTC (35100s) to 2209 UTC (36550s) then the value of circulation at 2145 UTC would be approximately  $1 \times 10^5 \text{ m}^2 / \text{s}$  (the same as in the simulated May tornado). This suggests that the baroclinic

zone set up by the April supercell was stronger than the May supercell and caused a more intense tornado.

## Chapter 6

### SUMMARY AND CONCLUSIONS

#### 6.1 Summary of Both Cases

When these simulations were begun, there was no guarantee that the model would be able to explicitly form deep tropospheric convection without the aid of cumulus parameterization, warm bubbles or any other sophisticated data assimilation technique.

When both simulations were first done, the soil moisture was initialized horizontally homogeneous. No dry line developed in either case. The moisture gradient seen at 1200 UTC near the surface remained essentially unchanged in the afternoon. A simulated dry line did form when the the initial fields contained a soil moisture mapping based on the past few months of observed precipitation.

The ability of the model to produce convection explicitly, had a dependence on the surface characteristics; soil type, variable soil moisture, and variable vegetation. In both these simulations only one soil type was used in the entire model domain. The author wonders what impact a variable soil type data set, for the United States, would have on simulated mesoscale processes.

Having the surface characteristics initialized as realistic as possible, allowed the surface to heat up and warm the boundary layer the most in a relatively long and thin region. Vertical motion developed in the warm region and low level horizontal convergence developed in response to it. The horizontal convergence enhanced the moisture gradient as the dry line formed in both simulations.

As the dry lines developed, the horizontal winds backed in the moist boundary layer to the east. This resulted in a larger vertical shear profile. Before the dry lines formed, the winds near the surface were from the south and above the boundary layer they were



from the southwest. When the dry lines were developing, the winds near the surface were southeasterly and above the boundary layer they remained from the southwest. Vertical motion associated with the dry lines, and large values of CAPE, formed deep tropospheric convection.

As a supercell thunderstorm evolved from the convection an eastward bulge formed in the dry line for both cases. Organized horizontal rotation at the nose of the bulge was evident near the surface for both cases.

The enhanced vertical shear ultimately fed the storms' rotation. The evolution of the hook echo and associated downdraft was influenced by thunderstorm rotation. As the precipitation downdraft expanded cyclonically around the back side of the storm, tilting of horizontal vorticity occurred in a larger horizontal area in the lowest few hundred meters. The intensification of the tornado in the boundary layer occurred simultaneously with the expanding precipitation downdraft.

A necessary, but not sufficient, condition for tornadic thunderstorms to form in both simulations was the inclusion of proper surface characteristics, ie, variable vegetation and a soil moisture profile based on observed precipitation. The initial instability of the troposphere and solar heating allowed large values of CAPE to form and fuel the parent thunderstorms.

Both simulated tornadoes formed upward from the boundary layer. This was a result of positive tilting of horizontal vorticity in the downdrafts within the lowest few hundred meters. If one or both of the simulated tornadoes was in cyclostrophic balance, in the boundary layer, then the value of horizontal convergence must have been zero. Since the horizontal convergence was not zero in either tornado then the horizontal winds were not in cyclostrophic balance. Therefore, the dynamic pipe effect could not have formed a tornado down from the parent thunderstorm.

Material curve analysis suggests the thunderstorms increased the circulation of a material curve by baroclinic processes. In both simulations the horizontal vorticity, in the lowest few hundred meters, pointed towards the west or southwest ahead of the storm. When the horizontal vorticity vectors were influenced by the storm they ended up pointing

towards the south. The southward pointing vectors were in a more favorable position to be positively tilted by the downdraft. The vertical vorticity generated by the tilting was converged and amplified exponentially, over a finite time interval, to allow the tornado to form.

## 6.2 Conclusions

A conceptual model, viewed from above, of the tornado genesis process based on both simulations is presented in Figure 6.1. As seen in Figure 6.1a a convective line was triggered by the dry line. A supercell thunderstorm evolves and a noticeable bulge forms in the dry line. The forward flanking precipitation downdraft began to form as did the beginning vortex on the nose of the bulge, denoted by BV in Figure 6.1b. As the storm moves away from the dry line the rotation associated with the low-level mesocyclone began to wrap the precipitation downdraft towards the rear flanks. The expanding downdraft provided more rotation for the intensifying vortex, denoted by IV in Figure 6.1c. In the final stages, the hook echo was fully formed and bounded the mature vortex, denoted by MV in Figure 6.1d. The gust front, trailing from the mature tornado, is the leading edge of downdraft air rotating cyclonically towards the storms' southern flanks.

A three dimensional conceptual model is presented in Figure 6.2. East of the dry line low-level horizontal vortex lines point towards the southwest (see Figure 6.2a). The beginning vortex was associated with pre-existing vertical vorticity on the dry line bulge. Further to the north, vortex lines were being tilted upward at the southern side of the forward precipitating downdraft, as seen in Figure 6.2b. In time, the storm moved away from the dry line. The precipitation downdraft began to wrap around the intensifying vortex towards the rear flanks. A larger region of horizontal vorticity was tilted (Figure 6.2c) into the vertical and horizontally converged to feed the tornado as it evolved upward into the parent thunderstorm. Finally, the hook echo bounded the mature tornado. Positive tilting of horizontal vorticity in the downdraft occurred to the north, west, and south of the vortex (Figure 6.2d). The vertical vorticity produced was horizontally converged to feed

the mature tornado. At that time the tornado extended from the surface to the top of the parent thunderstorm.

### 6.3 Future Research

These simulations have shed some light on the formation of tornadoes. It is important to state that the ideas presented in this thesis, dealing with the formation of the two simulated tornadoes, are only valid for these two storms. There are more mesoscale and thunderstorm processes that need to be addressed. A brief discussion of them follows;

- As the dry lines developed, especially in the April simulation, the winds to the east backed in time. The new vertical wind profile may have had a significant impact on thunderstorm rotation. Perhaps the old vertical wind profile could not support supercell storms and the new vertical wind profile would. An idealized simulation could examine the impact these wind profiles may have on supercell dynamics.
- Both dry lines acted as efficient conveyer belts, transporting moist air from the lower boundary layer to levels above the boundary layer, prior to thunderstorm formation. Moist layers deepened downwind of the dry lines. What impact does this have on thunderstorms that form on a dry line and move toward the northeast into a deeper moist layer?
- Both simulated dry lines had an eastward bulge underneath a supercell thunderstorm. Associated with these bulges was a region of vertical vorticity. Both thunderstorms were able to horizontally converge the vorticity. The result was the beginning of rotation. Although not the main vorticity source for either tornado, the origins of the vertical vorticity on the dry line bulge should be investigated.
- As convection above the dry line was developing, the moisture gradient increased. Was this a result of the warm convective towers lowering the pressure at the surface? The lower pressure would cause an increase in the horizontal pressure gradient and



enhance the convergence, of moist air to the east and dry air to the west, into the dry line.

- Outflow from the precipitation downdraft accelerated west toward the dry line. This occurred in both simulations. How does this outflow interact with the dry line?
- It is quite possible for outflow from one thunderstorm to interact with a nearby storm. Is there tilting of horizontal vorticity in such outflows? If so, can the vertical vorticity produced be amplified into tornadic strength?
- The 45.0 km north-south line of initial convection on the dry line did not split into a right and left mover. The evolution of the line was quite different from a simulated warm bubble rising to form a supercell. This suggests that the size and shape of the forcing influences the splitting process. An idealized simulation of convection with different forcing shapes and sizes can help answer this.
- Were the strongest horizontal winds on the southeast side of the tornado simply due to the movement of the tornado? This appears to be the case for the two simulated tornadoes. Could there be another mechanism?
- How is the pressure field maintained in a tornado?
- An analysis of the central downdraft in the two tornadoes should be done. What was causing the downward motion? Does the sinking affect the surface pressure? What role, if any, does the sinking play in forming a multiple vortex tornado?
- Would the introduction of a seventh nested grid with a horizontal grid spacing of 30.0m resolve the evolution of multiple vortices and the occurrence of a condensation funnel down to the lowest model level?
- What mechanism controls the radius of maximum horizontal winds in a tornado?
- More tornadoes should be simulated using a procedure similar to the one in this study. This will allow one to demonstrate whether one process leading to tornado genesis occurs more often than another.

- Do anti-cyclonic tornadoes form in a manner similar to cyclonic tornadoes?
- Simulations of rotating non-tornadic thunderstorms, using an initialization similar to this study, should be done. The results can be compared to rotating tornadic storms.
- Using the correct surface characteristics was a very important element to include in the simulations. This is an area that needs further study. Can the location and timing of deep tropospheric convection be improved by changing the surface features? Can tornadic thunderstorms, associated with dry lines, be eliminated by changing the surface properties?

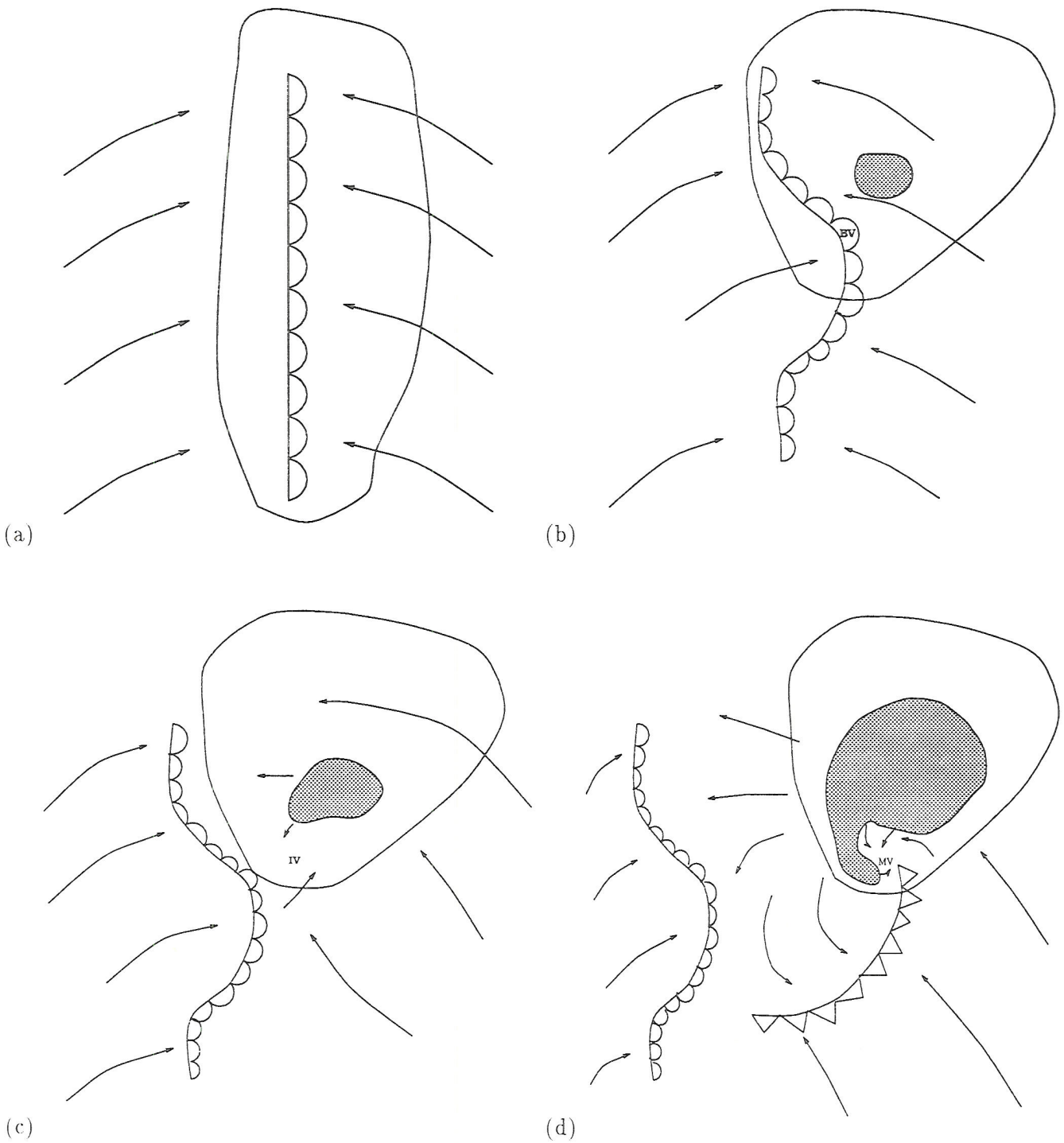


Figure 6.1: Time sequence of (a) convection initiated on dry line (b) dry line bulge forming (c) forward precipitation downdraft beginning to wrap around the rear side of the storm and (d) fully developed hoop echo and trailing gust front. In the figure the half moons denotes the dry line. The precipitation downdraft is shown as the shaded region along with surface streamlines. The large region bounded by the solid contour is the anvil canopy.



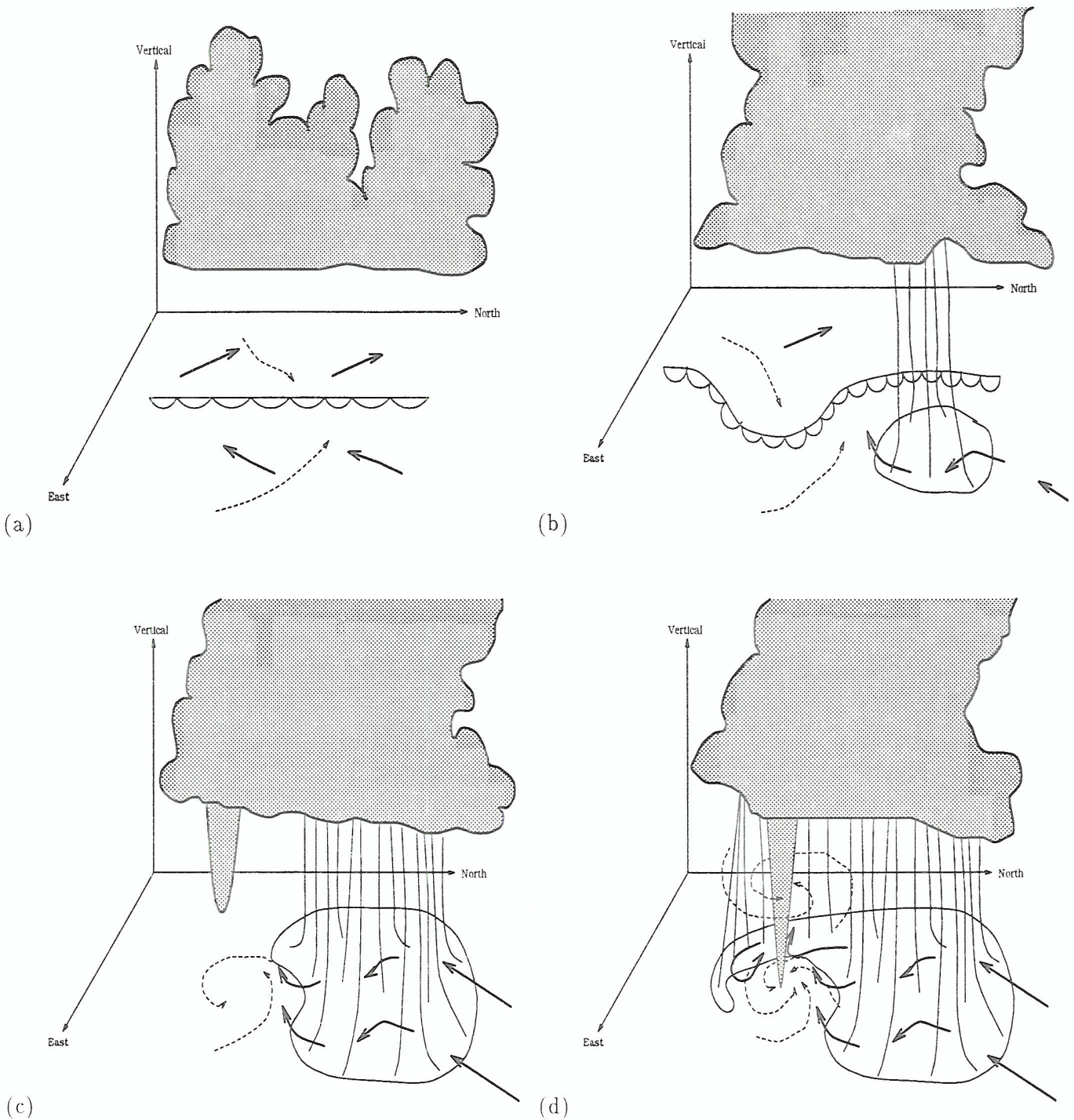


Figure 6.2: Time sequence of (a) convection initiated on dry line (b) dry line bulge forming (c) forward precipitation downdraft beginning to wrap around the rear side of the storm and (d) fully developed hoop echo. In the figure the half moons denotes the dry line. Bold solid lines with arrows are sections of vortex lines in the lowest few hundred meters. Dashed lines are surface stream lines. The surface signature of the rainfall is shown as the continuous closed line. The parent storm and tornado are shaded.

## Chapter 7

### REFERENCES

- Arakawa, A., and V. Lamb, 1981: A potential enstrophy and energy conserving scheme for the shallow water equations. *Mon. Wea. Rev.*, **109**, 18-36.
- Avissar, R., and R.A. Pielke, 1989: A parameterization of heterogeneous land surfaces for atmospheric numerical models and its impact on regional meteorology. *Mon. Wea. Rev.*, **117**, 2113-2136.
- Benjamin, S.G., and T.N. Carlson, 1986: Some effects of surface heating and topography on the regional severe storm environment. Part I: 3-D simulations. *Mon. Wea. Rev.*, **114**, 330-343.
- Bluestein, H.B., 1983: Measurements in the vicinity of severe thunderstorms and tornadoes with toto: 1982-1983 results. Preprints, *13th Conf. on Severe Local Storms*, Boston, MA, Amer. Meteor. Soc., 89-92.
- Brady, R.H., and E.J. Szoke, 1989: A case study of nonmesocyclone tornado development in northeast Colorado: Similarities to waterspout formation. *Mon. Wea. Rev.*, **117**, 843-856.
- Brown, R.A., L.R. Lemon, and D.W. Burgess, 1978: Tornado detection by pulsed doppler radar. *Mon. Wea. Rev.*, **106**, 29-38.

- Burgess, D.W., 1976: Single-doppler radar vortex recognition: Part 1: Mesocyclone signature, in Preprints, *17th Conference on Radar Meteorology*, pp. 97-103, American Meteorological Society, Boston, Mass.
- Clark, T.L., and R.D. Farley, 1984: Severe downslope windstorm calculations in two and three spacial dimensions using anelastic interactive grid nesting: A possible mechanism for gustiness. *J. Atmos. Sci.*, **41**, 329-350.
- Copeland, J.H., 1995: Impact of soil moisture and vegetation distribution on July 1989 climate using a regional climate model. Atmospheric Science Paper No. 574, 124pp. [Available from the Dept. of Atmospheric Science, Colorado State University, Fort Collins, CO 80523.]
- Cotton, W.R., M.A. Stephens, T. Nehrkorn, and G.J. Tripoli, 1982: The Colorado State University three-dimensional cloud/mesoscale model-1982. Part II: An ice phase parameterization. *J. de Rech. Atmos.*, **16**, 295-320.
- Cotton, W.R., and R.A. Anthes, 1989: *Storm and Cloud Dynamics.*, Academic Press, Inc., San Diego. International Geophysics Series. Vol. 44., 883 pp.
- Cotton, W.R., G.J. Tripoli, R.M. Rauber, and E.A. Mulvihill, 1986: Numerical simulation of the effect of varying ice crystal nucleation rates and aggregation process on orographic snowfall. *J. Climate Appl. Meteor.*, **25**, 1658-1680.
- Davies, J.M., 1993: Wind and instability parameters associated with supercell and non-supercell tornado events in the southern high plains. *17th Conf. Severe Local Storms.*, St. Louis, MO, Amer. Meteor. Soc.
- Davies-Jones, R., and H.E. Brooks, 1993: Mesocyclone genesis from a theoretical perspective. *The Tornado: Its Structure, Dynamics, Prediction and Hazard, Geophys. Monogr.*, No. **79**, Amer. Geophys. Union, 105-114.



- Davies-Jones, R.P., 1986: Tornado Dynamics, in Thunderstorm Morphology and Dynamics, 2nd ed., edited by E. Kessler, pp 197-236, University of Oklahoma Press, Norman.
- Grasso, L.D., and W.R. Cotton, 1995: Numerical Simulation of a Tornado Vortex. *J. Atmos. Sci.*, **52**, 1192-1203.
- Grasso, L.D., 1992: A numerical simulation of tornado genesis. Atmospheric Science Paper No. 495, 102pp. [Available from the Dept. of Atmospheric Science, Colorado State University, Fort Collins, CO 80523.]
- Hane, C.E., C.L. Ziegler, and H.B. Bluestein, 1993: Investigation of the dryline and convective storms initiated along the dryline: Field experiments during COPS-91. *Bull. Amer. Meteor. Soc.*, **74**, 2133-2145.
- Howells, P.A. et al. 1988: A comparative study of atmospheric and laboratory analogue numerical tornado vortex models. *Q.J.R. Meteorol. Soc.*, **114**, 801-822.
- Klemp, J.B. and R.B. Wilhelmson, 1978a: The simulation of three-dimensional convective storm dynamics. *J. Atmos. Sci.*, **35**, 1070-1096.
- Klemp, J.B. and R.B. Wilhelmson, 1978b: Simulations of right and left moving storms produced through storm splitting. *J. Atmos. Sci.*, **35**, 1097-1110.
- Klemp, J.B., R.B. Wilhelmson, and P. Ray, 1981: Observed and numerically simulated structure of a mature supercell thunderstorm. *J. Atmos. Sci.*, **38**, 1558-1580.
- Klemp, J.B., and R. Rotunno, 1983: A study of the tornadic region within a supercell thunderstorm. *J. Atmos. Sci.*, **40**, 359-377.
- Lewellen, W.S., 1993: Tornado vortex theory. *The Tornado: Its Structure, Dynamics, Prediction and Hazard*. Geophys. Monogr., No. **79**, Amer. Geophys. Union, 19-39.
- Lilly, D.K., 1962: On the numerical simulation of buoyant convection. *Tellus*, **14**, 148-172.

- Lilly, D.K., 1982: The development and maintenance of rotation in convective storms. Topics in Atmospheric and Oceanographic Sciences: Intense Atmospheric Vortices. L. Bengtsson and J. Lighthill, Eds., Springer-Verlag, Berlin and Heidelberg, 149-182.
- Lilly, D.K., 1986a: The structure, energetics and propagation of rotating convective storms. Part I: Energy exchange with the mean flow. *J. Atmos. Sci.*, **43**, 113-125.
- Lilly, D.K., 1986a: The structure, energetics and propagation of rotating convective storms. Part II: Helicity and storm stabilization. *J. Atmos. Sci.*, **43**, 126-140.
- Loveland, T.R., J.W. Merchant, D.O. Ohlen, and J.F. Brown, 1991: Development of a land-cover characteristics database for the conterminous U.S. *Photo. Eng. Rem. Sens.*, **57**, 1453-1463.
- Ludlam, F.H., 1963: Severe local storms: A review. *Meteor. Monogr.*, **5**, No. 27, Amer. Met. Soc., Boston.
- Mahrer, Y., and R.A. Pielke, 1977: A numerical study of the airflow over irregular terrain. *Beitr. Phys. Atmos.*, **50**, 98-113.
- Newton, C.W. et al., 1978: Severe Thunderstorms: Their nature and their effects on society. *Interdiscip. Sci. Rev.*, **3**, 71-85.
- Pielke, R.A., W.R. Cotton, R.L. Walko, C.J. Tremback, W.A. Lyons, L.D. Grasso, M.E. Nicholls, M.D. Moran, D.A. Wesley, T.J. Lee, J.H. Copeland, 1992: A comprehensive meteorological modeling system-RAMS. *Metero. and Atmos. Phys.*, **49**, 69-91.
- Rhea, J.O., 1966: A study of thunderstorm formation along dry lines. *J. Appl. Meteor.*, **5**, 58-83.
- Rotunno, R., and Klemp, J.B., 1982: The influence of the shear-induced pressure gradient on thunderstorm motion. *Mon. Wea. Rev.*, **110**, 136-151.

- Rotunno, R., and Klemp, J.B., 1985: On the rotation and propagation of a simulated supercell thunderstorm. *J. Atmos. Sci.*, **42**, 271-292.
- Schaefer, J.T., 1974: A simulative model of dryline motion. *J. Atmos. Sci.*, **31**, 956-964.
- Schlesinger, R.E., 1978: A three-dimensional numerical model of an isolated thunderstorm: Part I. Comparative experiments for variable ambient wind shear. *J. Atmos. Sci.*, **35**, 690-713.
- Schlesinger, R.E., 1980: A three-dimensional numerical model of an isolated thunderstorm: Part II. Dynamics of updraft splitting and mesovortex couplet evolution. *J. Atmos. Sci.*, **37**, 395-420.
- Shaw, B.L., 1995: The effect of soil moisture and vegetation heterogeneity on a great plains dryline: A numerical study. Atmospheric Science Paper No. 576, 93pp. [Available from the Dept. of Atmospheric Science, Colorado State University, Fort Collins, CO 80523.]
- Smagorinsky, J., 1963: General circulation experiments with the primitive equations. Part 1: The basic experiment. *Mon. Wea. Rev.*, **91**, 99-164
- Smith, R.K., and L.M. Leslie, 1979: A numerical study of tornado genesis in a rotating thunderstorm. *Quart. J. Roy. Meteor. Soc.*, **105**, 107-127.
- Sun, W.Y., and C.C. Wu, 1992: Formation and diurnal variation of the dryline. *J. Atmos. Sci.*, **49**, 1606-1618.
- Tremback, C.J., and R. Kessler, 1985: A surface temperature and moisture parameterization for use in mesoscale numerical models. Preprints, *7th Conference on Numerical Weather Prediction*, 17-20 June 1985, Montreal, Canada, AMS.



- Tremback, C.J., G.J. Tripoli, and W.R. Cotton, 1985: A regional scale atmospheric numerical model including explicit moist physics and a hydrostatic time-split scheme. Preprints, *7th Conference on Numerical Weather Prediction*, 17-20 June 1985, Montreal, Canada, AMS.
- Tripoli, G.J., and W.R. Cotton, 1981: The use of ice-liquid water potential temperature as a thermodynamic variable in deep atmospheric models. *Mon. Wea. Rev.*, **109**, 1094-1102.
- Tripoli et al., 1982: The Colorado State University three dimensional cloud mesoscale model, 1982. Part I: General theoretical framework and sensitivity experiments. *J. Rech. Atmos.*, **16**, 185-220.
- Tripoli, G.J., 1986: A numerical investigation of an orogenic mesoscale convective system. Ph.D. dissertation, Colorado State University, Dept. of Atmospheric Science, Fort Collins, Colorado 80523, 290 pp. (Atmospheric Science Paper No. 401).
- Tripoli et al., 1989a: A numerical study of an observed orogenic mesoscale convective system. Part 1. Simulated genesis and comparison with observations. *Mon. Wea. Rev.*, **117**, 273-304.
- Tripoli et al., 1989b: A numerical study of an observed orogenic mesoscale convective system. Part 2. Analysis of governing dynamics. *Mon. Wea. Rev.*, **117**, 305-328..
- Uccellini, L.W., and D.R. Johnson, 1979: The coupling of upper and lower tropospheric jet streaks and implications for the development of severe convective storms. *Mon. Wea. Rev.*, **107**, 682-703.
- Vasiloff, S.V., 1993: Single-doppler radar study of a variety of tornado types. *The Tornado: Its Structure, Dynamics, Prediction and Hazard*, *Geophys. Monogr.*, No. **79**, Amer. Geophys. Union, 223-232.

- Wakimoto, R.M. and J.W. Wilson, 1989: Non-supercell tornadoes. *Mon. Wea. Rev.*, **117**, 1113-1140.
- Ward, N.B., 1972: The exploration of certain features of tornado dynamics using a laboratory model. *J. Atmos. Sci.*, **29**, 1194-1204.
- Walko, R.L. and R. Gall, 1986: Some effects of momentum diffusion on axisymmetric vortices. *J. Atmos. Sci.*, **43**, 2137-2148.
- Walko et al., 1995: New RAMS cloud microphysics parameterization. Part I: The single moment scheme. *Atmos. Res.*, **38**, 29-62.
- Weisman, M., and J. Klemp, 1982: The dependence of numerically simulated convective storms on vertical wind shear and buoyancy. *Mon. Wea. Rev.*, **110**, 504-520.
- Wetzel, P.J., and J.T. Chang, 1988: Evapotranspiration from nonuniform surfaces: A first approach for short-term numerical weather prediction. *Mon. Wea. Rev.*, **116**, 600-621.
- Wicker, L.J., and R.B. Wilhelmson, 1995: Simulation and Analysis of tornado development and decay within a three dimensional supercell thunderstorm. *J. Atmos. Sci.*, **52**, 2675-2703.
- Wilhelmson, R., 1974: The life cycle of a thunderstorm in three dimensions. *J. Atmos. Sci.*, **31**, 1629-1651.
- Ziegler et. al., 1994: A modeling study of a dry line. *J. Atmos. Sci.*, **52**, 263-285.